THE APPLICATION OF REAL-TIME PHOTOELECTRON SPECTROSCOPY TO CARBON-BASED SEMICONDUCTORS

THESIS

submitted to

Aberystwyth University

by

Owain Rhys Roberts *MPhys (Hons)*

In candidature for the degree of

Philosophiæ Doctor

September 2009

DECLARATION

This work has not previously been accepted in substance for any degree and is not being concurrently submitted in candidature for any degree.

Signed …… (candidate)

Date ……

STATEMENT 1

This thesis is the result of my own investigations, except where otherwise stated. Where correction services have been used, the extent and nature of the correction is clearly marked in a footnote(s).

Other sources are acknowledged by footnotes giving explicit references. A bibliography is appended.

Signed …… (candidate)

Date ……

STATEMENT 2

I hereby give consent to my thesis, if accepted, to be made available for photocopying and for inter-library loan, and for the title and summary to be made available to outside organisations.

Signed …… (candidate)

Date ……

ACKNOWLEDGEMENTS

There are many people without whose help and support this work would not have been possible. First and foremost I would like to thank my supervisor Prof. Andrew Evans for giving me the opportunity to study this field, for all his useful advice, discussions and for tirelessly working to secure continued funding for this work. During my time at the Institute of Mathematics and Physics I have had the opportunity to work with many people. However, I would like to mention a few in particular. Dr. David Langstaff has given me invaluable support relating to instrumentation and data processing and has taught me a great deal. Dr. Stephen Evans was always on-hand to provide much needed guidance. Dr. Alex Vearey-Roberts gave valuable help and encouragement during my first year of study. Gruffudd Williams, Geraint Jones and Andrew McGlynn are great co-workers and made synchrotron beamtimes a much more enjoyable experience. Dave Francis and John Parry in the mechanical workshop along with Matt Gunn provided invaluable technical support and advice and greatly enhanced my ability to conduct experimental work. I would also like to acknowledge Dr. Nigel Poolton, Dr. Sunil Patel and Dr. Vin Dhanak and the rest of the Synchrotron Radiation Source (SRS) staff at Daresbury Laboratory. I also acknowledge the following funding sources: the Engineering and Physical Sciences Research Council (EPSRC); the Aberystwyth University Garrod Thomas Scholarship Fund and Element Six Ltd, Ascot, UK. However, my greatest thanks is reserved to my family and in particular my parents who have been unwavering in their support and encouragement throughout the years. Finally, I would like to thank Hawys for her continued support and care but above all – for her patience!

ABSTRACT

This thesis reports on the development of a new method for studying the growth of thin films and the dynamics of surface processes. Real-time photoelectron spectroscopy enabled by advances in electron detection technology has been applied to the study of metal overlayers on a p-type CVD (001) diamond single crystal and tin (II) phthalocyanine (SnPc) overlayers on Si (111), GaAs (001) and polycrystalline Au substrates. The performance of the Aberystwyth real-time electron spectroscopy (REES) system is also reviewed.

Temperature-dependent real-time photoelectron studies of an oxygen-terminated boron-doped CVD (001) single crystal diamond is performed with a fully reversible temperature dependent Fermi level shift of ~ 1 eV observed on the oxygen-terminated 1 x 1 surface up to a temperature of 700 °C. This shift is found to correlate with oxygen coverage where the maximum reversible shift reduces in magnitude with decreasing oxygen coverage.

The growth of aluminium contacts on the (001) diamond surface is investigated with the formation of a Schottky contact for which current-voltage measurements yield a barrier height of 1.05 eV and an ideality factor of 1.4. Real-time measurements monitor the formation of the contact revealing the transition from layered to clustered growth of the aluminium film during *in vacuo* deposition. During annealing of the contact to 860 °C real-time measurements reveal a direct correlation between the transition from Schottky to Ohmic behaviour and the formation of interfacial carbide at 482 °C.

Deposition of iron on the (001) diamond surface is found to form an uniform layer with iron carbide species present at the interface. Subsequent annealing of the diamond to 850 °C results in the formation of a graphite layer with iron acting as a catalyst for the graphitisation process. AFM and NEXAFS of the resulting graphite layer reveal an ordered surface. A mechanism is proposed for the graphitisation.

Finally, the growth of SnPc is investigated on Si (111), GaAs (001) and polycrystalline Au. Growth is found to proceed in two stages and re-organisation of the molecules is detected by real-time measurements and found to continue after deposition for a period of up to 30 minutes. Studies also suggest that substrate temperature affects the angle of stacking and the rate of molecular re-organisation. A theoretical molecular model for this re-organisation was successfully developed.

PUBLICATIONS

D. A. Evans, O. R. Roberts, G. T. Williams, A. R. Vearey-Roberts, F. Bain, S. Evans, D. P. Langstaff, D. J. Twitchen, *Diamond–metal contacts: interface barriers and real-time characterization*, Journal of Physics: Condensed Matter **21** (2009) 364223

D. P. Langstaff, D. A. Evans, O. R. Roberts, X. Zhu, *Progress on the Aberystwyth electron counting array*, Nuclear Instruments and Methods in Physics Research Section A: Accelerators, Spectrometers, Detectors and Associated Equipment **604** (2009) 133-135

D. A. Evans, O. R. Roberts, A. R. Vearey-Roberts, D. P. Langstaff, D. J. Twitchen, M. Schwitters, *Direct observation of Schottky to Ohmic transition in Al-diamond contacts using real-time photoelectron spectroscopy*, Applied Physics Letters **91** (2007) 132114

TABLE OF CONTENTS

Chapter 1
Introduction

Materials science plays a key role in the development of technologies which underpin most aspects of modern life. The range of materials used by engineers is constantly expanding and new materials are continually being developed and applied to a diverse range of applications ranging from spacecraft to solar cells. However, if the potential of new materials is to be fully realised it is vital that their fundamental characteristics and properties are properly understood. Therefore the availability of efficient and effective characterisation techniques is of key importance. For example, techniques such as X-ray absorption spectroscopy and X-ray diffraction are used to study and understand the corrosion of aluminium used in aircraft manufacturing [1, 2].

Many functional materials depend on processes at interfaces and on surfaces, therefore specific techniques are needed to study their effects. Such processes include surface chemistry (in the case of catalysis and cutting tools) and electronic behaviour (in the case of photovoltaic cells and light emitting diodes). The semiconductor industry

(which in 2008 had a market worth US$249bn) [3] is an excellent example of an industry that is heavily reliant upon effective surface and interface characterisation of materials and devices. Determining and manipulating the bulk electronic and optoelectronic properties is an important aspect of semiconductor material development and can be achieved by conductivity measurements and the study of crystal defects and doping levels. For example, defect states and charge dynamics can be studied using optical techniques such as optical luminescence [4-7]. However, the way that charge carriers transit across interfaces is a critical aspect in the operation of all electronic devices. For example, for a traditional metal-semiconductor junction it is the alignment of the energy levels at the interface and the presence of surface states which determines the characteristics of that device. Many devices such as photovoltaic cells now rely on large multi-layer architectures. As these devices are miniaturized the decrease in interlayer thickness means that the effect of interface processes on their operational characteristics is significantly enhanced.

Such developments have continually driven forward the development of new characterisation techniques and have demanded that established techniques acquire enhanced capabilities. The semiconductor industry benefited greatly from the advent of surface science techniques in the 1960s [8] since surfaces could be studied in much greater detail than was previously possible. The emergence of synchrotron facilities and other new photon sources during the same period accelerated these advances by opening up further possibilities, spawning new techniques, and extending the capabilities of existing techniques.

X-ray Photoelectron Spectroscopy (PES) is one such example. As a technique it has facilitated a greater understanding of semiconductor surfaces and made a great contribution to fields such as heterogeneous catalysis [9]. The PES technique, developed in the 1960s by Siegbahn *et al* [10] using X-ray laboratory sources (as XPS) has since been used with tunable X-ray sources in the form of soft x-ray photoelectron spectroscopy (SXPS) as well as laboratory ultra-violet sources as ultraviolet photoelectron spectroscopy (UPS) and is even applied as a form of microscopy (as Photoemission Electron Microscopy or PEEM) [11].

X-ray photoelectron spectroscopy is an ideal technique for the characterization of semiconductor surfaces and interfaces since its surface sensitivity gives information regarding the electronic states within the material to a depth of a few nanometres. This direct measurement of electrons emitted from the occupied states gives detailed information regarding chemical composition and makes it possible to construct a band alignment diagram for any given interface. Phenomena such as band bending can be accurately measured and the presence of surface states indirectly detected. Information is also provided regarding the growth mode and morphology of deposited thin films.

However, some limitations exist, including the fact that all experiments must be performed under Ultra High Vacuum (UHV) conditions primarily so that clean surfaces can be retained. There is also the requirement that the electron mean free path must be long enough for the electrons to be analysed and detected. This means that it can be difficult to apply this technique to real-world environments although there have been successful attempts in the development of systems which use differential pumping to allow a higher pressure (~ 1 mbar) to be maintained at the sample while still keeping

the analyser and detector at a low enough pressure for successful operation [12, 13]. Other techniques such as scanning probe microscopy are powerful probes of surface morphology and electrical characterisation but do not provide information regarding the atomic core levels. For a full understanding of the electronic configuration photoelectron spectroscopy must be used in order to observe changes in the electronic configuration of the occupied states.

While photoelectron spectroscopy has benefited from significant advancements in photon sources (such as synchrotron radiation) electron detection technology has not changed substantially since the first detectors were fitted to the first XPS machines in the 1960s. This has meant that the acquisition of photoelectron spectra continues to be an inherently slow process.

Effective signal detection is a key (and often neglected) part in the advancement of any experimental technique. This thesis will demonstrate how advanced detector technology developed at Aberystwyth has been used to enable the development of real-time photoelectron spectroscopy – an enhancement in which spectral features are imaged as snapshots (in tens of milliseconds) allowing the dynamics of surface processes and reactions to be followed in real-time. Within the wider field of materials characterisation there is now a great emphasis upon measurement of dynamics in both the time and spatial domain. For example, techniques such as extended X-ray absorption fine structure (EXAFS) [14] and Raman spectroscopy [15] are now also being applied in real-time.

Although the semiconductor industry is still largely based on inorganic semiconductor materials such as Si and GaAs there is an ever increasing interest in new semiconducting carbon-based materials. Carbon-based materials are currently at the forefront of many technological advances. Carbon fibre [16] has been in production for decades and is extensively used for a large range of high performance applications from sports equipment to aircraft and spacecraft. Carbon nanotubes [17] show great potential for applications such as polymer reinforcement, adsorption, catalysis, electronics and medicine while the recent discovery of graphene has sparked frantic research activity (current progress has been reviewed by Geim *et al* [18]). There is also a renewed interest in the electronic properties of carbon-based materials that exhibit semiconducting properties.

Diamond and organic small-molecules are two carbon-based semiconductors investigated in this thesis. Diamond is a wide band gap material that has considerable potential for use in high power and high temperature applications as well as in various extreme environments. The interest in small-molecules and polymers arises from their comparatively low production and processing costs, low-toxicity and their optical band gaps which allow light absorption and emission in the visible range, making them suitable for a range of optical and lighting applications. They have also been used to extend and enhance current inorganic devices by incorporation into hybrid organic-inorganic devices [19].

This work will demonstrate how real-time photoelectron spectroscopy can be used to study these advanced carbon-based semiconducting materials in greater detail. The capabilities of the Aberystwyth real-time electron spectroscopy (REES) system will be

explored and temperature-dependent real-time photoelectron spectroscopy demonstrated as a novel technique that can provide an unique insight into the processes that occur on the surfaces of these materials.

Chapter 2 will introduce X-ray Photoelectron Spectroscopy as a technique along with other complementary characterization techniques employed during the course of these studies. Chapter 3 will present the photon sources and instrumentation used to conduct the experiments along with the enhancements afforded by new detector technology developed at Aberystwyth. The real-time electron spectroscopy (REES) system will be introduced and some of its capabilities demonstrated. In chapter 4 diamond will be introduced as an electronic material and experimental data relating to the application of real-time photoelectron spectroscopy to clean p-type semiconducting single crystal (001) diamond will be presented. In chapter 5 the main focus will be the study of metal-diamond contacts that are a fundamental part of any diamond-based electronic device. This will highlight the ability of the technique to follow chemical state changes at interfaces and includes the catalytic effect of iron overlayers on the graphitisation of diamond at high temperatures. Chapter 6 will concentrate on the application of real-time photoelectron spectroscopy to organic thin films and its ability to yield information regarding the growth modes of thin vacuum deposited films of tin (II) phthalocyanine (SnPc). The molecular re-organisation of these molecules on different substrates and at elevated temperatures will be investigated. Chapter 7 will contain conclusions and outline the opportunities for further work.

References

1. Greegor, R.B. and F.W. Lytle, *Investigation of Cr, Cu and Zn sites in corroded/uncorroded aluminum by X-ray absorption spectroscopy (XAS).* Corrosion Science, 1997. **39**(12): p. 2095-2116.
2. Staron, P., et al. *Residual stresses in laser beam welded butt joints of the airframe aluminium alloy AA6056*. in *7th European Conference on Residual Stresses (ERCS 7)*. 2006. Berlin, GERMANY: Trans Tech Publications Ltd.
3. *Semiconductor Industry Association Factsheet.* [cited 2009 30 July 2009]; Available from: http://www.sia-online.org/cs/industry_resources/industry_fact_sheet.
4. Evans, D.A., et al., *Determination of the optical band-gap energy of cubic and hexagonal boron nitride using luminescence excitation spectroscopy.* Journal of Physics-Condensed Matter, 2008. **20**(7) 075233
5. Evans, D.A., A.R. Vearey-Roberts, and N.R.J. Poolton, *Locating hexagonal and cubic phases in boron nitride using wavelength-selective optically detected x-ray absorption spectroscopy.* Applied Physics Letters, 2006. **89**(16) 161107
6. Poolton, N.R.J., B. Hamilton, and D.A. Evans, *Synchrotron-laser pump-probe luminescence spectroscopy: Correlation of electronic defect states with x-ray absorption in wide-gap solids.* Journal of Physics D - Applied Physics, 2005. **38**(9): p. 1478-1484.
7. Poolton, N.R.J., et al., *Synchrotron-laser interactions in hexagonal boron nitride: an examination of charge trapping dynamics at the boron K-edge.* New Journal of Physics, 2006. **8**: p. 76.
8. Woodruff D.P., *Modern Techniques of Surface Science - Second Edition*. Cambridge Solid State Science Series. 1994: Cambridge University Press.
9. Fadley, C.S., *X-ray photoelectron spectroscopy: From origins to future directions.* Nuclear Instruments & Methods in Physics Research Section A - Accelerators Spectrometers, Detectors and Associated Equipment, 2009. **601**(1-2): p. 8-31.
10. Siegbahn, K., et al., *ESCA: Atomic Molecular Solid State Structure Studied by means of Electron Spectroscopy*. 1967, Uppsala: Almquist & Wiksells.
11. Bauer, E., *Low-energy-electron microscopy.* Reports on Progress in Physics, 1994. **57**(9): p. 895-938.
12. Ruppender, H.J., et al., *In situ X-ray photoelectron-spectroscopy of surfaces at pressures up to 1 mbar.* Surface and Interface Analysis, 1990. **15**(4): p. 245-253.

13. Salmeron, M. and R. Schlögl, *Ambient pressure photoelectron spectroscopy: A new tool for surface science and nanotechnology*. Surface Science Reports, 2008. **63**(4): p. 169-199.
14. Allen, P.G., et al., *Direct observation of surface oxide formation and reduction on platinum clusters by time-resolved x-ray-absorption spectroscopy*. Journal of Electroanalytical Chemistry, 1995. **384**(1-2): p. 99-103.
15. Motz, J.T., et al., *Real-time Raman system for in vivo disease diagnosis*. Journal of Biomedical Optics, 2005. **10**(3): p. 7.
16. Bacon, R., *Growth, structure, and properties of graphite whiskers*. Journal of Applied Physics, 1960. **31**(2): p. 283-290.
17. Iijima, S. and T. Ichihashi, *Single-shell carbon nanotubes of 1-nm diameter*. Nature, 1993. **363**(6430): p. 603-605.
18. Geim, A.K. and K.S. Novoselov, *The rise of graphene*. Nature Materials, 2007. **6**(3): p. 183-191.
19. Vearey-Roberts, A.R. and D.A. Evans, *Modification of GaAs Schottky diodes by thin organic interlayers*. Applied Physics Letters, 2005. **86**(7) 072105.

Chapter 2
Techniques

In this chapter the experimental techniques used during the course of this study for the characterisation of carbon-based semiconductors are described. The primary technique, X-ray Photoelectron Spectroscopy (PES) which provides chemical state and morphological information is complemented by techniques including Near-Edge X-ray Absorption Fine Structure (NEXAFS), Atomic Force Microscopy (AFM), Low Energy Electron Diffraction (LEED) and Current-Voltage measurements (I-V).

2.1 Ultra High Vacuum

Surface science techniques are typically applied in an ultra high vacuum (UHV) environment. Measurements are taken in a vacuum chamber with a typical base pressure of around 1 x 10^{-10} mbar. The reason for this is two-fold. Firstly, most techniques rely on the measurement of photoelectrons emitted or scattered from the sample surface, therefore a lower pressure is needed to increase the mean free path of the electrons so that they can reach the detector, which for PES could be around 1 m.

This requires low pressure but UHV is not a requirement in this respect. Secondly, the need for UHV pressures arise from the fact that these techniques typically probe only the top 1 or 2 nm of a material therefore it is critical that the sample surface is clean. 'Real' surfaces at atmospheric pressure are always contaminated with layers of adsorbed contaminants such as oxygen and hydrocarbons that are adsorbed from the atmosphere [1]. Such contamination on the sample surface would distort the sample signal therefore 'clean' surfaces must be achieved by cleaning (or chemical passivation) in UHV. Using the simple kinetic theory of gases the rate at which particles arrive at the surface can be calculated in terms of pressure. A common form of this equation defines pressure in mbar, with *T* in K and where *m* is substituted with molecular weight, *M* multiplied by the atomic mass unit resulting in the following equation:

$$r = \frac{3.51 \times 10^{22} P}{(T M)^{\frac{1}{2}}} \qquad (Equation\ 2.1)$$

As an example, N_2 molecules of molecular weight (M = 28) at a temperature of 293 K will have an arrival rate of 3.88 x 10^{20} molecules cm^{-2} s^{-1} at 1 mbar if it is assumed that every atom which impinges on the surface sticks. If a monolayer is defined as 10^{15} atoms cm^{-2} then at UHV (< 10^{-9} mbar) the time taken for one monolayer to form is just under 1 hour. Therefore in order to obtain accurate information regarding such phenomena as surface states or the presence and effect of adsorbed molecules it is important to work at these low pressures and within these time frames.

2.2 Thin Film Growth

Vacuum deposition of thin films provides a way of producing very pure multi-layered structures and as a consequence it is the preferred method for the production of most multi-layered electronic devices. Techniques such as Molecular Beam Epitaxy (MBE) and Metalorganic Vapour Phase Epitaxy (MOVPE) are well established methods for the manufacture of electronic and optoelectronic devices. These methods can be used for materials ranging from thermally stable organic molecules to metals. For organic materials such as small-molecules Organic Molecular Beam Deposition (OMBD) is a technique which provides a reliable means of growing thin organic films in UHV. OMBD is discussed in detail by Forrest [2]. In OMBD the organic material is deposited on to the sample using a device known as a Knudsen cell (K-cell) illustrated in figure 2.1. A wide range of materials can be evaporated using this device including metal, inorganic and organic materials. They are evaporated from a heated ceramic crucible and form a beam of material which travels through the vacuum to the sample. This method allows a high degree of control over the deposition rate since the fine tuning of power supplied to the K-cell crucible allows accurate control of the temperature.

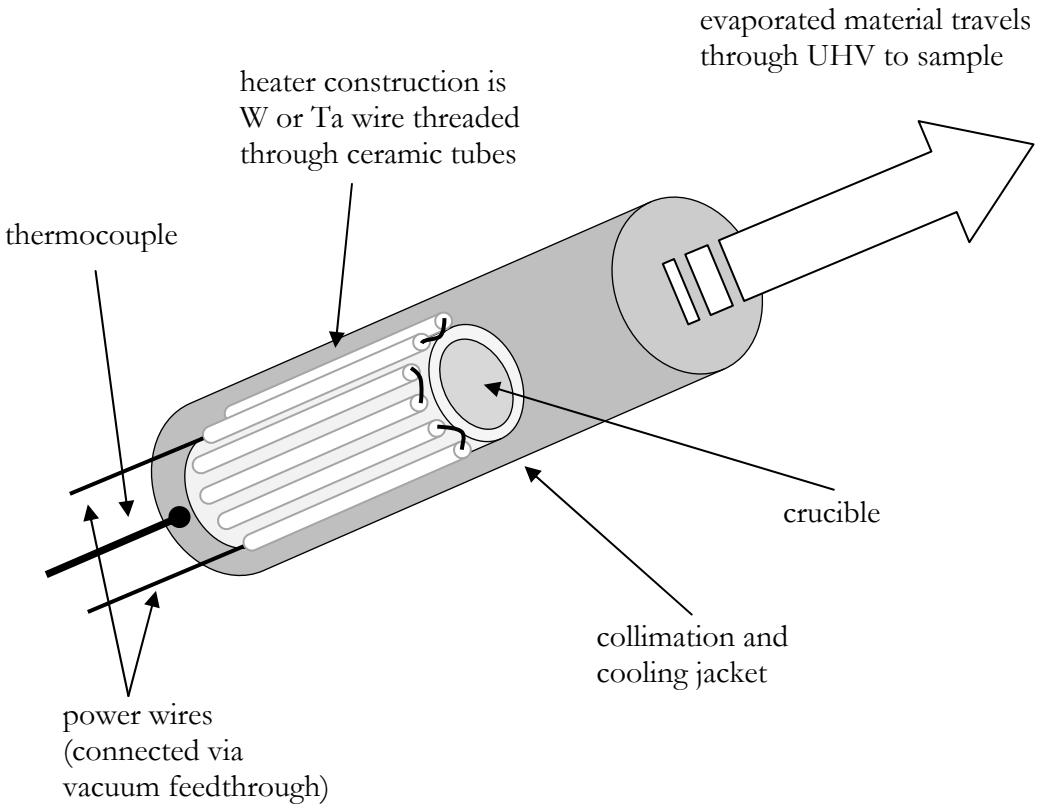

Figure 2.1 – *Schematic diagram of a Knudsen cell used for OMBD. Similar cell designs are used to evaporate metals and inorganic material.*

2.2.1 Film Thickness Monitoring

An oscillating quartz crystal mounted on a shutter situated between the Knudsen cell and the sample (or next to the sample in some cases) was used to monitor the deposition rate of thin film growth for both the phthalocyanine molecules and the metals. The crystal used had a 6 MHz Eigen frequency and was connected to a Sycon Instruments 'STM-100 Thickness Rate Monitor' [3]. By coupling the frequency shift with the mass loading characteristics changes in film thickness of less than a monolayer can be determined. It is assumed that the crystal and sample have the same sticking coefficient i.e. the same fraction of every unit mass reaching the surfaces formed part of the deposited film. The thickness is then calculated using equation 2.2.

$$A_f = \frac{N_q D_q}{\pi\, D_f\, F_c\, Z} \arctan\left[Z\, \tan\frac{\left(\pi\left(F_q - F_c\right)\right)}{F_q}\right] \qquad (Equation\ 2.2)$$

Where A_f is the film thickness, N_q the frequency constant of the crystal (in this case 1.668 x 10^{13} Hz Å^{-1}). D_q is the density of the quartz, F_q the Eigen frequency of the sensor crystal before deposition and F_c the Eigen frequency of the loaded crystal. The film density is D_f while Z is the Z-factor (the square root of the ratio of density multiplied by the shear modulus of the quartz to that of the deposited film). For SnPc the film density used was 1.722 g cm^{-3} [4] and for the Z-factor the same value as for graphite was used (Z = 3.26). For aluminium and iron deposition, the values used for D_f and the Z-factor were 2.73 g cm^{-3} and 1.08 for aluminium and 7.86 g cm^{-3} and 0.349 for iron respectively [3].

2.2.2 Growth Modes

It has been established that growth modes generally fall into three main categories (illustrated in figure 2.2). The first is called Frank-Van der Merwe mode (or layer-by-layer). As the name implies every layer is completed before another layer is started. The second, Volmer Weber, is when nucleation of molecules arriving at the surface is observed which then form island-like clusters which grow with increasing coverage. These two modes are very different and the growth mode encountered in a system is dependent on the relative strength of molecule-molecule interaction and molecule-substrate interaction. For the Volmer Weber mode the molecule-molecule interaction dominates while for Frank-Van der Merwe molecule-substrate interaction dominates. The third mode is Stranski-Krastanov growth where the initial growth is layer-by-layer until a critical thickness is reached where the mode changes to island growth.

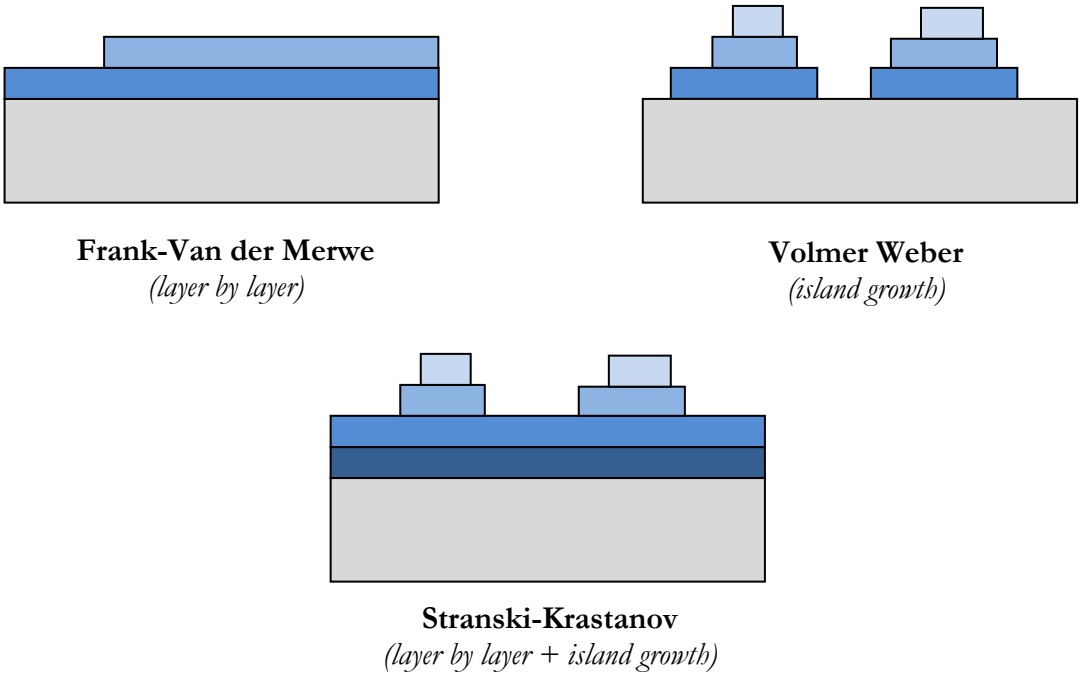

Figure 2.2 – *Schematic of different types of growth modes.*

2.3 Photoelectron Spectroscopy (PES)

Photoemitted electrons were first detected by Hertz while he irradiated materials with ultraviolet light. The findings were published in 1887 in a paper titled 'On the influence of ultraviolet light on the electric discharge'. This work was further developed by Einstein who managed to explain this phenomenon in 1905 by ascribing a quantum nature to light. X-Ray photoelectron spectroscopy (PES) is a powerful surface technique since it yields parallel information on elemental composition, chemical state, occupied valence states and allows direct measurement of energy parameters such as work function. It was developed by Kai Siegbahn and his co-workers in Uppsala, Sweden during the 1960s under the acronym ESCA (electron spectroscopy for chemical analysis) [5, 6] and eventually earned him a Nobel Prize in 1981. Over the following years the technique has been refined and it is now commonly referred to as

PES. The technique has been thoroughly and extensively reviewed by several authors over the last few decades with Hufner [7] being one of the most recent. An introduction will now be given to the basic theory of PES.

When a material is bombarded with photons of a fixed energy (hυ), electrons can be emitted (figure 2.3) – this is a process known as the photoelectric effect. The equation for this process can be given as:

$$h\upsilon = KE + \Phi_S \qquad (Equation\ 2.3)$$

Where hυ is the photon energy, KE is the kinetic energy and Φ_S the work function of the material. PES is performed in an UHV environment, therefore electrons escaping from the surface of the irradiated sample have long mean free paths of up to a few meters. This allows for the kinetic energy of the emitted photoelectrons to be measured using an electron energy analyser and detector. The spectrometer has a work function which is primarily attributed to effects at the entrance slit of the analyser. Therefore the measured kinetic energy has to be adjusted by a fixed value (commonly referred to as the analyser work function) to obtain the kinetic energy for the emitted electron. In practice, this value is an arbitrary offset determined by internal voltage settings within the analyser electronics. The binding energy (BE) of an electron is defined as the difference in energy between the Fermi level and the core level from which the electron has been emitted. In PES (see figure 2.3) it can be expressed as:

$$BE = h\upsilon - KE_M - \Phi_{\mathrm{A}} \qquad (Equation\ 2.4)$$

Where $h\upsilon$ is the energy of the incident photon, KE_M is the kinetic energy measured by the analyser while Φ_{A} is the analyser work function. The Fermi level (E_f) of the material is used as a reference point since at E_f the binding energy is equal to zero, providing the sample and the spectrometer are in electrical contact. The use of E_f as a

reference point is very useful when studying semiconductors since properties such as band-bending induce changes in the band edges with respect to the Fermi level position.

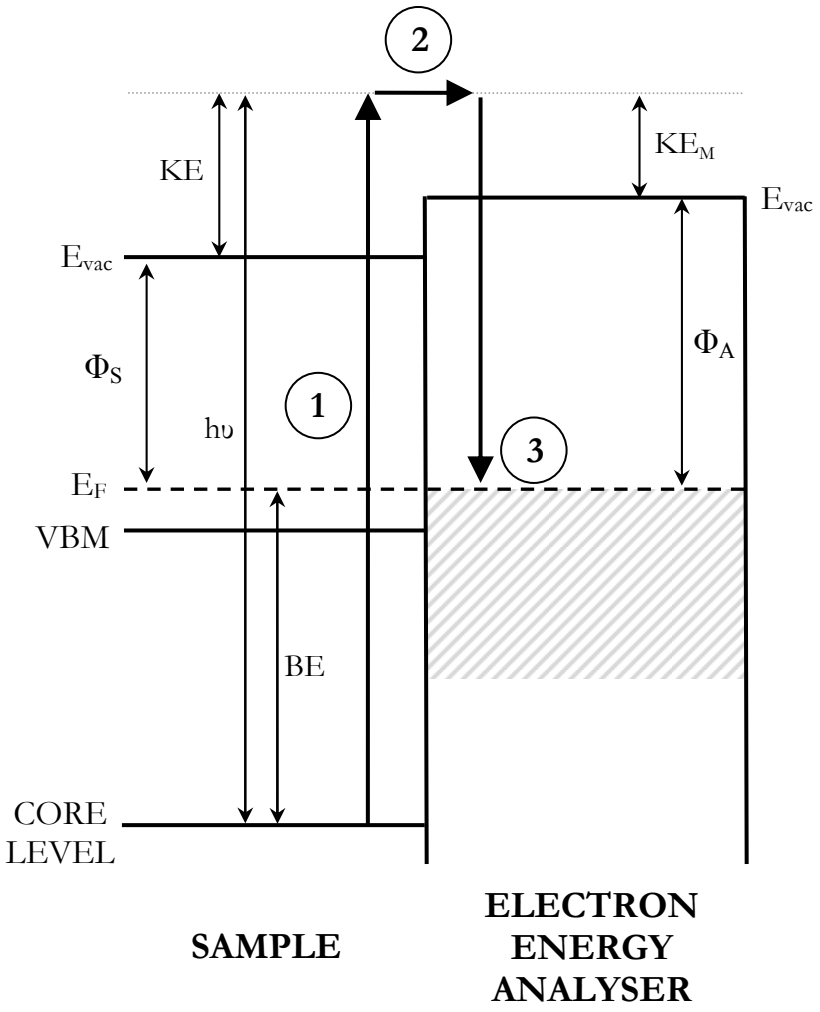

Figure 2.3 – *Excitation and detection of photoelectrons in photoelectron spectroscopy where (1) is the excitation of photoelectron from a core level of a semiconductor and out of the atom due to an interaction with a photon, (2) electron travels to the surface and emitted with a kinetic energy then (3) the electron is detected by the analyser.*

2.3.1 Spectral Features of PES

In PES the continuous flux of photoelectrons emitted from a sample irradiated by photons are separated into their respective kinetic energies, detected by the electron detector, and then presented as an intensity distribution of electrons over a range of

kinetic (or binding) energies. The presence of well defined peaks in the spectrum can be attributed to specific core level and valence band electrons derived from atoms in the sample surface. Consequently, PES can yield an elemental composition of the surface by observation of the peaks present in the spectrum along with their intensities. However, many other spectral features are observed in photoelectron spectra and will now be discussed. Some of these features are illustrated in figure 2.4.

2.3.2 Spin-Orbit Splitting

Spin-orbit splitting is a consequence of the interaction between the spin magnetic dipole moment, s and the orbital angular momentum, l of the electron orbiting within an atom. The total angular momentum, j can be given as:

$$j = |l \pm s| \; where \; s = \frac{1}{2} \qquad (Equation\ 2.5)$$

For s-orbital electrons the orbital angular momentum is zero and the orbital remains as a single peak. However, for p, d and f orbitals which have non-zero orbital angular momentum the total angular momentum has more than one value, e.g. for the 2p orbital, $j = 1/2$ or $3/2$ which will lead to two peaks in the photoelectron spectrum. The number of electrons which contribute to each peak (or the degeneracy of the energy level) is given by $2j + 1$ and the intensity of the core level peak will broadly be proportional to the number of electrons present in that energy level. The relative intensity of split peaks is called the branching ratio, R and is dependent on the value of l and is given as:

$$R = \frac{2\,(l - s) + 1}{2\,(l + s) + 1} \qquad (Equation\ 2.6)$$

The magnitude of the effective nuclear charge experienced by the electron determines the magnitude of the splitting, therefore the energy difference is larger for high atomic numbers, decreasing principal quantum number (i.e. 2p > 3p > 4p) and decreasing orbital angular momentum (i.e. 4p > 4d > 4f).

2.3.3 Auger Emission Peaks

Following emission of an electron from the surface the resultant core-level holes can be repopulated in two different ways. The first is with the emission of X-ray fluorescence, where outer electrons decay into the hole resulting in the emission of a photon at that characteristic wavelength. The second is the Auger process which is similar but the photon emission is replaced by the emission of a secondary electron with a characteristic energy (this process is described further in section 2.4.1). Auger peaks (labelled in figure 2.4) can be readily identified in comparison to PES peaks since their kinetic energy is fixed and independent of the photon energy. There are two types of Auger emissions: Coster-Kronig transitions are observed when the Auger electron is emitted from a sub-shell which has the same principal quantum number as the core hole. Super Coster-Kronig transitions occur when the electron transition also originates from a sub-shell with the same principal quantum number as the initial vacancy. The probability of emission of Auger electrons is also related to the photoelectron cross-section which will be discussed in section 2.3.7. Since the energy of Auger electrons depend on the element, they are widely used in Auger spectroscopy using electron or X-ray sources for surface analysis [8]. This technique can be used to determine the composition of the top few monolayers and is a surface sensitive technique in the same way as photoelectron spectroscopy. A chemical composition image can be obtained with a fine electron beam.

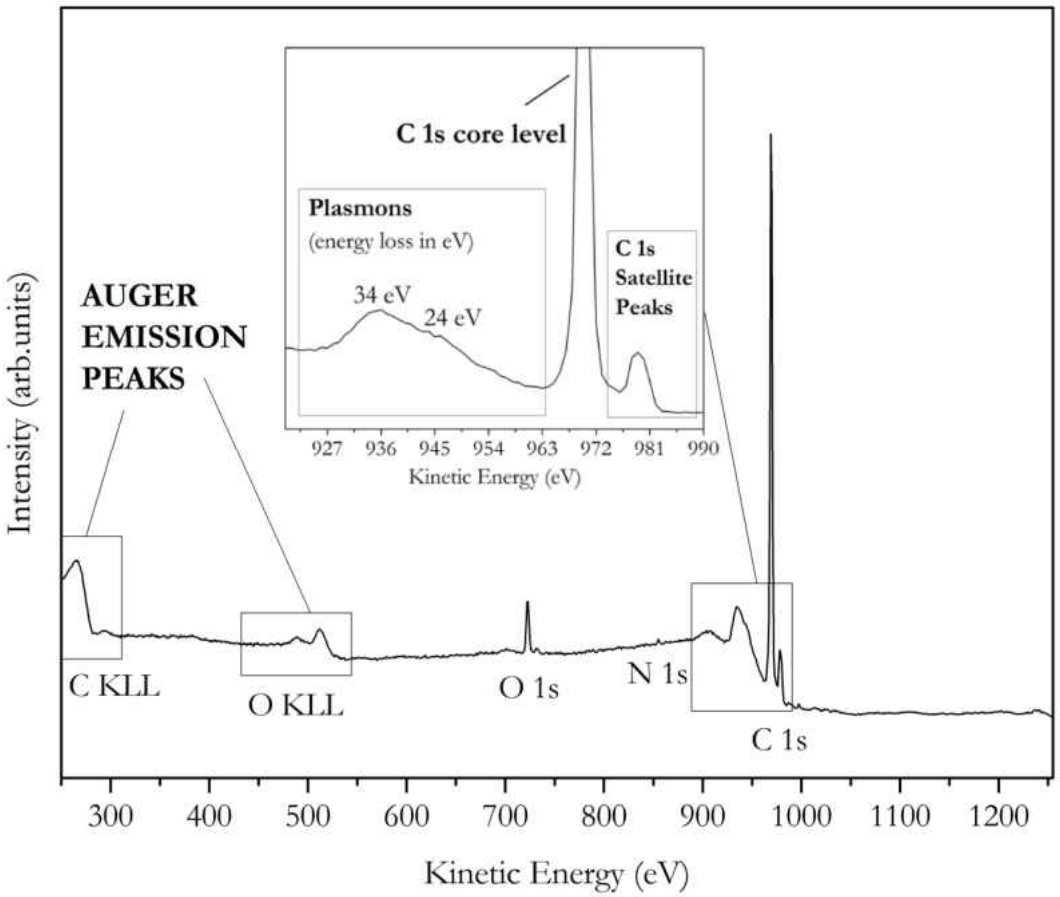

Figure 2.4 – *An XPS survey scan of an acid-etched (001) CVD diamond taken using a Mg Kα laboratory source. Core level peaks (C 1s, O 1s and N 1s) Auger emission peaks (C KLL and O KLL), surface plasmons and satellite peaks are all labelled.*

2.3.4 Peak Shift and Changes in Lineshape

One of the most useful characteristics of PES is its ability to distinguish between different chemical species of the same element present on the sample surface. Where multiple species are present multiple peaks are observed and for small shifts (which are of the order of the experimental resolution) it will result in a change in the lineshape. For this instance peak fitting can be employed. Figure 2.5 (left) shows a C 1s core level for a film of tin (II) phthalocyanine (SnPc). The two most intense peaks in the spectrum (I and II) are a consequence of the two species of carbon present in the SnPc

molecule (figure 2.5 - right). The binding energy of a core level electron is determined by the interaction of the electron with the nucleus, the shielding of that interaction by other electrons and the addition or removal of electrons due to bonding which also affects the shielding. For example, the removal of a valence electron due to oxidation will result in an increase in the binding energy for the remaining electron. This is an example of an initial (or ground) state effect and is usually the dominant effect. This can be caused by variances in the chemical environment of an atom, its oxidation state or its position within a lattice structure.

Koopmans theorem [9] assumes that the binding energy of the electron is simply the difference between the initial and final state (this is called the "frozen orbital approximation") and assumes that the remaining electrons in the ionised atom remain unperturbed. This would make it equal to the binding energy calculated using the Hartree-Fock energy of the orbital, which is evaluated from the total energies of the initial and final states. However, in reality, the loss of the electron from the atom causes the other electrons to react, minimising the energy of the ionised atom. The result of this, called relaxation, is that the emitted electron gains additional energy giving it a perceived lower binding energy.

Other factors may affect the appearance of the photoelectron spectrum, and may be categorised as intrinsic and extrinsic effects. Intrinsic (or final state) effects modify the photoelectron before it leaves the parent atom. Examples include multiplet splitting and multi-electron processes such as shake ups (which are observed in phthalocyanine molecules). Multiplet splitting occurs when an unpaired electron residing in the valence shell of the atom couples with the photoelectron to produce a number of different final

states which can appear as multiple peaks in PES. Multi-electron processes are observed when the removal of the photoelectron causes the excitation of valence electrons into a higher unfilled state (shake-up) or unbound continuum (shake-off) so lowering the kinetic energy of the exiting photoelectron. An example of shake-up peaks can be observed in the C 1s photoelectron core level of the SnPc molecule (figure 2.5). Each of two main peaks correspond to photoelectrons excited without loss from the outer benzene ring (C-C/C-H) (peak I) and the pyrrole group (C-N) (peak I). Corresponding shake-up peaks for each these core levels can be observed at a lower kinetic energy (also labelled I and II).

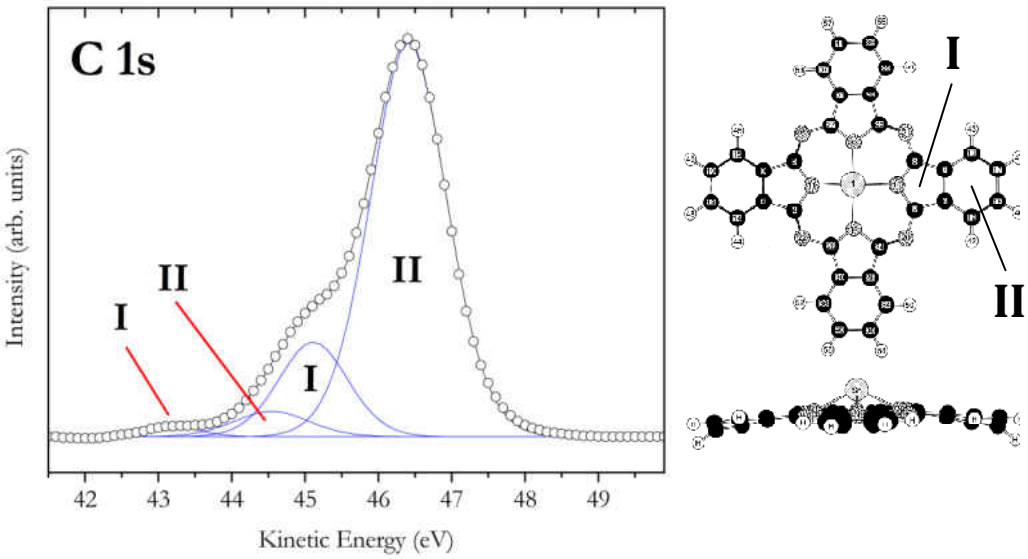

Figure 2.5 – *The C 1s photoelectron core level for and tin (II) phthalocyanine (SnPc) (left). A diagram of the SnPc molecule (right) is taken from [10]. The pyrrole (I) and the benzene (II) rings are labelled along with their corresponding shakeups.*

It is a related effect which is responsible for the asymmetry of metal core level peaks. In metals, conduction electrons are sufficiently free-electron-like to produce a continuum of states around the Fermi level into which valence electrons can be promoted, resulting in a core level peak which exhibits broad asymmetry on the high

binding energy side such as is the case for aluminium and graphite. Extrinsic effects occur when the photoelectrons pass through the sample to the surface. Photons incident on the sample can penetrate hundreds of nanometres into the sample producing photoelectrons deep inside the material, however only the elastically scattered photoelectrons (which escape without any energy loss) are detected in PES as the main photoelectron peaks. Diffraction of elastically scattered electrons can be used to study the sample structure and is achieved in certain cases by measuring the variation in peak intensities as a function of detection angle.

2.3.5 Inelastic Scattering

Some of the inelastically scattered electrons escape and are the cause of the continuous background signal observed in PES spectra (figure 2.4). Inelastic scattering events can contribute two other features to the spectrum. One are electron excitations (or inter band transitions) and the other Plasmon excitations. A Plasmon may be defined as a quantised collective oscillation of the valence (or free) electrons in a solid lattice. During its transport to the surface it is possible for an electron to excite one or more of these oscillations which occur at harmonic frequencies. This effect is observed as a sequence of satellites diminishing in intensity at the high binding energy side of a core level peak. Surface plasmons also exist and their energies are related to bulk plasmons. It has been shown that for a free electron metal $\omega^2_{surface} = ½\ \omega^2_{bulk}$ [11]. For diamond the bulk and surface plasmons occur at 33 - 34 eV and 23 - 26 eV below the main C 1s core level respectively (see figure 2.4).

2.3.6 Charging

One of the limitations of PES is that charging can occur on insulating samples or those which have low conductivity. As electrons are emitted from the surface the insulating nature of the sample means that no electrons can travel through the bulk to replace them. This results in the build up of a positive charge on the surface which increases the barrier encountered by the photo-excited electrons as they leave the surface. As a result more energy is lost by the electrons as they are transmitted into the vacuum and they are hence observed to have a lower kinetic energy (or higher apparent binding energy) than expected, causing the photoelectron peak to shift. This problem can be overcome by supplying a flux of low energy electrons to the surface while the experiment is performed. However, for the purposes of this study no charging effects were observed since all samples were sufficiently conducting.

2.3.7 Photoelectron Cross Section

The presence of core level peaks in the spectrum allows a full elemental composition of the sample to be obtained. The presence and intensity of the peaks can be used to provide a quantitative analysis. However, one important quantity should be considered when undertaking quantitative analysis and that is the photoelectron cross section. It is defined as the number of electrons excited per unit time divided by the number of incident photons per unit time per unit area. It is dependent on the photon energy and is the sum of all individual ionisation probabilities of each orbital in the system. The transition probability per unit time from an initial state to a final state can be calculated using Fermi's Golden Rule which is expressed as:

$$P_{if} = \frac{2\pi}{\hbar} \left|M_{if}\right|^2 \rho_f(E) \qquad (Equation\ 2.7)$$

Where M_{if} is the matrix element for the interaction and $\rho_f(E)$ is the density of the final state. In this approach the cross-section is considered as the probability of transition per unit time from one eigenstate (initial energy state) in a quantum system into a continuum of eigenstates (final state) which is expressed as a function of energy. The validity of this rule depends on the initial state not having been significantly depleted by transition of electron to final states. The Hamiltonian is the operator that corresponds to the total energy of the system and the electromagnetic wave (X-ray in XPS) is considered as a time-dependent perturbing Hamiltonian which affects this quantum system. The matrix element for this interaction is derived from this Hamiltonian. Therefore, the matrix element represents the strength of the coupling between the initial and final state upon which the transition rate depends. Hence, a strong coupling combined with a high density of final states will yield a high intensity photoelectron peak in the PES spectrum.

When performing quantitative analysis of PES spectra it is critical that this factor is applied so that a correct result is obtained. For fixed photon sources the cross section values remain constant for each core level, but for tuneable sources the values change depending on the photon energies used. The cross section can be measured or calculated and values are widely available for standard sources such as a Mg Kα laboratory source. An additional consideration when calculating the elemental composition of a sample is the analyser transmission function. This quantity is important since at different kinetic energies the efficiency of the analyser at transmitting electrons changes and can be experimentally determined from test sample data for each analyser. Therefore both these corrections must be applied to any spectra before determination of the elemental composition.

2.3.8 Surface Sensitivity

The surface sensitivity or sampling depth of PES is dependent upon the scattering of electrons within the sample. As has already been mentioned, photoelectron spectroscopy is principally concerned with electrons which have been elastically scattered and have not undergone any energy loss. Although the incident photons penetrate up to few hundred nanometres into the sample the actual analysable depth is much less. The probability of an electron escaping from the material while only experiencing inelastic scattering events is represented by a quantity called the inelastic mean free path (IMFP or λ). This is dependent upon the medium through which the photoelectrons travel before reaching the vacuum (this includes the sample itself and any overlayers) as well as their kinetic energy. The escape depth changes with the angle of emission and it is possible to achieve a certain surface to bulk sensitivity by measuring electron emission at different angles to the spectrometer. The number of electrons reaching the surface is given by:-

$$I(x) = I_0 e^{\frac{-x.cos\,\theta}{\lambda}} \qquad (Equation\ 2.8)$$

Where I_0 is initial number of photoelectrons generated at a distance x from the surface, θ the angle of emission with respect to the surface, λ is the inelastic mean free path which is independent of the angle and x is the distance from the surface at which the electrons are generated.

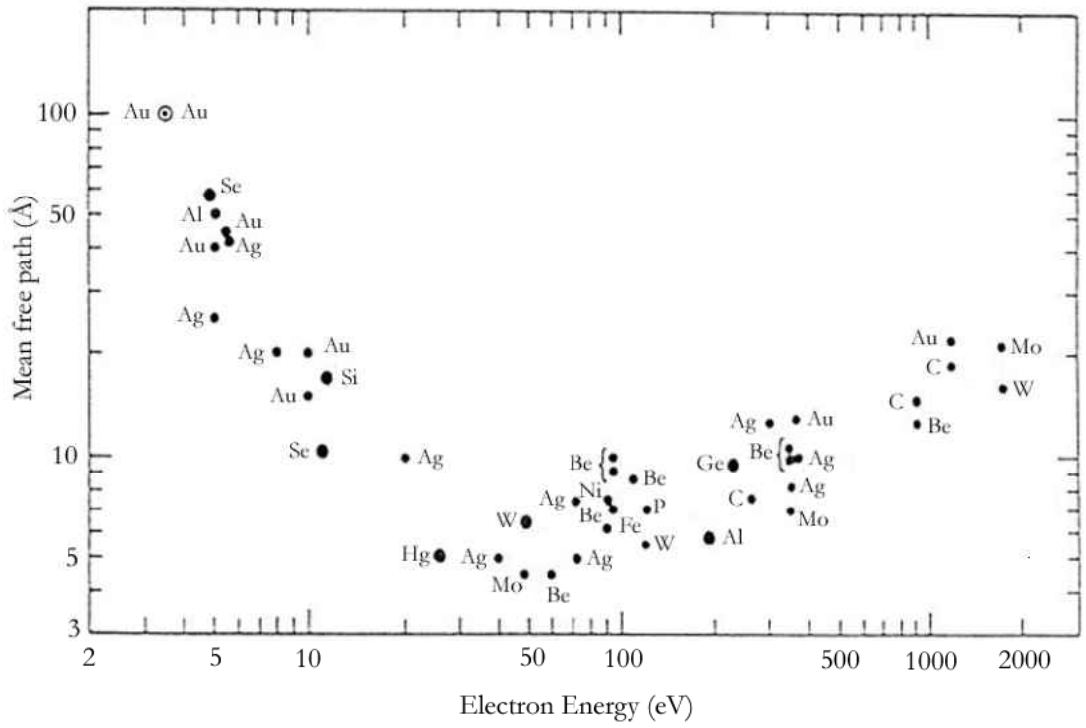

Figure 2.6 – *Taken from [12]. Experimentally measured values of the mean free path (λ in Å) at different electron energies.*

The variation of mean free path with energy for a range of materials is shown in figure 2.6 [12]. As can be seen in figure 2.6 the values for λ gradually increase from around 5 Å to around 20 Å for kinetic energies above 100 eV. The rate of the increase has been shown to be described by a power law equation [12]. Therefore, photoelectron spectroscopy is a truly surface technique probing only the top 1 - 2 nm of the sample when conventional laboratory sources are used. However, as the diagram illustrates the surface sensitivity is most pronounced at kinetic energies in the range 30 - 100 eV. This enhanced surface sensitivity is obtainable provided the energy of the photoelectron is in this energy range – this is possible with a tunable photon source. Synchrotron radiation has made this experimentally possible and will be discussed in chapter 3.

2.3.9 Core-level Intensity

Much information can been obtained about the growth of thin films by monitoring the core level intensity. Once the initial peak intensity for a clean surface has been measured any intensity loss due to layer-by-layer growth of an overlayer can be calculated using this equation:

$$\frac{I}{I_0} = e^{(-\frac{x}{\lambda})} \qquad (Equation\ 2.9)$$

Where I is the intensity of the substrate core level, I_0 is the intensity for the clean substrate, x is the thickness of the overlayer and λ, the inelastic mean free path. It is also possible to determine the overlayer thickness by measurement of the overlayer core level using the following equation:

$$I = I_\infty \left[1 - e^{\left(-\frac{x}{\lambda}\right)}\right] \qquad (Equation\ 2.10)$$

Where I_∞ is the intensity of an infinitely thick overlayer which can be approximated to the intensity of the core level for a thickness which is much greater than the mean free path of the electron through the overlayer material. Monitoring of the substrate core level intensities during deposition processes therefore allows determination of properties such as growth mode since layer-by-layer growth will yield a straight line in a plot of $\ln I/I_0$ against coverage, x (figure 2.7 – region A). From equation 2.9 the gradient can be used to determine an experimental value for the inelastic mean free path introduced in the previous section. The existence of a second gradient (figure 2.7-B) in the attenuation curve indicates that the growth mode (introduced in section 2.2.2) is Stranski-Krastanov. These concepts will be applied in the experimental results (chapters 5 and 6).

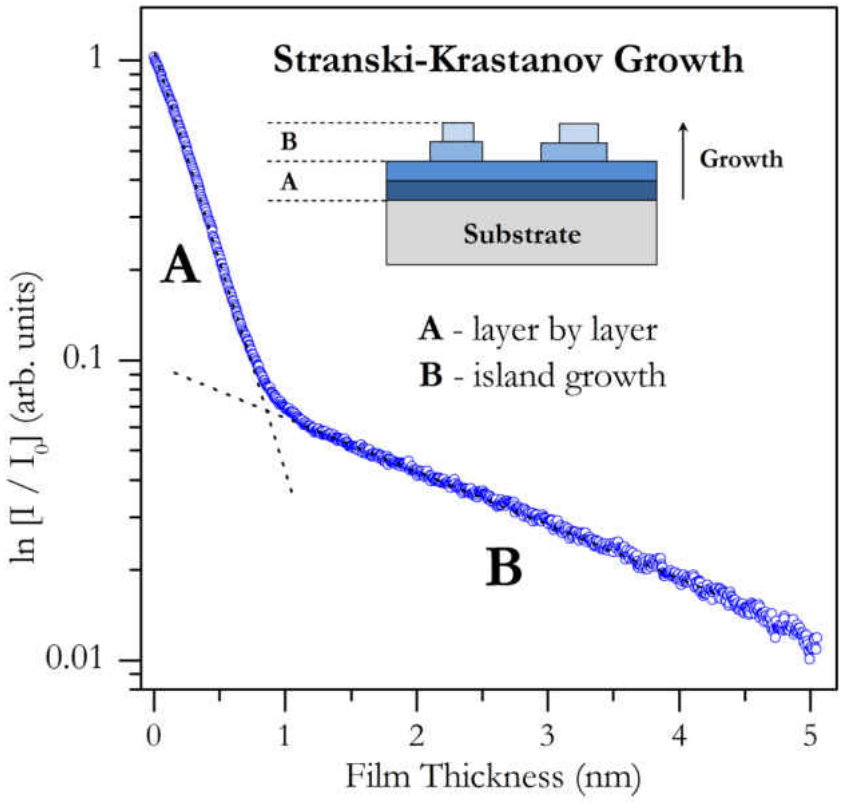

Figure 2.7 – *The attenuation curve for a Ga 3d core level obtained by real-time SXPS during deposition of SnPc on GaAs. The Stranski-Krastanov growth mode is defined by the change in attenuation rate. Region A of the curve represents layer-by-layer growth while region B represents the island growth.*

2.4 Complementary Techniques

Additional techniques were employed in the course of these studies to complement photoelectron spectroscopy. A brief introduction to each technique will now be given in this section.

2.4.1 Near Edge X-ray Absorption Fine Structure (NEXAFS)

It has already been demonstrated that PES provides detailed information about the occupied states of materials therefore these techniques are very well complemented by NEXAFS spectroscopy which provides information about the density of unoccupied

states. Electrons excited by X-rays from their initial states populate unoccupied states above the Fermi level. This absorption process is dependent on the X-ray absorption cross-section (already discussed in section 2.3.7). The energy of the incident photons is scanned across the ionization energy for a pre-selected core level (e.g. the carbon K-shell). At the ionization energy there is marked increase in absorption (referred to as an absorption edge) as electrons are excited from the core state to the lowest unoccupied state above the Fermi level. As the incident photon energy is increased further the unoccupied states which exist at higher energies are populated in turn. For materials such as graphite the lowest unoccupied state is referred to as π^* orbitals and are a consequence of its structure. The stark difference between NEXAFS spectra for the C K-edge for diamond and graphite (figure 2.9) make this technique a powerful tool for the study of the graphitisation of diamond.

This technique requires a tunable X-ray source such as a synchrotron (introduced in the next chapter) and can be applied in parallel with SXPS. Since all photons are absorbed within the sample (thickness ~ mm) at soft X-ray energies the absorption can only be measured indirectly by measurement of emitted electrons. For materials with low atomic number, such as carbon it is the Auger emission which is dominant (figure 2.8). Therefore measurement of electron yield as a function of incident photon energy provides an indirect measurement of the X-ray absorption. Electrons can only escape from the near-surface region of the material. Two methods of electron detection exist. Total electron yield is obtained by measurement of the sample drain current which detects all electrons emitted from the sample. For Auger (or partial) electron yield only the electrons emitted at a pre-selected energy are detected using an energy analyser.

This means that inelastically scattered electrons originating from deeper inside the material are retarded by the energy analyser resulting in enhanced surface sensitivity.

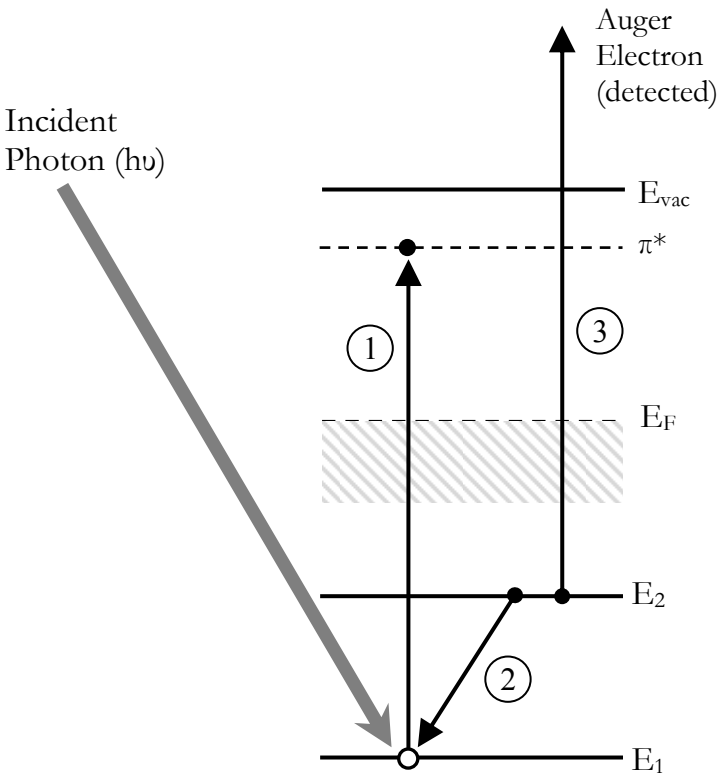

Figure 2.8 – *Schematic diagram of processes involved in the NEXAFS technique. An incident soft X-ray photon excites a core level electron into an unoccupied state (1), another electron from a higher energy state decays to fill the core hole left by the excited electron transferring its liberated energy to a second electron (2), which is then emitted as an Auger electron providing the kinetic energy transferred is higher than the binding energy of the second electron (3).*

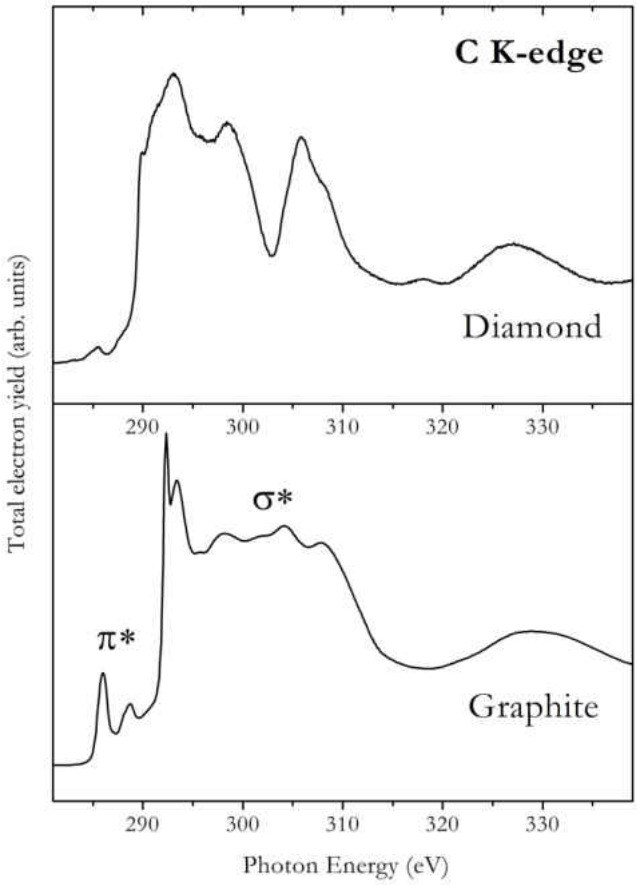

Figure 2.9 – *NEXAFS spectra of the C K-edge for diamond and graphite. The drastic difference in two spectra makes NEXAFS an useful tool for the study of graphitisation of diamond.*

2.4.2 Low Energy Electron Diffraction (LEED)

Low Energy Electron Diffraction (LEED) utilises the wave-like nature of electrons in order to probe the surface structure of materials. For low energy (non-relativistic) electrons their wavelength can be determined by applying the de Broglie relation to the kinetic energy equation. For electrons which have kinetic energies between 10 – 200 eV their de Broglie wavelength is of the order of 1 - 2 Å or less. These values correspond to the typical spacing within crystal lattices which means that diffraction can occur when electrons encounter an ordered lattice structure. The inelastic mean free path (IMFP) already described in this chapter means that this technique is very

surface sensitive probing only the top 3 – 4 Å of the sample surface. The diffraction patterns observed can be considered simply in the 1-dimensional case as the diffraction of two waves passing through a series of slits which have a separation equal to a. The path difference, d, which gives rise to interference between two waves passing through two adjacent slits can be expressed as:

$$d = a \sin\theta \qquad (Equation\ 2.11)$$

With θ the angle at which the waves are incident to the plane of the slits. The variation in intensity of the diffracted waves vary as a function of θ and are at a maximum when the Bragg Condition is met i.e. the path length *d*, is equal to an exact multiple of the incident wavelength and is expressed as:

$$n\lambda = d \sin\theta \qquad (Equation\ 2.12)$$

where *n* is an integer. A real lattice surface has to satisfy this condition in two orthogonal directions for a diffraction pattern to be observed. However if these conditions are met the diffracted electrons form a pattern which contain a series of discrete diffraction spots. Since the wavelength of the incident electrons are of the order of angstroms the atomic spacings within crystals can be probed. Also these wavelengths correspond to electron energies of ~ 100 eV meaning that the technique is very surface sensitive. This technique (illustrated in figure 2.10) is performed in an UHV environment since retention of a clean sample surface is important. A parallel monochromatic beam of electrons is directed at a normal angle towards the sample surface. Electrons are then backscattered with a proportion of these undergoing elastic scattering. These electrons are detected on a phosphor screen where a diffraction pattern is displayed. The inelastically scattered electrons are prevented from reaching the screen due to a retarding potential applied to the mesh. The image which appears on the screen is a representation of the lattice in reciprocal space with larger spot

spacing corresponding to smaller inter-atomic distances. However, the energy of the electron beam can be varied and corresponds to changing the wavelength of the electrons. Consequently, the electron energy used changes the spacing of the spots.

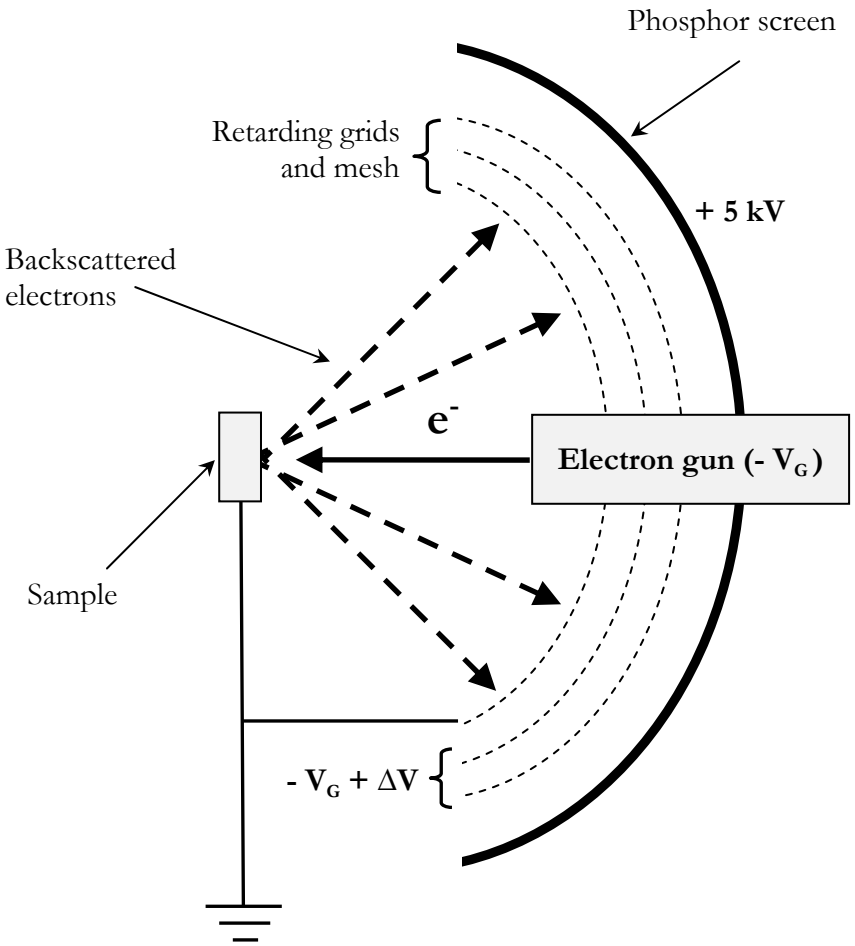

Figure 2.10 – *Schematic diagram of the experimental setup for a low energy electron diffraction (LEED) experiment.*

For orthogonally symmetric surface such as for the diamond (001) surface its representation in reciprocal space appears the same while less symmetric surfaces such as the (110) have a pattern which is rotated by 90° in reciprocal space. When performing a LEED experiment the intensity of the spot relative to the background is of greatest concern, since a high background suggests that there are irregularities in the

surface. Disordered or amorphous surfaces will not give a LEED pattern, but a number of small ordered domains are indistinguishable from a large single area domain.

2.4.3 Atomic Force Microscopy (AFM)

Atomic force microscopy is a scanned probe technique which yields information on the topography or morphology of a surface. In 1980s it became a truly practical tool for detailed measurements of a sample surface. Much of the development work was done by Binning et al [13] in an attempt to find an alternative to scanning tunnelling microscopy (STM). The most advanced AFM systems operate in UHV and at temperatures of ~ 4 K and have achieved atomic resolution. A group at IBM in Zurich successfully imaged the hexagonal shapes of the five carbon rings as well as the carbon atoms in pentacene. Even the positions of the hydrogen atoms of the molecule have been deduced from the image [14]. The instrument used for the work in this thesis was a Park XE-100 instrument with all samples measured *ex situ* under atmospheric conditions at room temperature.

The atomic force microscope uses the interaction of a very fine tip with the surface. This tip is attached to a cantilever and as the tip is scanned across the sample surface it moves in accordance due to interaction with the surface atoms. The movement of the tip is determined using a laser beam which is reflected on to the back of the cantilever and detected using a position sensitive detector as shown in figure 2.11. Since the angle of reflection changes with movement of the cantilever the change in the position of the beam at the detector can be used to create an accurate image of the sample surface.

AFM measurements can be conducted in a number of different modes. The two modes used in this study are known as contact mode (or C-AFM) and non-contact mode (NC-AFM). In contact mode the probe scans the sample surface and is deflected due to electrostatic repulsion between the probe and the surface atoms. The topography is obtained by keeping the probe at a fixed distance from the surface by correcting for any deflections caused by interaction with the surface. This correction then yields a direct image of the sample surface. The forces experienced by the cantilever will typically be in the 1 – 10 nN range hence the cantilevers have small spring constants (typically 0.1 – 3 N m^{-1}).

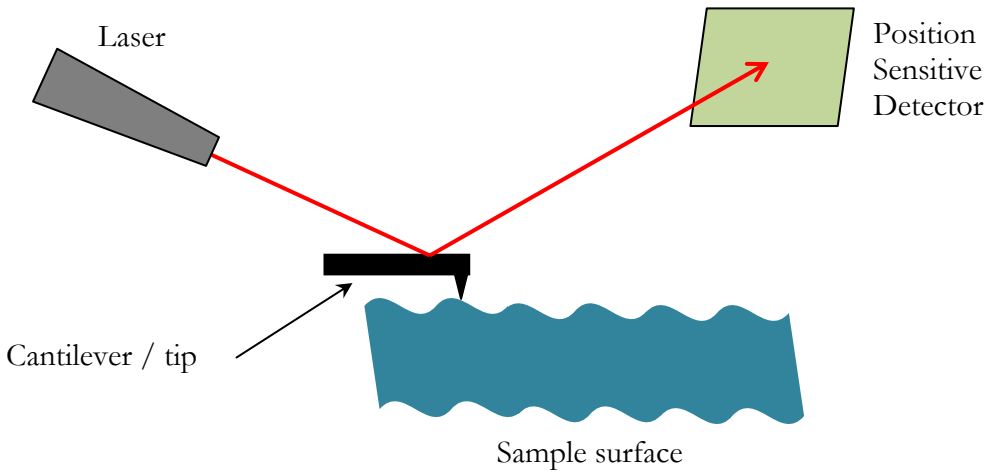

Figure 2.11 – *Principle of operation of an Atomic Force Microscope (AFM)*

Non-contact AFM (NC-AFM) exploits the intrinsic property of the cantilever – its spring constant. The tip is held further away than for C-AFM while the cantilever is oscillated using small piezos. The amplitude and phase of the oscillating cantilever is detected by the laser. As the tip experiences attractive Van der Waals forces this lowers the effective spring constant of the oscillating cantilever and reduces its resonant frequency. This means that the amplitude of the oscillation is very sensitive to the tip-

sample separation and therefore to maintain a constant amplitude tip-sample separation must be constantly adjusted. The correction needed to maintain this constant amplitude gives a direct image of the sample surface.

Dynamic Force Microscopy (DFM, also known as tapping mode) involves vibrating the cantilever at a frequency slightly above its resonant frequency. As the tip oscillates it gently 'taps' the sample surface on each cycle. This contact with the surface increases the effective spring constant decreasing the amplitude. The height of the cantilever is corrected until the attractive (Van der Waals) forces become dominant again.

2.4.4 Current-Voltage Measurements (I-V)

The Schottky Barrier Height (SBH) determines the magnitude of rectification for a metal-semiconductor junction. This barrier and can be determined by fitting of the I-V characteristics of a particular device. The current density, J derived from thermionic-emission theory [1] can be expressed as:

$$J = J_0 \left[exp^{\frac{qV}{nkT}} - 1 \right] \qquad (Equation\ 2.13)$$

J_0 can be written as:

$$J_0 = A^{**}T^2 exp^{\frac{-q\,\phi_b}{kT}} \qquad (Equation\ 2.14)$$

Where J_0 is the reverse saturation current density, q is the magnitude of the electronic charge, V the voltage, n the ideality factor, k Boltzmann's constant and T the absolute temperature. A^{**} is the Richardson Constant modified to take account of the effective mass of electrons in the semiconductor, while ϕ_b is the Schottky Barrier Height. In the experimental setup described in figure 2.12 the quantity measured is the total current

therefore since J is the current density it is important to determine an accurate value for the contact area, S so that a value is obtained for the current density.

For voltages where $V > 3kT/q$ the current density can be written in a simpler form as in equation 2.15.

$$J = J_0 \, exp^{\frac{qV}{nkT}} \qquad (Equation\ 2.15)$$

A plot of ln J against V (equation 2.15) in the forward direction will give a straight line. However, for an ideal diode if the values for A^{**} and J_0 is known as the barrier height ϕ_b and can be determined by re-arrangement of equation 2.14.

The ideality factor, n gives an indication of the quality of a diode with values closer to unity (e.g. n < 1.1) indicating that the application of thermionic emission theory is appropriate. Larger values for n would suggest that other factors such as interfacial layers are affecting the transport of charge causing a deviation from the ideal diode behaviour predicted by thermionic emission theory. Modelling of this junction also includes additional components (figure 2.12) such as leakage currents which dominate at low voltages and series resistance which dominates at higher voltages.

In this study I-V measurements are performed on simple Al/p-diamond contacts the results of which are presented in chapter 5. *In situ* experiments were performed in a UHV chamber with a base pressure of around 5 x 10^{-10} mbar. The experimental setup is described in figure 2.13. A gold probe fitted on a linear drive was used to apply a voltage supplied by a Keithley 236 Source Measure Unit (SMU) to the top of the contact. The voltage was then increased incrementally and a pre-determined delay (programmed into the voltage sweep) was executed before the current is measured at

each voltage. The SMU was controlled using a LabVIEW interface and provided an I-V curve in the form of an ASCII file output.

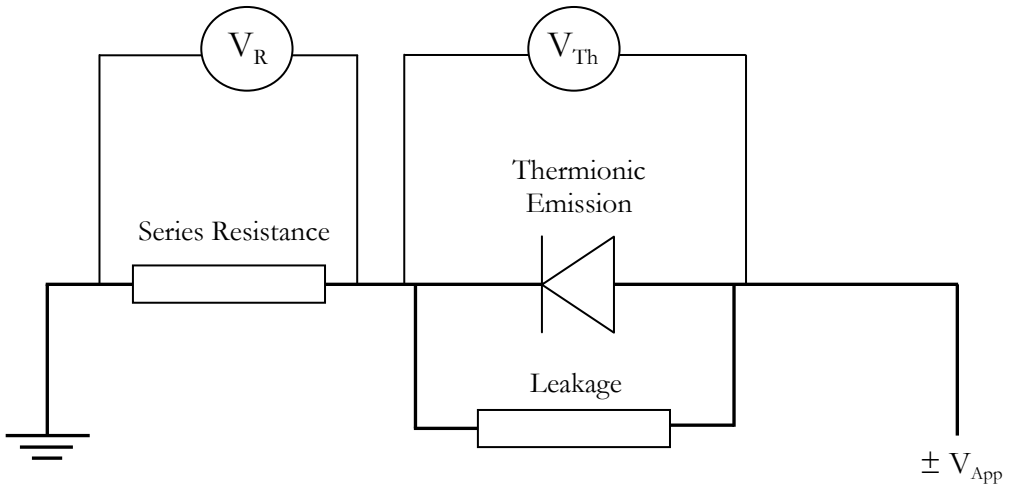

Figure 2.12 – *Model used for the determination of the I-V characteristics.*

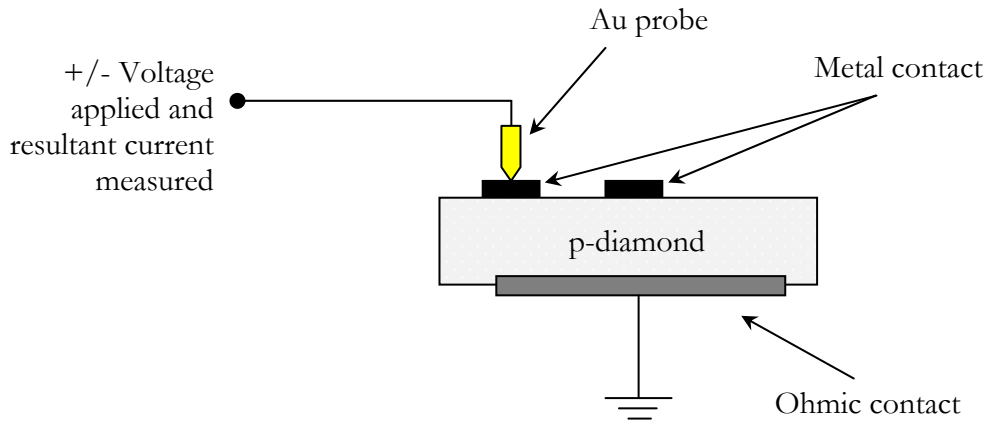

Figure 2.13 – *Schematic diagram showing the experimental setup for current-voltage measurements on an metal/p-diamond contact.*

2.5 Chapter Summary

In this chapter the methods used during this study have been introduced along with the theory of X-ray Photoelectron Spectroscopy (PES). Other complementary techniques employed in these studies have also been outlined. This forms a basis for the next chapter where the instrumentation needed to perform PES is described along with the Aberystwyth Real-time Electron Spectroscopy System.

References

1. Rhoderick, E.H., *Metal-semiconductor Contacts*. 1988: Oxford University Press.
2. Forrest, S.R., *Ultrathin organic films grown by organic molecular beam deposition and related techniques*. Chemical Reviews, 1997. **97**(6): p. 1793-1896.
3. *Sycon Instruments STM-100 Thickness/Rate Monitor User's Manual*. 1988, Sycon Instruments Inc.
4. Kubiak, R. and J. Janczak, *X-ray analysis of phthalocyanines formed in the reaction of Au-Cu and Au-Sn alloys with 1,2-dicyanobenzene*. Journal of Alloys and Compounds, 1992. **189**(1): p. 107-111.
5. Siegbahn, K., et al., *ESCA: Atomic Molecular Solid State Structure Studied by means of Electron Spectroscopy*. 1967, Uppsala: Almquist & Wiksells.
6. Siegbahn, K., *Electron Spectroscopy For Chemical Analysis (Esca)*. Philosophical Transactions of The Royal Society of London Series A - Mathematical and Physical Sciences, 1970. **268**(1184): p. 33
7. Hufner, S., *Photoelectron Spectroscopy*. Advanced Texts in Physics. 2003 (3rd Edition): Springer.
8. Woodruff D.P., *Modern Techniques of Surface Science - Second Edition*. Cambridge Solid State Science Series. 1994: Cambridge University Press.
9. Koopmans, T., *Über die Zuordnung von Wellenfunktionen und Eigenwerten zu den Einzelnen Elektronen Eines Atoms*. Physica, 1934. **1**(1-6): p. 104-113.
10. Day, P.N., Z. Wang, and R. Pachter, *Calculation of the structure and absorption spectra of phthalocyanines in the gas-phase and in solution*. Journal of Molecular Structure: THEOCHEM, 1998. **455**(1): p. 33-50.
11. McFeely, F.R., et al., *X-ray photoemission studies of diamond, graphite, and glassy carbon valence Bands*. Physical Review B, 1974. **9**(12): p. 5268-5278.
12. Zangwill, A., *Physics at Surfaces*. 1988: Cambridge University Press.
13. Binnig, G., C.F. Quate, and C. Gerber, *Atomic Force Microscope*. Physical Review Letters, 1986. **56**(9): p. 930-933.
14. Gross, L., et al., *The Chemical Structure of a Molecule Resolved by Atomic Force Microscopy*. Science, 2009. **325**(5944): p. 1110-1114.

Chapter 3
Instrumentation

Instrumentation development plays a vital role in the development of any characterisation technique such as X-ray photoelectron spectroscopy (PES). The theoretical basis for PES has already been presented in the previous chapter. This chapter introduces the basic instrumentation required to perform PES. Current developments in the field of fast electron detection will be reviewed since this work forms the basis for enhancements such as real-time photoelectron spectroscopy. Finally, the custom-built Real-time Electron Spectroscopy (REES) system developed at Aberystwyth will be outlined and demonstrated using example spectra.

3.1 Photon Sources

The use of different photon sources provides a way of probing different aspects of a material. For example, varying the photon energy allows selection of surface sensitivity. Different sources also vary in intensity and polarisation etc. In this section the photon

sources used during the course of these studies will be outlined along with their specific characteristics.

3.1.1 Laboratory Sources

The conventional setup for laboratory PES (referred to as XPS) is to use metal anodes to produce the X-rays. The VG Twin anode X-ray gun used in this study has Al and Mg anodes producing photons primarily at 1486.6 eV (Al Kα) and 1253.6 eV (Mg Kα). However, all data presented in this study was obtained using the Mg Kα which has the narrowest line width of the two anodes at ~ 0.7 eV. The twin anode X-ray gun produces X-rays by accelerating electrons emitted from a filament into a target anode that is at high voltage relative to the filament and ground. This produces a series of X-ray lines that are dominated by the Kα transition at 1253.6 eV for the Mg and 1486.6 eV for the Al anode. Other X-ray lines are also emitted causing excitation of electrons that leads to satellite peaks appearing in the spectrum. Since the kinetic energy of the electrons is related to the excitation source the same peak appears at different energies in the spectrum although it originates from the same core level. These extra peaks are called satellite peaks and can be subtracted in software prior to quantitative analysis.

3.1.1.1 Heating Effects of the Twin Anode X-ray Source

Energy is released from the X-ray gun in the form of heat as the anode temperature increases due to electron bombardment requiring a constant flow of cooling water to regulate its temperature. Even with water cooling, significant heating of the sample occurs when it was irradiated with X-rays and measurements were carried out to investigate this effect. A correlation was found between the X-ray power and the increase in sample temperature following switching on the X-rays (figure 3.1). Under

some conditions the sample temperature was found to increase to 43.6 ˚C over a 5 hr period. The temperature curve for the Mg target at 300 W was fitted yielding an exponential function which had a time constant of ~ 1.1 hrs (figure 3.1 – inset). It is conceivable that for exceptional cases and specific volatile samples this elevated temperature could cause changes in the sample being measured giving inaccurate readings. However, for most samples this effect is negligible. It should also be noted that for synchrotron sources (introduced in the next section) no sample heating occurs.

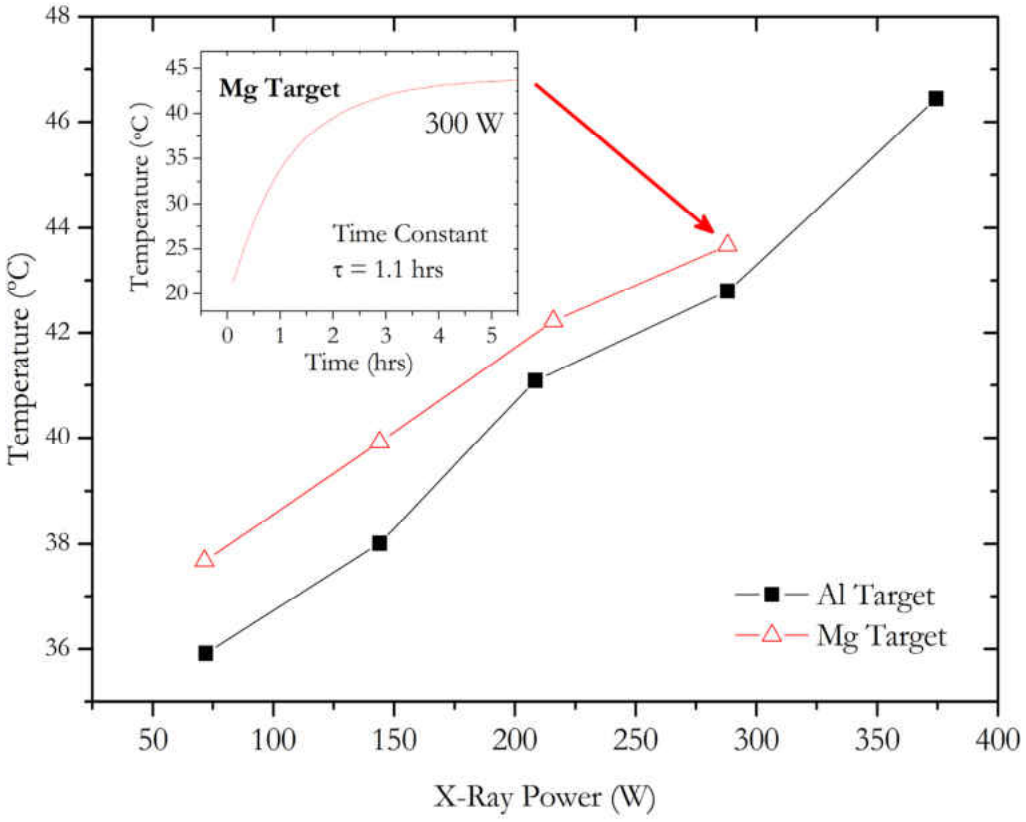

Figure 3.1 – *Sample temperature in ˚C following exposure to X-rays for 5 hrs against X-ray power for the Mg Kα (open red triangles) anode and Al Kα (filled black squares) anode of the VG laboratory twin anode X-ray source. Also plotted is the sample temperature against the duration since X-rays are switched on at 300 W using the Mg anode (inset).*

3.1.2 Synchrotron Radiation

The advent of synchrotron radiation and storage rings as a tunable photon source opened up new possibilities in controlling surface sensitivity of measurements. Soft X-ray Photoelectron Spectroscopy (SXPS), as the name implies, uses soft X-rays (photons which are roughly in 50 eV - 1 keV energy range) which allows for much greater surface sensitivity. A synchrotron source also has the added advantage of being able to deliver a higher photon flux to the sample as well as providing higher resolution due to a narrower source line width produced by the monochromator.

Synchrotron radiation [1] was generated undiscovered for many years in particle accelerators although it had been predicted by Schott at Aberystwyth in 1907 [2]. These first synchrotrons were built to study atomic collisions. In 1947, synchrotron light was first observed by a group working for General Electric in the United States when they observed visible light being emitted from their 70 MeV synchrotron. However, it was in the late 1960s at Daresbury laboratory that the first ever synchrotron radiation experiments were conducted using radiation coming from NINA, a fast cycling electron synchrotron. These were called 'parasitic' experiments due to the fact that they took advantage of the unused radiation coming from the particle physics experiments [3].

As the advantages of synchrotron radiation became more apparent a dedicated synchrotron radiation source was constructed on the site of the NINA synchrotron. This facility, called the Synchrotron Radiation Source (SRS), was opened in 1980 [4] with the first papers published in 1981 [5, 6]. It operated for 27 years and closed after

producing 'Two million hours of science' [7]. In January 2007 the Diamond Light Source near Oxford, a new 3rd generation source, replaced the SRS as the United Kingdom's synchrotron radiation facility.

3.1.2.1 Principle of Operation

When electrons are accelerated they emit electromagnetic radiation. Radio transmitters are wholly dependent on this phenomenon since electrons are accelerated in a radio antenna to produce radio waves. In this case the electrons are accelerated to low velocity well below the point where they become relativistic and as a consequence the radiation emitted is in a dipole radiation pattern (figure 3.2-A). However as an electron's velocity increases the radiated power increases and the emission pattern becomes a cone extending in the forward direction of the electrons' circular motion but perpendicular to the acceleration (figure 3.2-B).

In a synchrotron radiation source (figure 3.2-C) electrons are typically produced by passing a large DC current through a filament (or cathode) causing thermionic emission of electrons. These electrons are accelerated into a linear accelerator (or linac) and their energy boosted using a powerful pulsating electric field. The electrons will be travelling close to the speed of light as they leave the linac and transfer into the booster. In the booster the electrons are forced into a circular path for the first time by bending magnets as they are accelerated even further to energies of a few GeV. Quadrupole magnets in between the bending magnets focus the bunches into a fine beam inside the vacuum vessel.

For most synchrotron radiation sources the electrons are accelerated up to their stored energy before being injected into the storage ring, however the SRS in Daresbury was different. It had a 600 MeV (10 Hz) booster which fed the main storage ring where the electrons were then accelerated to their stored energy of 2 GeV. The storage ring is a larger version of the booster with straight sections, bending magnets, focusing magnets and RF cavity(ies) situated periodically around the ring. The RF cavities are used to replenish the energy of the electron bunches since they constantly lose energy in the form of synchrotron radiation. At each bending magnet the beam is forced in a circular path towards the centre of the ring emitting radiation extending from the infrared to hard X-rays as a "sweeping searchlight" (figure 3.3 – top).

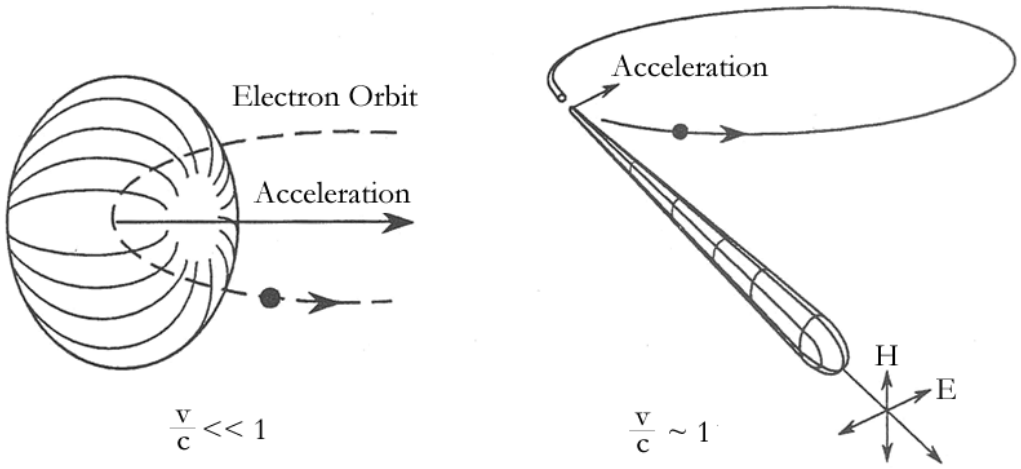

(A) **(B)**

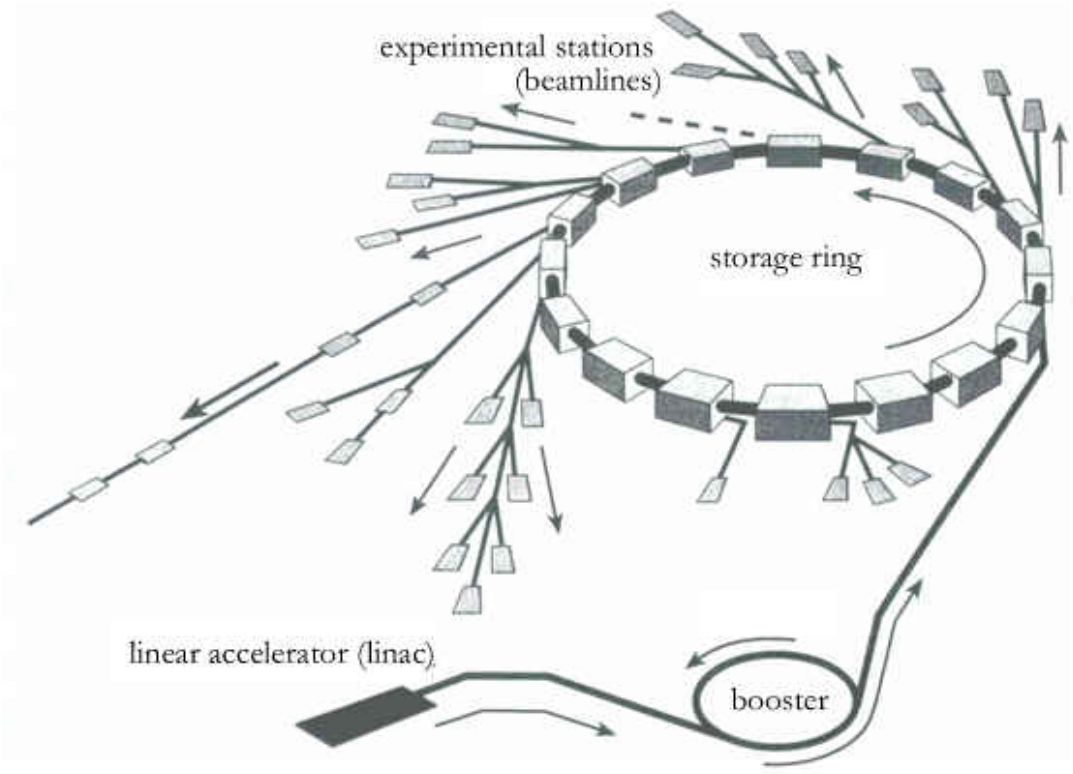

(C)

Figure 3.2 – *Taken from [8]. The principle of operation of a synchrotron source. The pattern of radiative emission for electrons accelerated in a circular orbit for the non-relativistic case (A) and the relativistic case (B). v is the speed of the electron while c represents the speed of light. H and E refer to the magnetic and electric vectors of the electromagnetic radiation. Also shown (C) is a schematic of a synchrotron radiation source.*

3.1.2.2 Insertion Devices

Initially, bending magnets were the only devices used to extract the radiation from the beam (figure 3.3 - top), however in order to obtain more intense radiation, insertion devices were later introduced on the straight sections. Two types of insertion devices are undulators and wigglers (figure 3.3 – middle and bottom). These devices give enhanced brightness by forcing the electrons to oscillate as they travel through causing them to emit cones of radiation at the extremities.

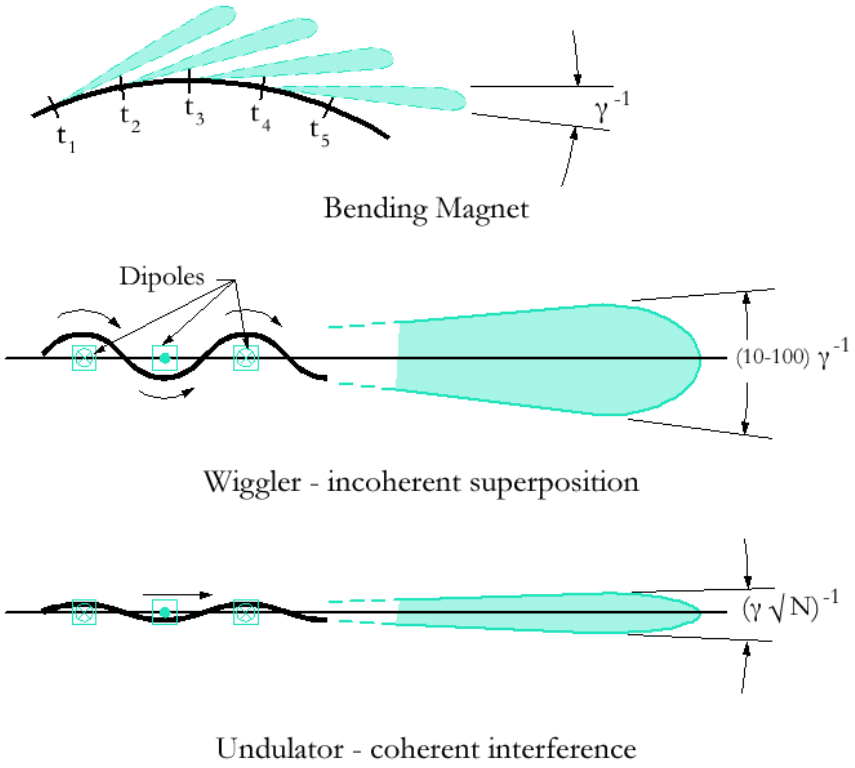

Figure 3.3 –*Taken from [8]. Principle of operation for a bending magnet (top), wiggler (middle) and undulator (bottom).*

The oscillation is produced in both cases using an array of dipole magnets, however, the actual processes of radiation amplification are very different for both types of insertion device. The wiggler uses incoherent superposition of the radiation cones to

increase the intensity while an undulator relies on coherent interference for amplification. For undulators, cones overlap giving an intense collimated beam of radiation at a fundamental frequency, while interference effects give rise to additional higher harmonics.

3.1.2.3 Beamlines

The radiation is then focused into a beam by collecting optics and the use of a monochromator provides a range of monochromatic photon beams with line widths superior to those of a laboratory X-ray gun. Specific beamlines are optimised to deliver different ranges of energy. The beamline that was used for work in this thesis was a multipole wiggler designated MPW 6.1 at the Synchrotron Radiation Source (SRS), Daresbury [9]. MPW 6.1 was an XUV beamline (figure 3.4) that uses the output from a 2 tesla multi-pole wiggler. The setup is that of a spherical grating monochromator (SGM) and this produces photons in the 40 - 470 eV range. This energy range is ideal for the study of carbon-based semiconductor surfaces since, for photoemission, the kinetic energy of the C 1s core level at photon energies of around 300 eV corresponds to the minimum value for the inelastic mean free path which is of the order of 4 Å (see figure 2.6).

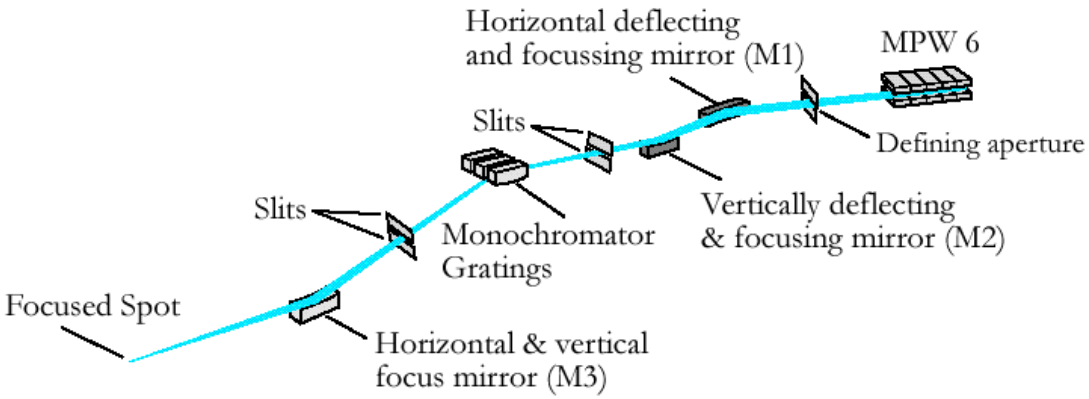

Figure 3.4 – *Taken from [10]. Schematic of the MPW 6.1 XUV beamline at the SRS, Daresbury.*

3.2 The Electron Energy Analyser

Regardless of the X-ray source used the principle of operation of the instrumentation remains the same, although the setup parameters may vary. An electron energy analyser is used to separate the photoelectrons emitted from the sample into their respective kinetic energies allowing an electron intensity curve as a function of kinetic energy (known as the PES spectrum) to be produced.

Once the photoelectrons are emitted from the sample they are collected by a hemispherical electron analyser that uses electrostatic lenses to guide the electrons in to a path between two hemispherical plates which are separated by a constant voltage. The voltage selected allows the measured electron intensity to be selected according to the kinetic energy. The electron detector lies at the opposite end of the curved hemispheres and only electrons within a certain window or range of kinetic energies will reach the detector. A schematic of a concentric hemispherical analyser (CHA) is presented in figure 3.5. As the voltage between the hemispheres (radius R_1 and R_2 in figure 3.5) is changed the acceptance energy of the analyser changes and electrons with different kinetic energies (corresponding to that specific voltage) are measured at the detector. The pass energy of the analyser determines the window of energies that falls on the detector (shaded corridor in figure 3.5). The electron whose kinetic energy exactly corresponds to the analyser energy follows a path of radius R_0 striking the detector in the middle while electrons with higher and lower kinetic energies follow a path where the radius is greater and lower than R_0 respectively.

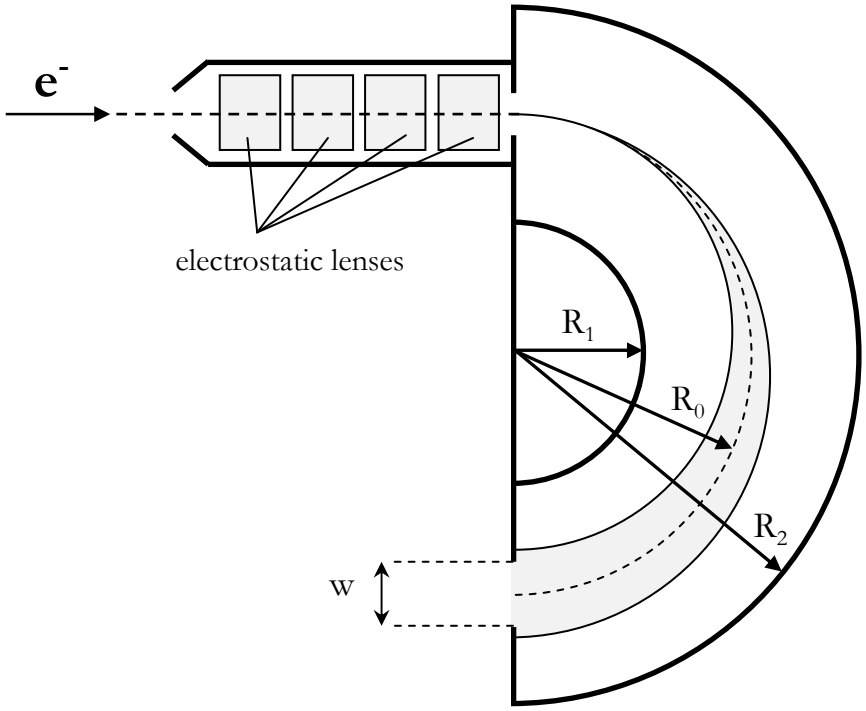

Figure 3.5 – *Schematic diagram of a concentric hemispherical analyser (CHA). R_1 and R_2 are two hemispheres. W is the exit slit width, and R_0 is the path of the detected electrons for conventional single channel detection systems.*

3.3 Review of Real-time Photoelectron Spectroscopy

One of the longstanding drawbacks of the PES technique is that its relatively slow data acquisition rates makes it unable to follow surface processes at the milliseconds to seconds timescale. This means that PES is typically applied by comparing spectra before and after processing (e.g. take spectra; heat up sample (processing); measure again; compare spectra) where information regarding the process itself (including intermediate states etc.) is lost.

The key factor in breaking through into the milliseconds regime is improvement in electron detection. Due to the typical scanning speed of current electron analysers it is

not possible to collect a spectrum of data by quickly scanning without a considerable loss of energy resolution. Achieving second and sub-second time resolution has been approached by changing the way in which data is acquired. An alternative approach to scanning is to increase the number of detectors (or channels) situated across the focal plane of the analyser. In this way the kinetic energies of the electrons are spatially resolved and it is possible to take 'snapshots' of the focal plane (W in figure 3.5). Firstly, examples will be given of acquisition times obtained using conventional, commercially available machines in scanned mode.

Conventional PES systems from the beginning have employed channeltrons for electron detection with more recent systems being fitted with multiple channeltrons (up to 5 or more) which has decreased spectrum acquisition times. They are used in scanning mode to perform PES faster but the typical time per spectrum for scanning mode is limited to around 25 s as reported by Papp *et al* in 2007 [11]. The means of data acquisition is constrained by the necessity to scan the electron energies (although snapshot mode using a channeltron device allows the intensity at a single energy to be measured [12]).

With multiple channeltron systems many of the electrons landing on the focal plane between the channeltrons are not detected. This is where a large number of small detectors positioned side by side across the focal plane of the analyser (i.e. a multi-channel detector) can be advantageous, improving electron detection efficiency and exploiting fast 'snapshot mode' spectroscopy.

The advent of charge-coupled devices (or CCD) is the latest development to have impacted the development of electron detection in electron spectroscopy instrumentation. The latest electron analysers are fitted with CCD cameras which image a fluorescent screen situated in front of the MCP. CCD cameras have a very high pixel density and have the ability to acquire 'snapshot' images of the analyser focal plane in short time intervals. However, so far there has been little evidence in literature that these systems, fitted with CCD cameras are being used to perform real-time (or time-resolved) PES measurements. Torelli *et al* used a SCIENTA SES 2002 analyser fitted with a two dimensional detector in snapshot mode to measure spectra every 5 s [13]. However, one possible drawback is that their dynamic range will not allow for simultaneous measurement of very intense and very weak signals. On the other hand, CCD cameras have the distinct advantage of being two-dimensional detectors which allow electron energy to be resolved in one dimension with the second dimension giving spatial information about the sample surface or the ability to map momentum-space. These kinds of measurements lead into other fields such as the use of toroidal analysers (for k-space mapping) and development of photoemission electron microscopy (PEEM) which allows spatial resolution across the sample [14]. Paolucci *et al* proposed real-time PES with toroidal analysers in 1990 [15]. The concern of this review however, is real-time (or time-resolved) PES and the development of detectors for this purpose.

Recent advances in purpose-built real-time PES instrumentation have made data collection in the second to millisecond timescale a reality. Work on real-time PES first emerged in the early 1990s when two beamlines dedicated to real-time PES were constructed at the NTT R&D Center second-generation synchrotron radiation facility

in Atsugi, Japan [16] and ELETTRA third-generation source in Trieste, Italy [17, 18]. The first of these two groups to publish was the Trieste group with a paper by Baraldi *et al* in 1995 [19]. The first data from the NTT beamline was published a year later [20]. Both systems used at NTT and ELETTRA are multi-channel detector devices which take spectra in snapshot mode with the spectrum dispersed spatially across the analyser plane and detected by multiple channels. Both groups have gone on to reliably study chemical systems in the following years.

In 1995 the first real-time PES results from the SuperESCA beamline were published [19] followed in 1996 by another paper presenting temperature-programmed real-time PES as a new technique for studying surface kinetics [21]. The need for this new approach of using a third generation source and dedicated instrumentation was questioned by Nettesheim *et al* [22] stating that it was possible to perform fast PES using conventional, commercially available systems. Baraldi justified the need for the specific system in question suggesting that the capability displayed by Nettesheim *et al* was down to a stronger signal due to a larger coverage and at the expense of energy resolution [23]. The SuperESCA beamline at ELETTRA has a double-pass electron energy analyser [24] fitted with a 96 channel detector [25] which is reported to be able to collect a spectrum every 100 ms. Much of the work published so far has been using a 48 channel detector [26]. The work done on surface reactions up to 2002 has been comprehensively reviewed by Baraldi *et al* [27]. Numerous institutions have taken advantage of the facility at Trieste and published papers on fast PES [28-30].

Maeda *et al* first published results from the NTT real-time crystal-growth analysis system in 1996 [20] with a study of GaSb growth. The NTT system comprises a

conventional analyser fitted with a 114 channel multi channel detector with a resistive anode [31] which is reported to measure a spectrum every 100 ms using the 2nd generation NTT synchrotron source. Work has continued on the study of GaAs surfaces [32].

The fastest PES spectra reported to date is the 50 ms snapshots reported by Nambu *et al* in 2004. This was using a 768 channel detector developed at Lawrence Berkeley National Laboratory and installed on the ALS, a 3rd generation source. It is described as a 768 channel with a high readout rate and a number of technical papers have been published relating to it [33-36]. However, no more results have been reported since 2004.

This thesis presents real-time PES measurements taken using the Aberystwyth Real-time Electron Spectroscopy (REES) System using a laboratory source (described in the next section) [37, 38]. Data taken using MPW 6.1 at the SRS will also be used to demonstrate the capabilities of this system.

3.4 The Real-time Electron Spectroscopy (REES) System

The Aberystwyth system used to acquire the data presented in this thesis will now be described. The Aberystwyth Real-time Electron Spectroscopy (REES) system is a multi-chamber UHV system which allows *in situ* characterisation using a variety of surface science techniques. This system has been described comprehensively by Bushell [39].

3.4.1 The Aberystwyth Array Detector

The technology for the array detector was originally developed for mass spectroscopy and the detection of ions [40]. The first detector fabricated consisted of a 192 channel one dimensional detector [40-44] mounted on a ceramic substrate beneath a micro channel plate electron multiplier (figure 3.6). The channels had 25 μm pitch giving a pixel density of around 400 cm^{-1}. This technology was then used to produce a detector for electron spectroscopy [45]. The current detector is fitted to a commercial VG CLAM4 electron energy analyser and has 768 channels on a 25 μm pitch giving a total length in the dispersive direction of 19.2 mm [46]. The width of the detector in the non-dispersive direction is 3 mm while the MCP has an active area of 20 x 4 mm. Development of a 1536 pixel detector is underway and initial test data has been reported by Langstaff *et al* [47]. The CLAM4 analyses electrons emitted from a sample area measuring ~ 4 x 3 mm. Since the width of this sampling area varies according to the size of the analyser entrance slit it should be noted that the value quoted here (4 mm) corresponds to a 1 mm entrance slit width.

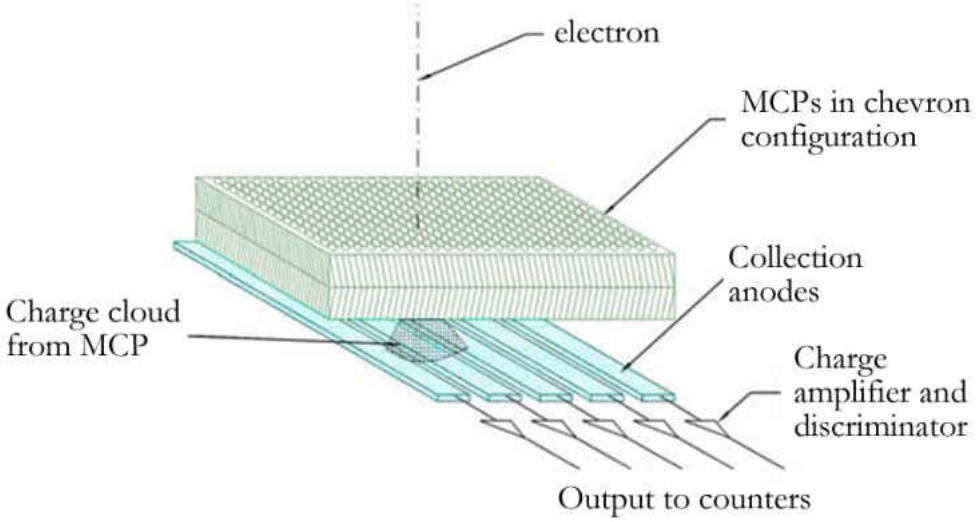

Figure 3.6 – *Taken from [45]. The principle of operation of the array detector. The electrons are directly detected on collection anodes situated underneath a multi-channel plate electron multiplier. Each anode is in direct contact with its pre-amplifier and discriminator circuitry.*

The 768 channel detector coupled to the VG CLAM4 analyser has been used both offline at Aberystwyth using a Mg Kα laboratory source and has also been transported to the Synchrotron Radiation Source (SRS) at Daresbury and fitted to UHV surface analysis spectrometers for experiments on beamline MPW 6.1 and beamline 4.1. Figure 3.7 is a schematic diagram of the system which incorporates data from all parts of the instrument into a single data file.

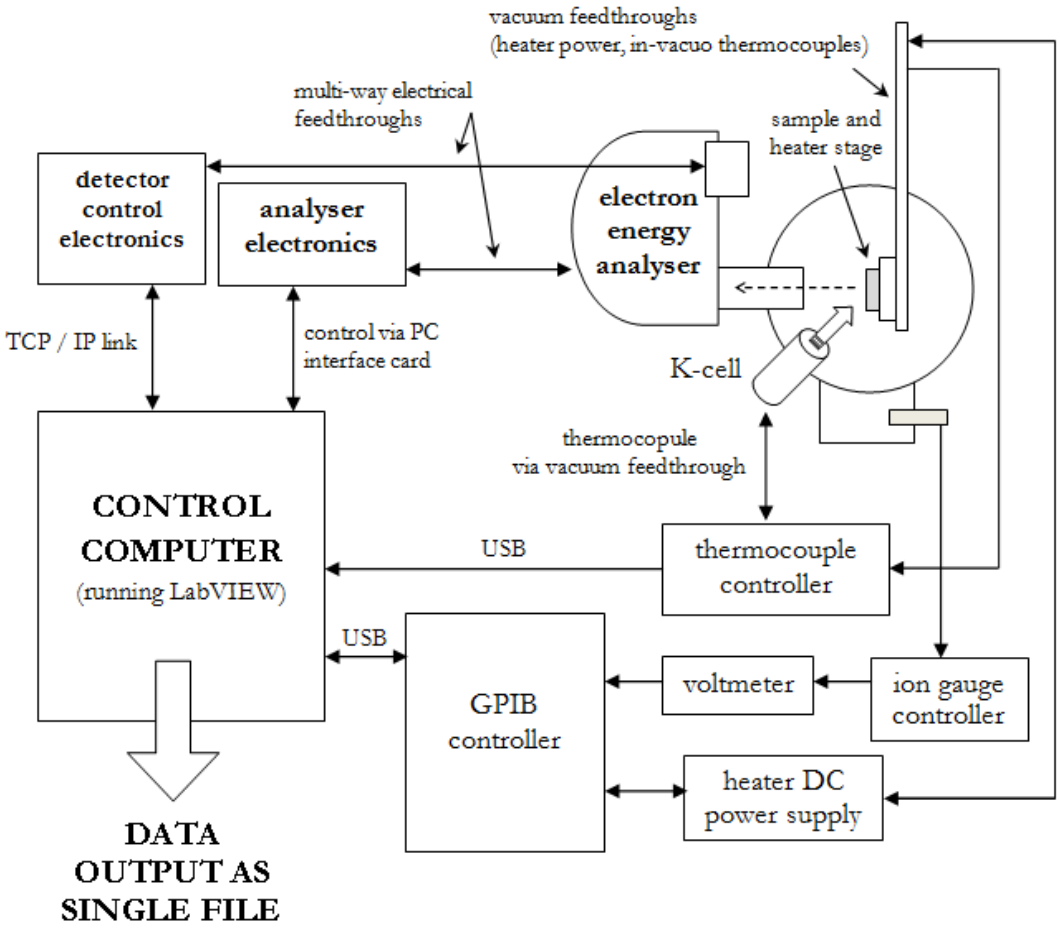

Figure 3.7 – *Schematic diagram of the REES system.*

The detector is controlled from a stand-alone controller outside the vacuum within which a Linux computer (iPEngine) communicates with the control computer by TCP/IP protocol while the analyser is controlled using a VISA card fitted into the control computer.

3.4.2 Sample Processing and Monitoring

Using a USB thermocouple interface, live temperature measurements from the system are recorded at fixed time intervals (typically every second) and logged with the data. Heating of the sample (figure 3.8) was provided using a graphite/BN heater powered by a programmable Kenwood PDS60-12 Regulated DC Power Supply unit. This setup allowed programmed temperature heating cycles to be performed while all parameters and data were recorded by LabVIEW in a single file. Temperatures were monitored by two K-type thermocouples: one situated in a laser driven hole inside the heater and the second under a mounting bolt on the stage (labelled in figure 3.8). An optical pyrometer was used to calibrate the sample temperature which was found to be roughly halfway between that measured by heater and bolt thermocouples. This general observation can be confirmed by comparing the colour of the different components at high temperature (figure 3.8). The temperature difference between the two thermocouple readings increases steadily with increasing temperatures reaching a value of ~ 100 °C for an indicated heater temperature of 850 °C. The chamber pressure was also logged by measurement and conversion of the voltage output on the back of the ion gauge controller. The sample holder and sample stage was constructed out of Ta and Mo to withstand the extreme annealing temperatures which can be in excess of 1000 °C.

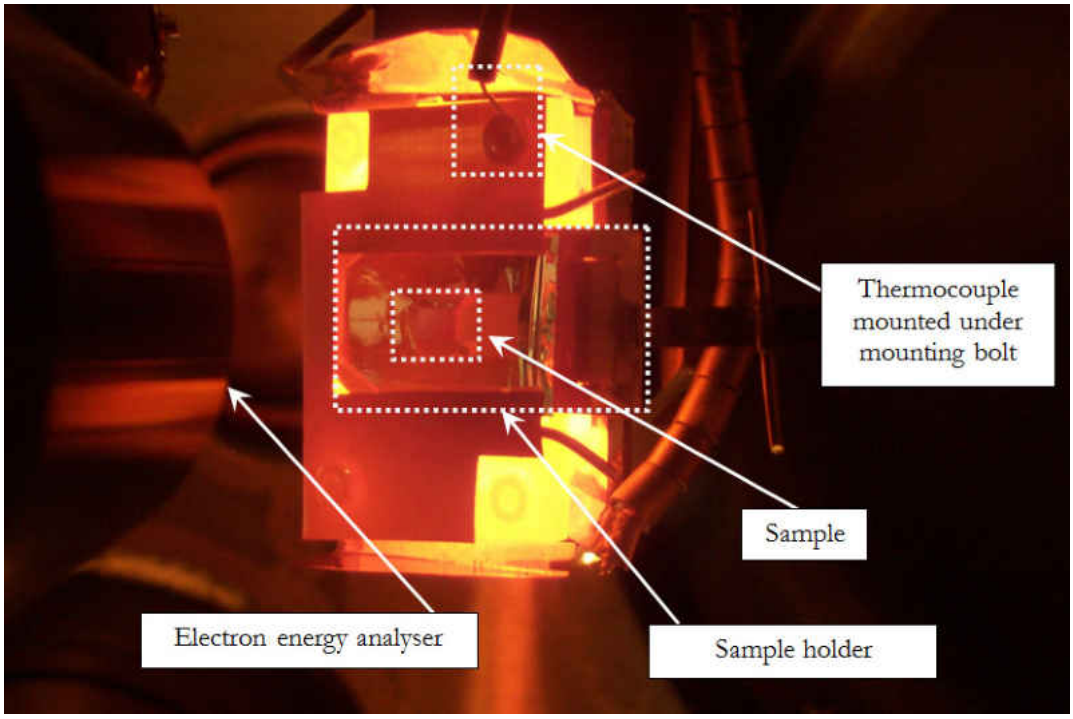

Figure 3.8 – *Labelled photograph of a highly B-doped CVD Diamond (001) 10 nm delta layer in the REES chamber at a temperature of 700 °C and pressure of 8 x 10^{-10} mbar.*

3.4.3 Array Correction

The array detector can also be used in conventional scanning mode and as every pixel is a discrete detector it greatly reduces the data acquisition time due to the efficient method of electron detection. The ability to scan the spectrum across the plane of the analyser provides crucial information regarding the detector which can then be used to process real-time snapshot data. One characteristic of the array detector is a slight variation in the sensitivity of each pixel.

During an energy scan, each pixel is exposed to electrons of the same kinetic energy (or part of the spectrum) in turn as the peak "moves" across the focal plane of the analyser, as illustrated in figure 3.9. This means that all pixels measure the same part of the spectrum at some point during a complete scan allowing a direct comparison of pixel-to-pixel sensitivity. This data is then used to produce a correction file in which a

relative sensitivity ratio is assigned to every pixel (an example of which is found in figure 3.10).

All data taken using the detector is corrected by multiplying each pixel by this correction ratio. However, the variation in relative sensitivity ratios is not only due to the actual pixel sensitivity of the detector but also includes information about the focal plane of the analyser. After prolonged operation of the array detector (2 - 3 years) some pixels were found to malfunction returning no counts. These pixels, designated as 'dead' pixels are easily identified and are removed from the data.

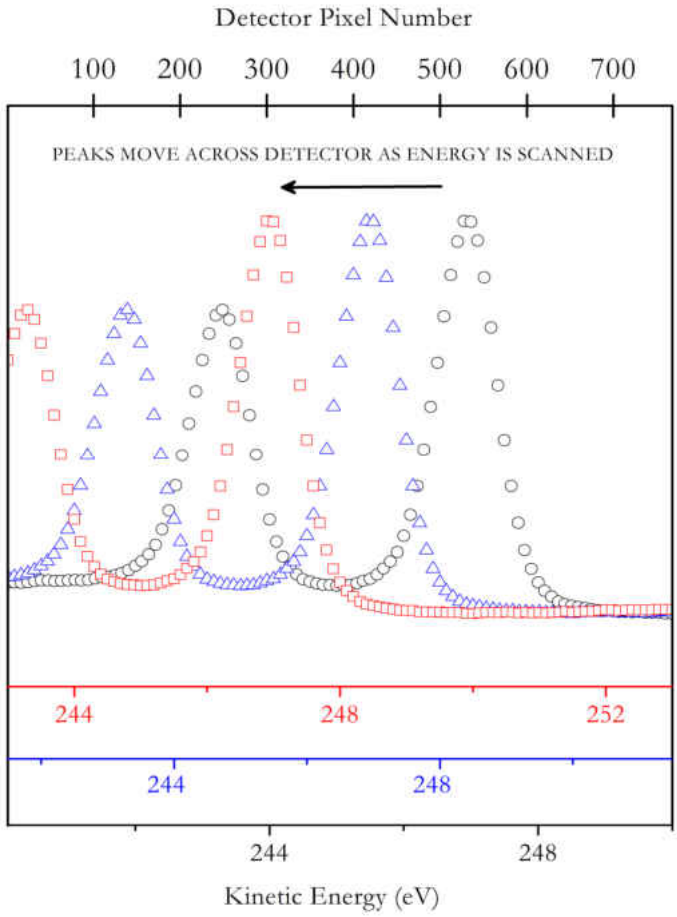

Figure 3.9 – *A schematic of the operation of the array detector in scanning mode. Three snapshots acquired during scanning of a Au 4f core level are displayed. The core level moves across the detector from right to left as the energy of the analyser is increased. The separation of a peak at different energies combined with the energy of the analyser can be used to determine the number of detector pixels per eV for that particular pass energy.*

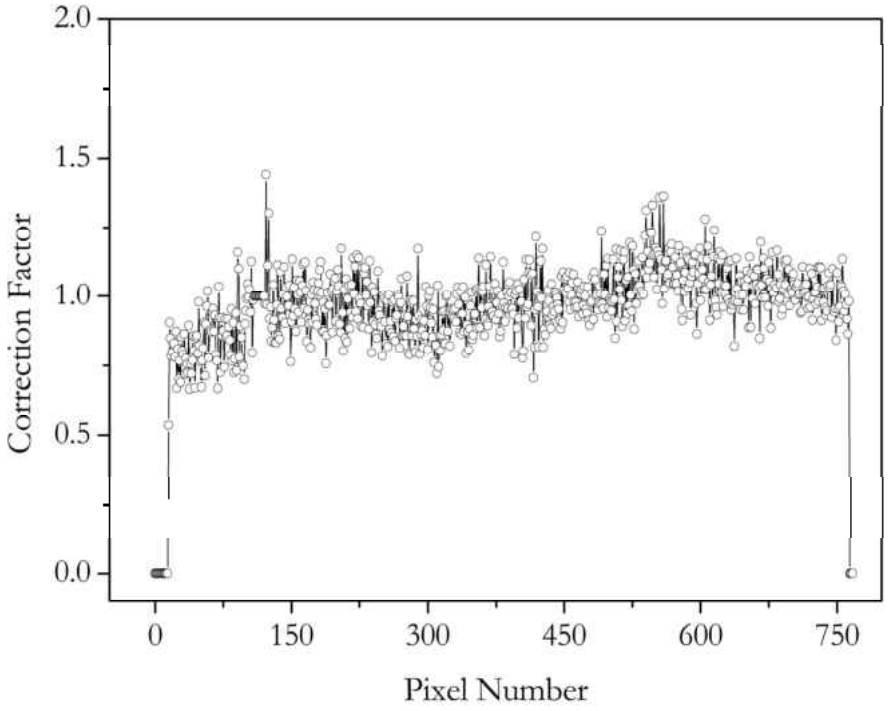

Figure 3.10 – *Example set of correction factors with the "dead" pixels at the edges. Higher pixel numbers correspond to higher values of kinetic energy. Correction factors were obtained with the analyser in Constant Analyser Energy (CAE) mode.*

3.4.4 Weaving of Scanned Spectra

By the end of a scanning run the system will have acquired a snapshot for every kinetic energy interval in the scan window (as illustrated in figure 3.9). These snapshots are then combined by a process referred to as weaving (see figure 3.11) where corresponding kinetic energies from each snapshot are combined resulting in a woven spectrum which has a much higher signal-to-noise ratio than the individual snapshots. For the weaving to be successful an accurate number must be determined for the ratio between the kinetic energy scale and the pixel/channel width (i.e. the number of pixels on the array detector corresponding to one energy step in figure 3.11). This ratio can be determined by identifying the pixel number for an identifiable spectral feature (such as a core level peak) at various analyser energies during the scan thus yielding a value

for the number of pixels per energy step. Alternatively, if two peaks in a snapshot have a known peak separation (measured in energy) the separation in pixels can be used to determine the number of pixels per eV which is used to align the snapshots in energy terms.

The counts from the snapshots which correspond to the same kinetic energy are then summed creating an array of virtual pixels. However, the pixel per eV number obtained will not typically be an integer value and since it is not possible to separate a pixel into smaller components this leads to a variation in the number of actual snapshot pixel data contributing to each specific kinetic energy in the final spectrum. For example, at the extreme edges of the energy axis in figure 3.11 only one snapshot is taken of that kinetic energy window whereas at the centre three snapshots (for this simplified case) contribute to the data at that kinetic energy. To overcome this issue an array mask is produced which determines which actual pixel(s) correspond to a specific virtual pixel. The array mask also eliminates any data produced by dead or defective pixels from the weaving process. Division of the virtual array with the virtual array mask (which contains information regarding the number of snapshots contributing to each pixel in the virtual array) ensures that the relative count rate between pixels remains in proportion. The data at the edges of the energy scale is typically disregarded since it will be outside the energy range selected by the user for the scan. This data will also contain more noise as a lower number of snapshots have contributed to those particular energy ranges at the extremities. This weaving process allows scanned spectra to be taken more quickly than conventional systems using channeltrons for electron detection.

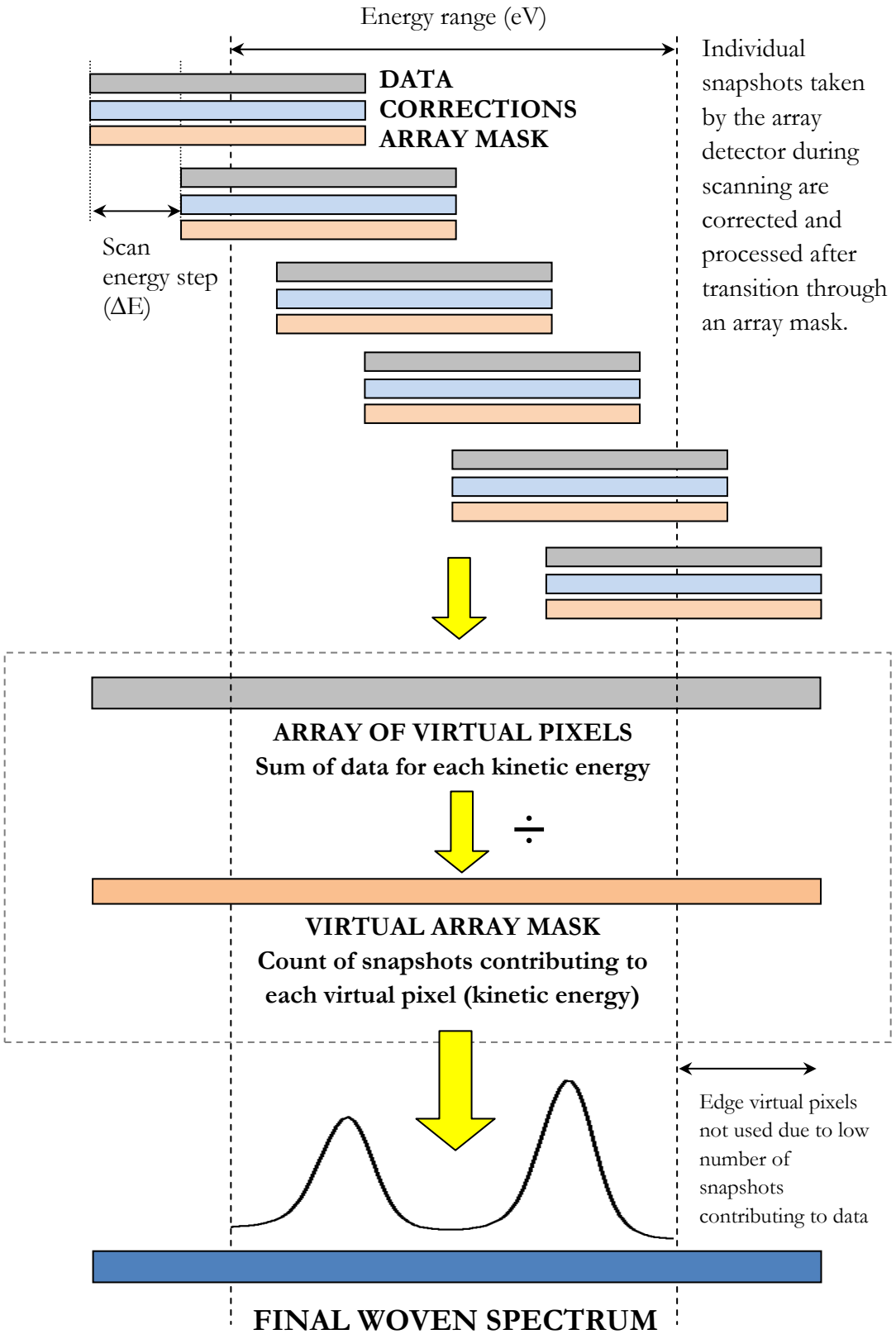

Figure 3.11 – *A schematic diagram of the weaving process where snapshot data acquired during the scan is used to improve the signal-to-noise ratio.*

3.4.5 Real-time Experiments

In this section C 1s core level data obtained for a diamond sample will be used to demonstrate the capabilities of the REES system and the methods used to process real-time spectra. Real-time experiments can be performed by monitoring core-level peaks during surface processing such as thin film deposition and annealing. The parameters for the experiment are chosen beforehand, and include the range of energies to be monitored. The LabVIEW programme allows measurement in 'multisnap mode' meaning that more than one core level or spectral feature can be monitored during an experiment. This is done by setting the central kinetic energy for each region along with the desired collection time. The maximum number of spectral features that can be monitored is ultimately limited by the ability of the analyser to switch between energies and the required collection time due to the intensity of the signal. Once the data has been obtained it can be processed in the time and energy domains. Snapshot spectra can then be sequentially fitted and the parameters plotted against a variable such as time, temperature or overlayer coverage.

Figure 3.12 presents a real-time snapshot taken in 25 ms of a C 1s core level of a single crystal diamond taken on the MPW 6.1 beamline at the SRS, Daresbury. Spectral features such as this core level are imaged across the 768 pixels of the Aberystwyth array detector with the energy window determined by the pass energy of the analyser (a lower pass energy decreases the size of the energy window). The kinetic energy range over which the snapshot will be taken is selected by setting the analyser energy(ies) at the start of the experiment. In photoelectron spectroscopy, resolution is governed by a combination of the analyser settings (including pass energy and slit size) and the line width of the photon source. A lower pass energy and a smaller slit size will yield

greater resolution at the expense of the count rate which results in lower statistics, increasing the required counting time (if the same signal-to-noise level is to be retained).

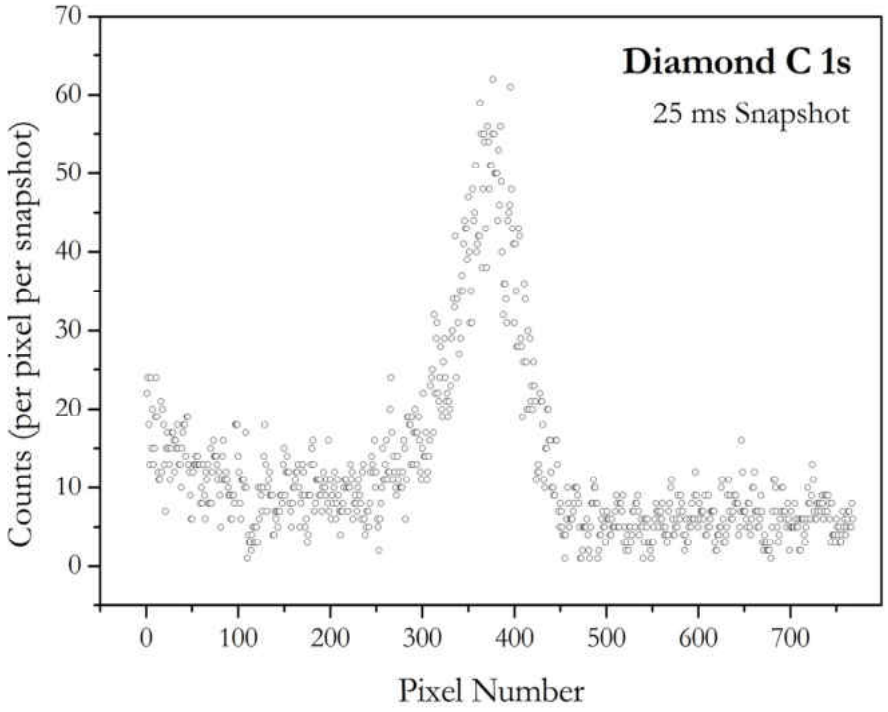

Figure 3.12 – *Example of a C 1s core level for a synthetic single crystal (001) diamond taken in 25 ms at the MPW 6.1 beamline at the SRS, Daresbury.*

The array detector has a very high ultimate resolution due to the high pixel density which means (in theory) that each pixel behaves as a small 25 μm slit. However, in reality the resolution of the spectrum is still governed by the analyser entrance slit width therefore the role of the detector is to provide the most accurate representation possible of the image presented at the analyser exit slit. The extra resolving power of the array detector means that higher pass energies can be used allowing a larger energy window to be monitored as well as increasing the intensity of the signal. The pass energy used for measurements in this thesis was in the range 80 – 200 eV with the entrance analyser slit size set to 1 mm.

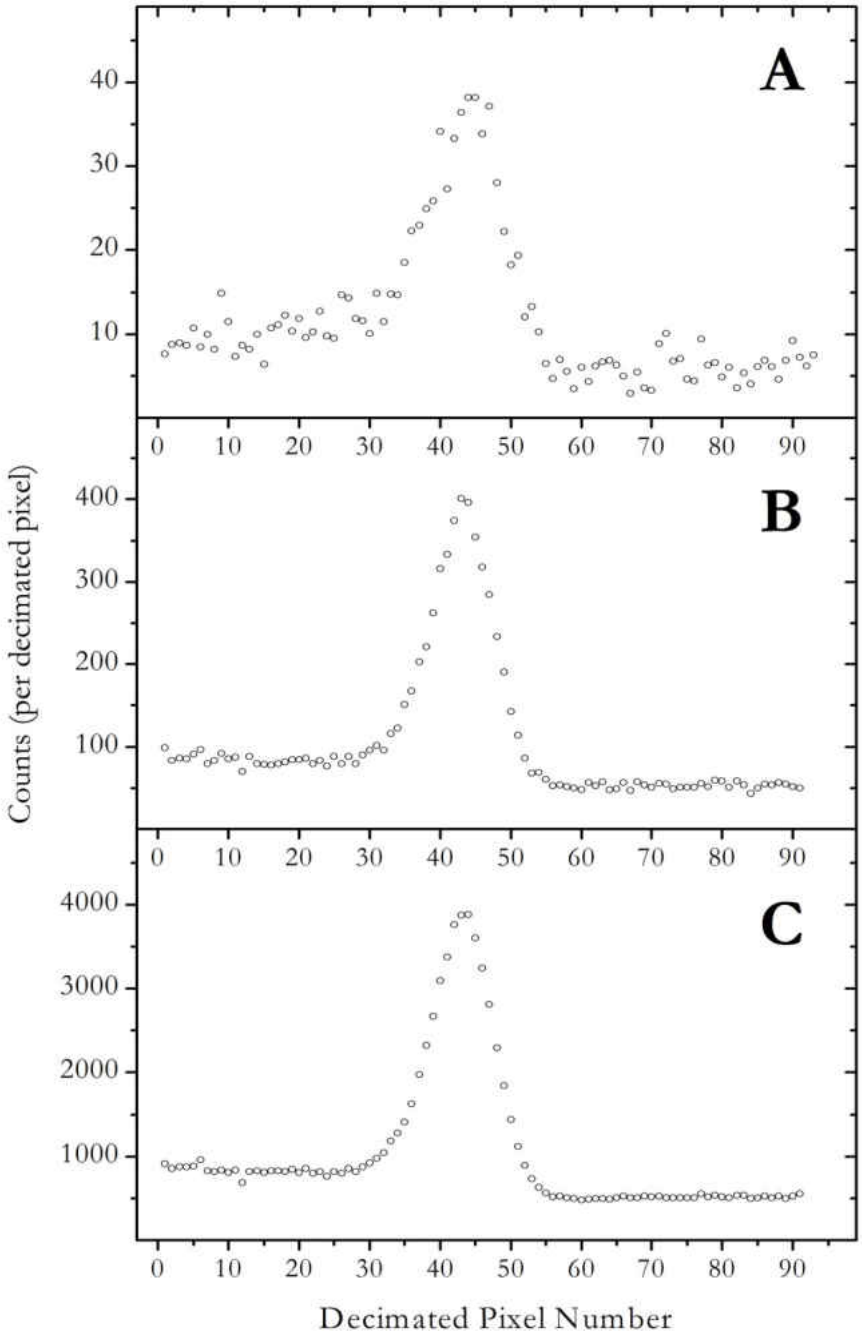

Figure 3.13 – *The C 1s core level of a (001) diamond (originally measured in 25 ms) all decimated by 8 in the energy domain (total decimated pixels = 96) with no decimation in the time domain (A), decimated by 10 in the time domain (total integration time per decimated snapshot = 250 ms) (B) and decimated by 100 in the time domain (total integration time per decimated snapshot = 2.5 s) (C). The value of the decimated pixels are an average over eight pixels.*

3.4.6 Decimation of Real-time Data

Improvement in the signal-to-noise can be achieved through a process known as decimation where data from adjacent pixels are grouped together and averaged or summed to create a snapshot composed of decimated pixels e.g. 768 pixels decimated by a factor of 8 results in 96 decimated pixels (where each set of 8 real pixels across the array are grouped together and located at the centrepoint of the 8 decimated pixels). Decimation always decreases the maximum resolution of the system therefore the decimation factor should be chosen carefully so that no important information is lost in the process.

All data presented in this thesis was decimated by a factor of 8 since 96 data points provided adequate resolution for all spectral features measured in the course of this work. Figure 3.13 (A) illustrates the results of decimation (by a factor of 8) of the 25 ms snapshot presented in figure 3.12.

Further improvement in signal-to-noise levels can be achieved by decimation in the time domain. If a data set has been taken with a very short integration time (as in figure 3.13 (A)) multiple snapshots can be grouped together by summing or addition i.e. decimation in the time domain. For example, figure 3.13 (B) is the C 1s core level (A) (taken using a 25 ms integration time) decimated by a factor of 10 resulting in a set of decimated spectra each representing data collected over 250 ms. Also shown in figure 3.13 (C) is the result of decimation by a factor of 100 which gives an effective electron counting time of 2.5 s. At this point is should be noted that there is a lag or "dead time" between each of the original 25 ms snapshots during which data is read off the array detector chip. Therefore although the actual electron counting time is 250 ms for

10 spectra a single decimated spectra produced by decimation will also include the "dead time" between each of the original snapshots in the group resulting in the decimated spectra representing a longer interval in actual experimental time. This issue, however, does not pose a problem since each snapshot has a time stamp (measured in ms) which ensures that the time axis does not become distorted during the experiment. Consequently, increasing the integration time results in less "dead time" allowing more time to be used counting electrons. This however, has to be balanced against the resolution requirement in the time domain. Obviously it is not possible to decimate by a factor of less than 1 therefore the integration time chosen for the experiment decides the lowest possible time resolution for the data set.

3.5 Chapter Summary

Since its inception in the 1960s PES as a technique has been continually refined. Over the years improvement in both analyser design and detector design has resulted in reduced data acquisition times. The use of multiple channeltrons in electron analysers allows for sampling times in the region of 1 min (with 25 s the fastest reported scanned spectra to date). To decrease the sampling time even further it seems that it is necessary to perform 'snapshot mode' spectroscopy, where the analyser energy remains constant and the photoemission spectrum is dispersed across the focal plane. The arrival of commercial analysers fitted with two-dimensional CCD detectors makes this much easier even though they may be limited by issues such as dynamic range. There seems to be little indication at the moment that these instruments are being used in such a way. Purpose-built, multi-channel real-time PES detectors have been developed by four groups worldwide with the fastest spectrum produced being 50 ms. A 100 ms spectra is the fastest to have been produced consistently. However, all these

enhancements to date (apart from the Aberystwyth array detector) have relied on using synchrotron radiation as their photon source. If this technique is to become a versatile and ubiquitous *in situ* method of characterisation then it needs to be able to operate without synchrotron radiation being a requirement. Real-time PES coupled with capabilities such as variable-temperature PES provides an opportunity to study surface processes dynamically as never before. This thesis presents fast real-time spectra obtained using a laboratory source [36, 37] and has demonstrated the ability of the Aberystwyth REES system to measure a core level in 25 ms using a 2nd generation synchrotron radiation source.

This chapter has outlined the main instrumentation requirements for X-ray photoelectron spectroscopy and has given an overview of current developments in the field of fast electron detection which underpins the ability to perform real-time photoelectron spectroscopy. It was demonstrated how the Aberystwyth array detector when coupled to the REES system allows temperature-dependent real-time photoelectron spectroscopy to be performed using synchrotron and laboratory sources. Data processing methods have also been introduced. The following chapters will present experimental data gathered using this system.

References

1. Duke, P., *Synchrotron Radiation Production and Properties*. 2000: Oxford University Press.
2. Schott, G.A., *XI. On the electron theory of matter and on radiation.* Philosophical Magazine Series 6, 1907. **13**(74): p. 189 - 213.
3. Williams, R.H., et al., *Photoemission from gallium selenide using synchrotron radiation.* Journal of Physics C: Solid State Physics, 1974. **7**(2): p. L29-L32.
4. Pendry, J.B., *Tripping The Light Fantastic.* Nature, 1981. **294**(5837): p. 109-110.
5. Greaves, G.N., et al., *Near-Edge X-Ray Absorption-Spectra for metallic Cu and Mn.* Nature, 1981. **294**(5837): p. 139-142.
6. Greaves, G.N., et al., *Local-structure of silicate-glasses.* Nature, 1981. **293**(5834): p. 611-616.
7. Greaves, G.N., et al., *Two million hours of science.* Nature Materials, 2008. **7**(11): p. 827-830.
8. Hodgson, K.O., *Fundamentals of Synchrotron Radiation – production and properties*, in *Synchrotron Radiation Summer School*. 2006 (unpublished).
9. Bowler, M., et al., *A new XUV beamline on a multi-pole wiggler in the SRS.* Surface Review and Letters, 2002. **9**(1): p. 577-581.
10. *Multipole Wiggler Station 6.1 "Phoenix" - Station Layout.* [cited 2009]; Available from: http://srs.dl.ac.uk/XUV-VUV/science/mpw6.1/layout.html.
11. Papp, C., R. Denecke, and H.P. Steinruck, *Adsorption and reaction of cyclohexene on a Ni(111) surface.* Langmuir, 2007. **23**(10): p. 5541-5547.
12. Yamaguchi, W., et al., *Non-destructive deposition and diffusion-aggregation of size-selected silver nanoclusters on glassy carbon substrates as probed by real-time X-ray photoelectron spectroscopy.* Chemical Physics Letters, 1999. **311**(6): p. 415-420.
13. Torelli, P., F. Sirotti, and P. Ballone, *Surface alloying and mixing at the Mn/Fe(001) interface: Real-time photoelectron spectroscopy and modified embedded atom simulations.* Physical Review B, 2003. **68**(20).
14. Bauer, E., *Low-energy-electron microscopy.* Reports on Progress in Physics, 1994. **57**(9): p. 895-938.
15. Paolucci, G., M. Marsi, and A. Santoni, *Conceptual study of a toroidal electrostatic analyzer suitable for time-Resolved XPS experiments with high-flux synchrotron radiation*

sources. Nuclear Instruments & Methods in Physics Research Section A-Accelerators Spectrometers Detectors and Associated Equipment, 1990. **291**(1-2): p. 140-145.

16. Muramatsu, Y., et al., *A VUV beamline (ABL-3B) for real-time photoelectron spectroscopy at the NTT Synchrotron Radiation Facility*. Nuclear Instruments & Methods in Physics Research Section A - Accelerators, Spectrometers, Detectors and Associated Equipment, 1994. **342**(2-3): p. 596-599.
17. Casalis, L., et al., *ESCA Microscopy Beamline at ELETTRA*. Review of Scientific Instruments, 1995. **66**(10): p. 4870-4875.
18. Abrami, A., et al., *Super Esca - First Beamline Operating At Elettra*. Review of Scientific Instruments, 1995. **66**(2): p. 1618-1620.
19. Baraldi, A., et al., *Time resolved core level photoemission experiments with synchrotron radiation*. Journal of Electron Spectroscopy and Related Phenomena, 1995. **76**: p. 145-149.
20. Maeda, F., et al., *GaSb-growth study by realtime crystal-growth analysis system using synchrotron radiation photoelectron spectroscopy*. Japanese Journal of Applied Physics Part 1-Regular Papers Short Notes & Review Papers, 1996. **35**(8): p. 4457-4462.
21. Baraldi, A., et al., *Temperature programmed X-ray photoelectron spectroscopy: A new technique for the study of surface kinetics*. Surface Science, 1996. **367**(3): p. L67-L72.
22. Nettesheim, S., M. Handschuh, and R. Zenobi, *Comment to: A. Baraldi et al., Surf. Sci. 367 (1997) L67: Temperature programmed X-ray photoelectron spectroscopy: a new technique for the study of surface kinetics*. Surface Science, 1998. **401**(3): p. L452.
23. Baraldi, A., et al., *Reply to "Comment on `Temperature programmed X-ray photoelectron spectroscopy: a new technique for the study of surface kinetics" by S. Nettesheim, M. Handschuh and R. Zenobi*. Surface Science, 1998. **401**(3): p. L455.
24. Baraldi, A. and V.R. Dhanak, *Design Study of a Double-Pass Hemispherical Electron-Energy Analyzer with Multichannel Detection*. Journal of Electron Spectroscopy and Related Phenomena, 1994. **67**(1): p. 211-220.
25. Gori, L., et al., *An embedded control and acquisition system for multichannel detectors*. Nuclear Instruments & Methods in Physics Research Section A-Accelerators Spectrometers, Detectors and Associated Equipment, 1999. **431**(1-2): p. 338-346.

26. Gregoratti, L., et al., *48-Channel electron detector for photoemission spectroscopy and microscopy.* Review of Scientific Instruments, 2004. **75**(1): p. 64-68.
27. Baraldi, A., et al., *Real-time X-ray photoelectron spectroscopy of surface reactions.* Surface Science Reports, 2003. **49**(6-8): p. 169-224.
28. Lee, A.F., et al., *On the coverage-dependent adsorption geometry of benzene adsorbed on Pd{111}: A study by fast XPS and NEXAFS.* Journal of Physical Chemistry B, 2000. **104**(49): p. 11729-11733.
29. Williams, F.J., et al., *Mechanism, selectivity promotion, and new ultraselective pathways in Ag-catalyzed heterogeneous epoxidation.* Journal of The American Chemical Society, 2004. **126**(27): p. 8509-8514.
30. Weststrate, C.J., et al., *Synchrotron XPS and desorption study of the NO chemistry on a stepped Pt surface.* Surface Science, 2006. **600**(10): p. 1991-2001.
31. Maeda, F., Y. Watanabe, and M. Oshima, *Real-time analysis of GaSb(001) during Sb desorption by core-level photoelectron spectroscopy.* Physical Review Letters, 1997. **78**(22): p. 4233-4236.
32. Maeda, F. and Y. Watanabe, *Time-resolved core-level photoelectron spectroscopy and reflection high-energy electron diffraction study of surface phase transition on GaAs(001).* Applied Surface Science, 2004. **237**(1-4): p. 224-229.
33. Mannella, N., et al., *Correction of non-linearity effects in detectors for electron spectroscopy.* Journal of Electron Spectroscopy and Related Phenomena, 2004. **141**(1): p. 45-59.
34. Bussat, J.M., et al., *A next generation, high speed detector for synchrotron radiation research.* IEEE Transactions on Nuclear Science, 2004. **51**(5): p. 2341-2346.
35. Bussat, J.M. and C. Fadley, *Gigahertz-range detector enables improved experiments.* Laser Focus World, 2006. **42**(6): p. 99-+.
36. Nambu, A., et al., *An ultrahigh-speed one-dimensional detector for use in synchrotron radiation spectroscopy: first photoemission results.* Journal of Electron Spectroscopy and Related Phenomena, 2004. **137-40**: p. 691-697.
37. Evans, D.A., et al., *Diamond-metal contacts: interface barriers and real-time characterization.* Journal of Physics: Condensed Matter, 2009. **21**(36): p. 364223.
38. Evans, D.A., et al., *Direct observation of Schottky to Ohmic transition in Al-diamond contacts using real-time photoelectron spectroscopy.* Applied Physics Letters, 2007. **91**(13): p. 132114.

39. Bushell, A., *A New Multi-channel Detector for Electron Spectroscopy and its Application to Single Crystal Diamond*. 2005, PhD Thesis, University of Wales, Aberystwyth.
40. Langstaff, D.P., et al., *A New Ion Detector Array And Digital-Signal-Processor-Based Interface*. Measurement Science & Technology, 1994. **5**(4): p. 389-393.
41. Narayan, D.J., D.P. Langstaff, and K. Birkinshaw, *Simulation Of A Discrete Electrode Detector Array Performance*. International Journal of Mass Spectrometry, 1995. **150**: p. 439-449.
42. Birkinshaw, K., *Advances In Multidetector Arrays For Mass-Spectrometry - A Link (Jims) Project To Develop A New High-Specification Array*. Transactions of The Institute of Measurement and Control, 1994. **16**(3): p. 149-162.
43. Birkinshaw, K. and D.P. Langstaff, *Silicon Technology In Ion Detection - A High-Resolution Detector Array*. International Journal of Mass Spectrometry and Ion Processes, 1994. **132**(3): p. 193-206.
44. Birkinshaw, K. and D.P. Langstaff, *Resolving Power Of A Discrete Electrode Detector Array*. International Journal of Mass Spectrometry and Ion Processes, 1994. **136**(1): p. 71-83.
45. Langstaff, D.P., et al., *A fully integrated multi-channel detector for electron spectroscopy*. Nuclear Instruments & Methods in Physics Research Section B: Beam Interactions with Materials and Atoms, 2005. **238**(1-4): p. 219-223.
46. Langstaff, D.P. and T. Chase, *A multichannel detector array with 768 pixels developed for electron spectroscopy*. Nuclear Instruments & Methods in Physics Research Section A: Accelerators, Spectrometers, Detectors and Associated Equipment, 2007. **573**(1-2): p. 169-171.
47. Langstaff, D.P., et al., *Progress on the Aberystwyth electron counting array*. Nuclear Instruments and Methods in Physics Research Section A: Accelerators, Spectrometers, Detectors and Associated Equipment, 2009. **604**(1-2): p. 133-135.

Chapter 4
Diamond

The first category of carbon-based semiconductor studied using real-time PES was diamond. Firstly this chapter will present some background information relating to diamond, focusing specifically on the production and characterisation of synthetic electronic grade single crystal diamonds. Secondly, temperature-dependent real-time XPS data on a oxygen-terminated (001) diamond will be presented.

4.1 Introduction to Diamond

Diamond is in many ways unique. It is a material which possesses many extreme properties including high thermal conductivity, extreme hardness and an optical transparency ranging from the far IR to UV [1] (see figure 4.1). Its high refractive index of 2.417 makes it a very attractive gemstone and even though diamond was first mined in India over 4000 years ago it remained a rare gem until 1866 when a large deposit was discovered in Kimberly, South Africa. Following this discovery natural diamond became more widely obtainable. However, the price remained high enough to

keep diamond as a gemstone and away from industrial applications, although there are some early instances of diamond being used as an abrasive [2].

- Extreme mechanical hardness (*ca.* 90 gPa) and wear resistance
- Highest bulk modulus (1.2×10^{12} N m^{-2})
- Lowest compressibility (8.3×10^{-13} m^2 N^{-1})
- Highest room temperature thermal conductivity (2×10^3 Wm^{-1} K^{-1})
- Thermal expansion coefficient at room temperature very low (1×10^{-6} K)
- Broad optical transparency from the deep ultraviolet to the far infrared
- Highest sound propagation velocity (17.5 km s^{-1})
- Very good electrical insulator (room temperature resistivity is *ca.* 10^{13} Ω cm)
- Diamond can be doped, becoming a semiconductor (wide bad gap of 5.5 eV)
- Very resistant to chemical corrosion
- Biologically compatible
- Some surfaces exhibit very low or 'negative' electron affinity

Figure 4.1 - *Selected properties of diamond - taken from [1].*

4.1.1 Structure

Diamond is a metastable allotrope of carbon which is only kinetically stable at standard temperature and pressure. The thermodynamically preferred allotrope is graphite, therefore the existence of diamond at room temperature is due to the large activation barrier for conversion from diamond to graphite. Graphite is marginally more stable than diamond with the difference in standard enthalpy of 2.9 kJ mol^{-1} [3]. The carbon atom has a valency of four and in diamond every carbon atom is covalently bonded to four other carbon atoms creating a rigid tetrahedral network where all atoms are equidistant from their 4 nearest neighbours. This bonding arrangement is referred to

as sp^3 bonding and the resultant crystal structure is a face centred cubic (FCC) arrangement with a C-C spacing of 1.54 Å. Combined with a C-C bond strength of 344 kJ mol^{-1} this arrangement is responsible for diamond's high melting point and extreme hardness. Electrically, diamond is a wide band gap material (E_B = 5.5 eV) which exhibits semiconducting properties when doped. In contrast, graphite is sp^2 bonded and has a planar structure.

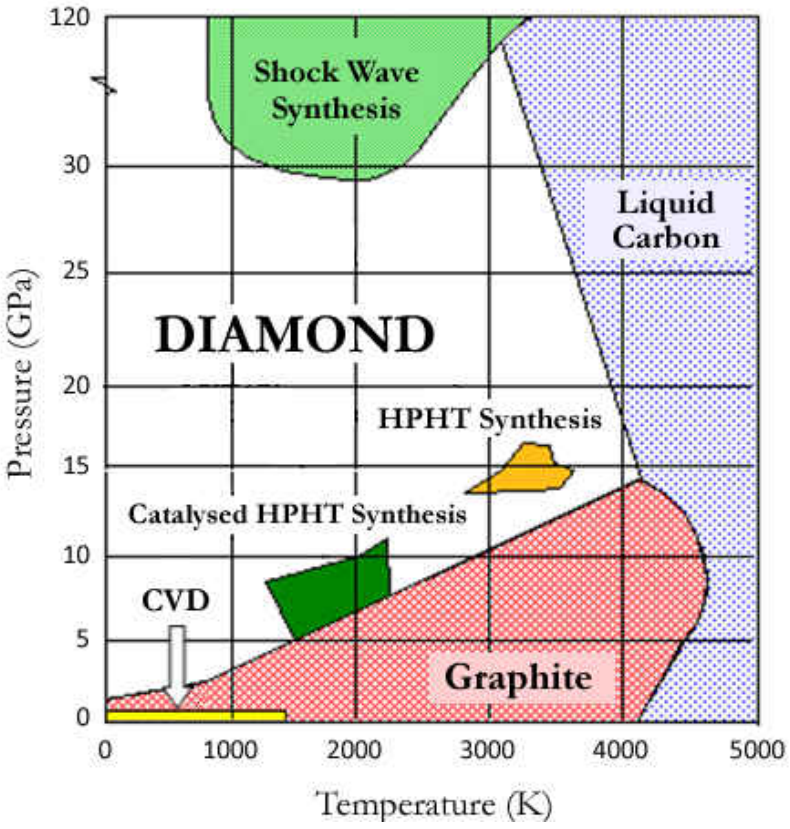

Figure 4.2 – *The phase diagram for carbon.*

4.1.2 Natural Diamonds

Natural diamonds are only formed deep underground (more than 150 km below the surface) where very high temperatures and pressures prevail. The rocks from which diamonds are mined are typically much younger than the diamonds themselves since the diamonds are believed to have formed deep in the mantle. As can be deduced from

figure 4.2, when diamond is heated under atmospheric pressure any broken bonds will re-form as sp^2 graphite islands within the diamond.

Natural diamonds are classified according to the amount of impurities which they contain. Every natural diamond contains some form of impurity, the most common being nitrogen and boron. These impurities give natural diamonds their colour and adds to their desirability as gemstones. Classification of diamonds into type I and II was proposed by Robertson, Fox and Martin in 1934 [4, 5] and in 1952 Custers discovered p-type conductivity in diamond and subdivided type II to two sub-types [6]. The classes are as follows:

Type Ia – The most common type for natural diamonds (Nitrogen content up to 0.3%)

Type Ib – A rare type of natural diamond (accounts for less than 0.1%), where the Nitrogen content can be up to 500ppm.

Type IIa – Very rare in nature. So little nitrogen that it is not easily detected by optical methods.

Type IIb – Extremely rare in nature, nitrogen levels are very low and the crystal exhibits p-type semiconductivity due to the presence of boron which acts as a dopant.

4.1.3 Synthetic Diamond

During the 1950s General Electric in the United States successfully produced the first synthetic diamond [7] by means of a technique which came to be known as the High Pressure High Temperature method (HPHT). They filed patents for the method in 1954 and started large scale production in 1956. The production of HPHT diamonds has been increasing ever since. The method involves using a hydraulic press to compress graphite in the presence of a metal catalyst (originally FeS) at a temperature exceeding 2000 K. These synthetic diamonds have been extensively used as abrasives for countless industrial applications including drilling, mining and polishing. The most recent HTHP diamonds are large enough to be used as gems. Other techniques have been developed to manufacture synthetic diamonds including the shock detonation method [8] which produce nanodiamonds principally for abrasive applications. Laser irradiation of graphite under certain conditions can also form diamond [9]. One of the most recent methods which is still under development is the manufacture of diamond by ultrasound cavitation [10] - this method is attractive since it does not require extreme pressures or temperatures.

The chemical vapour deposition (CVD) method of diamond synthesis (described in section 4.1.5) was developed from the late 1950s onward, with the first experiments being those of Eversole in 1958 who worked for Union Carbide Corporation (USA). Boris Deryagin and his group at the Physical Chemistry Institute in Moscow first published results in 1968 and over the following years improved the growth rates and developed the use of atomic hydrogen and growth on non-diamond substrates in 1976. During the 1980s Nobuo Setaka at the National Institute for Research in Inorganic Materials (NIRIM) in Japan made significant improvements in growth rates and

developed the hot filament method. In the early 1990s there was much excitement surrounding CVD diamond and its prospects for applications in electronics and mechanical components. However there are many obstacles to overcome before diamond can be widely applied to electronic applications.

4.1.4 Diamond Thin Films

Chemical Vapour Deposition (CVD) already provides the highest quality thin films for compound semiconductor structures used for advanced electronic and optoelectronic semiconductor devices [11, 12]. As the name implies this technique when used for diamond growth involves the deposition of carbon species during gas phase chemical reaction onto a solid surface. All low pressure synthetic diamonds are manufactured in CVD reactors which work on the principle of liberating carbon atoms from carbon-containing precursor molecules in the gas phase. For diamond growth the precursor used is CH_4 in a H_2 rich environment. Additionally, the substrate is required to be heated to around 700 °C to obtain growth. Two different types of reactors are illustrated in figure 4.3. In the Hot Filament CVD (HFCVD) method a filament is heated to around 2200 °C in the presence of a precursor gas, resulting in diamond growth on a substrate (figure 4.3-A). The filament lifetime limits the amount of diamond that can be grown in one run while contamination makes it unsuitable for producing electronic grade diamond where purity is critical. The preferred methods for producing electronic grade diamond is to use microwaves to transfer energy to the gaseous phase directly, leading to heating and dissociation of the precursor molecules (figure 4.3-B). The plasma created encompasses the substrate and it is in this environment that the carbon atoms form the tetrahedral network on the heated substrate. Microwave activation has the advantage of maintaining a cleaner

environment producing purer samples with different gas mixtures not possible with a hot filament. An alternative to these include the plasma jet and the combustion flame method which are essentially high power techniques which can yield very high growth rates. However, the drawbacks include the inability to produce large area diamonds and the fact that the high power involved make them less controllable. Hence microwave CVD (MWCVD) is the preferred choice for producing electronic grade diamond.

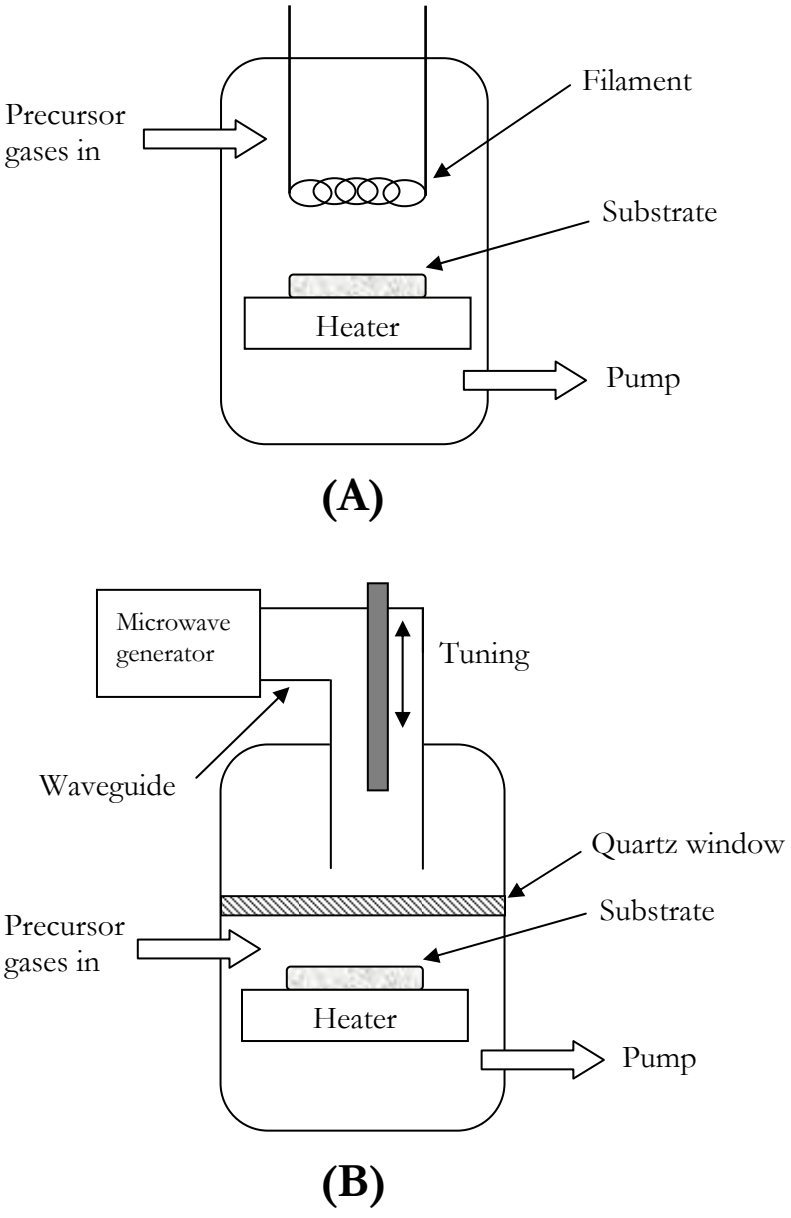

Figure 4.3 - *Common CVD reactors: a hot filament CVD reactor (A) and a MWCVD reactor (B).*

The emerging field of diamond electronics has been reviewed by many authors including May and Kalish [1, 13]. In his article in Science magazine in April 2008 [14] Paul W May outlines the main challenges facing diamond film manufacturers today. These include the ability to produce large-scale, single crystal substrates as any defects in the film (including grain boundaries which are graphitic in nature), significantly degrade its performance as a semiconducting material. Secondly, the relatively slow growth rates achieved mean that CVD diamond remains expensive. Thirdly, the high substrate temperature required for CVD growth means that integration of thin films with other materials such as metals is inherently problematic. This point highlights the incentive for pursuing methods such as ultrasonic cavitation, although this method is still in its very early stages of development. Despite these shortcomings, diamond films have already found numerous applications [15] such as zero wear coatings [16], laser windows [17], heat spreaders [18], bio sensors [19] and even as tweeters in sound system speakers.

4.1.5 Industrial Applications

One of the most exploited physical properties of diamond has been its hardness which is measured as 10 on the Mohs scale – making it one of the hardest material known to man. The use of diamond as an abrasive is reported from the 18th century onwards as natural diamonds were set into saws and drill bits. In 1854 the St Denis tunnel in the Alps was dug using machinery fitted with natural diamond drill bits. Due to the advent of Chemical Vapour Deposition (CVD) diamond more and more applications are emerging. These applications were not previously possible with HTHP diamond. For example CVD diamond films are used today to coat cutting tools and as laser windows,

but the most promising areas for CVD is that of diamond electronics where high crystalline quality and controlled doping is a necessity for semiconductor grade material.

4.1.6 Doping of Diamond

Some natural diamonds exhibit p-type conductivity due to the boron incorporated into them during geological formation and are classified type IIb diamonds. Boron dopants can be incorporated into CVD diamonds by controlling the amount of boron introduced into the system during the growth stage. Although the boron acceptor level is relatively deep at 0.37 eV, boron-doped diamond can still be used for room or high temperature applications. There remains the challenge of a reliable method of producing n-type diamond and therefore the electronic applications to date have been restricted to unipolar boron doped p-type diamond devices. The obvious donor to produce n-type conductivity in diamond is nitrogen however it yields a rather deep donor level at 1.7 eV [20] making it unsuitable for most applications. Further, because of the restricted space in the diamond lattice (due to the comparatively small size of the carbon atom) many other dopant atoms are simply too big. Some success has been achieved by using phosphorus as a dopant. However, at 0.6 eV, the donor level still lies relatively deep in the band gap yielding very low conductivities at room temperature. There has been a lot of interest in this approach and a body of literature is slowly forming in this field. Another way of producing n-type conductivity is by deuteration of boron-doped p-type diamond, a method first reported in 2003 [21] and which is rapidly gaining interest [22-24]. The incentive for producing n-type which has good conductivity at room temperature is large due to the potential of bipolar diamond devices. Reports of n-type devices are now appearing in literature [23]. A large amount

of effort and activity continues in the field of p-type devices [25] and this is where this study will concentrate.

4.2 Single Crystal Diamond Surfaces

Although issues remain regarding doping in the bulk, the surface properties of diamond play an equally important role in the application of diamond for electronics. The properties of almost perfect natural single crystal diamond surfaces have been studied for decades but the latest single crystal CVD diamonds have been shown to outperform their natural counterparts in terms of defect density and carrier mobilities [26]. This means that understanding the electronic surface properties of CVD diamond is critical if they are to be tuned or tailored to specific device applications.

Before 1970 the studies of diamond were largely conducted on powdered samples, but the development of surface science techniques during the 1960s onwards facilitated a much better understanding of single crystal surfaces. The first LEED measurements were by Lander and Morrison in 1966 on the (111) crystal face which revealed information regarding the ordered surface structure [27]. The subsequent development of spectroscopic techniques (such as X-ray photoelectron spectroscopy) and later, scanned-probe microscopy (such as AFM and STM) has facilitated a comprehensive understanding of all aspects of diamond surfaces.

Work on the surface properties of diamond has been reviewed by many authors including Ristein in 2006 [28]. The (001) and (111) surfaces has received the most attention to date. This is due to the fact that (001) surfaces can be selectively grown as polycrystalline CVD diamond films whereas other faces are unstable under CVD

growth. The (111) face is the natural cleavage face of diamond. It should also be noted that the interest in (110) surfaces arises from the fact that the bonding arrangement occurs at steps of (001) and (111) terraces.

4.2.1 The (001) Surface

The (001) surface has emerged as the most important crystal face for device applications. This is due to the fact that it is less prone to stacking faults than the (111) surface and can be grown on a variety of non-diamond substrates such as silicon [29].

The clean bulk-terminated (001) 1 x 1 surface (top panel in figures 4.4 and 4.5) reflects the symmetry of the bulk lattice with the topmost atoms all equidistant to each other with a separation of 2.523 Å [30]. This configuration however, is unstable since each carbon atom has two dangling bonds which (in the absence of any adsorbants) reconstruct into a more energetically favourable 2 x 1 configuration (bottom panel in figures 4.4 and 4.5). Each surface carbon forms a π-bonded dimer with its nearest neighbour resulting in a surface which has a reduced number of unbonded electrons on the surface atoms. The dimers line up along the <110> direction. Due to their interaction with the dangling bonds, bonding – anti-bonding splitting is observed between the occupied and unoccupied π orbitals in the dimers. A distance of 2.523 Å is retained between the surface dimers in one direction. The consequence of this is that the surface band structure is semiconducting with a band gap of 1.3 eV between occupied and unoccupied surface states [31]. These states however can play no part in conduction since they sit within the valence band of the bulk diamond which means that they cannot exchange charge carriers with the bulk [32].

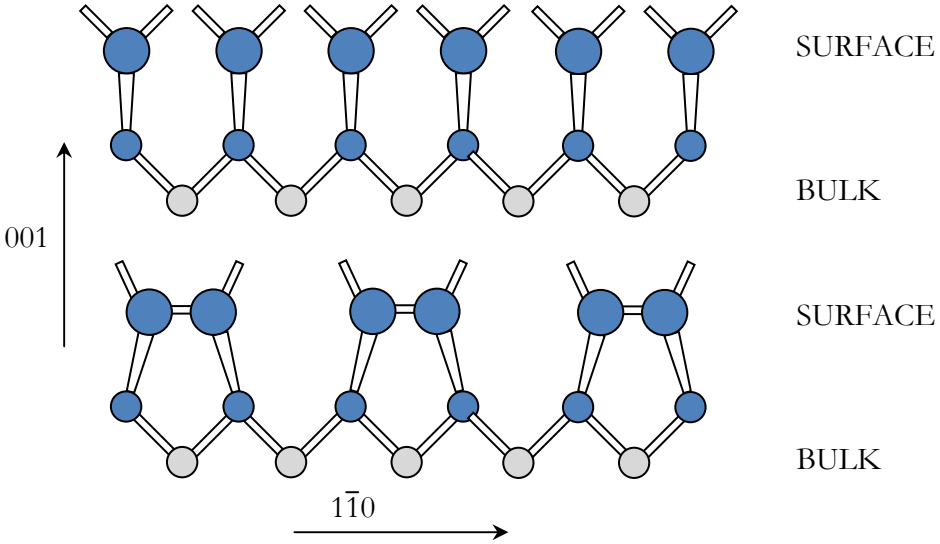

Figure 4.4 – *Cross-section of the clean (001) diamond: for the 1 x 1 surface (top) the reconstructed 2 x 1 surface (bottom).*

The most widely studied surface adsorbate for diamond is hydrogen. It is an obvious choice since CVD diamonds come out of the reactor vessel with a hydrogen-terminated surface due to the presence of hydrogen in the plasma. Hydrogen-terminated surfaces also form naturally during polishing in oil but higher quality surfaces are obtained if they are prepared in a plasma [33]. The hydrogen-terminated (001) surface has a 2 x 1 LEED pattern and it therefore appears that this surface is reconstructed with one hydrogen atom bonded to each surface carbon atom. This surface is referred to as diamond (001) 2 x 1:H.

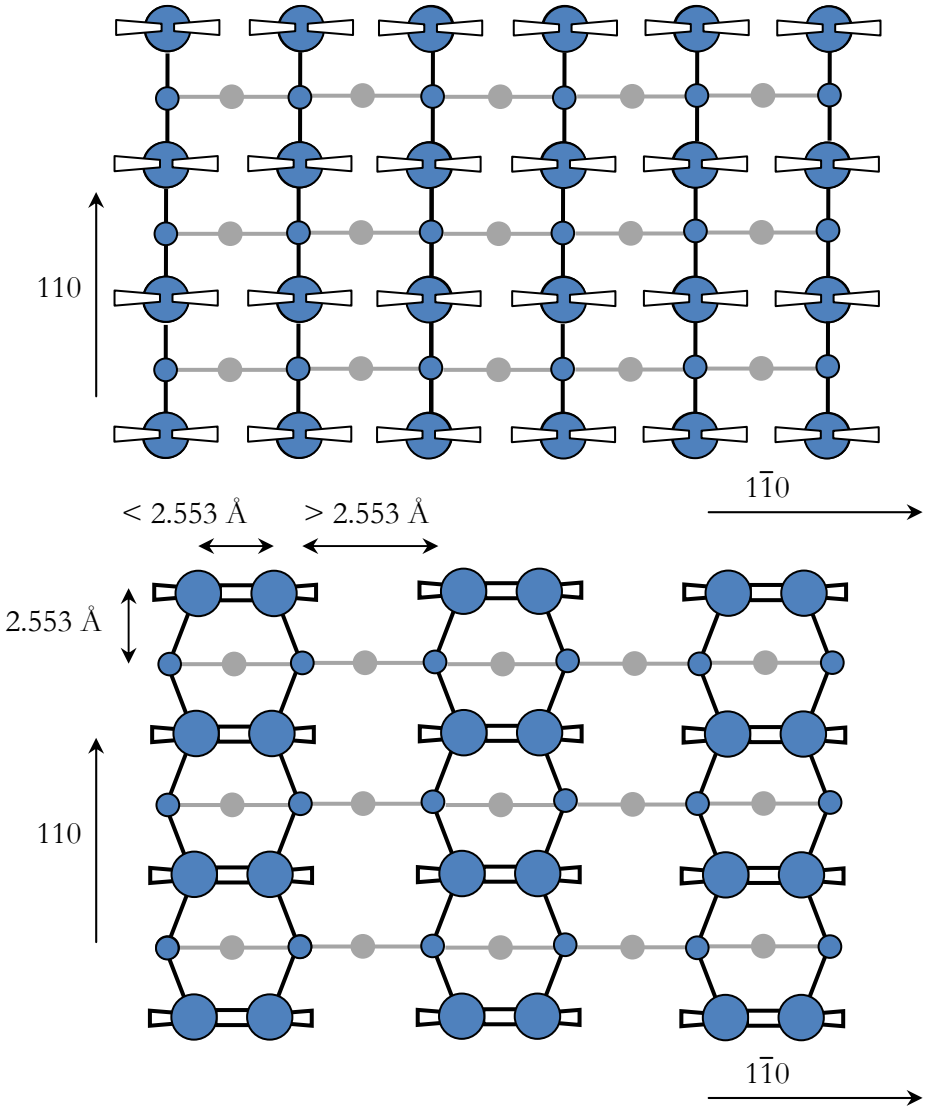

Figure 4.5 – *The view in the <001> direction of the 1 x 1 (top) and 2 x 1 surface (bottom). The large blue atoms are the closest to the surface followed by the small blue atoms and grey atoms.*

Oxygen is also frequently used as an adsorbate on diamond. The oxygen-terminated (001) has been shown by low energy electron diffraction (LEED) to have a 1 x 1 surface periodicity [34]. This surface, referred to as diamond (001) 1 x 1:O has two possible bonding structures. The first is the ketone or top site model (figure 4.6-A). In this configuration, one oxygen is double bonded to each surface atom. The second possibility is the ether model where each oxygen forms a bridge between two neighbouring surface atoms (figure 4.6-A). However, in the presence of hydrogen a

hydroxyl termination can also occur [35]. Theoretical calculations for these models give comparative values in terms of energetic stability with some preferring the top site model [36] while others support the ether model [37]. However most experimental data support the ether model [28]. Photoemission spectroscopy has revealed an occupied surface state around 3 eV below the Fermi level on a boron-doped type IIb [38].

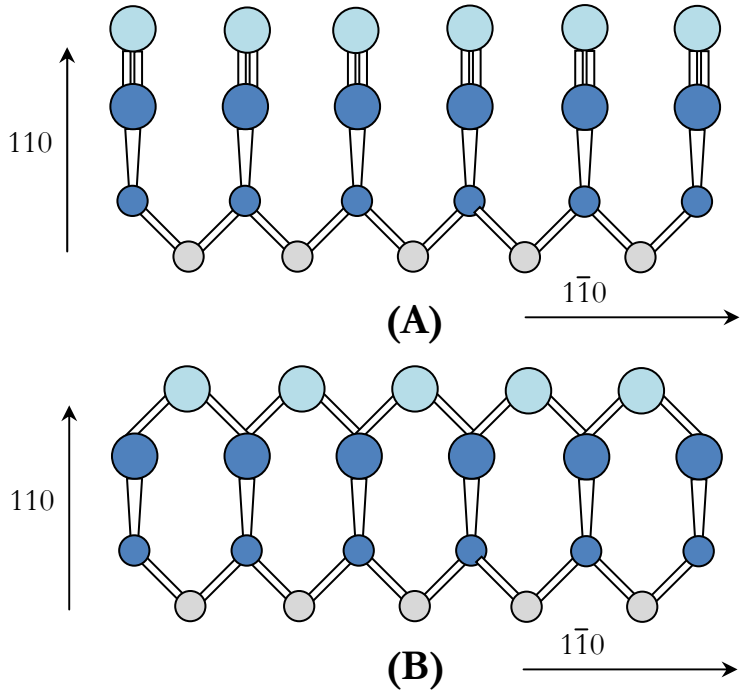

Figure 4.6 – *Possible bonding configurations for the (001) 1 x 1:O diamond surface: the ketonic (or top site) model (A) and the ether (or bridging oxygen) model (B).*

4.2.2 The (111) Surface

In the 1 x 1 configuration there is one dangling bond per surface atom. For this surface the bulk-terminated structure reconstructs at high temperature to a 2 x 1 geometry which has been described by Pandey [39]. In this configuration all the surface atoms become nearest neighbours with a separation of around 1.43 Å, almost identical to that

found in graphite. Occupied surface states have been observed in the gap up to 0.4 eV above the VBM.

Unlike the (001) surface, hydrogen termination of the (111) surface stabilises the bulk-terminated configuration. Covalent bonding of hydrogen to the surface atoms is responsible for bonding states 4 eV below the VBM. Concerning oxygen termination there is much less experimental data. It is easier to oxidise a pre-hydrogenated surface, with hydrogenation of an oxidized surface a much harder task. Oxygen-terminated diamond does not reconstruct back to a 1 x 1 configuration since it appears that the divalent oxygen bonds to bridge sites on the π-bonded Pandey chains [32]. Some real-time XPS measurements relating to the reconstruction of the (111) surface were reported by Bushell [40].

4.2.3 Surface Termination and Negative Electron Affinity

As it has been shown the main crystallographic planes (001, 111) are very well understood in their adsorbate-free form with a large body of literature constituted of theoretical calculations supported by experimental results. For most practical applications all diamond surfaces are terminated by adsorbates and the observed configurations for these planes have been outlined. The ability to change the termination (known as functionalisation) allows surfaces to be customised for different applications. It is clear that diamond does not behave in the same way as conventional semiconductors and this unconventional behaviour has drawbacks as well as advantages.

As it has already been mentioned the most common surface termination for diamond is hydrogen. Due to carbon's relatively high electronegativity hydrogen termination has been shown to lower the electron affinity. Negative electron affinity (NEA) was first reported by Himpsel on the (111) diamond surface [41] and was latter observed on the (001) surface by Van der Weide [33] and has also been observed on polycrystalline diamond [42]. This observation raised the possibility of using diamond as a cold electron emitter since an NEA means that any electron reaching the conduction band is immediately emitted from the surface. However Ristein notes [28] that that there is an additional requirement that electrons are carried through the semiconductor as majority carriers and hence will depend on the success of achieving n-type doping. Oxygen has a very high electronegativity and has the opposite effect to that of hydrogen. Therefore an oxygen-terminated surface exhibits a higher positive electron affinity. Oxidation is often used as a means to lower the conductivity of diamond surfaces [37].

4.3 Experimental Results on Clean Diamond

In this section results on a clean, oxidised single crystal diamond surface are presented. The sample used was a moderately boron-doped ($N_B \sim 2 \times 10^{16}$ cm^{-3}) synthetic (001) CVD grown single crystal diamond (7.5 x 7.5 x 1.5 mm^3) provided by Element Six Ltd.

4.3.1 Experimental Setup

X-ray photoelectron spectroscopy was carried out in a UHV chamber using a Mg Kα X-ray source coupled to a SPECS Phoibos 100 Electron Energy Analyser fitted with a CCD detector. Indirect heating of the sample was provided by means of a graphite/BN heater controlled by a programmable temperature ramping and collection

system. In addition to conventional measurements, spectra were collected every 4 s enabling changes to be monitored from room temperature to over 1000 °C. The spectra were subsequently fitted allowing the key parameters of the C 1s and O 1s core levels to be monitored during heating. LEED measurements were also performed *in situ* using a VG rear-view LEED system.

4.3.2 Sample Preparation

The method described here supplies an oxygen-terminated surface. Prior to transfer into the vacuum spectrometer the (001) surface was polished using 25 μm diamond paste and then heated in sulphuric acid for 10 minutes followed by the addition of potassium nitrate and heating for a further 10 minutes. The diamond was then rinsed and sonicated in de-ionized water. An existing aluminium carbide contact present on the back of the sample survived the etching process and a thin layer of Au was deposited on top using an automatic Au sputter coater operating under low pressure, ensuring a good Ohmic contact between the back of diamond and the sample holder. Following examination by optical microscopy the front face was wiped with methanol and dried using clean nitrogen gas before loading into the UHV system.

4.3.3 Characterisation of the Clean Surface

The XPS spectra of the diamond surface were measured both as loaded and after a series of annealing cycles. XPS survey scans (Figure 4.7-A) are dominated by the C 1s core level at 969 eV (on the kinetic energy scale) and a small O 1s component at 722 eV. The as loaded spectrum also contained a small but detectable peak at 855 eV which is identified as the N 1s core level and indicated that a sub-monolayer coverage of

nitrogen was present on the surface. Upon annealing to a relatively low temperature of 240 ˚C the nitrogen signal disappeared. The amount of oxygen detected (figure 4.7-A) was 10 % of the total peak area (after correction for the transmission function of the analyser) for the as loaded sample (Figure 4.7-A) but with sequential annealing of the surface to temperatures of 400 ˚C , 550 ˚C (figure 4.7-B), 700 ˚C and 1000 ˚C (figure 4.7-C) the coverage decreases and stabilises at ~ 6 %. The relative peak areas of the C 1s and O 1s were used to calculate the relative abundance of each element in the sample volume.

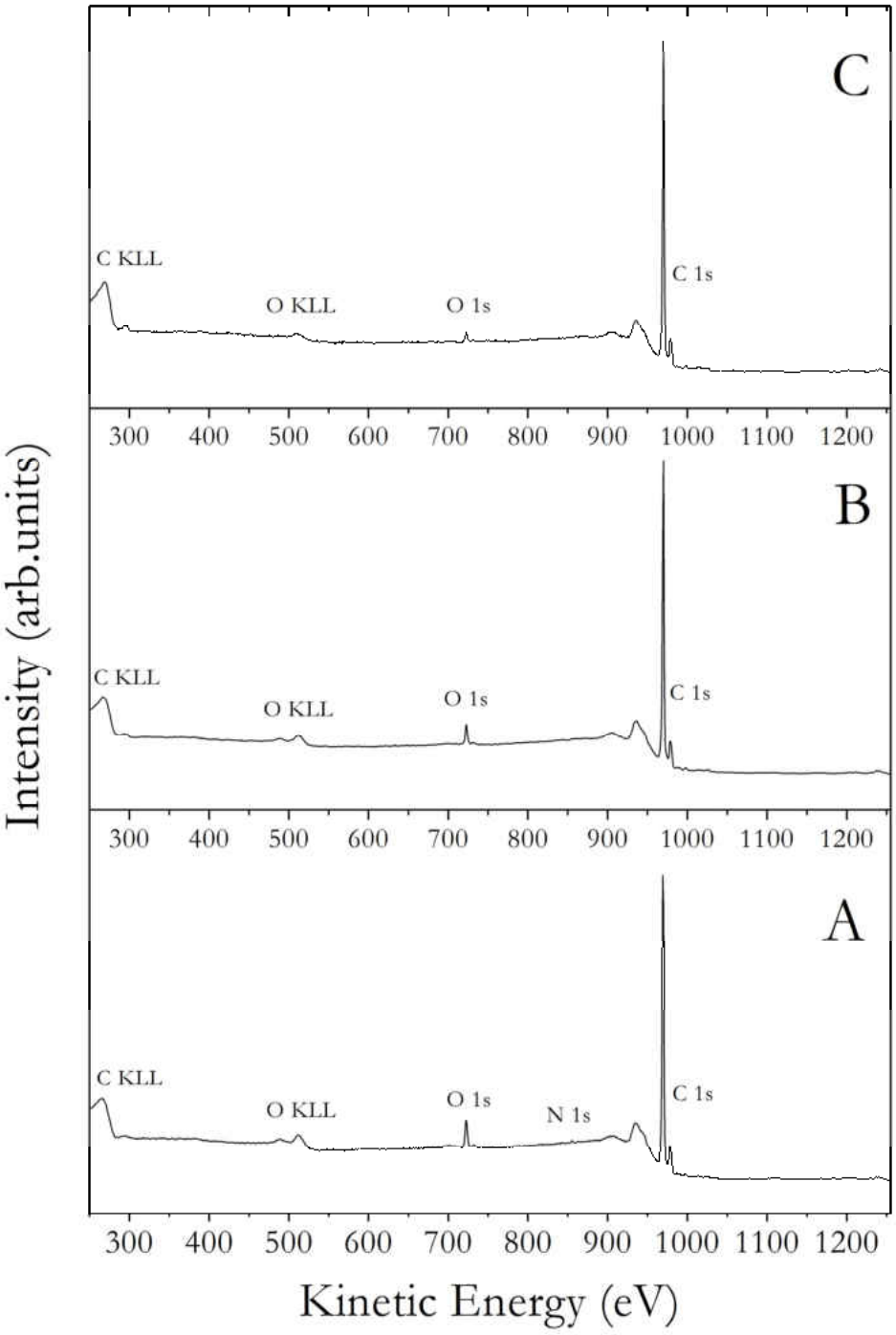

Figure 4.7 – *XPS survey scans of the oxygen-terminated p-type (001) diamond surface: as loaded (A), following heating to 550 ^{0}C (B) and 1000 ^{0}C (C).*

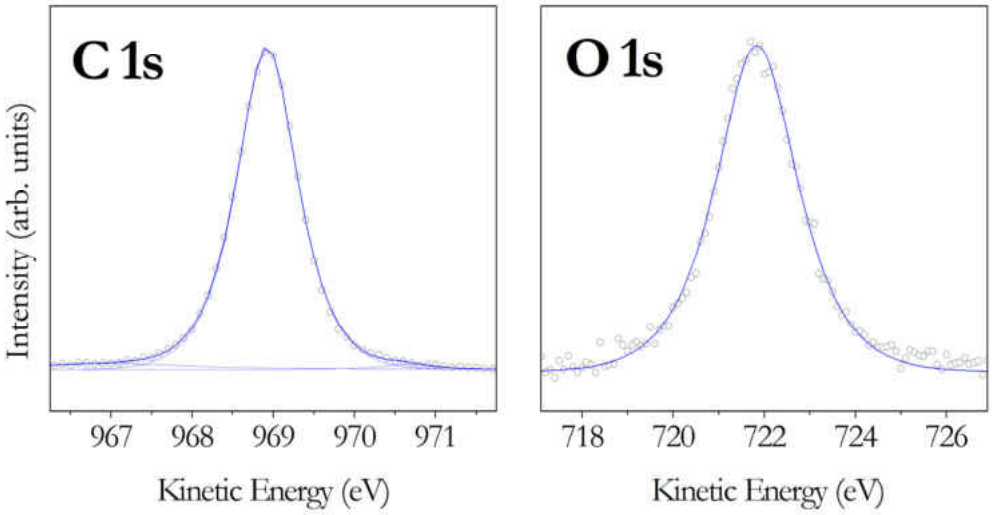

Figure 4.8 – *XPS spectra of the C 1s and O 1s core levels for the oxygen-terminated p-type (001) diamond surface after annealing to 400 ˚C.*

Detailed spectra of the C 1s and O 1s core level were recorded (figure 4.8) following annealing of the diamond to 400 ˚C. For the C 1s, the main component centred at 968.9 eV is the bulk component related to sp^3 bonding. The FWHM of this peak when fitted with a Voigt function is 0.90 eV indicating a high quality surface. A smaller component on the high kinetic energy side is attributed to C-H bonds originating from trace amounts of hydrocarbons present on the surface. LEED measurements confirm the existence of a 1 x 1 surface structure (figure 4.9). The O 1s core level (figure 4.8 – right) can be fitted with a single component with a kinetic energy of 721.8 eV and a FWHM of 2.1 eV indicating a single oxygen-carbon absorption arrangement at the surface. Previous work by Evans *et al* on the heated (110):O plane fitted the O 1s peak with multiple components each with a FWHM of around 2 eV. The single component in figure 4.8 (right) when referenced to the C 1s peak position of the bulk diamond corresponds to a ketonic oxygen configuration where each oxygen (which is divalent) forms a double bonds with each surface carbon atom as illustrated in figure 4.6-A.

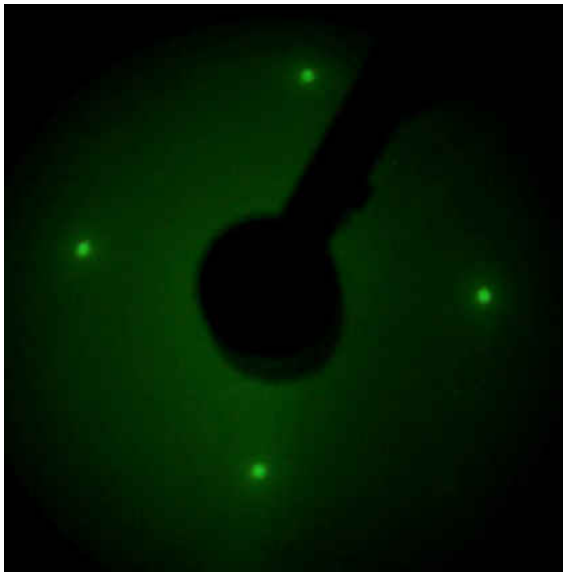

Figure 4.9 – *1 x 1 LEED pattern (beam energy = 85 eV) observed for the oxygen-terminated p-type (001) diamond surface following annealing to 400 °C.*

4.3.4 Annealing of the Clean Surface

During an annealing cycle to 550 ˚C the C 1s core level of the diamond was measured using real-time XPS (figure 4.10-A). The time axis represents a heating cycle from 20 ˚C to 550 ˚C and subsequent cooling. Figure 4.10-B presents the temperature, heater power and chamber pressure as a function of time during the cycle. At 40 s the heater was switched on and the power gradually increased, reaching its maximum value of 33.5 W at time 2450 s; it was then decreased steadily back to zero by 3645 s. The temperature follows the heater power with a time lag of ~ 30 s measured between the point of maximum power and maximum temperature. Measurements continued during cooling of the sample until 7500 s at which point the temperature had decreased to 68 ˚C. Two significant pressure increases were observed during heating at 300 s, 1500 s with a smaller increase at ~ 2200 s. These pressure increases correspond to desorption of water (at ~ 100 ˚C) and hydrocarbon molecules (at ~ 350 ˚C) from the surface of the sample during heating. The heating caused large pressure increases since it this was the first annealing cycle performed since the diamond was introduced from atmosphere in to the UHV system. The pressure quickly recovers as the sample cools after 2520 s. Desorption of contaminants from the diamond surface is confirmed by the increase in intensity observed for the C 1s peak of diamond (figure 4.10-A) with the count rate increasing from 1.6 x 10^5 to 1.8 x 10^5 counts per second per pixel by time 7500 s. A totally reversible temperature dependent shift was also observed in the peak position during the cycle, the origins of which are discussed further in this section.

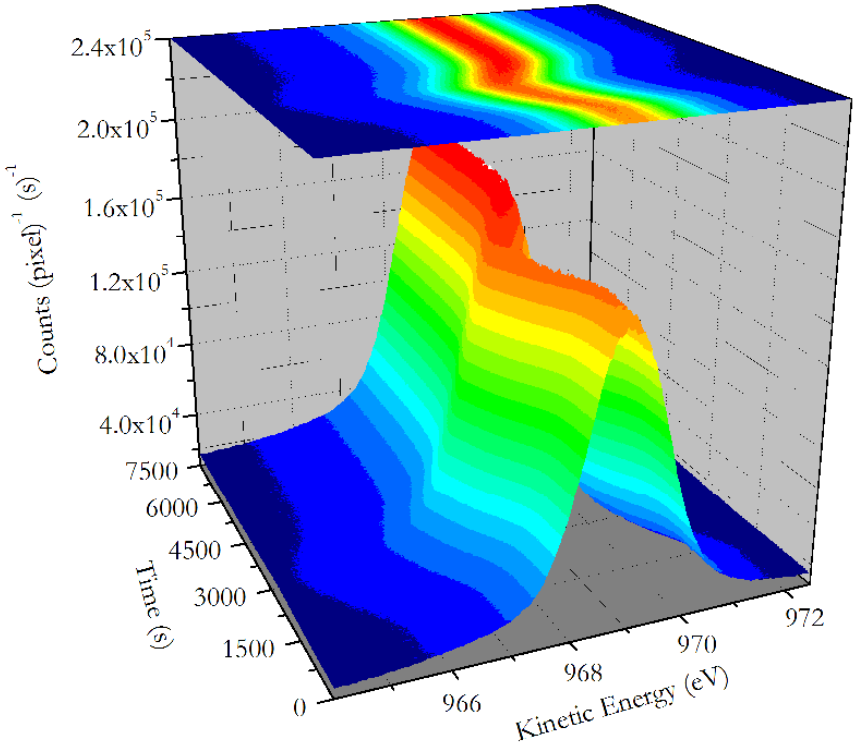

(A)

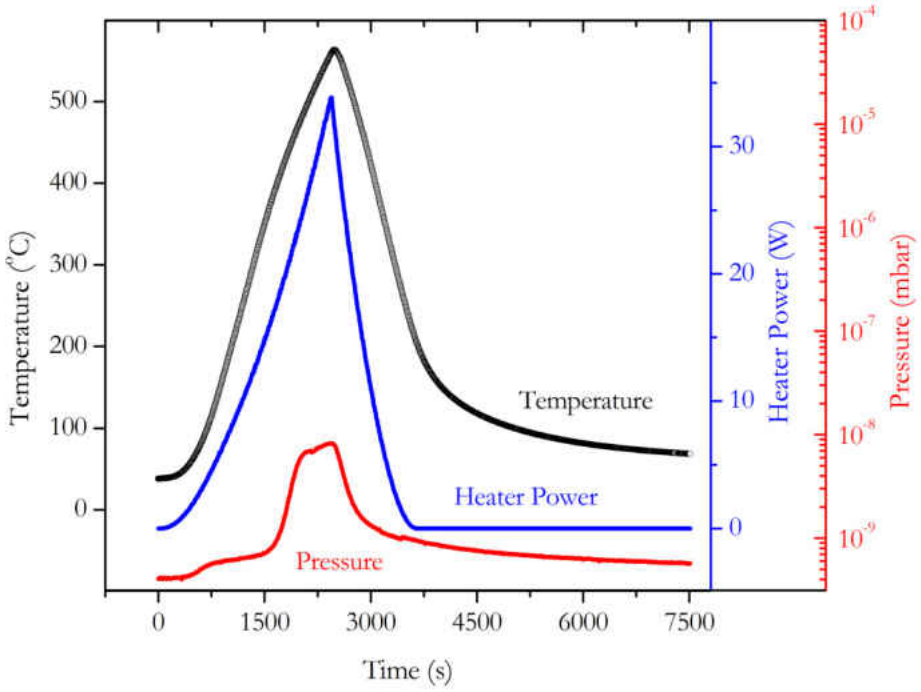

(B)

Figure 4.10 – *Real-time XPS for an annealing cycle up to 550 ˚C which includes: a 3D plot of the (001) diamond C 1s core level (A) and a time plot of temperature (black), heater power (blue) and pressure (red) during the cycle (B).*

In figure 4.11 the peak shift is plotted against sample temperature for two such heating cycles. All temperatures displayed are direct thermocouple measurements. In both cases (330 ˚C and 490 ˚C) the peak returns to its original energy position at the end of the cycle. The first heating cycle to 330 ˚C (red squares) shows a slightly larger hysteresis than the second heating to 490 ˚C (black circles) and is due to the lag between the thermocouple temperature and the actual sample temperature since its magnitude is dependent on the rate of heating and cooling. The heating rate was 0.35 °C s^{-1} for the 330 ˚C cycle and 0.25 °C s^{-1} for the 490 ˚C cycle. The top inset shows the peak position of the Ta on the sample holder (with same scale as lower panel) during a similar experiment (heating rate of 0.15 °C s^{-1}) which confirms that the shift is not an instrumental effect and that it is only the diamond which exhibits this large shift in kinetic energy of the C 1s core level.

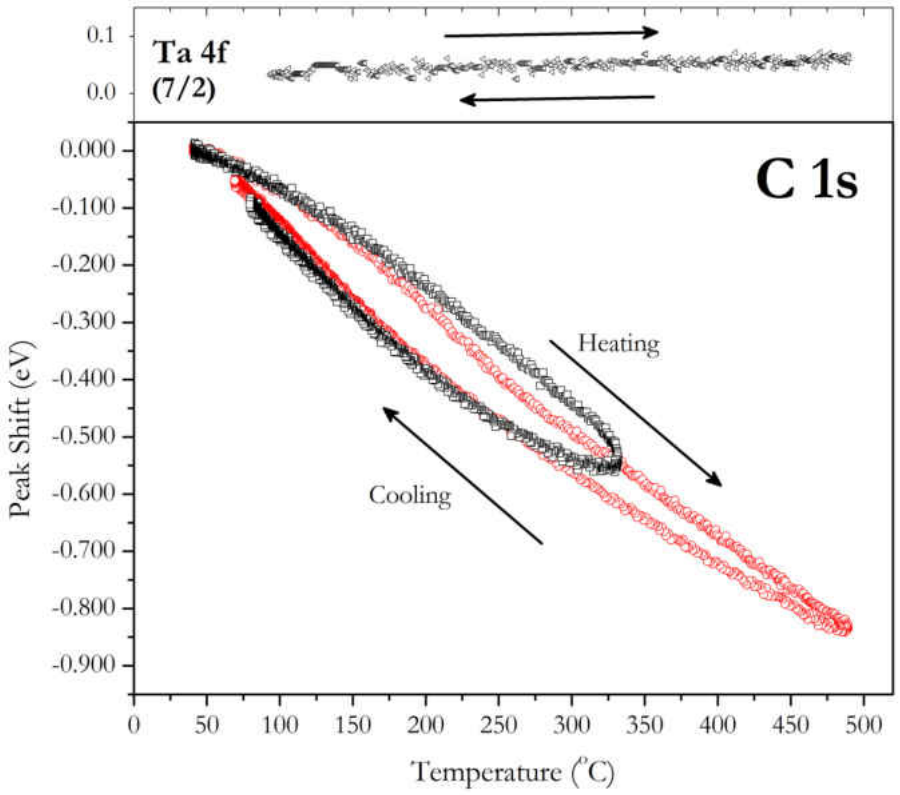

Figure 4.11 – *A plot of the shift in peak position (kinetic energy) vs. temperature for the diamond C 1s core level (main panel) and the sample holder (Ta 4f 7/2) core level (top panel).*

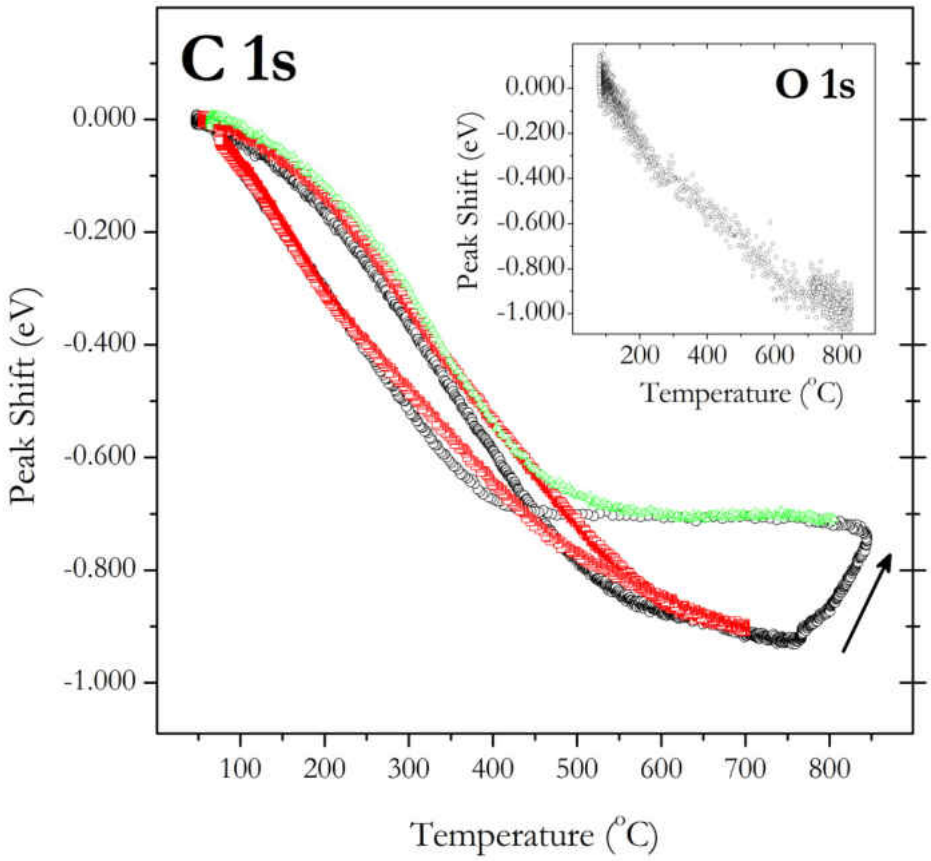

Figure 4.12 – *Peak shift vs. temperature for the (001) diamond C 1s core level (main panel). Three anneal cycles were performed in the following order: red squares (700 ˚C), black circles (845 ˚C) , green triangles (800 ˚C) and O 1s (inset).*

When the annealing temperature is increased further in figure 4.12 the shift in peak position reaches a maximum of 0.93 eV at around 700 ˚C and retains its reversibility (red squares). But when the subsequent anneal is performed and exceeds this temperature (figure 4.12 - black circles) the peak shift reverses and gradually moves back to higher kinetic energies while the temperature continues to increase. Once cooling commences the peak position becomes temperature independent over a range of ~ 300 ˚C before reverting to the reversible path at around 400 ˚C. The peak returns to the original position at room temperature. A further cycle (green triangles) shows a different behaviour in that the maximum peak shift is fixed at the final position of the

preceding cycle. This phenomenon shows that the shift is dependent on the history of the surface, indicating that the higher temperature behaviour is modified by the annealing process, while the lower temperature behaviour is not. Figure 4.12 (inset) shows the peak position of the O 1s core level during an anneal cycle to 800 °C. It is observed that the O 1s shifts by the same magnitude as the C 1s which is expected since the oxygen present is bonded to the surface of the diamond. Figure 4.13 presents data taken using the same sample but after re-oxidation of the surface. The peak shift reverts to its reversible behaviour and initial magnitude shift values of ~ 1 eV following re-oxidation suggesting that oxygen is a key component in the explanation of this phenomenon. Again a reversal of the peak shift is observed at a higher temperature of around 900 °C and there is replication of the temperature independent region which is observed between 1000 and 400 °C. This temperature independent region now defines the maximum peak shift of 0.5 eV at temperatures up to 1000 °C for the following anneal cycle (green triangles). The discrepancy in the maximum temperature for the reversible shift may be attributed to different thermal contacts between the diamond and the sample holder for the two experimental runs. However, it is also possible that the re-oxidised surface is not equivalent to the original surface due to the residual effect of the previous annealing cycles.

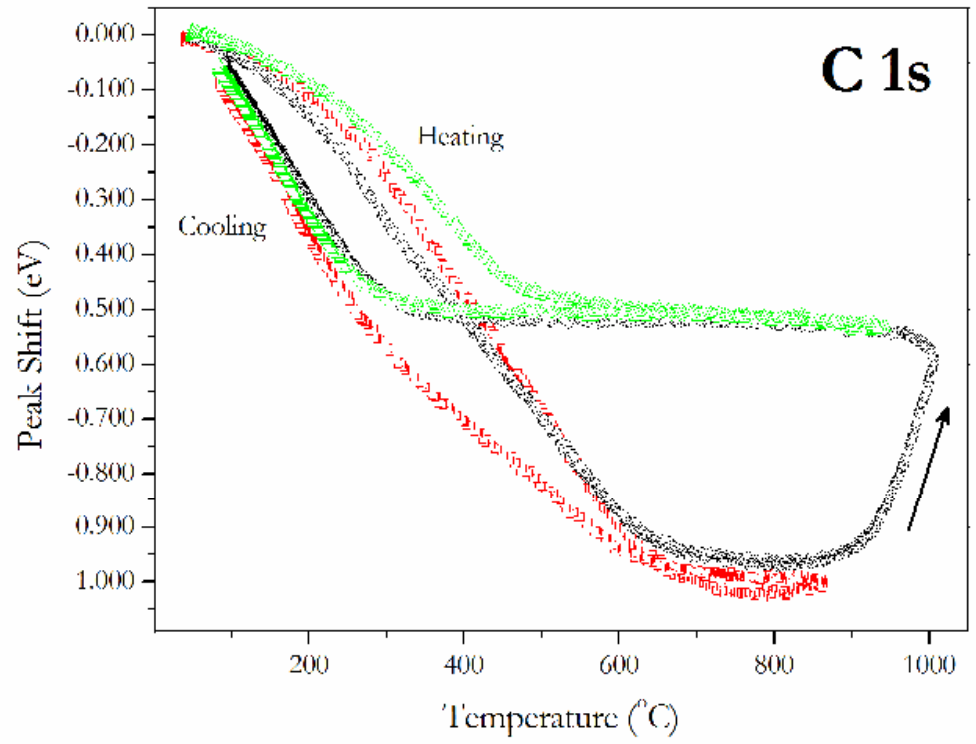

Figure 4.13 - *Peak shift vs. temperature for the (001) diamond C 1s core level after re-oxidization of the surface by acid etch. Three anneal cycles were performed in the following order: red squares (865 ˚C), black circles (1005 ˚C), green triangles (950 ˚C).*

The correlation between the amount of adsorbed oxygen and the extent of peak shift was investigated by plotting the percentage of oxygen present following each anneal cycle with the maximum peak shift (or temperature independent region) as presented in figure 4.14. This shows a strong correlation between the presence of oxygen and the maximum shift value which implies that the reversal in peak position observed in figures 4.12 and 4.13 is the start of a gradual desorption of oxygen from the surface. Further desorption is believed to take place since the reversal in position continues from the previous maximum if the temperature exceeds that for the preceding annealing cycle.

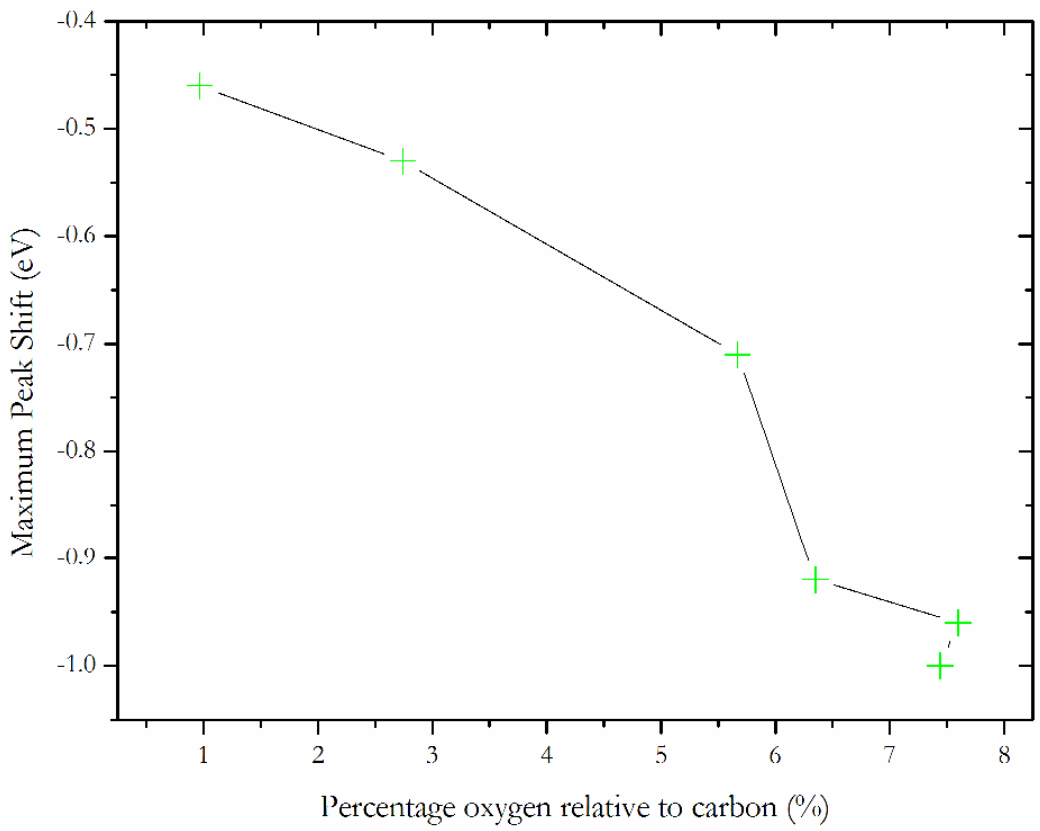

Figure 4.14 – *Maximum peak shift plotted against relative oxygen content peak for the clean (001):O diamond surface*

4.3.5 Discussion

Temperature dependent changes in the C 1s core level position accompanied by a corresponding and equal shift in the O 1s peak position (figure 4.12 - inset) suggests that this band-bending is modified by changes in surface state occupancy at high temperature. The reversibility and unchanging core level lineshape suggests that this is a temperature dependent Fermi level shift of the diamond surface and not a chemical change. Anneal cycles which yield a reversible peak position shift points to the modification of the surface state density and/or their occupancy which determines the surface Fermi level position relative to the band edge (see figure 4.15). As the surface cools back to room temperature the surface regains its original configuration bringing

the Fermi level back to its original position. At higher temperatures the surface state change becomes fixed (or intermediate) as oxygen is desorbed from the surface creating an oxygen-stabilised surface configuration with resultant surface states which pin the Fermi level at an intermediate position in the gap. The relative percentage of oxygen to carbon (figure 4.14) which correlates with the maximum peak shift represents the incremental change in the creation of intermediate surface states. A LEED pattern for the diamond surface was measured at 650 °C (figure 4.15) which suggests that the surface retains the 1 x 1 configuration (observed at 20 °C) at high temperature and is evidence that the changes in peak position is not related to reconstruction of the surface.

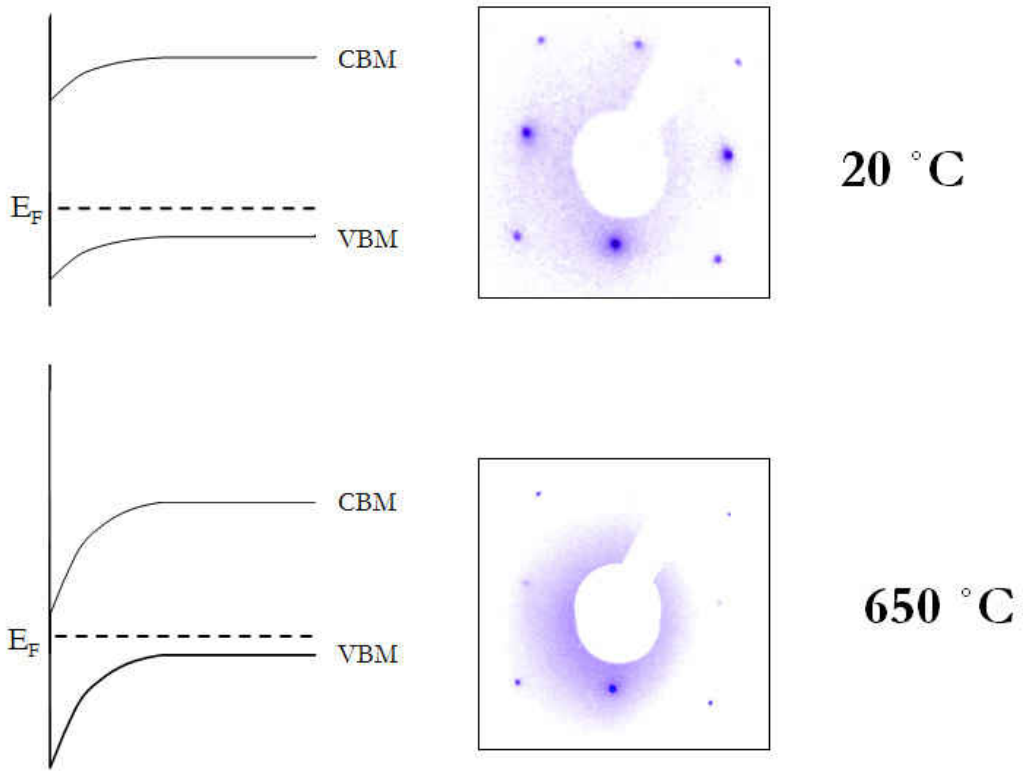

Figure 4.15 – *Proposed band diagram and recorded LEED pattern (beam energy = 127 eV) for the oxygen-terminated (001) diamond surface at room temperature (top) and at 650 °C (bottom).*

4.4 Chapter Summary

This chapter has presented background information relating to the use of synthetic diamond as an electronic material and current understanding of surface terminations and reconstructions for the (001) surface. Temperature-dependent studies of the oxygen-terminated (001) diamond surface have revealed a temperature-dependent Fermi level shift caused by intermediate states in the band gap which correlate with oxygen coverage suggesting that adsorbed oxygen has the potential to control the pinning position of the diamond surface at high temperature. In the next chapter real-time PES is used to study the growth of metal layers on this diamond surface since metal-diamond contacts are key in the development of electronic diamond devices.

References

1. May, P.W., *Diamond thin films: a 21st-century material.* Philosophical Transactions of the Royal Society of London Series A - Mathematical Physical and Engineering Sciences, 2000. **358**(1766): p. 473-495.
2. Habashi, F., *History of diamonds.* CIM Bulletin, 2002. **95**(1064): p. 78-84.
3. Bundy, F.P., *The P, T Phase and Reaction Diagram for Elemental Carbon.* Journal of Geophysical Research, 1980. **85**: p. 6930.
4. Robertson, R., J.J. Fox, and A.E. Martin, *Two Types of Diamond.* Philosophical Transactions of the Royal Society of London. Series A, containing Papers of a Mathematical or Physical Character, 1934. **232**: p. 463-535.
5. Robertson, R., J.J. Fox, and A.E. Martin, *Further Work on Two Types of Diamond.* Proceedings of the Royal Society of London. Series A, Mathematical and Physical Sciences, 1936. **157**(892): p. 579-593.
6. Custers, J.F.H., *Unusual phosphorescence of a diamond.* Physica, 1952. **18**(8-9): p. 489-496.
7. Bundy, F.P., et al., *Man-made Diamonds.* Nature, 1955. **176**(4471): p. 51-55.
8. Greiner, N.R., et al., *Diamonds in detonation soot.* Nature, 1988. **333**(6172): p. 440-442.
9. Sun, J., et al., *Ultrafine diamond synthesized by long-pulse-width laser.* Applied Physics Letters, 2006. **89**(18). 183115.
10. Khachatryan, A.K., et al., *Graphite-to-diamond transformation induced by ultrasound cavitation.* Diamond and Related Materials, 2008. **17**(6): p. 931-936.
11. Veuhoff, E., et al., *Metalorganic CVD of GaAs in a molecular beam system.* Journal of Crystal Growth, 1981. **55**(1): p. 30-34.
12. Abernathy, C.R., *Compound semiconductor growth by metallorganic molecular-beam epitaxy (MOMBE).* Materials Science & Engineering R-Reports, 1995. **14**(5): p. 203-253.
13. Kalish, R., *Diamond as a unique high-tech electronic material: difficulties and prospects.* Journal of Physics D-Applied Physics, 2007. **40**(20): p. 6467-6478.
14. May, P.W., *Materials Science: The New Diamond Age?* Science, 2008. **319**(5869): p. 1490-1491.

15. Balmer, R.S., et al., *Chemical vapour deposition synthetic diamond: materials, technology and applications.* Journal of Physics: Condensed Matter, 2009. **21**(36): p. 364221.
16. Hayward, I.P., I.L. Singer, and L.E. Seitzman, *Effect of roughness on the friction of diamond on CVD diamond coatings.* Wear, 1992. **157**(2): p. 215-227.
17. Beck, C.M. and C.J. Brearley, *CVD diamond as infra-red and optical windows.* GEC Review, 1999. **14**(2): p. 115.
18. Graebner, J.E., et al., *Unusually high thermal-conductivity in diamond films.* Applied Physics Letters, 1992. **60**(13): p. 1576-1578.
19. Nebel, C.E., et al., *Diamond for bio-sensor applications.* Journal of Physics D-Applied Physics, 2007. **40**(20): p. 6443-6466.
20. Farrer, R.G., *On the substitutional nitrogen donor in diamond.* Solid State Communications, 1969. **7**(9): p. 685-688.
21. Teukam, Z., et al., *Shallow donors with high n-type electrical conductivity in homoepitaxial deuterated boron-doped diamond layers.* Nature Materials, 2003. **2**(7): p. 482-486.
22. Pinault, M.A., et al., *The n-type doping of diamond: Present status and pending questions.* Physica B-Condensed Matter, 2007. **401**: p. 51-56.
23. Nesladek, M., *Conventional n-type doping in diamond: state of the art and recent progress.* Semiconductor Science and Technology, 2005. **20**(2): p. R19-R27.
24. Chevallier, J., et al. *Different approaches for the n-type doping of diamond.* in *14th International Workshop on the Physics of Semiconductor Devices.* 2007. Mumbai, INDIA: IEEE.
25. Kohn, E. and A. Denisenko, *Concepts for diamond electronics.* Thin Solid Films, 2007. **515**(10): p. 4333-4339.
26. Isberg, J., et al., *High carrier mobility in single-crystal plasma-deposited diamond.* Science, 2002. **297**(5587): p. 1670-1672.
27. Lander, J.J. and J. Morrison, *Low energy electron diffraction study of (3) diamond surface.* Surface Science, 1966. **4**(3): p. 241-&.
28. Ristein, J., *Diamond surfaces: familiar and amazing.* Applied Physics A-Materials Science & Processing, 2006. **82**(3): p. 377-384.
29. Jiang, X., et al., *Epitaxial diamond thin-films on (001) silicon substrates.* Applied Physics Letters, 1993. **62**(26): p. 3438-3440.
30. *The Properties of Natural and Synthetic Diamonds, pp 181-214*, ed. J.E. Field. 1992: Academic Press Ltd.

31. Kern, G., et al., *(2 × 1) reconstruction and hydrogen-induced de-reconstruction of the diamond (100) and (111) surfaces.* Surface Science, 1996. **352-354**: p. 745-749.
32. Ristein, J., *Surface science of diamond: Familiar and amazing.* Surface Science, 2006. **600**(18): p. 3677.
33. Van der Weide, J., et al., *Negative-Electron-Affinity Effects on the Diamond (100) Surface.* Physical Review B, 1994. **50**(8): p. 5803-5806.
34. Wang, Y.M., et al., *Recent studies on diamond surfaces.* Diamond and Related Materials, 2000. **9**(9-10): p. 1582-1590.
35. Tamura, H., et al., *Periodic density-functional study on oxidation of diamond (100) surfaces.* Physical Review B, 2000. **61**(16): p. 11025-11033.
36. Zheng, X.M. and P.V. Smith, *The stable configurations for oxygen-chemisorption on the diamond (100) and (111) surfaces.* Surface Science, 1992. **262**(1-2): p. 219-234.
37. Long, R., Y. Dai, and M. Guo, *Characterization of diamond (100) surface with oxygen termination.* Applied Surface Science, 2008. **254**(9): p. 2851-2855.
38. Zheng, J.C., et al., *Oxygen-induced surface state on diamond (100).* Diamond and Related Materials, 2001. **10**(3-7): p. 500-505.
39. Pandey, K.C., *New Dimerized-Chain Model For The Reconstruction Of The Diamond (111)-(2x1) Surface.* Physical Review B, 1982. **25**(6): p. 4338-4341.
40. Bushell, A., *A New Multi-channel Detector for Electron Spectroscopy and its Application to Single Crystal Diamond.* 2005, PhD Thesis, University of Wales, Aberystwyth.
41. Himpsel, F.J., et al., *Quantum Photoyield Of Diamond(111) - Stable Negative-Affinity Emitter.* Physical Review B, 1979. **20**(2): p. 624-627.
42. Krainsky, I.L., et al., *Negative-electron-affinity effect on the surface of chemical-vapor-deposited diamond polycrystalline films.* Physical Review B, 1996. **53**(12): p. R7650-R7653.

Chapter 5
Metal-diamond Interfaces

In the preceding chapter the oxygen-terminated (001) surface of diamond was characterised and the effects of high temperature annealing observed. It was also explained that understanding of such surfaces has great relevance due to diamond's potential for use as a component in high power and microwave switching diodes. The realisation of this potential depends to a large extent on the ability to produce reliable Schottky and Ohmic contacts which utilise a low boron doped semiconducting diamond layer as the active part. Consequently, studies of p-type metal-diamond interfaces are of great interest [1-3]. This chapter presents real-time XPS and SXPS data relating specifically to aluminium-diamond and iron-diamond interfaces. The formation of these interfaces by *in vacuo* metal deposition and the evolution of these interfaces during high temperature annealing is investigated.

5.1 Metal-semiconductor Contacts

A brief introduction will first be given to metal-semiconductor junctions. The band structure of a metal/p-diamond junction is illustrated in figure 5.1. The Schottky barrier height (SBH) for a near-ideal metal-semiconductor contact can be obtained and confirmed by current-voltage (I-V) measurements on the contact (as outlined in chapter 2). These measurements are taken close to the conditions under which a real devices operates. However, accurate measurement of the SBH using I-V requires that all components within the electron conduction path (apart from the interface in question) must be modelled accurately. The SBH can also be determined using PES measurements.

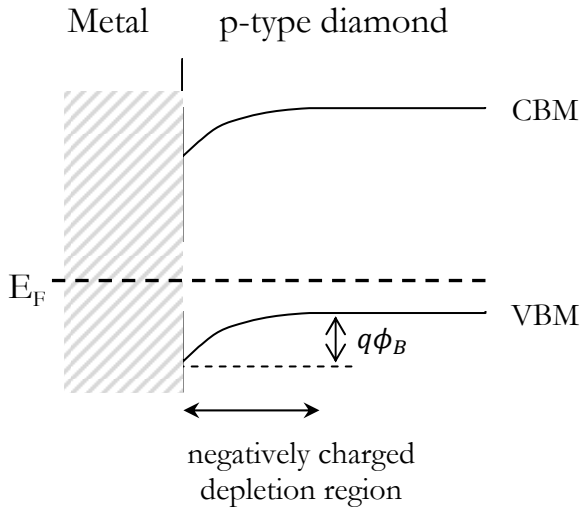

Figure 5.1 - *A metal/p-diamond contact band diagram where $q\phi_B$ is the energy barrier (or Schottky Barrier Height) encountered at the interface.*

5.2 Metal-Diamond Contacts

A variety of factors including surface termination, morphology, temperature and interface chemistry appear to be key in determining the characteristics of metal-diamond contacts. The heterointerface is ultimately one of the limiting factors in the

performance of semiconducting diamond devices. One of the most important parameters for metal-diamond contacts (both rectifying and Ohmic) is the Schottky barrier height (SBH) which is strongly dependent on the energetics (energy band alignment) and distribution of interface states at the metal-diamond junction [4]. The SBH of a conventional idealised metal-semiconductor junction (where no interface states are present) is determined by the comparative values of the metal work function and the electron affinity of the semiconductor. Uncompensated charge present in the depletion region of the semiconductor and the near-surface region of the metal sustains the energy imbalance. This is known as the Schottky-Mott model where $q\phi_B$ for a p-type semiconductor is given by:

$$q\phi_B = E_{gap} - (\phi_M - \chi_s) \qquad (Equation\ 5.1)$$

Where E_{gap} is the band gap of the semiconductor, q the electronic charge, ϕ_M the work function of the metal and χ_s is the electron affinity of the semiconductor. However, if the density of interface states is large the value of the SBH is independent of the work function and the Fermi level is said to be 'pinned' by the high density of interface states. Bardeen [5] developed a model which took account of this effect. Since there is a variation in the density of interface states for different materials a value called the S-parameter is used to represent a linear variation between the two models. Therefore $q\phi_B$ is often expressed as:

$$q\phi_B = S\left[E_{gap} - (\phi_M - \chi_s)\right] + C \qquad (Equation\ 5.2)$$

Where C is a constant and therefore $S = 1$ corresponds to the Schottky-Mott model where the barrier depends on the metal work function, while $S = 0$ gives the Bardeen model where there a high density of interface states is present.

In 1978 Ihm *et al* suggested that the value of the S-parameter for diamond is low [6]. As the body of knowledge regarding metal-diamond contacts increased it soon became evident that these predictions could not be universally applied but predictions for certain specific sub-sets of diodes were possible [7, 8]. The lack of predictability is not surprising considering the complexity of metal-diamond chemistry [9] and the inherent differences in electron affinity and density of surface states within the band gap of clean diamond surfaces [10].

Metal-diamond contacts have been reviewed by many workers including Evans [9] and Kawarada [7]. The first metal-diamond Schottky contact was reported in 1987 by Geis *et al* [11] using a W contact. It was soon found that the termination of the diamond was a critical factor in controlling leakage currents. Oxygen-terminated surfaces are found to be highly resistive [12] while p-type surface conductivity was reported in hydrogen terminated surfaces [13]. At room temperature metal-diamond contacts are usually abrupt with little extensive chemical disruption at the interface. At elevated temperatures the contacts differ and can be arranged into broad categories. The first category are inert contacts which include metals such as Cu, Ag and Au. These metals do not readily bond with the diamond surface, however some bonding has been reported on certain surfaces for Cu [14] and it has been claimed that Au can diffuse into the diamond lattice [15].

The second group are carbide forming contacts. These metals, which include Al, Ti, Mo, Ta and V form carbide compounds upon heating producing Ohmic (non-rectifying) contacts [9, 16]. The ability to produce reliable Ohmic contacts on diamond is critical for device applications [17]. Ti is the preferred metal since it forms a carbide

at relatively moderate temperatures [18, 19]. Other methods employed to form Ohmic contacts are the use of different metal combinations [20], ion sputtering [21], increased surface doping [3], and graphitic contacts [22]. The third category is the group of metals which act as catalysts to graphitisation when heated (these include Ni, Co and Fe). Catalytic graphitisation has been observed at temperatures as low as 450 °C [23].

5.3 Aluminium-Diamond Interface

Aluminium has been used to form contacts on single crystal p-type diamond for many years. However there still exists a large amount of variation in the reported Schottky barrier heights. This is surprising considering that it is a contact which is employed in device applications [24]. The reported values for the Schottky barrier height when grown at room temperature under various conditions range from 0.8 to 2.2 eV [25-30]. Heating of these aluminium Schottky contacts has been adopted as a reliable method of forming Ohmic contacts on diamond. The exact temperature at which this transition takes place is important if this contact is to be used reliably for high temperature diamond electronics. Stable rectification has been reported at temperatures up to 430 ^{o}C [31, 32]. However, others report Ohmic behaviour in the same temperature range [33].

5.4 Experimental Results on the Al-Diamond Contact

In this section experimental data relating to the formation and the performance of Al-diamond contacts at high temperature are presented. Data obtained using AFM, conventional XPS and I-V measurements will be presented first followed by real-time XPS data of metal deposition and high temperature annealing.

The substrate sample used was a synthetic boron-doped (001) CVD single crystal diamond (7.5 x 7.5 x 1.5 mm^3 and $N_B = 2 \times 10^{16}$ cm^{-3}) provided by Element Six Ltd. It was polished and acid-cleaned before being loaded into the vacuum system (for further details on the preparation procedure see section 4.3.2). The measurements were performed with the VG CLAM4 electron energy analyser coupled to the 768 channel Aberystwyth array detector (the setup is described in detail in chapter 3). The photon source used was a Mg Kα laboratory source.

Ex situ AFM measurements of the clean diamond surface was performed in contact mode after deposition of circular Al contacts on the sample surface. An image representing a 500 x 500 nm area of the clean diamond surface between the contacts is presented in figure 5.2. These measurements confirmed a smooth surface which had large flat areas where the roughness was measured to be < 0.2 nm over distances extending to 250 nm (see figure 5.2–A) while larger undulations of around 1 nm exist over longer distances (figure 5.2-B).

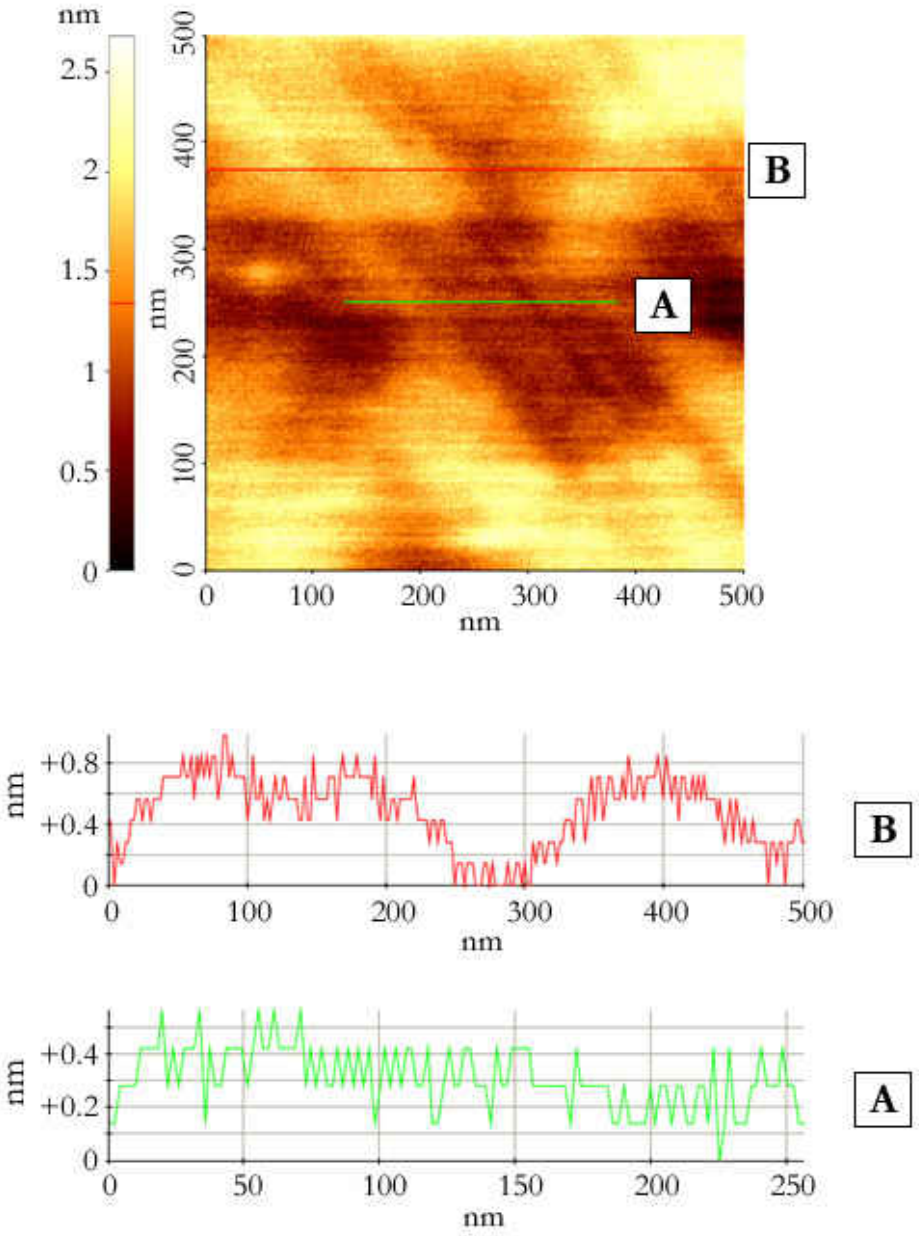

Figure 5.2 – *Ex situ AFM image of the clean p-type (001) CVD diamond taken in contact mode under ambient conditions. A 500 x 500 nm of the diamond surface is shown with two profile lines (A) and (B) extracted from the main image. The lines extending from the top left hand corner to the bottom right hand corner of the image are polishing lines.*

5.4.1 Conventional Photoelectron Spectroscopy (PES)

After loading into the vacuum system a clean diamond underwent a series of heating cycles to 1000 °C while retaining the 1 x 1 periodicity as demonstrated in chapter 4. In this state the C 1s core level peak in figure 5.3 (A) is fitted using a Gaussian/Lorentzian mix function centred at a kinetic energy of 969.2 eV. The full width half maximum of the main component was 0.95 eV, an acceptable value when compared to published diamond studies [9]. Two smaller components at a lower (- 1.5 eV) and higher (+ 1.9 eV) kinetic energy were also fitted and correspond to surface carbon atoms. More specifically, the lower energy component is attributed to C-O bonding since its relative intensity to the bulk diamond peak (at around 7%) correlates well with the amount of oxygen present on the diamond surface. The higher energy component is much less intense (around 1% of the bulk diamond peak) and is attributed to sp^2 bonded carbon on the surface. The absence of any features in figure 5.3-I confirms that there is no Al present on the surface of the clean diamond.

Deposition of Al (total coverage ~ 3 nm) on the clean diamond surface results in the spectra presented in figure 5.3–B and II. It can be noted that the lineshape of the C 1s peak remains constant confirming that no significant sub surface interaction has taken place between the diamond and the Al overlayer with all C-C bonds remaining intact. It should be noted however, that the intensity of the lower energy C-O component has decreased while the higher energy component (attributed to sp^2 bonded carbon) has increased by a similar value. This suggests that much of the oxygen present on the diamond surface forms an oxide with the metallic aluminium. As a consequence the carbon atoms contributing to the C-O components are reduced and exist as sp^2 species resulting in the intensity increase and decrease of the high (sp^2) and low (C-O) kinetic

energy components respectively. The lack of significant sub-surface interaction with the diamond is consistent with previous studies of Al-diamond contacts [33].

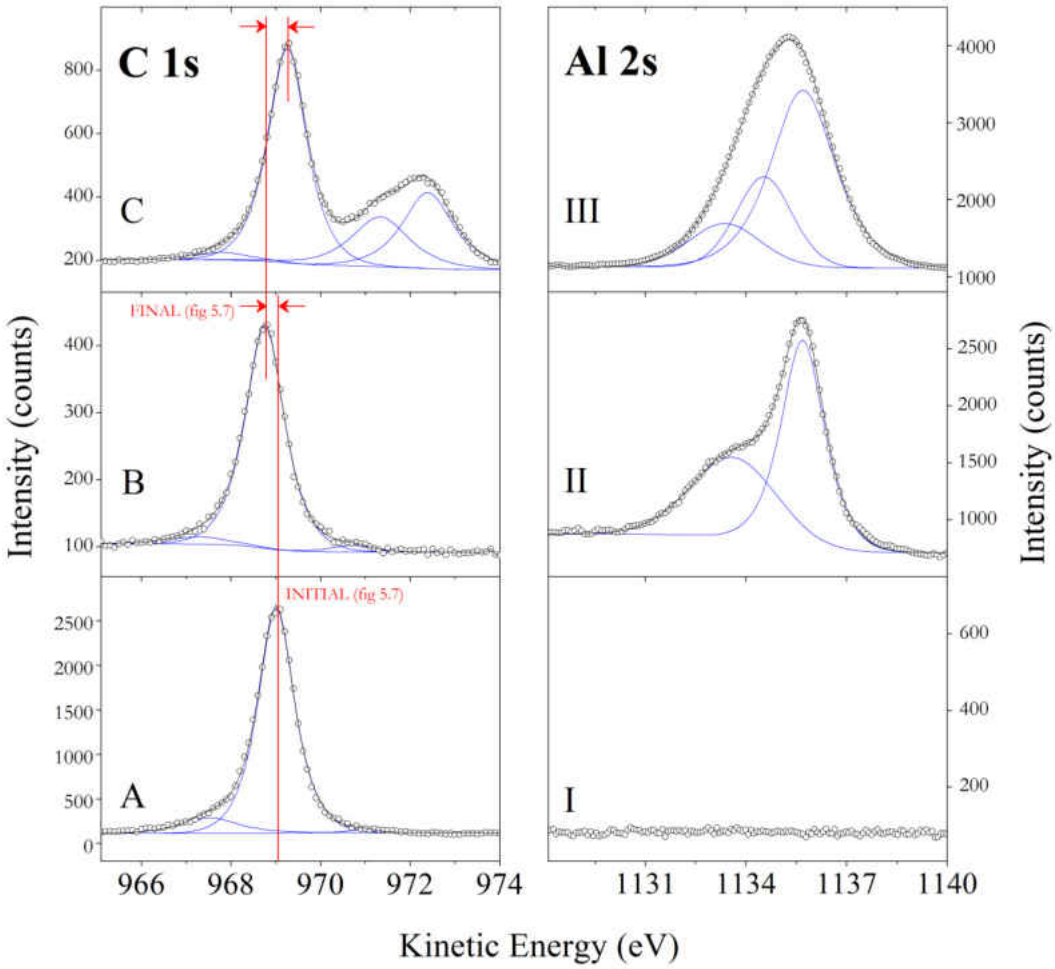

Figure 5.3 – *Fitted core level spectra for C 1s of the (001) diamond substrate (left panel) and the Al 2s of the Al overlayer (right panel): for the clean annealed diamond surface (A and I), the metallized surface (B and II) and for the annealed metallized surface (C and III).*

Changes in the energy of the main diamond C 1s component reflects changes in the Fermi level position relative to the band edge. The positions of the C 1s components have all shifted by around 260 meV to a lower kinetic energy reflecting the metal-induced band bending which gives rise to the barrier formed at the interface. This contact is therefore rectifying at room temperature. The Al 2s core level for the

overlayer consists of two components corresponding to metallic Al at 1135.5 eV and another at 2 eV lower kinetic energy corresponding to multiple Al–O bonding species. The total oxygen intensity detected is larger than that present on the oxidised diamond surface and therefore any additional oxygen must have been present as a residual gas within the experimental chamber. However, it can be stated that the contact is metallic Al since this is the dominant peak in the spectrum.

In order to test the performance of this contact at high temperatures the sample was heated to 860 °C *in situ*. Following this annealing cycle two additional components appear in the C 1s (figure 5.3–C) region at a higher kinetic energy indicating the presence of two new non-diamond bonded carbon species at the surface. The 0.52 eV shift in peak position to higher kinetic energy also shows that the contact is less rectifying since there is a pronounced reduction in the metal-induced band bending at the interface. The Al 2s lineshape changes significantly upon annealing (figure 5.3 – III). Due to the absence of any resolved structure only three components could be confidently fitted. There is considerable broadening in the total width of the peak. The dominant fitted component lies close to the previous metallic Al peak, while there is a small peak near to the original oxide component and a third component of intermediate intensity at an intermediate kinetic energy. These changes in the spectra are in agreement with previous work on polycrystalline diamond-Al contacts [33].

5.4.2 Current-Voltage Measurements (I-V)

The conclusions derived from the conventional photoelectron spectroscopy data were supported by *in situ* and *ex situ* I-V measurements. I-V characteristics for the contact, (prepared *in vacuo* but measured *ex situ*) are presented in the left-hand panel of figure 5.4 on a linear scale. The unheated contact (Curve A) clearly exhibits rectifying behaviour while the annealed contact (Curve B) displays Ohmic characteristics with the forward current yielding a series resistance of around 20 kΩ. Further analysis of the rectifying contact (Curve A) reveals that it can be modelled using thermionic emission theory (introduced in section 2.4.4): the ideality factor of all diodes measured *ex situ* were larger than 2 meaning that no reliable value for the barrier height could be obtained. The process of annealing the metallized region resulted in loss of rectifying properties. This phenomenon has been reported before and aluminium-diamond can be described as a carbide-forming contact [33] since the transition to an Ohmic (or non-rectifying) contact at high temperature is characterised by formation of a metal carbide compound at the interface as has been demonstrated by the PES measurements.

Sequential *in situ* measurements for the UHV-grown contact are presented on a semi-logarithmic scale in the right-hand panel of figure 5.4. Fitting of the I-V characteristics of a freshly grown contact using thermionic emission theory yielded a barrier height of 1.05 eV and an ideality factor of 1.4 (Curve I). The *in situ* barrier height falls within the range of values already published [7, 9]. A barrier height of 1.05 eV for the *in situ* contact does appear not to equate to the smaller 260 meV shift of the C 1s peak during deposition. This discrepancy is explained by the fact that the hydrogen-free surface exhibits an initial downward band bending of the order of ~ 0.9 eV [34]. There is degradation of the contact over time *in vacuo* which can be seen by the steadily

increasing leakage resistances for curves I, II and III (taken at 30 min intervals). It is therefore apparent that this initial stage of contact degradation occurs before exposure to atmospheric pressure. The ideality factor for curves II and III were greater than 2.

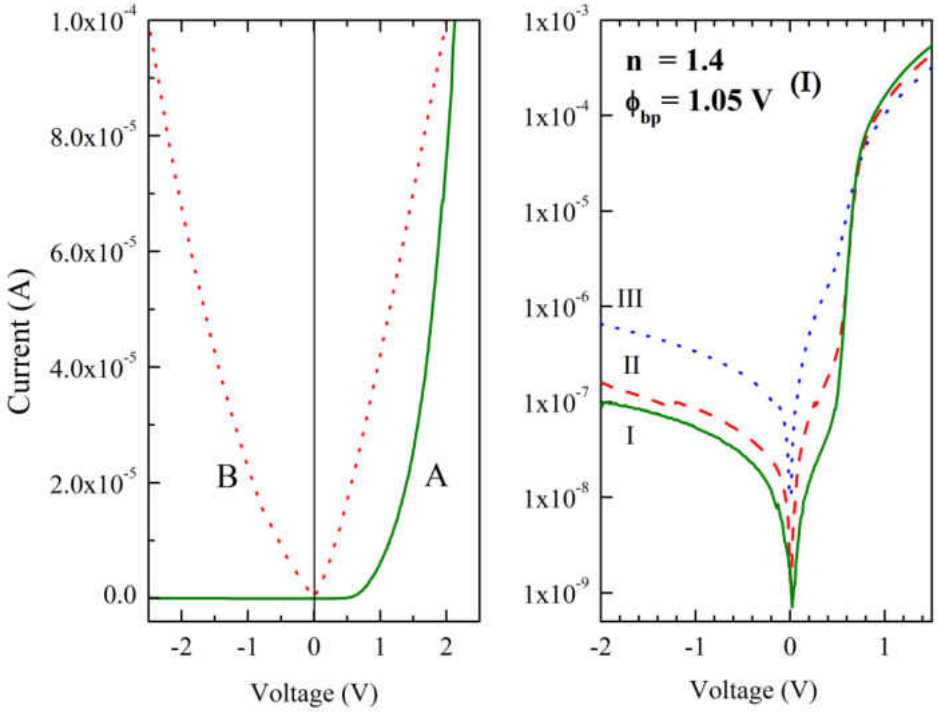

Figure 5.4 – *I-V characteristics for the Al-diamond contact plotted on a linear scale (left panel) and semi-logarithmic scale (right panel). Contacts were grown in vacuo and measured ex situ before annealing (curve A) and after annealing (curve B). Curves I, II, III were grown in vacuo and recorded in vacuo at increasing time intervals following contact formation.*

5.4.3 AFM Measurements of the Al contact

The morphology of the Al contacts were further probed using AFM measurements taken *ex situ* in contact mode and are presented in figure 5.5. The main image shows the edge of a 1 mm diameter Al contact as used for I-V measurements. At 18 nm the height of this contact produced for I-V measurement confirms the thickness estimated during deposition *in vacuo* using a quartz microbalance placed in the Al flux. Region A is a reproduction of figure 5.2 and shows (for comparison) the region of the diamond substrate which was not exposed to the Al flux. The value for its roughness is around

0.2 nm over 300 nm with few polishing lines visible. Some 1 nm undulations are observable over larger distances. The Al is uniform across the contact (as confirmed by the PES measurements) however, the clustered nature of the Al film is clearly resolved in region B. Each cluster has an average height of 1 - 1.5 nm while their average length is around 200 nm each.

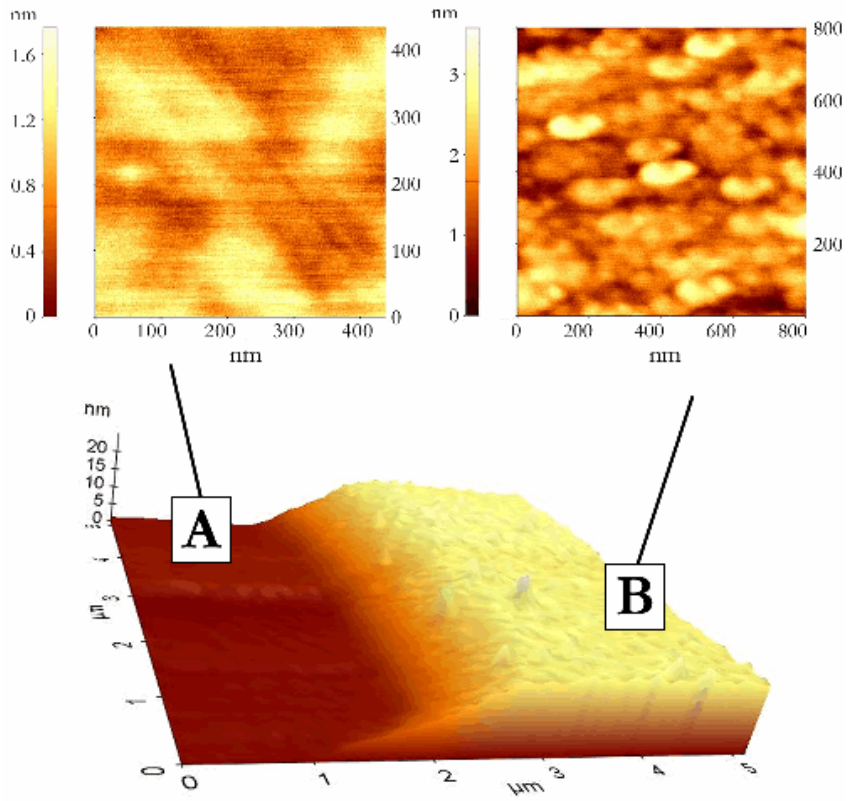

Figure 5.5 – *AFM image (taken in contact mode) of the edge of an Al contact on the (001) diamond surface. Region A (a reproduction of figure 5.2) is a selected section of the clean diamond surface while Region B is on top of the metal contact.*

5.4.4 Real-time Photoelectron Spectroscopy

Further information about the formation and annealing of the rectifying Al-diamond contact was obtained by means of real-time XPS measurements and is presented here.

5.4.4.1 Aluminium Deposition

A Knudsen cell was used to deposit a thin continuous Al overlayer on the diamond surface. The deposition rate was monitored using a quartz microbalance and determined to be ~ 0.3 nm min^{-1}. It was assumed that the deposition rate remained constant during deposition of the Al layer. The C 1s diamond core level was monitored along with the Al 2s core level using real-time XPS. The spectra were recorded using the Aberystwyth array detector fitted to the CLAM4 analyser in snapshot mode every 6.85 s. In this configuration an energy window of around 6.3 eV can be projected across the 768 pixels of the array detector at a pass energy of 100 eV. The data presented in figure 5.6 are the result of averaging the snapshots to produce a series of decimated spectra at 35 s intervals. Figure 5.6 contains a 3-dimensional plot and top contours of the C 1s and Al 2s peaks evolving during growth. Figure 5.6 clearly shows the way that real-time XPS can follow the attenuation of the substrate peak (A) while also monitoring the growth of the overlayer peak (B). The contour plots for the C 1s (C) and Al 2s (D) give an overview of the changes in peak intensity and position as the deposition progresses. These contours clearly show the permanent peak shift in the C 1s core level, while there is no corresponding shift in the Al 2s. The peak position has been used as an indicator of the band edge position with respect to the Fermi level at the surface since real-time XPS directly measures the change in surface band bending as a function of overlayer thickness. Band-bending in the diamond increases steadily following exposure to the Al and the final peak position is reached at around 2 nm coverage. The lack of any detectable peak shift in the Al 2s level confirms that this shift is not due to surface charging. There are numerous published reports of such shifts in PES spectra for metal-diamond rectifying contacts [27, 29, 35-41]. Sequential fitting of these spectra in figure 5.6 with a Gaussian/Lorentzian mix function allows the

peak parameters to be extracted from the data giving an overall picture of the way in which growth proceeds. These parameters for the C 1s core level are presented in figure 5.7.

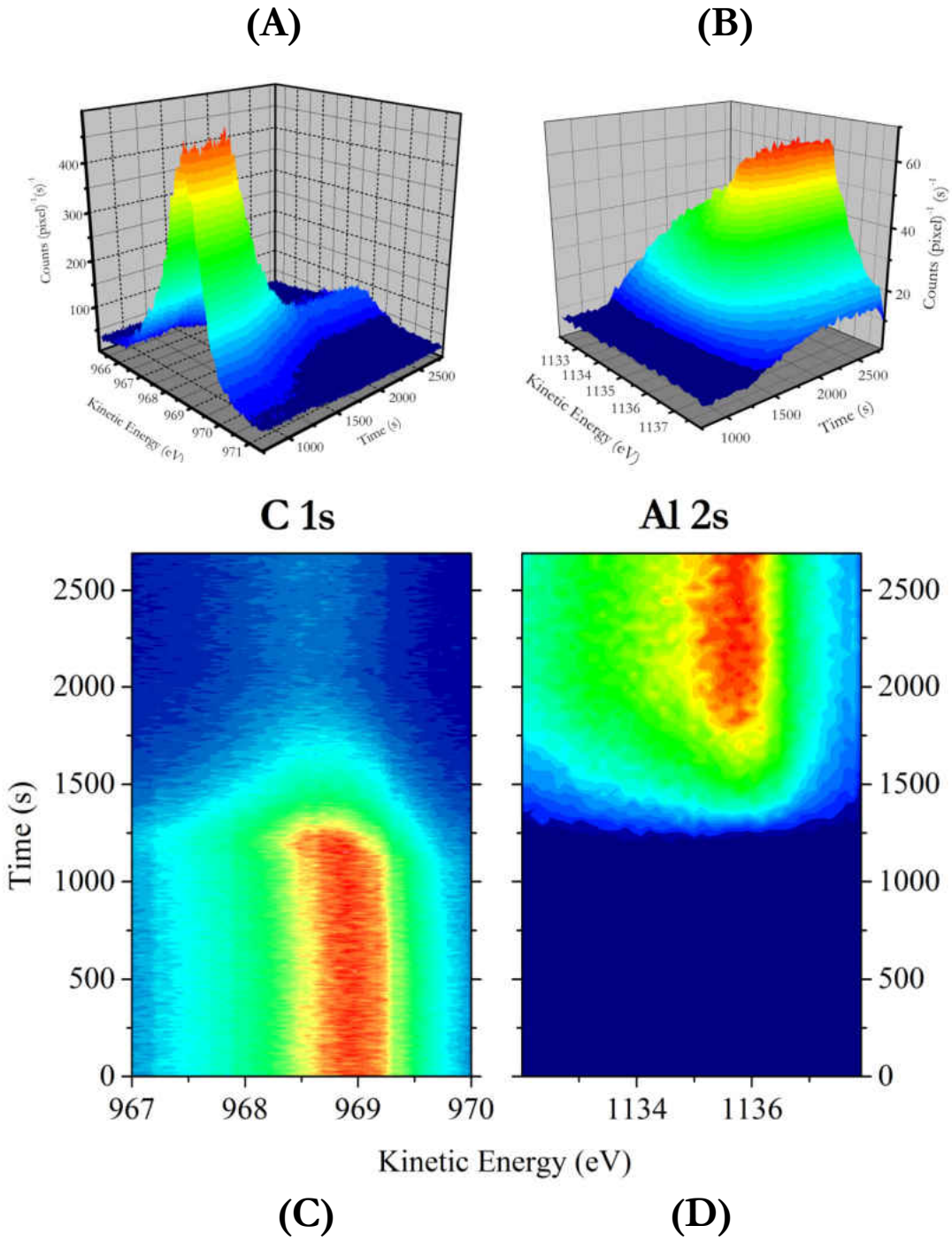

Figure 5.6 – *Real-time XPS data of Al deposition on (001) diamond including: a 3D plot of the diamond C 1s core level (A) and Al 2s core level (B). Also shown are contour plots the core levels during deposition: C 1s (C) and Al 2s (D). Deposition starts at 1100 s.*

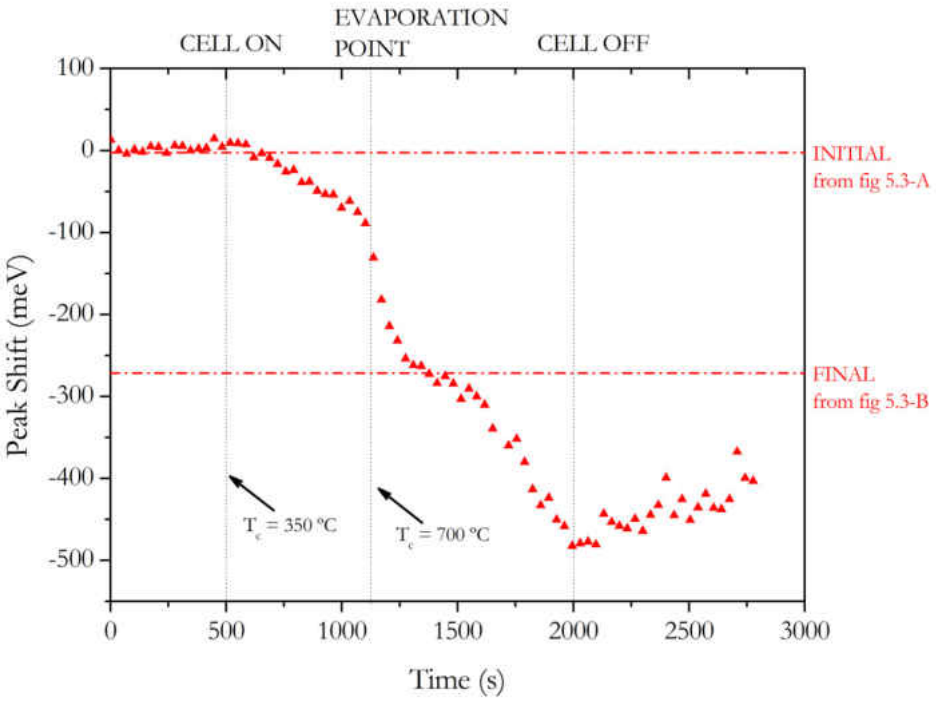

(A)

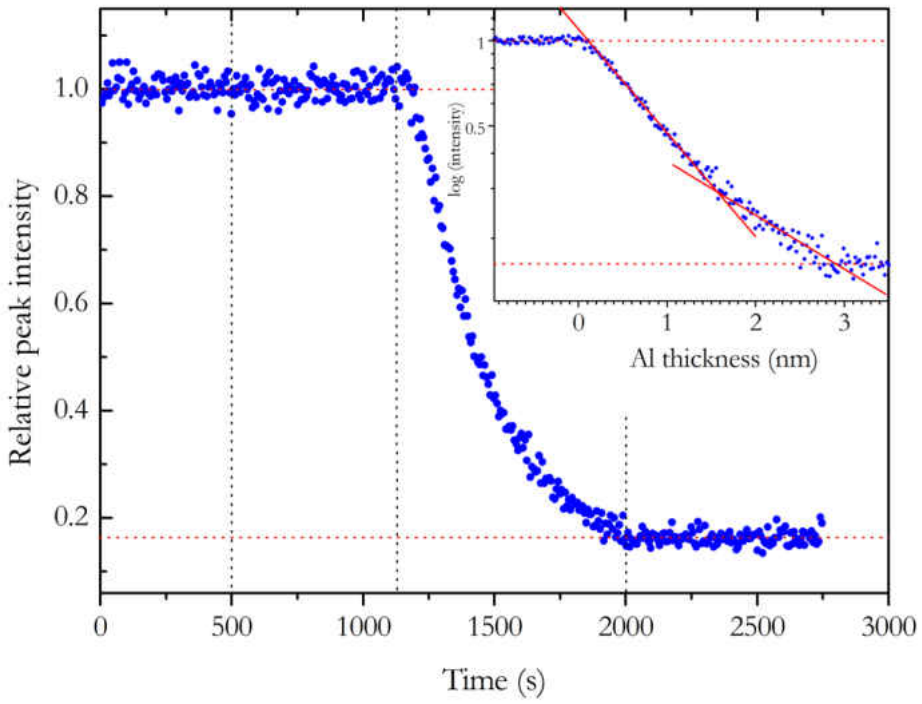

(B)

Figure 5.7 – *The C 1s core level peak parameters extracted from the real-time XPS data of Al growth on the (001) diamond including: a plot of the C1s peak position (A - red filled triangles), and the relative peak intensity (B) on both linear (main panel) and logarithmic scales (inset). The evaporation cell thermocouple temperature is also shown (T_C) for two points in the experiment (A)*

The time (coverage) evolution of two diamond C 1s components (peak position and peak intensity) extracted by fitting of the core level spectra of figure 5.6-A are presented in figure 5.7. The first parameter is the peak position (figure 5.7-A). It is notable that a measurable shift in the C1s peak position is initiated at around 500 s into the experiment before any change is observed in the relative peak intensity. This early shift is attributed to the fact that the Al source was not shuttered from the sample as it was heating up to evaporation temperature. As a consequence the shift between 500 s and 1150 s (the point at which the change in relative peak intensity is first detected in figure 5.7-B) is caused by radiative heat from the source raising the surface temperature. The direction of the shift is consistent with the temperature-dependent reversible shift observed on the clean diamond surface (chapter 4) and could account for this initial 88 meV shift. Between 1000 s and 1250 s the peak position shifts more rapidly by a further 170 meV when the coverage of aluminium completes the formation of the contact within 175 s. At 1340 s the peak position corresponds with the position measured in scanned spectra conducted following the experiment (marked FINAL in figure 5.7-A). When the deposition of aluminium is terminated at 2000 s the peak position has shifted further – a combined total of 330 meV. However after the cell is switched off the peak position immediately starts reversing towards the final position (260 meV) measured after the experiment. Evidence suggests that the formation of the Al contact does not drastically change the energetics on the surface of the diamond since a reversible shift with temperature (reported in the previous chapter) seems to occur under the Al overlayer. Hence what is observed after the end of deposition (2000 s onwards) is the reversal of the temperature-dependent Fermi level shift as the diamond cools. This is reasonable since, as it has already been noted, the conventional

XPS does not show any significant chemical interactions between the clean diamond and the Al overlayer.

The relative peak intensity (figure 5.7–B) of the fitted spectra provides information on the growth mode of the metal film. The first 1000 s of the experiment shows a stable peak intensity until the Al starts to evaporate (vertical dotted line) and ceases at 2000 s (second vertical dotted line) when the cell power is switched off. The initial attenuation of the diamond C 1s peak is linear, indicating uniform (layer by layer) growth of aluminium from which the electron escape depth was determined to be 1.2 nm. Subsequent growth however does not follow this linear trend. A semi-logarithmic plot (figure 5.7-B inset) can be fitted with two linear functions which correspond to layer-by-layer growth followed by a second region of clustered growth (Stranski-Krastanov mode). An approximate value of 1.5 nm was obtained for the critical thickness at which the transition from layered to clustered growth takes place.

5.4.4.2 High Temperature Annealing

Following the growth of a 3 nm Al overlayer the C 1s substrate core level was still detectable underneath the Al layer. During programmed annealing of the contact from 22 °C to 860 °C at a rate of 1.3 °C s^{-1} the C 1s core level was monitored in snapshot mode with an integration time of 10 s. The evolution of the peak is seen in figure 5.8. At time 0 s there is a single component peak but during the experiment it is possible to see the emergence of the carbide component(s) on the high kinetic energy side (reported earlier in this figure 5.3) as well as changes in the bulk diamond peak position and intensity.

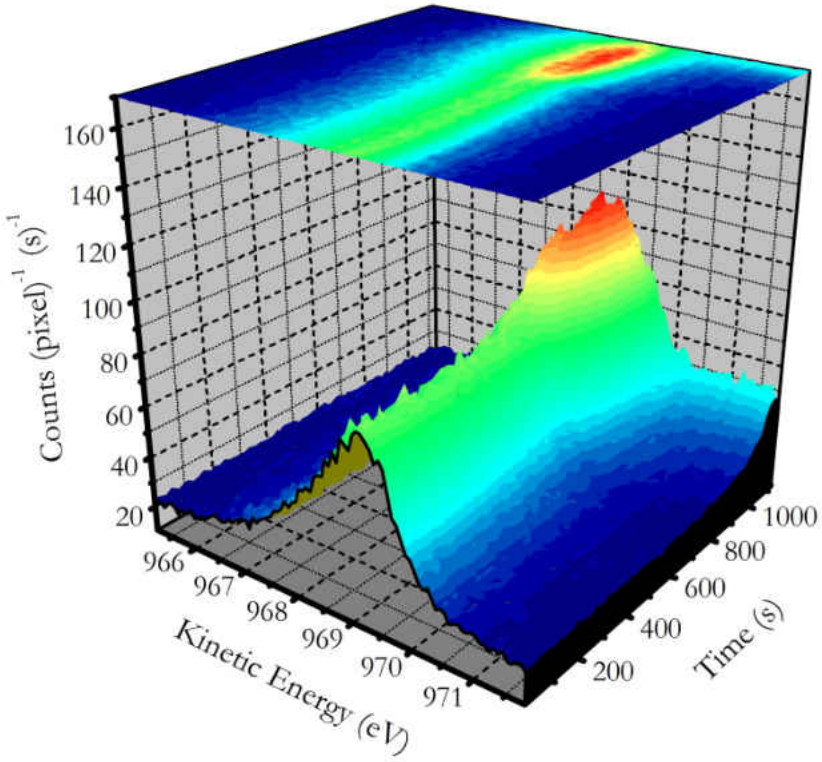

Figure 5.8 – *A series of C 1s core level spectra recorded by real-time XPS during in situ annealing to 860 ˚C of an Al contact on p-type diamond (001).*

Sequential fitting of these spectra allows for a detailed analysis of the stages and processes involved in the transition from a Schottky (rectifying contact) to an Ohmic contact. The result of the peak fitting is presented in figure 5.9. Between 22 ˚C and 482 ˚C the peak position of the main diamond peak (solid red line) shifts gradually to a lower kinetic energy reaching a maximum of 250 meV at 482 ˚C. This shift is believed to be due to the temperature-dependent Fermi level shift that increases the band bending at the diamond surface. This shift corresponds to that observed during growth of the Al film following initial formation of the contact (Figure 5.7-A). Above 482 ˚C there is an abrupt reversal in the peak position towards a higher kinetic energy – this is a movement which accelerates sharply above 800 ˚C. The reversal in peak shift above 482 ˚C corresponds to a decrease in the band bending at the surface and indicates that

the electrical characteristics of the contact are changing with a decrease in the size of the Schottky barrier height. This shift to increasingly higher kinetic energy ultimately renders the contact Ohmic. Therefore, it can be stated that 482 °C was identified as the onset temperature for the transition of this contact from Schottky to Ohmic. Previous studies on such systems [31, 32] have indicated that rectification is observed up to a temperature of 430 °C in the absence of surface pre-sputtering [33]. This observation however is the lowest temperature reported for a high quality diamond substrate and is also lower that that reported for Ti on diamond [19].

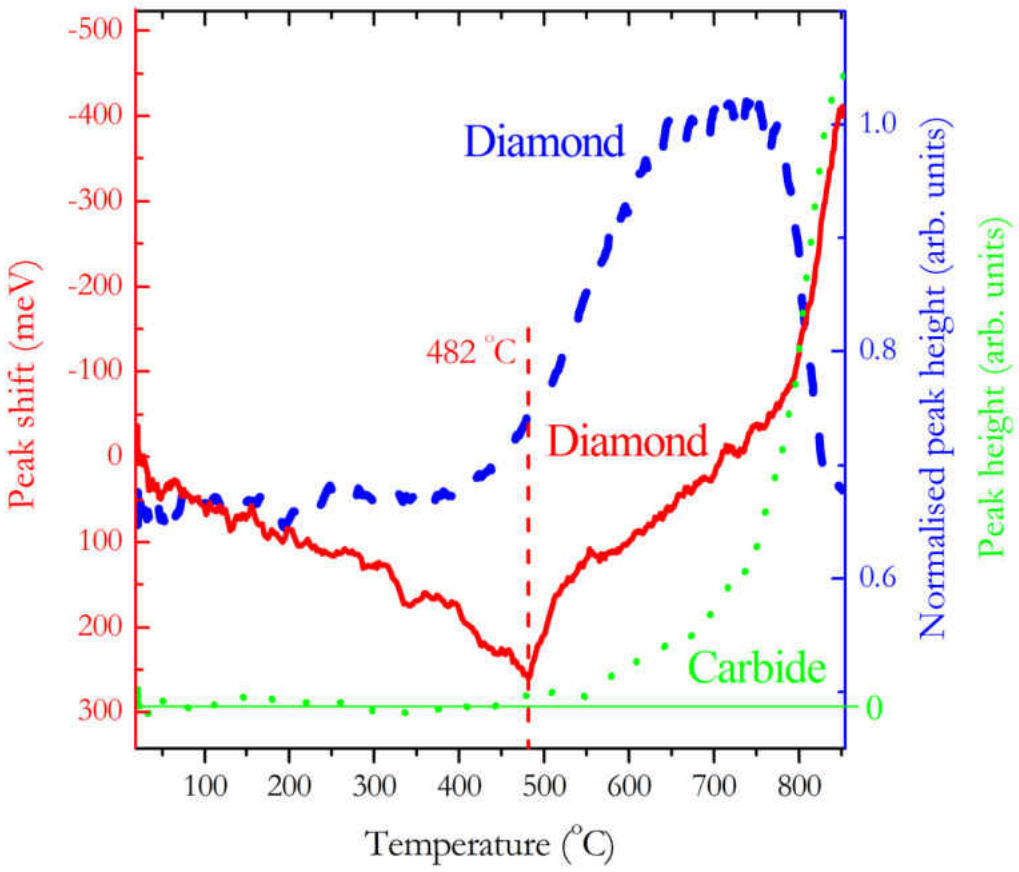

Figure 5.9 – *Changes in the C 1s core level with temperature during annealing of Al diamond contact obtained following sequential fitting of the real-time XPS data. The solid red line represents the position of the main diamond peak while the dashed blue line represents the main diamond peak intensity with the dotted green line showing the intensity of the carbide component.*

The intensities (defined as the peak heights) of the substrate peak (dashed blue line) and C 1s carbide component (dotted green line) are also presented in figure 5.9. No change is observed in the intensity of the substrate peak up to a temperature of 410 °C but there then follows a steady increase of up to 50 % by 610 °C. This increase is due to the increased mobility of the Al atoms at these temperatures, which leads to strong clustering of the Al film resulting in increased exposure of the substrate atoms.

At 770 °C a rapid drop in the C 1s diamond peak intensity commences due to the formation of new chemical phases on top of the substrate, thus reducing the electron emission from the substrate. At the same time, a corresponding rapid increase is seen in the intensity of the new C 1s carbide components (dotted green line). These carbide components which appear on the high kinetic energy side of the diamond C 1s peak initially appear at around 480 °C, the same temperature as the reversal in peak position and continue to gradually increase up until 770 °C where the rapid increase is observed. This would suggest that there is a correlation between the formation of the carbide species and the transition of this contact from rectifying to Ohmic. There are two distinct stages in this transition. The first, which is preceded by the clustering of the Al layer at 410 °C, occurs at 480 °C with the emergence of the carbide component and the abrupt reversal of the peak shift. The second is the rapid change of all three spectral indicators at 770 °C. During the first stage (480 – 770 °C) only the surface atoms of the diamond are reacting to form the carbide. However, above 770 °C the reaction proceeds to include sub-surface diamond atoms. This bulk carbide formation renders the contact completely Ohmic.

5.4.5 Summary of Al-Diamond Studies

The potential use of metal-diamond single crystal contacts for high power/high voltage applications has been highlighted as well as the ability of conventional photoemission measurements to characterise these interfaces. Conventional photoelectron spectroscopy has been used to study the formation of a rectifying Al/p-diamond contact by deposition of Al in UHV. Oxygen from the growth environment is shown to influence the composition and I-V characterisation of the contact. High temperature annealing to 860 °C has been shown irreversibly render the contact Ohmic due to the formation of a carbide layer. I-V measurements confirm this transition from Schottky to Ohmic. It has been demonstrated that real-time photoelectron spectroscopy can give new insights into the formation of the contact as well as providing detailed information about the nature of the transition from rectifying to Ohmic behaviour.

5.5 Iron-Diamond Interface

Although much of current research activity relating to diamond is concerned with its electronic applications, the study of diamond interaction with ferrous materials such as iron has a longstanding motivation. As already reported, the use of natural diamond as drill bits and abrasives dates back to the mid-19th century. With increased availability of low cost synthetic diamond it has become a commonly used material as drill bits for oil wells and platforms. It has long been known that diamond tools are not effective for cutting ferrous materials and it has been discovered that the high temperatures to which the drill bits are exposed causes the diamond to graphitise at a much lower temperature than expected for diamond. This lowering of the graphitisation temperature was attributed to the catalytic effect of iron. This section will focus on the growth and high temperature annealing of iron layers deposited *in vacuo* on single crystal diamond surface in order to gain a new insight into the mechanism of catalytic graphitisation at the surface. PES is ideally suited to tackle this issue since it yields information such as chemical state changes at the surface. First, a brief introduction will be given to the graphitisation of diamond. However, it should also be noted that there is still interest in the electronic properties of Fe-diamond interface since Fe is expected to give a Schottky contact while graphitic contacts have been proposed as alternative Ohmic contacts [42].

5.5.1 Graphitisation of Diamond

Diamond is thermodynamically unstable at normal pressures and it is only at high pressures does diamond become carbon's most stable form [43]. Under atmospheric conditions the most stable form of carbon is graphite. Graphitisation is defined as 'a

solid-state transformation of thermodynamically unstable non-graphitic carbon into graphite by means of heat treatment' [44] and in this study the non-graphitic carbon of interest is diamond. Graphitisation of diamond at normal pressures has been known for a long time. However, obtaining a temperature for the graphitisation of diamond is a significant challenge. In the presence of reactive agents the temperature for the onset of graphitisation can be different to that for 'true' non-catalysed graphitisation.

In 1924 Friedel and Ribaud [44] observed a bright and hard black layer forming on diamond between 1770 - 2070 K. The black layer was dissimilar to the graphite associated with the 'burning' of diamond. They also reported that at 2158 ± 5 K diamond undergoes a change which is accompanied by loss of birefringence and change in volume (i.e. total transformation to graphite).

Phinney in 1954 [45] reported that the graphitisation rate below 1473 K was zero. He observed superficial graphitisation of clear, industrial grade crystals at 2048 K with diamond powders graphitizing 323 - 373 K below that temperature. In 1958 Seal [46] studied the surfaces of octahedral diamonds after heating to 2073 K. He observed raised triangular pyramids of graphite as well as graphite forming under the surface and emerging at the surface.

Howes (1962) [47] used two diamond flats to protect octahedral diamonds from chemical attack while heating to a temperature of 1673 K for 20 hrs and then up to 5 hrs at 1873 K in a vacuum of 6.5×10^{-6} mbar. Under these conditions no graphitisation was observed with an optical microscope. However, complete graphitisation of these small 0.02 g octahedral diamonds was achieved at 1700 K in a time > 12 hrs. At higher

temperatures of 2200 K and 2400 K it took around 10 – 30 min and 10 s – 3 min respectively. Howes showed that the graphite formed within the crystals was linked to defects in the crystal structure, and was true for both surface and internal graphitisation. On the surface he observed propeller like shapes stretching in the three <112> directions, then side branching until the surface was completely roughened with both ordered and unordered graphite. Internally any graphitisation which is initiated in defect sites within the diamond was inhibited by the diamond crystal itself exerting pressure on the graphite. The loss of birefringence observed by Friedel and Ribaud was caused by this internal pressure within the diamond. If the graphite is close enough to the surface it can emerge out of the crystal onto the surface as a raised triangular pyramid as observed by Seal (1958) [46]. Howes also indicated that the graphitisation nuclei form preferentially on <111> cleavage planes and steps as well as other defect sites such as trigons, growth sheets and ring cracks.

In 1964 a TEM study was undertaken by Evans and James [48]. This study used thin diamond <111> fragments protected by two diamond flats in a vacuum of $< 10^{-6}$ mbar. No graphitisation was observed due to oxidation. With one exceptionally thin sample graphitisation was achieved by heating to 1800 K for 45 mins but all other sample required 45 mins at 1900 K. Electron diffraction showed that these samples had been lightly graphitized. The pattern was only observable when the <111> sample surface was perpendicular to the electron beam. This proves that the initial graphite on the surface was lying with its c axes perpendicular to the surface which had not been extensively pitted. As the diamonds were heated to 1950 – 2000 K for 45 mins more extensive graphitisation was observed in the form of graphite crystallites where the c axis of the graphite became a cone which had a semi-angle of around 30° from the

<111> surface. These crystallites were found to be 12 - 12.5 nm in size. As the temperature was increased to 2000 – 2100 K for 45 mins the diamond underneath was found to buckle resulting in the graphite changing with diffraction patterns showing graphite ordered in the <112> and <110> planes. It was found later by Evans and Wild (1965) [49] that at these high temperatures diamond is in fact plastic. Finally the diamond was heated to 2100 - 2200 K for 5 minutes. This resulted in very heavy graphitisation with the c axis of the graphite orientated in a variety of directions but tending to project along the four directions of the <111> diamond plane. It was concluded that grain growth of graphite crystallites occurred after primary graphitisation. The random orientation of the c axis was attributed to the buckling and roughening of the diamond substrate as well as new crystallites pushing their way to the surface and changing the orientation of the earlier crystallites. The work outlined here however does not provide any information regarding the actual process of graphitisation (i.e. the way in which the carbon atoms leave the diamond surface forming graphite) therefore work relating to the process will now be reviewed.

It has been established that 'true' graphitisation is an autocatalytic process initiated at discrete nuclei and then spreading across the surface. However, it depends which surface is observed and in some cases there may be more than one plane involved. Davies and Evans (1972) [50] obtained an activation energy of 730 ± 30 kJ mol^{-1} for a <110> surface by measuring the rate, measured by weight loss per unit area per unit time against absolute temperature. The value for a <111> surface was obtained by roughening two flat <111> diamond pieces by oxidation, heating to 2150 - 2300 K and then cleaning, the rate of graphitisation was being determined by measuring the change in thickness. An Arrhenius plot indicated activation energy of 1060 ± 80 kJ mol^{-1}.

More work was done on this process by measuring the reduction in the rate of graphitisation with increasing pressure. This was done by Bridgman (1947)[51]. Eyring and Cagle (1952) [52] and Rodewald (1960) [53] obtained values of 63 cm^3 mol^{-1} and 120 cm^3 mol^{-1} respectively for activation volume with the latter number based on the most reliable results. Then Bovenkerk *et al* (1959) [54] and Bundy *et al* (1961) [55] obtained values of 160 and 170 cm^3 mol^{-1} which they interpreted as groups of atoms breaking away from the diamond surface. This gave an activation energy of 730 ± 30 kJ mol^{-1} at zero pressure, a value equal to the vaporization energy for diamond. Davies and Evans (1972) also made measurements at a higher pressure but obtained a much lower activation volume of 10.2 ± 2 cm^3 mol^{-1} for the <110> surface. These low volumes suggested that graphitisation is a single atom process. Therefore to conclude, it is assumed that for the <111> and <110> surface the carbon atoms break away one by one since it seems the most energetically favourable.

5.5.2 Metal-catalysed Graphitisation

Interest in metal-catalysed graphitisation stems from the fact that it is a phenomenon which occurs when diamond abrasives are used as tools to cut ferrous materials [56]. Although diamond is the hardest known material it is only metastable at room temperature and therefore susceptible to graphitisation at high temperatures as already discussed. Studies of diamond abrasion during polishing were undertaken by Wilks and Wilks [57] which revealed that the hardness of diamond varies according to crystal faces and direction of polishing. The large activation energy needed to convert diamond to graphite means that very high temperatures in the region of 1300 - 1900 °C are needed to obtain significant graphitisation under ultrahigh vacuum (UHV) conditions without a catalyst. However, experience with cutting tools has shown that graphitisation (and

hence wear of the diamond tipped tool) occurs at a much lower temperature than expected indicating a catalytic effect. This has motivated attempts to develop cutting methods which avoid this problem [58]. Evans and Ney reported the catalytic effect of cobalt on graphitisation in 1990 [59] and iron has also been reported to be used to etch channels in diamond for patterning applications [60]. A recent computational approach to the iron catalysed graphitisation of diamond has been undertaken by Narulkar [61]. In the next section experimental data will be presented relating specifically to the behaviour of the iron-diamond interface at high temperature.

5.6 Experimental Results for the Fe-Diamond Interface

The results presented in this section were obtained using beamline MPW 6.1 at the Synchrotron Radiation Source (SRS) at Daresbury, UK details of which were presented in chapter 3. Iron-diamond interactions were studied using Soft X-ray Photoelectron Spectroscopy (SXPS) and Near Edge X-ray Absorption Fine Structure spectroscopy (NEXAFS). The SXPS was performed using a VG CLAM4 electron energy analyser coupled to the 768 channel Aberystwyth array detector (the setup is described in more detail in chapter 3). The synchrotron radiation source allows SXPS which is much more surface sensitive than a laboratory Mg Kα source. All photoemission data was taken at a beam energy (hυ) of 330 eV.

5.6.1 Conventional Photoelectron Spectroscopy (PES)

After loading into the vacuum chamber cleaning of the diamond was performed by annealing to 850 °C. Subsequent survey scans of the diamond surface confirmed an acceptably clean surface with the C 1s peak (Figure 5.10 – bottom panel) consisting

only of 3 components: the main peak at 45.06 eV (kinetic energy), a second at + 0.69 eV (sp^2 bonded carbon) with the third at – 1.4 eV due to C-O bonding. Following cleaning and characterisation of the surface, a thin 7 Å layer of Fe was deposited on to the surface using a Knudsen cell at a rate of 1.5 Å min^{-1}. The SXPS spectrum for the thin layer (figure 5.10 – middle panel) reveals significant chemical interaction has occurred at the interface at room temperature. Firstly, the kinetic energy of the main bulk diamond peak has shifted – 0.5 eV (lower kinetic energy) suggesting that there is an increase in the metal-induced band bending at the surface (as was observed for the Al overlayer at room temperature – see section 5.4.1). A new component also appears on the high kinetic energy side of the main bulk diamond peak at ~ 46.6 eV. This component which lies + 2.06 eV away from the main peak is attributed to a new carbide species since previous work on clean diamond surfaces has not reported any surface component peaks more than ± 1 eV from the bulk peak [62]. This new carbide species has only one resolved component which lies close to one of the two components fitted for the aluminium carbide already reported in this chapter (at + 2.1 eV kinetic energy relative to diamond C 1s peak). After further deposition on the existing 7 Å layer the C 1s core level was completely attenuated. Subsequent annealing to 850 °C resulted in the re-emergence of a C 1s peak that had a characteristic lineshape of graphite (figure 5.10 – top panel). The graphite peak has a narrow width of ~ 0.8 eV and an asymmetric tail extending to lower kinetic energy side which is characteristic of conducting surfaces [63]. The 850 °C anneal has resulted in a significant Fe-induced graphitisation of this (001) diamond surface.

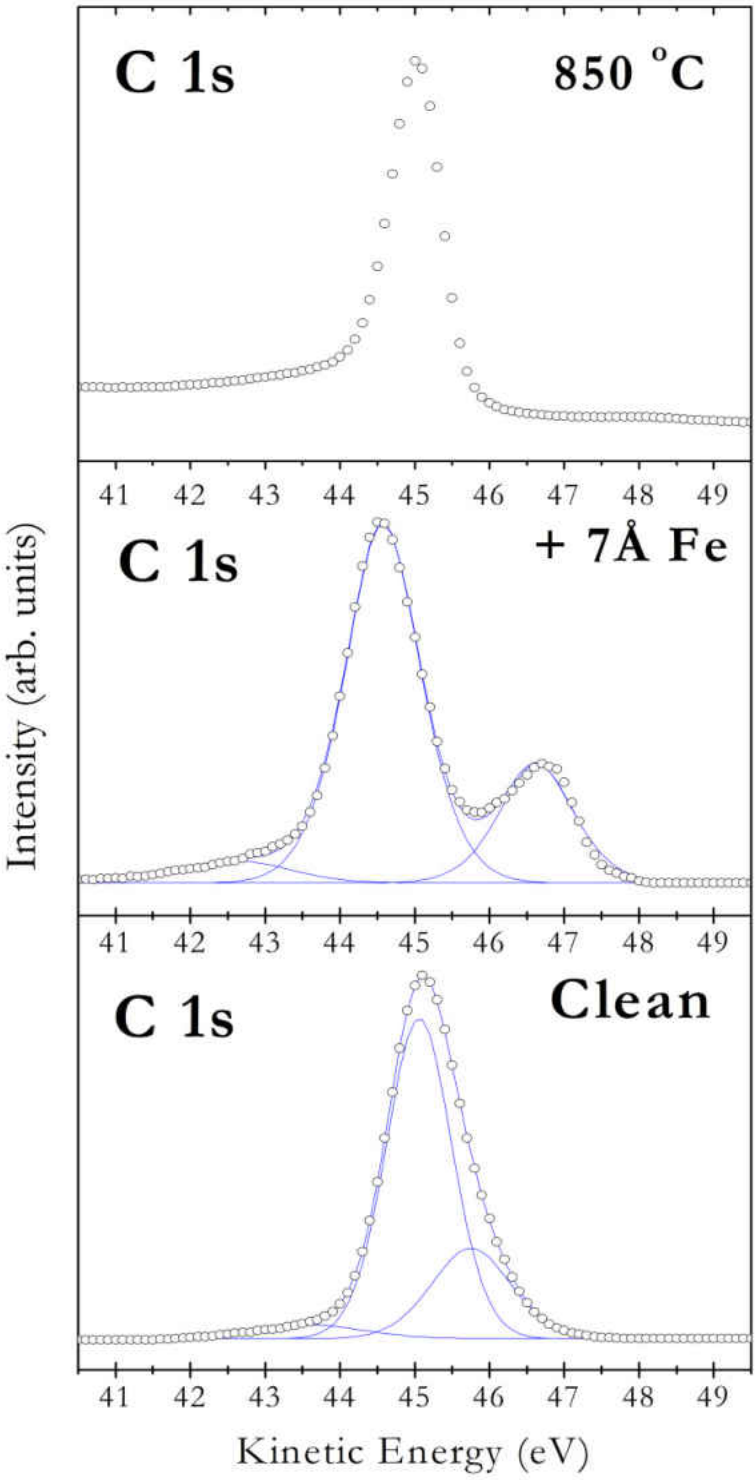

Figure 5.10 – *SXPS spectra of (001) diamond (taken at hυ = 330 eV): for the clean surface (bottom), with 7 Å of Fe (middle) and with thick layer of Fe annealed to 850 ˚C (top)*

5.6.2 Atomic Force Microscopy (AFM)

Following Fe-catalysed graphitisation of the diamond the surface was imaged using *ex situ* AFM (see figure 5.11). The graphite (region A) can be clearly distinguished from the clean diamond surface (region B). This abrupt boundary is the point at which the mounting clips for the diamond sample ended, therefore region B did not receive any Fe coverage and did not graphitise at this temperature retaining its smooth surface. However, this is not the case for the metallized region. Some structure can be observed in region A with the top down image (figure 5.11 – bottom) clearly showing graphitic sheets roughly of dimensions 0.20 x 0.15 nm laying "flat" on the surface. This observation is consistent with the planar structure of graphite.

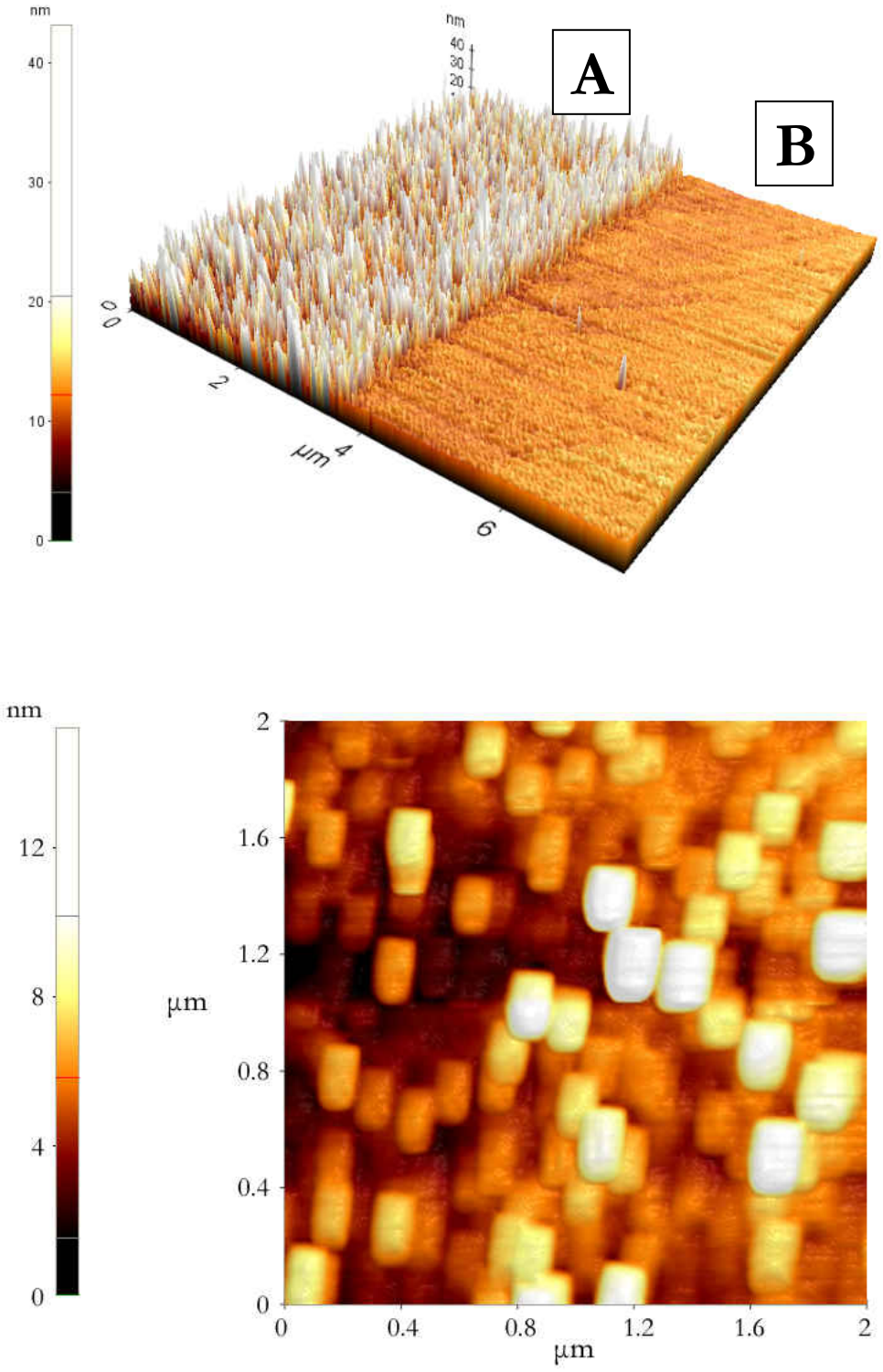

Figure 5.11 – *AFM images taken ex situ following graphitisation of diamond where top image shows the contrast between the graphitised region (A) the clean non-graphitised region (B). The total area of the top image is 7 x 7 µm. The bottom image is a detailed top down view of the graphitised region.*

5.6.3 Near-Edge X-Ray Absorption Fine Structure (NEXAFS)

To complement the photoemission and AFM measurements NEXAFS total electron yield (TEY) spectra are shown in figure 5.12 for the as loaded, cleaned, and annealed metallized surface. The loaded and cleaned spectra were taken with the diamond surface normal to the beam. While the graphitised spectra was taken at an angle of 35° from normal. For the as loaded surface the presence of some states below the carbon K-edge at 284 eV confirms presence of non-diamond sp^2 bonded carbon on the surface. The feature at ~ 301 eV photon energy, characteristic of diamond, is enhanced upon annealing to 850 °C indicating the presence of a cleaner diamond surface. It is also noted that intensity is lost from the region below the K-edge (284 eV) indicating that almost all sp^2 bonded carbon is desorbed from the surface. NEXAFS is an excellent tool for studying the graphitisation of diamond since the π^* states in graphite appear just below the K-edge resulting in a significantly different spectrum (figure 5.12 – bottom panel) to that for clean diamond, including the absence of the feature at 301 eV. The diamond spectra compare favourably with those found in literature [64-66].

The nature of the graphitic layer was further probed by angular resolved NEXAFS (figure 5.13). The π/π^*-electron states lie perpendicular to the plane of the graphite sheet while the σ/σ^*-electron states lie in-plane. Synchrotron light has a high linear polarisation which means that any molecular orientation of the graphitic sheets is detected as an intensity variation for components of the spectra associated with the unoccupied electronic states of graphite. By varying the angle at which the synchrotron light is incident upon the graphite layer the π^* and σ^* electron system resonate at different angles.

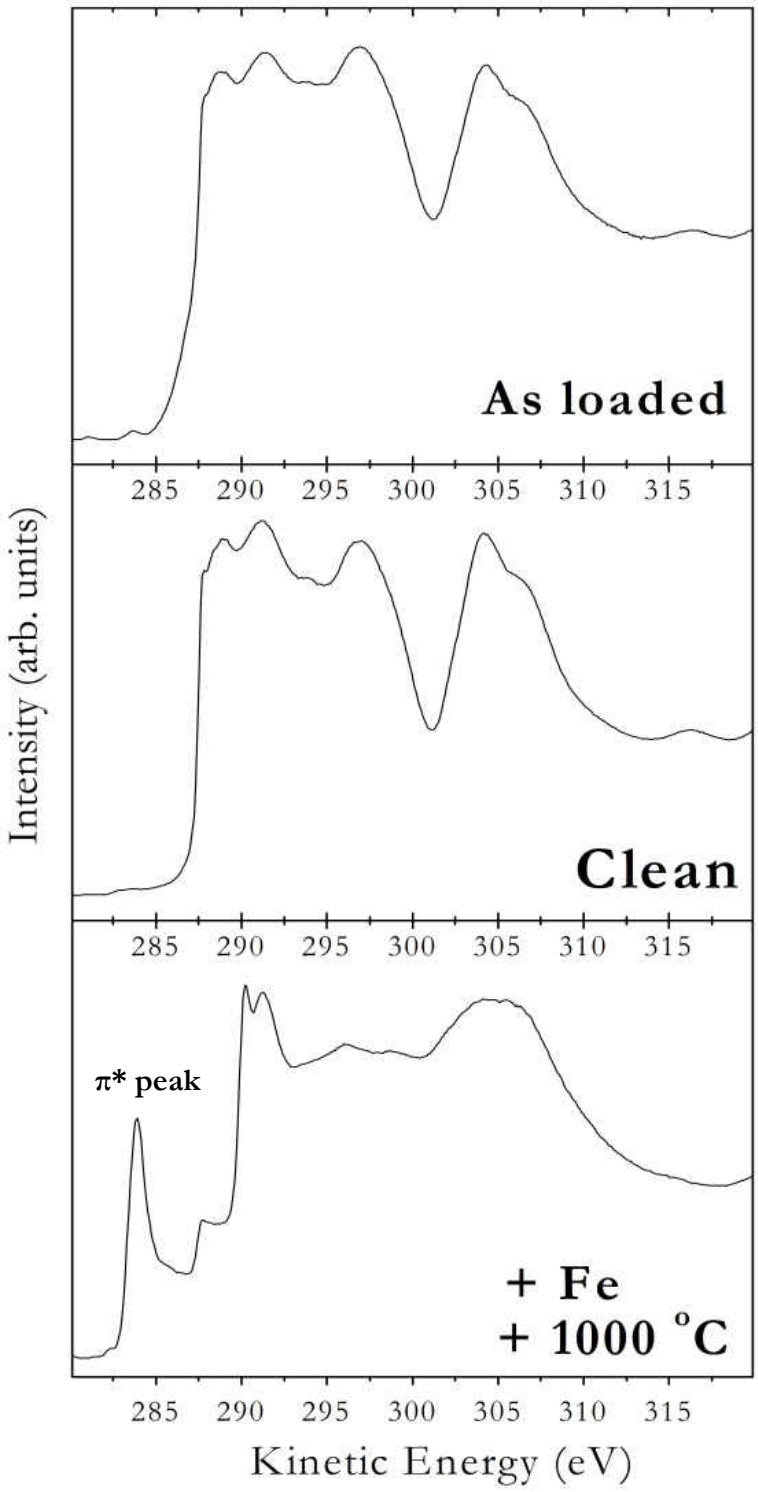

Figure 5.12 – *Total electron yield (TEY) spectra of (001) single crystal diamond as loaded (top), cleaned by annealing to 850 ˚C (middle) and following metallization and annealing to 850 ˚C (bottom). The loaded (top) and cleaned spectra (middle) were taken with the diamond surface normal to the beam. While the graphitised spectra (bottom) was taken at an angle of 35° from normal.*

The contributions of the π* and σ* states to the carbon K-edge spectrum are labelled in figure 5.13 and a clear correlation can be seen between the two systems. The intensity of the pre-edge π* feature at 284.4 eV increases with increasing angle while the σ* components at 296 eV and 304 eV decrease in intensity with increasing angle. This supports the measurements obtained using AFM since it suggests that the graphite sheets are ordered on the surface. The number of angular resolved spectra was not sufficient to be able to accurately model the molecular angle therefore further experiments which allow measurements to higher angles (~ 70°) on both sides would allow the molecular orientation of the graphite relative to the substrate to be established.

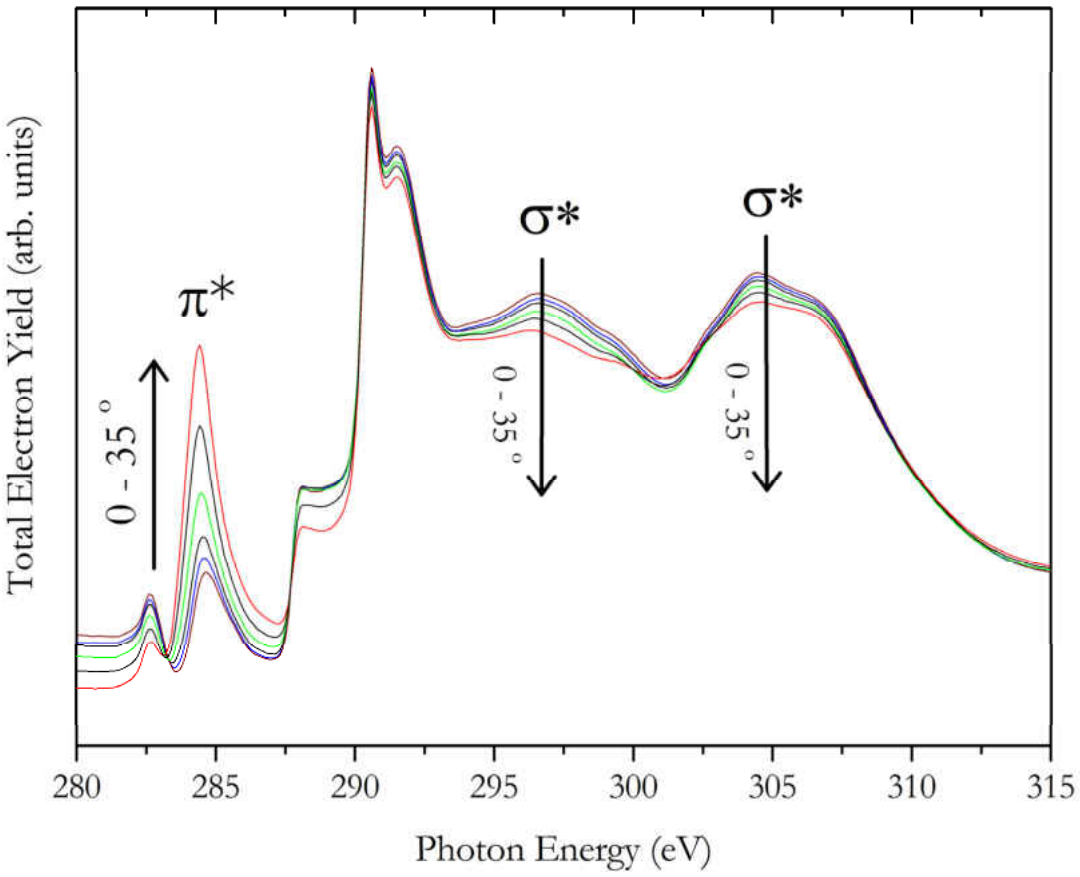

Figure 5.13 – *Angular resolved NEXAFS of the carbon K-edge for the graphitic layer at angles 0 – 35° where at 0° the surface of the (001) diamond was normal to the synchrotron beam.*

5.6.4 Iron Deposition

The deposition of the iron was monitored by fixing the monochromator energy at the top of the carbon K-edge while continuously measuring the intensity of the total electron yield during deposition. The attenuation of the signal is presented in figure 5.14. When plotted on a semi-logarithmic plot the attenuation can be fitted with a straight line. This confirms that the growth mode is layer-by-layer and that no clustering of the Fe layer occurs.

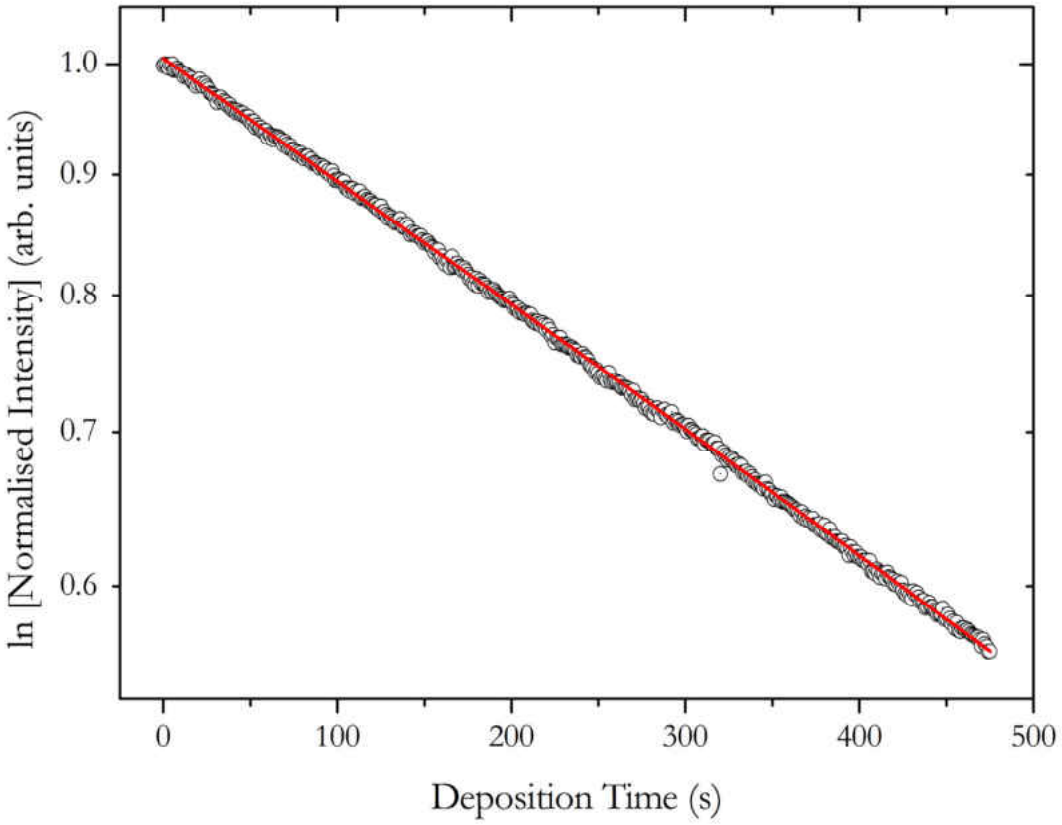

Figure 5.14 – *Attenuation of the carbon K-edge during deposition of a thin Fe layer on (001) diamond.*

5.6.5 Real-time Photoelectron Spectroscopy

Following deposition of a thicker layer of Fe where the diamond C 1s core level was completely attenuated, the Aberystwyth array detector was used to perform a real-time SXPS annealing experiment on the Fe-diamond interface. The C 1s peak was measured

every 1 s during an anneal up to a maximum temperature of 850 °C (see figure 5.15-A). At t = 0 s, the diamond C 1s peak is completely attenuated. The emerging graphite C 1s peak enables the evolving graphitisation process to be monitored. The peak intensities from these data were obtained by sequential fitting of the snapshots and are presented in figure 5.15-B. At 350 °C the first signs of a carbon signal are detected at 46.7 eV which corresponds to the carbide component observed in the C 1s spectra of the thin iron layer (figure 5.10 – middle panel). This peak continues to increase in intensity up to 750 °C before decreasing gradually. At 650 °C a second component at around 45.0 eV consistent with graphite appears and continues to increase, with the biggest rate of increase observed when the carbide peak is at its maximum intensity. The increase in graphite component continues until the temperature peaks at 850 °C at which point the surface is completely graphitic. These data suggest that carbide species play a key role in the catalytic graphitisation of diamond. In order for graphitisation to occur the carbon atoms must detach from the diamond surface, diffuse and migrate through the iron layer to form graphite at the vacuum interface. A schematic representation of this model is presented in figure 5.16. Clifton and Evans discuss the role of intermediate carbide species in the graphitisation of diamond [23, 67]. However, the presence of metal carbide species predicted was not directly detected in their XPS measurements which could be due to their use of a more bulk sensitive laboratory X-ray source. Nickel and cobalt are reported to have carbide phases which form at 350 and 450 °C and decompose at 400 and 490 °C respectively [68, 69]. It is also known that metals which catalyse diamond graphitisation posses carbides which become thermodynamically unstable at higher temperature leading to graphitisation. The carbides of non-catalysing metals such as aluminium (already reported in this chapter) and titanium remain stable at high temperatures, thus inhibiting graphitisation.

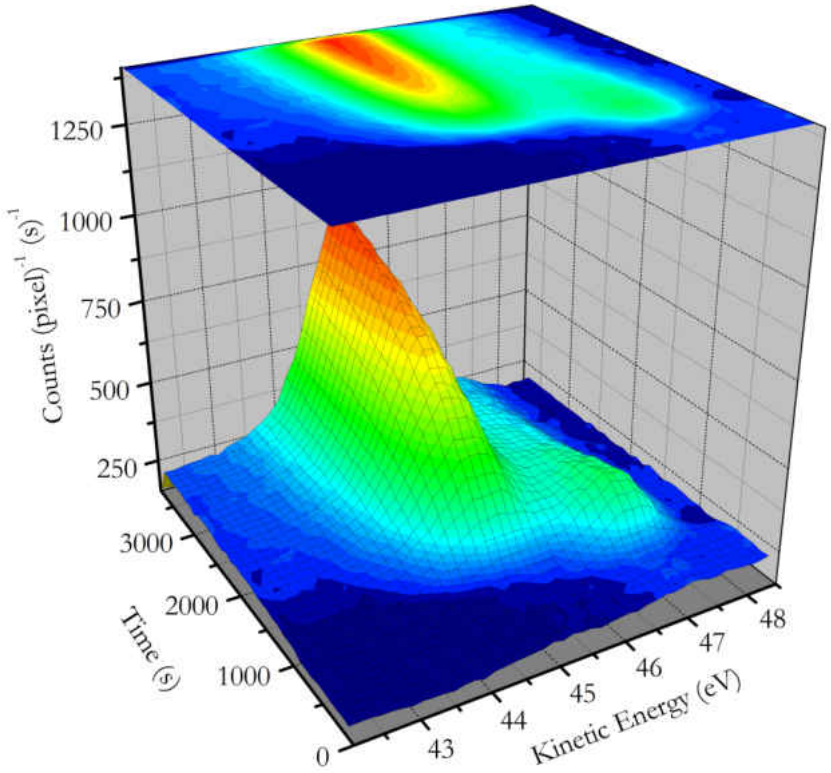

(A)

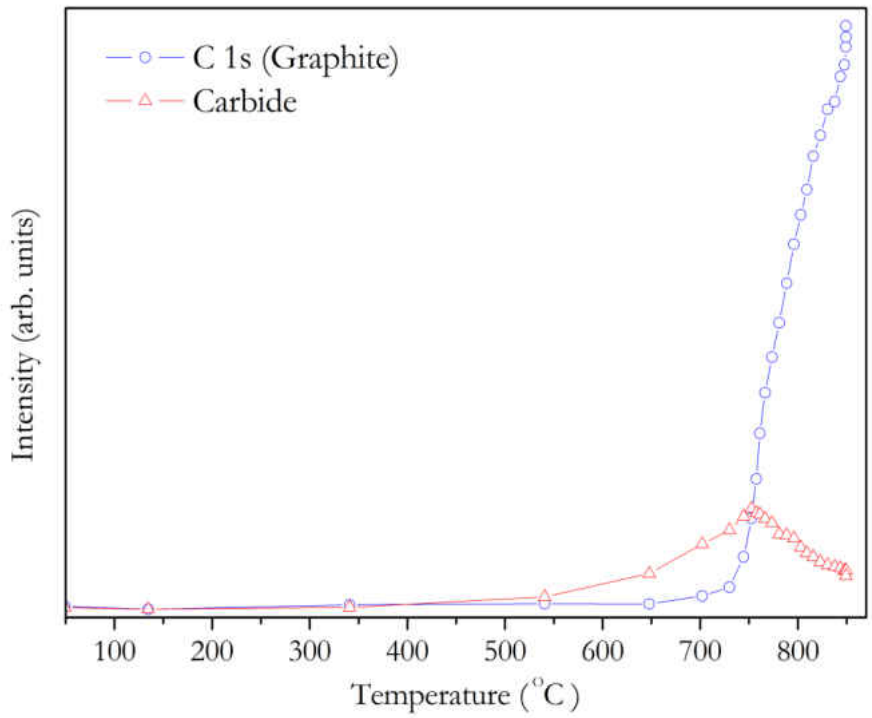

(B)

Figure 5.15 – *Real-time SXPS spectra of the C 1s core level (A) and the extracted peak intensities for the two components (B) during annealing of the Fe-diamond interface to 850 °C.*

5.6.5.1 Proposed Mechanism for Graphitisation

In the light of information acquired from the photoemission data (both conventional and real-time) the following mechanism is proposed (figure 5.17). Initially photoemission of a 7 Å layer of Fe on the clean diamond reveals the formation of a carbide species at the interface. The formation can be described as the diffusion of the carbon atoms from the diamond surface into the Fe layer forming a carbide diffusion layer. After the thick layer of iron is deposited the signal from the C 1s core level is completely attenuated. The carbide layer remains in equilibrium at the iron-diamond interface until the temperature reaches around 500 °C at which point the Fe layer becomes sufficiently flexible to allow the carbon atoms to diffuse further into the Fe layer as interstitial carbon (carbide). The intensity of the carbide continues to rise with temperature due to the steadily increasing number of interstitial carbon atoms diffusing through the layer. The high temperature causes the interstitial carbon (carbide) atoms to become unstable hence upon reaching the surface of the Fe layer they form the graphite layers (as in figure 5.16). Previous work by Clifton and Fyfe shows that different crystal faces have different activation energies for iron-catalysed graphitisation of diamond. Fyfe calculated the activation energy for the (111) surface to be 139 ± 18 kJ mol^{-1} [70] while Clifton determined a value of 340 ± 41 kJ mol^{-1} for the (110) surface [67]. Therefore the rate determining step for this process has to be dependent upon the detachment of the carbon atoms from the diamond surface and subsequent transfer into the Fe overlayer. As the temperature reaches 750 °C the rate of carbon detachment from the diamond surface accelerates resulting in a rapid increase in the thickness of the graphite layer growing above the iron. Consequently, there is a rapid decrease in the intensity of the carbide photoelectron peak intensity at temperatures above 750 °C as the Fe layer descends below the sampling depth of SXPS. As the

temperature increases further to 860 °C the Fe layer proceeds to 'bury' deeper into the diamond leaving an ever thicker layer of graphite detected as a rapid increase in the C 1s graphite core level intensity. Any functional groups present on the diamond surface (i.e. oxygen) before metallisation would also diffuse within the layer but the data reveals no information about their behaviour. This process is inherently complex and there is much scope for further work.

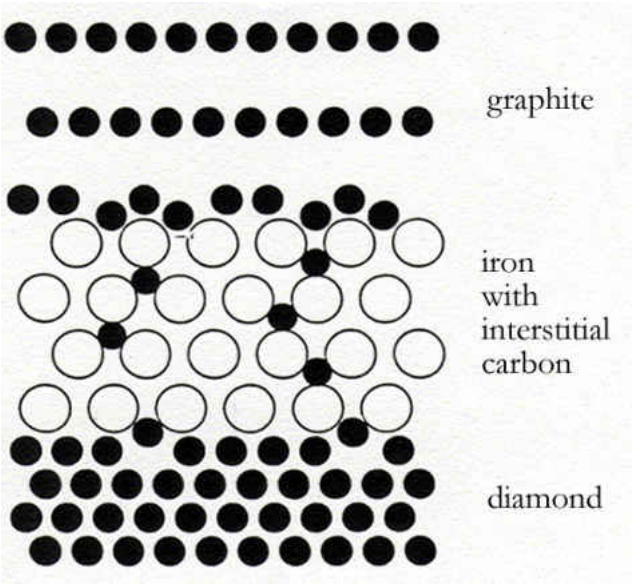

Figure 5.16 – *Taken from Evans and Ney [59]. A schematic representation of the proposed mechanism for the metal-catalysed graphitisation of diamond.*

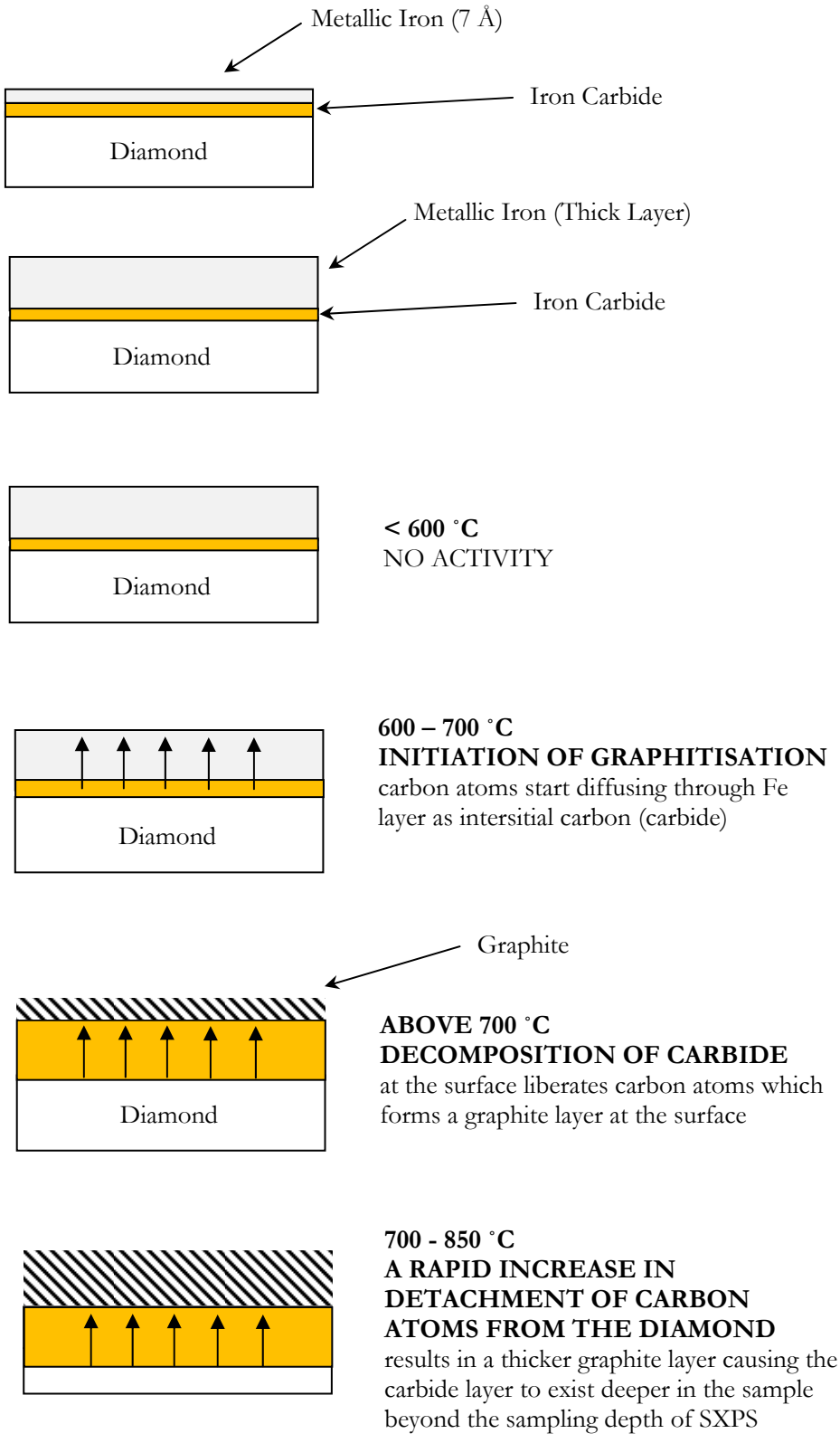

Figure 5.17 – *Proposed mechanism for the Fe-catalysed graphitisation of diamond.*

5.6.6 Summary of Graphitisation Studies

In this section the graphitisation of diamond at high temperature and the catalytic effect of iron on the process of graphitisation at high temperature has been reviewed. Conventional SXPS spectroscopy was used to characterise the surface following *in vacuo* deposition of a thin Fe layer. A carbide component was detected on the surface at room temperature. Following further deposition of Fe and subsequent annealing graphitisation of the surface was observed and the nature of the resulting graphite layer investigated using NEXAFS and AFM measurements revealing an ordered surface. A mechanism for the graphitisation process has been proposed based on data obtained from real-time SXPS measurements.

5.7 Chapter Summary

This chapter has given an overview of metal-diamond contacts and highlighted its relevance to current research activity in the field of diamond electronics. The formation and high temperature annealing effects of aluminium and iron interfaces with diamond have been investigated. High temperature real-time PES was successfully used to follow the dynamics of the transitions at these interfaces at high temperatures. Real-time photoelectron spectroscopy was complemented by I-V, AFM and NEXAFS measurements. Real-time PES revealed new information regarding the formation of these contacts and their behaviour at high temperature. The next chapter in this thesis will concentrate on the application of real-time PES to a second category of carbon-based semiconductors, namely, thin organic films.

References

1. Kohn, E. and A. Denisenko, *Concepts for diamond electronics.* Thin Solid Films, 2007. **515**(10): p. 4333-4339.
2. Kalish, R., *Diamond as a unique high-tech electronic material: difficulties and prospects.* Journal of Physics D-Applied Physics, 2007. **40**(20): p. 6467-6478.
3. Twitchen, D.J., et al., *High-voltage single-crystal diamond diodes.* IEEE Transactions on Electron Devices, 2004. **51**(5): p. 826-828.
4. Rhoderick, E.H., *Metal-semiconductor Contacts*. 1988: Oxford University Press.
5. Bardeen, J., *Surface states and rectification at a metal semi-conductor contact.* Physical Review, 1947. **71**(10): p. 717-727.
6. Ihm, J., S.G. Louie, and M.L. Cohen, *Diamond-Metal Interfaces and Theory of Schottky Barriers.* Physical Review Letters, 1978. **40**(18): p. 1208-1211.
7. Kawarada, H., *Hydrogen-terminated diamond surfaces and interfaces.* Surface Science Reports, 1996. **26**(7): p. 205-259.
8. Monch, W., *Electronic properties of ideal and interface-modified metal-semiconductor interfaces.* Journal of Vacuum Science & Technology B, 1996. **14**(4): p. 2985-2993.
9. Evans, S., *The Properties of Natural and Synthetic Diamonds, pp 181-214*, ed. J.E. Field. 1992: Academic Press Ltd.
10. Sque, S.J., R. Jones, and P.R. Briddon, *Structure, electronics, and interaction of hydrogen and oxygen on diamond surfaces.* Physical Review B, 2006. **73**(8). 085313
11. Geis, M.W., et al., *High-Temperature Point-Contact Transistors and Schottky Diodes Formed on Synthetic Boron-Doped Diamond.* IEEE Electron Device Letters, 1987. **8**(8): p. 341-343.
12. Shirafuji, J. and T. Sugino, *Electrical properties of diamond surfaces.* Diamond and Related Materials, 1996. **5**(6-8): p. 706-713.
13. Maier, F., et al., *Origin of surface conductivity in diamond.* Physical Review Letters, 2000. **85**(16): p. 3472-3475.
14. Wang, X.G. and J.R. Smith, *Copper/diamond adhesion and hydrogen termination.* Physical Review Letters, 2001. **87**(18). 186103
15. Zhen, C.M., et al., *Ohmic contacts to boron-doped diamond.* Optical Materials, 2003. **23**(1-2): p. 117-121.

16. Ney, M.R., *Some aspects of the surface chemistry of diamond*. 1991, PhD Thesis, University College of Wales, Aberystwyth.
17. Werner, M., et al., *How to fabricate low-resistance metal-diamond contacts*. Diamond and Related Materials, 1996. **5**(6-8): p. 723-727.
18. Moazed, K.L., *Metal-Semiconductor Interfacial Reactions*. Metallurgical Transactions A - Physical Metallurgy and Materials Science, 1992. **23**(7): p. 1999-2006.
19. Viljoen, P.E., E.S. Lambers, and P.H. Holloway, *Reaction between Diamond and Titanium for Ohmic Contact and Metallization Adhesion Layers*. Journal of Vacuum Science & Technology B, 1994. **12**(5): p. 2997-3005.
20. Looi, H.J., et al., *Engineering low resistance contacts on p-type hydrogenated diamond surfaces*. Diamond and Related Materials, 2000. **9**(3-6): p. 975-981.
21. Zhen, C.M., et al., *Ohmic contacts on diamond by B ion implantation and Ta-Au metallization*. Diamond and Related Materials, 2002. **11**(9): p. 1709-1712.
22. Chen, Y.G., et al., *Electrical properties of graphite/homoepitaxial diamond contact*. Diamond and Related Materials, 2002. **11**(3-6): p. 451-457.
23. Clifton P H, E.S., *XPS Studies of Diamond/Transition-Metal Interfaces*. Industrial Diamond Review, 1995. **55**(1): p. 26-31.
24. Mori, Y., H. Kawarada, and A. Hiraki, *Properties of Metal Diamond Interfaces and Effects of Oxygen Adsorbed onto Diamond Surface*. Applied Physics Letters, 1991. **58**(9): p. 940-941.
25. Mead, C.A. and T.C. McGill, *Schottky-Barrier Heights on P-Type Diamond and Silicon-Carbide (6h)*. Physics Letters A, 1976. **58**(4): p. 249-251.
26. Hicks, M.C., et al., *The Barrier Height of Schottky Diodes with a Chemical-Vapor-Deposited Diamond Base*. Journal of Applied Physics, 1989. **65**(5): p. 2139-2141.
27. Himpsel, F.J., P. Heimann, and D.E. Eastman, *Schottky Barriers on Diamond (111)*. Solid State Communications, 1980. **36**(7): p. 631-633.
28. Chen, Y.G., et al., *Investigation of specific contact resistance of ohmic contacts to B-doped homoepitaxial diamond using transmission line model*. Diamond and Related Materials, 2004. **13**(11-12): p. 2121-2124.
29. Maier, F., et al., *Spectroscopic investigations of diamond/hydrogen/metal and diamond/metal interfaces*. Diamond and Related Materials, 2001. **10**(3-7): p. 506-510.

30. Takeuchi, D., et al., *Spatial uniformity of Schottky contacts between aluminum and hydrogenated homoepitaxial diamond films.* Applied Surface Science, 2000. **159**: p. 572-577.
31. Hewett, C.A. and J.R. Zeidler, *Ohmic Contacts to Epitaxial and Natural Diamond.* Diamond and Related Materials, 1993. **2**(10): p. 1319-1321.
32. Chan, S.S.M., et al., *Aluminum and Nickel Contact Metallizations on Thin-Film Diamond.* Journal of Applied Physics, 1995. **78**(4): p. 2877-2879.
33. Tachibana, T. and J.T. Glass, *Effects of Argon Presputtering on the Formation of Aluminum Contacts on Polycrystalline Diamond.* Journal of Applied Physics, 1992. **72**(12): p. 5912-5918.
34. Saby, C. and P. Muret, *Photoelectron spectroscopy of boron-doped homoepitaxial diamond (100) surfaces with several terminations and related Schottky barriers.* Diamond and Related Materials, 2002. **11**(3-6): p. 851-855.
35. Baumann, P.K. and R.J. Nemanich, *Electron affinity and Schottky barrier height of metal-diamond (100), (111), and (110) interfaces.* Journal of Applied Physics, 1998. **83**(4): p. 2072-2082.
36. Van der Weide, J. and R.J. Nemanich, *Influence of Interfacial Hydrogen and Oxygen on the Schottky- Barrier Height of Nickel on (111) and (100) Diamond Surfaces.* Physical Review B, 1994. **49**(19): p. 13629-13637.
37. Baumann, P.K., et al., *Characterization of metal-diamond interfaces: Electron affinity and Schottky barrier height.* Diamond and Related Materials, 1997. **6**(2-4): p. 398-402.
38. Van der Weide, J. and R.J. Nemanich, *Schottky-Barrier Height And Negative Electron-Affinity Of Titanium On (111) Diamond.* Journal of Vacuum Science & Technology B, 1992. **10**(4): p. 1940-1943.
39. Tachibana, T., B.E. Williams, and J.T. Glass, *Correlation of the Electrical-Properties of Metal Contacts on Diamond Films with the Chemical Nature of the Metal-Diamond Interface .2. Titanium Contacts - a Carbide-Forming Metal.* Physical Review B, 1992. **45**(20): p. 11975-11981.
40. Muret, P., E. Gheeraert, and A. Deneuville, *Deep level spectroscopy in homoepitaxial diamond films studied from current transients in Schottky junctions.* Physica Status Solidi A - Applied Research, 1999. **174**(1): p. 129-135.
41. Muret, P., et al., *Carbide contacts on homoepitaxial diamond films.* Diamond and Related Materials, 1999. **8**(2-5): p. 961-965.

42. Sellin, P.J. and A. Galbiati, *Performance of a diamond x-ray sensor fabricated with metal-less graphitic contacts.* Applied Physics Letters, 2005. **87**(9). 093502.
43. *IUPAC Compendium of Chemical Terminology 2nd Edition (1997).*
44. Friedel, G., Ribaud, G Bull. Soc. Prang. Minkr., 1924. **47**: p. 94.
45. Phinney, F.S., *Graphitization Of Diamond.* Science, 1954. **120**(3114): p. 393-394.
46. Seal, M., *Graphitization And Plastic Deformation Of Diamond.* Nature, 1958. **182**(4645): p. 1264-1266.
47. Howes, V.R., *Graphitization Of Diamond.* Proceedings of The Physical Society of London, 1962. **80**(515): p. 648-&.
48. Evans, T. and P.F. James, *Study of transformation of diamond to graphite.* Proceedings of The Royal Society of London Series A - Mathematical and Physical Sciences, 1964. **277**: p. 260.
49. Evans, T., R. K. Wild, *Plastic bending of diamond plates.* Philosophical Magazine, 1965. **12**: p. 479-489.
50. Davies, G. and T. Evans, *Graphitization of diamond at zero pressure and at a high-pressure* Proceedings of The Royal Society of London Series A-Mathematical and Physical Sciences, 1972. **328**: p. 413.
51. Bridgman, P.W., *An experimental contribution to the problem of diamond synthesis.* Journal of Chemical Physics, 1947. **15**: p. 92-98.
52. H Eyring, C.F.W., *An examination into the origin, possible synthesis and physical properties of diamonds.* Zeitschrift Fur Elektrochemie, 1952. **56**: p. 480-486.
53. Rodewald, H.J., Helvetica Chimica Acta, 1960. **43**: p. 1657.
54. Bovenkerk, H.P., et al., *Preparation Of Diamond.* Nature, 1959. **184**(4693): p. 1094-1098.
55. Bundy, F.P., et al., *Diamond-graphite equilibrium line from growth and graphitization of diamond.* Journal of Chemical Physics, 1961. **35**(2): p. 383-&.
56. Shimada, S., et al., *Thermo-Chemical Wear Mechanism of Diamond Tool in Machining of Ferrous Metals.* CIRP Annals - Manufacturing Technology, 2004. **53**(1): p. 57-60.
57. Wilks, E.M. and J. Wilks, *Resistance of diamond to abrasion.* Journal of Physics D-Applied Physics, 1972. **5**(10): p. 1902-&.
58. Song, Y., et al., *Tool wear control in single-crystal diamond cutting of steel by using the ultra-intermittent cutting method.* International Journal of Machine Tools and Manufacture, 2009. **49**(3-4): p. 339-343.

59. Evans, S. and M.R. Ney, *Cobalt-catalysed graphitisation of diamond studied by XPS*. Journal of Hard Materials, 1990. **1**(3): p. 169.
60. Ralchenko, V.G., et al. *Catalytic interaction of Fe, Ni and Pt with diamond films - patterning applications*. in *3rd International Conf on the New Diamond Science and Technology (Icndst-3) / 3rd European Conf on Diamond, Diamond-Like and Related Coatings (Df 92)*. 1992. Heidelberg, Germany: Elsevier Science Sa Lausanne.
61. Narulkar, R., et al., *Graphitization as a precursor to wear of diamond in machining pure iron: A molecular dynamics investigation*. Computational Materials Science, 2009. **45**(2): p. 358-366.
62. Graupner, R., et al., *High-resolution surface-sensitive C 1s core-level spectra of clean and hydrogen-terminated diamond (100) and (111) surfaces*. Physical Review B, 1998. **57**(19): p. 12397-12409.
63. Hufner, S., *Photoelectron Spectroscopy*. Advanced Texts in Physics. 2003 (3rd Edition) pp.173: Springer.
64. Chelikowsky, J.R. and S.G. Louie, *First-principles linear combination of atomic orbitals method for the cohesive and structural properties of solids: Application to diamond*. Physical Review B, 1984. **29**(6): p. 3470.
65. Himpsel, F.J., J.F. van der Veen, and D.E. Eastman, *Experimental bulk energy bands for diamond using h nu -dependent photoemission*. Physical Review B, 1980. **22**(4): p. 1967.
66. Ma, Y., et al., *Soft-x-ray resonant inelastic scattering at the C K edge of diamond*. Physical Review Letters, 1992. **69**(17): p. 2598.
67. Clifton, P.H., *Diamond / Transition-Metal Interfaces: Catalytic Graphitisation and Schottky Barrier Formation studied by XPS*. 1996, PhD Thesis, University College of Wales, Aberystwyth.
68. Nagakura, S., *Study of metallic carbides by electron diffraction 4. Cobalt carbides*. Journal of the Physical Society of Japan, 1961. **16**(6): p. 1213-&.
69. Nagakura, S., *Study of metallic carbides by electron diffraction .1. Formation and decomposition of nickel carbide*. Journal of the Physical Society of Japan, 1957. **12**(5): p. 482-494.
70. Fyfe, D.J., *The Surface Properties of Diamond and Cubic Boron Nitride*. 2001, PhD Thesis, University of Wales, Aberystwyth.

Chapter 6
Organic Thin Films

In this chapter the application of real-time SXPS to organic thin films is presented. A brief introduction to the field of organic electronics will be given followed by the presentation of experimental data relating to the growth of a the organic semiconductor tin II phthalocyanine (SnPc). It will be demonstrated how real-time SXPS has been used to study the dynamics of layer growth as SnPc molecules (which form Van der Waals bonded thin films) are deposited *in vacuo* on a variety of substrates at room and at elevated substrate temperatures.

6.1 Organic Semiconductors

Organic small-molecules such as phthalocyanines are of great interest due to their potential use in electronic devices such as light emitting diodes [1], solar cells [2] and field effect transistors [3]. The growth mode and orientation of these molecules can significantly affect the electronic and transport properties of any device and is therefore of great importance. Electrically driven light emission, a process called

electroluminescence, was reported in organic crystals as early as 1962 [4] however, it was not until 1986 that Tang *et al* reported the production of a double layer organic light-emitting device (OLED) [5, 6]. Shortly after this a conducting polymer-based light emitting diode (LED) was introduced at Cambridge [7]. This opened up the possibility for organic material to be used in lighting and display devices [8]. Over the past decades there has been continued interest in this new field which consists of two types of material, namely, polymers and small-molecules. These semiconducting materials offer themselves as potential low-cost, low-toxicity alternatives to conventional inorganic materials. In these organic molecules π bonds are formed due to the overlapping of the p_z orbitals perpendicular to the C-C plane. For these π bonds the energy gap between the bonding and anti-bonding states are much less than for σ bonds and fall within the visible spectrum (1.5 – 3 eV). The band structures that result are molecular bands. Hence, the equivalent of the conduction band in organic semiconductors is the lowest unoccupied molecular orbital (LUMO) with the valence band equivalent being the highest occupied molecular orbital (HOMO). The band gaps of these molecular systems decrease with increased delocalisation of the π system making them ideal materials for optical applications. Organic Light Emitting Devices (OLEDs) are based on electroluminescence (illustrated in figure 6.1) rather than photoemission from a junction as in a conventional LED. Electroluminescence is a process whereby holes and electrons are injected into the material where they recombine to form excitons, which in turn recombine producing photons. It is not conceivable that organic materials will replace inorganic semiconductors as the next generation of high performance semiconductors due to the fact that their carrier mobilities are too low. However, it is clear that for some applications organic semiconductors have distinct advantages over inorganic semiconductors such as silicon

or gallium arsenide due to their low production cost and low toxicity [9]. The electroluminescent process illustrated in figure 6.1 can be optimised by better knowledge of the bonding within the films and at the interfaces by optimisation of the interface energetics. In this case, PES is an ideal technique since it gives information in parallel regarding both energetics and bonding.

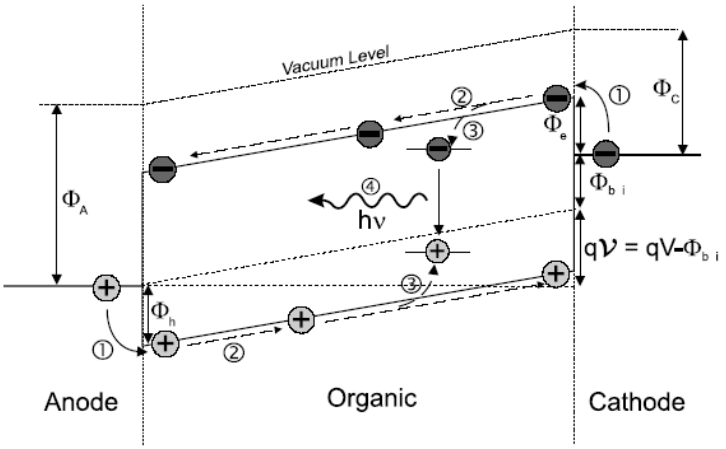

Figure 6.1 - *Original image from [10] – The basic steps of electroluminescence: (1) charge carrier injection, (2) charge carrier transport, (3) exciton formation, (4) radiative exciton decay. (ϕ_A – anode work function, ϕ_C – cathode work function, ϕ_h – hole injection barrier, ϕ_e – electron injection barrier, ϕ_{bi} – built-in potential, V – applied voltage, V – effective applied voltage across the organic layer, q – elementary charge)*

6.2 Phthalocyanines

The first report of phthalocyanine molecules dates back to 1907 when a sample was accidentally produced by Braun and Tcherniac while working for the South Metropolitan Gas Company in London [11]. However, it was not until 1928, when a reaction vessel cracked at the works of Scottish Dyes Ltd that its potential was realised. When the company was subsequently bought by ICI a patent was applied to cover the preparation and properties of this material. The first scientific studies date back to 1934 when a sample was given to Imperial College. Much of the work was published

by Linstead *et al* in the Journal of the Chemical Society [12]. A detailed account of early work on these molecules has been produced by McKeown [11]. It was Linstead who conceived the name phthalocyanine as a combination of the word phthal, originally from the Greek word Naphtha (rock oil) to emphasise the association with various phthalic-acid-derived precursors, and the Greek cyanine (blue). Their striking blue colour made them ideal candidates for use as inks and fabric dyes and they have been used extensively for this purpose. Most recently, they have been used in many other fields including optical data storage [13], photovoltaic cells [14], fuel cells [15] and even cancer therapy [16].

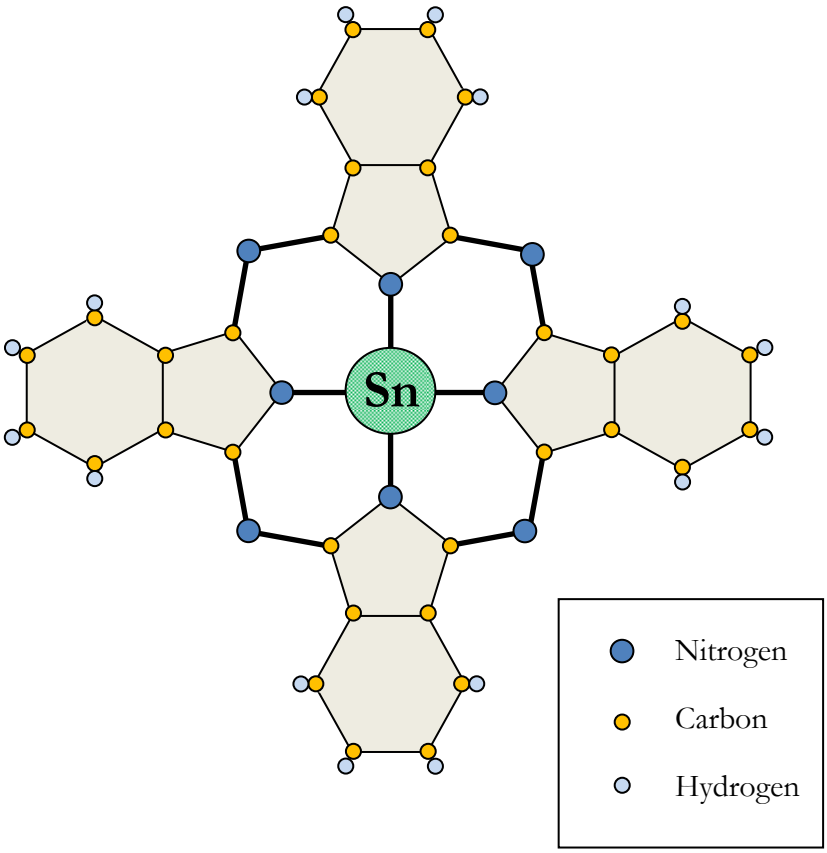

Figure 6.2 - *Schematic diagram of a tin phthalocyanine (SnPc) molecule.*

Phthalocyanines are closely related to the porphyrin molecule. They are planar macromolecules very similar to porphyrins and consist of 4 isoindole units as illustrated in figure 6.2. This means that they have a large delocalised cloud of electrons that is responsible for their unique properties and accounts for their wide range of applications. The four nitrogen atoms at the centre of the molecule can bond to a range of central atoms, usually hydrogen or metals. Up to 70 elements including single metal atoms can be used as central atoms. Thin layers of these organic molecules can be grown using a process called Organic Molecular Beam Deposition (OMBD) as described in chapter 2 [10] and can be grown to an accuracy of less than 1 monolayer (ML). The high purity of these materials, which contain typically 10^{14} - 10^{16} traps cm^{-3} is exceptional for organic materials. They also possess high thermal and chemical stability and most do not decompose below 900 °C. Strong acids or bases do not affect them and they can only be broken down to phthalimide or pthalic acid using very strong oxidising agents e.g. chromium (VI) or cerium (IV). H_2Pc was the first organic structure to yield to direct X-ray analysis [17]. Typically, for planar phthalocyanines two phases can exist in the crystalline form, these being α-phase and β-phase, with the main difference being the angle at which these planar molecules stack. The band gap has been found to be ~ 2 eV in H_2Pc and planar metal-phthalocyanine crystals. Usov and Bendersk [18] measured a room temperature conductivity of ~ 10^{-14} – 10^{-16} S cm^{-1}. In terms of optical properties there is an intense absorption band designated the Q band at 620 – 700 nm (1.7 – 2 eV) due to π-π* transitions (HOMO to LUMO) which is responsible of the intense blue colour of most metal phthalocyanines such as CuPc [11]. The optical band gap of SnPc has been reported to be around 1.80 eV [19] in the vapour phase and 1.77 eV [20] for a thin film in the α-phase.

6.2.1 Thermally Evaporated Films

Phthalocyanines have been evaporated *in vacuo* since the 1930s. Organic molecular beam deposition (OMBD) [21] (already introduced in chapter 2) is used in this experimental study. While inorganic semiconductors need accurate lattice matching to avoid misfit dislocation defects in thicker films, organic semiconductors depend much less on lattice matching. This is due to the fact that the energy bands are molecular, hence they are not as susceptible to defects. Conduction between the molecules in crystalline form is still affected by the molecular stacking and is ultimately responsible for the lower carrier mobilities compared to their inorganic counterparts. Overlapping of the π orbitals is required for effective conduction of electrons, hence for devices the structure and morphology of these layers is important. Bonding with the substrate is often achieved by Van der Waals bonding and therefore any strain due to lattice mismatching can be accommodated in these bonds. At thicker coverages the strain increases in these bonds and distinct changes can be observed in the growth mode (e.g. Stranski-Krastanov growth) [22].

6.2.2 Tin (II) Phthalocyanine

The number of publications relating to tin (II) phthalocyanine (SnPc) is still very low and unlike most metal-phthalocyanines this molecule is non-planar. This is due to the large size of the Sn^{2+} central metal ion which has a large radius ~ 1.18 Å causing protrusion out of plane by ~ 1.1 Å [23]. In this respect SnPc is similar to lead phthalocyanine (PbPc) however, a larger body of literature exists for PbPc [24]. Non-planar phthalocyanines also exhibit two phases: the monoclinic (α form) and the triclinic (β form) where stacking occurs along different axes of the molecule. It is

known that SnPc undergoes an irreversible transition from monoclinic to triclinic with increasing temperature [25].

Conventional PES is routinely used to study organic films and phthalocyanines allowing the energetics and energy-band alignment of interfaces to be studied in detail [26-28]. Work conducted by Steiner on copper phthalocyanine is one such example of this type of investigation [29, 30]. As for SnPc, the energetics of the p-GaAs/SnPc interface was studied extensively by means of SXPS by Cabailh *et al* [31] and Vearey-Roberts *et al* [32] who reported that thin SnPc interlayers can modify Schottky barrier heights in conventional inorganic GaAs/Ag diodes [33]. Studies of SnPc on polycrystalline iron have been conducted by Wells *et al* [34] while Peltekis *et al* [35] have investigated the local electronic structure of SnPc. However, this work will focus on the ability of real-time photoelectron spectroscopy to determine the morphology of the organic films when grown *in vacuo* by OMBD.

6.2.3 Orientation and Growth Modes of Phthalocyanines

The orientation and growth mode of these organic thin films have a considerable effect on electronic and transport properties of any device [36]. Therefore if these materials are to be routinely used in electronic devices a detailed understanding of their orientation and growth mode is critical. The first layer of any organic thin film has great importance since it is here that charge carrier injection into the material occurs. Many studies have investigated growth orientation of organic thin films on numerous single crystal substrates [21, 37-39] as well as on lower quality surfaces which are more technically relevant [40, 41]. Peisert *et al* reported a change in angle of CuPc molecules

with the molecules "lying flat" on single crystal surfaces but "standing up" on rougher less-defined surfaces [42]. Higher tilt angles have also been observed for instances where the molecule-substrate interaction was weak. The effect of substrate temperature on deposited CuPc layers was investigated by Karan *et al* [43] by means of AFM measurements showing increased cluster sizes at higher temperatures on polished silicon. A comprehensive review of ultra-thin phthalocyanine films has been undertaken by Papageorgiou *et al* [44]. This work concentrates on interface formation for passivated narrow band gap III-V semiconductor surfaces.

6.3 Experimental Results

The experimental results for these studies were obtained by soft x-ray photoelectron spectroscopy (SXPS) conducted at MPW 6.1 at the Synchrotron Radiation Source at Daresbury, UK which provided enhanced surface sensitivity. The measurements were performed with the VG CLAM4 electron energy analyser coupled to the 768 channel Aberystwyth array detector (the setup is described in detail in chapter 3). A simple schematic diagram of the experimental setup is presented in figure 6.3.

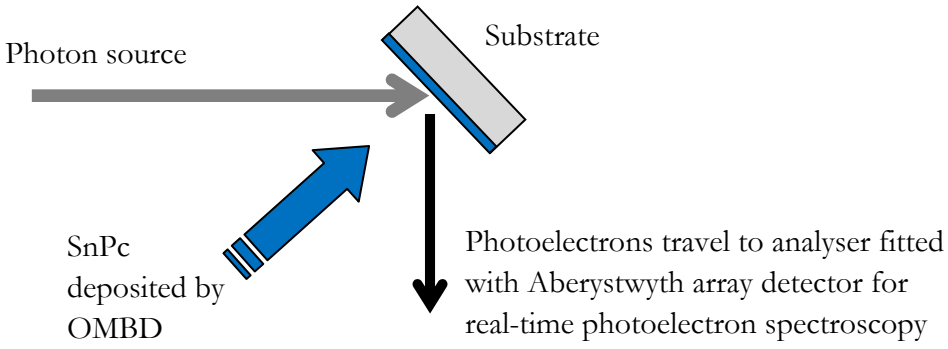

Figure 6.3 – *Schematic diagram of the experimental setup for real-time photoelectron spectroscopy performed at the SRS.*

Three different substrates were used for this study namely Si(111):H, GaAs(001):S and polycrystalline Au. The surfaces were chosen to be as chemically and electronically inert as possible while providing clean UHV surfaces for SnPc growth. The GaAs(001):S substrate was etched using sulphur monochloride (S_2Cl_2), reported by Gnoth *et al* [45], while the Si(111):H was etched using conventional methods using standard Si etching procedures described by Brieva [46]. The polycrystalline Au was polished, then annealed *in situ* prior to growth. Conventional SXPS was used to characterise these samples and to confirm the quality of the snapshot spectra.

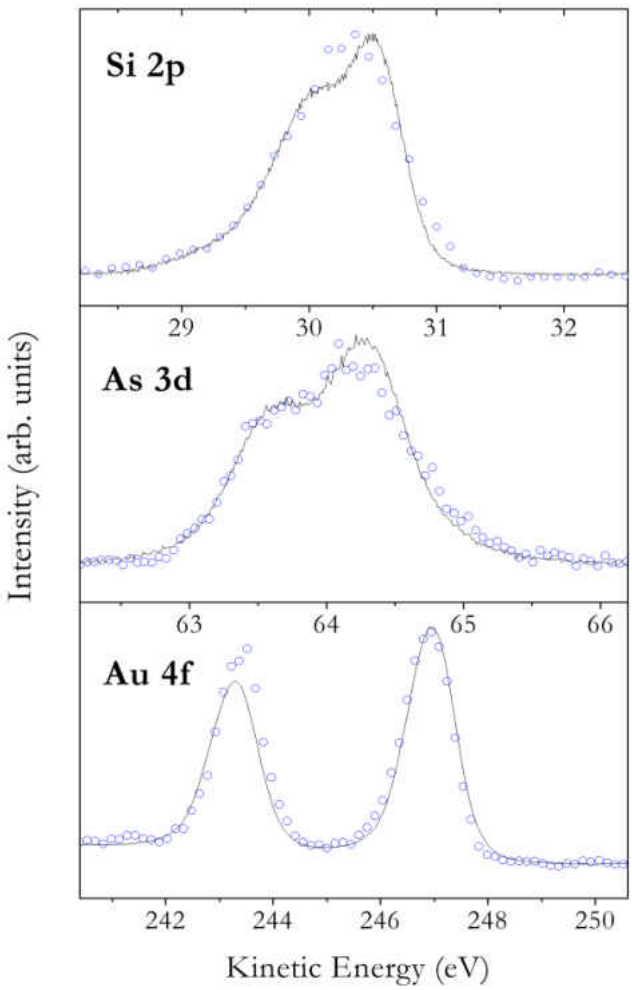

Figure 6.4 – *Comparison of conventional SXPS core-level spectra (solid black lines) and fast real-time spectra taken in snapshot mode (open blue circles) using the Aberystwyth array detector for the three clean substrates: Si 2p of Si(111):H with snapshot taken in 700 ms (top panel), As 3d of GaAs(001):S with snapshot taken in 250 ms (middle panel) and the Au 4f doublet of polycrystalline Au with snapshot taken in 100 ms (bottom panel).*

Selected substrate core levels for each substrate are presented in figure 6.4 with snapshot (fast) real-time spectra (open blue circles) overlaying the conventional scanned spectra (solid black lines). The Si 2p, As 3d and Au 4f snapshots were taken at 700, 250 and 100 ms time intervals respectively. It was demonstrated that the snapshot spectra although collected at sub-second intervals still provided adequate energy resolution as evident from figure 6.4.

Prior to growth the clean substrate peaks were monitored to ensure that the measurements were stable and reliable and that no other factors such as beam drift or instrumental changes were affecting the snapshot measurements. Once a series of consistent snapshots were obtained for the clean substrate, growth would be initiated. The SnPc was thermally evaporated using a Knudsen cell heated to around 350 °C - a process referred to as OMBD (Organic Molecular Beam Deposition) and already described in this thesis. The growth rate was monitored both before and after deposition by a quartz crystal microbalance placed near the substrate. The growth rate for Si was 0.07 nm min^{-1} while rates on GaAs were around 0.05 – 1.0 nm min^{-1} and 0.5 nm min^{-1} on the Au. Figure 6.5 presents the real-time spectra for the three substrate core levels before, during and after growth of the SnPc layer. Sequential fitting of these spectra allowed the peak attenuation to be extracted giving information about the morphology of the SnPc layer during growth for all three cases.

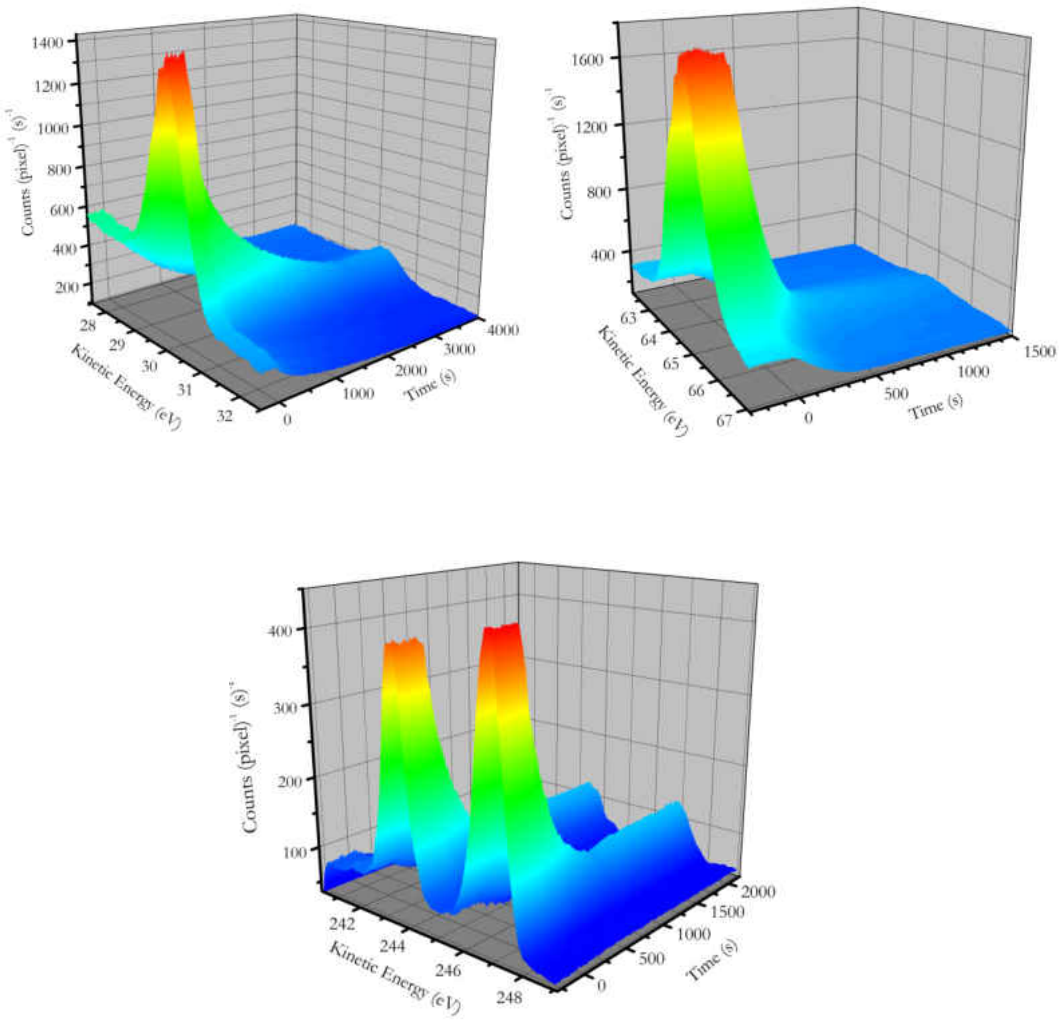

Figure 6.5 – *Real-time SXPS snapshot spectra during SnPc growth experiments. The three substrate core levels are: Si 2p of Si(111):H taken every 700 ms (top left), As 3d of GaAs(001):S taken every 250 ms (top right) and the Au 4f doublet of polycrystalline Au taken every 100 ms (bottom).*

6.3.1 Growth of SnPc at Room Temperature

The following general observations made for all three substrates in figure 6.5 are illustrated in figure 6.6 by means of a semi-logarithmic plot of substrate peak intensity against time. Rapid attenuation is observed in the peak intensity as the SnPc forms the first layer. This linear region ends at the transition point and is followed by a second region where growth continues but with a reduced rate of attenuation.

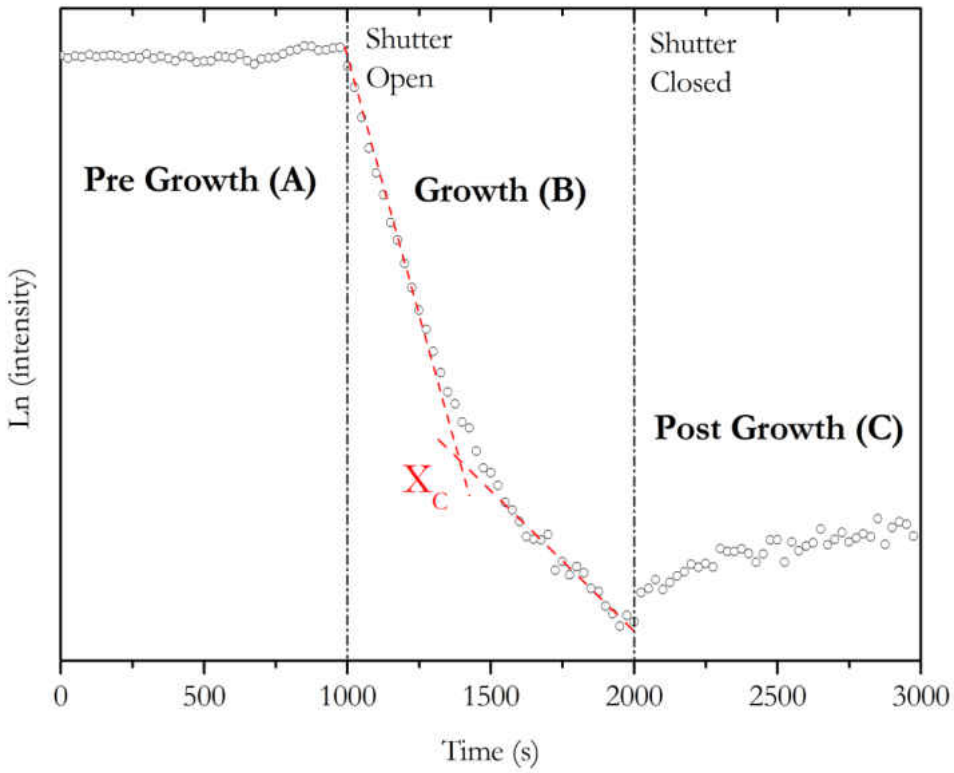

Figure 6.6 – *Peak intensity for the Au 4f 7/2 substrate peak obtained by sequential fitting of snapshot spectra. Three stages in the experiment are outlined and show the peak intensity before (A), during (B) and after (C) growth of thermally evaporated SnPc by OMBD in UHV with a substrate temperature of 30 ˚C. The transition point X_c is labelled and defined as the intercept of the two extrapolated lines of the linear regions.*

Finally, after the SnPc flux is switched off a small increase in the peak intensity ensues. Sequential fitting of the peak intensities using a Gaussian/Lorentzian mix function allows an accurate determination of the peak intensity from the data. Figure 6.6 shows a typical semi-logarithmic attenuation curve for an experimental run on the polycrystalline Au substrate – this specific data set is the Au 4f 7/2 substrate peak during growth and with a substrate temperature of 30 ˚C. The clean substrate is monitored to check for any instabilities (region A) until growth is initiated at 1000 s into the experiment and continues for 1000 s (region B) at which point the flux ceases and the peak intensity is measured for a further 1000 s (region C).

6.3.1.1 Electron Mean Free Path

When plotted as a semi-logarithmic plot region B in figure 6.6 is shown to contain two distinctive stages. The transition point between these two stages (referred to as X_c) distinguishes the end of the uniform first layer formation from the growth of the subsequent layers. Fitting of the initial substrate peak attenuation (as in figure 6.6) before the transition point gives a value for the mean free path (or escape depth) for SnPc (it is assumed that the growth rate of the overlayer remains constant). The values for the mean free path are dependent upon the kinetic energy of the electron (as described in section 2.3.8) therefore a different value was obtained for the three substrate core levels. These values were found to be 0.58, 0.32 and 0.80 nm for the Si 2p, As 3d and Au 4f substrate core levels respectively and are plotted in figure 6.7-A. For kinetic energies above 100 eV it has been found that the inelastic mean free path follows a power law equation and is dependent on the kinetic energy of electrons, E_K and Z, where $0.5 \leq Z \geq 0.79$ [47]. Using data from XPS measurements of CuPc layers on InSb Evans *et al* [30] determined the power law equation for a metal-phthalocyanine (CuPc) to be:

$$\lambda = 0.48\, E_K^{0.51} \qquad (Equation\ 6.1)$$

The mean free paths for SnPc obtained from the substrate core levels in this thesis are found to be in agreement with this function (labelled as 'Theory' in figure 6.7-A). Figure 6.7-B presents the data points in relation to the universal mean free path curve (presented in section 2.3.8) and proves that the values correspond well with data for other materials.

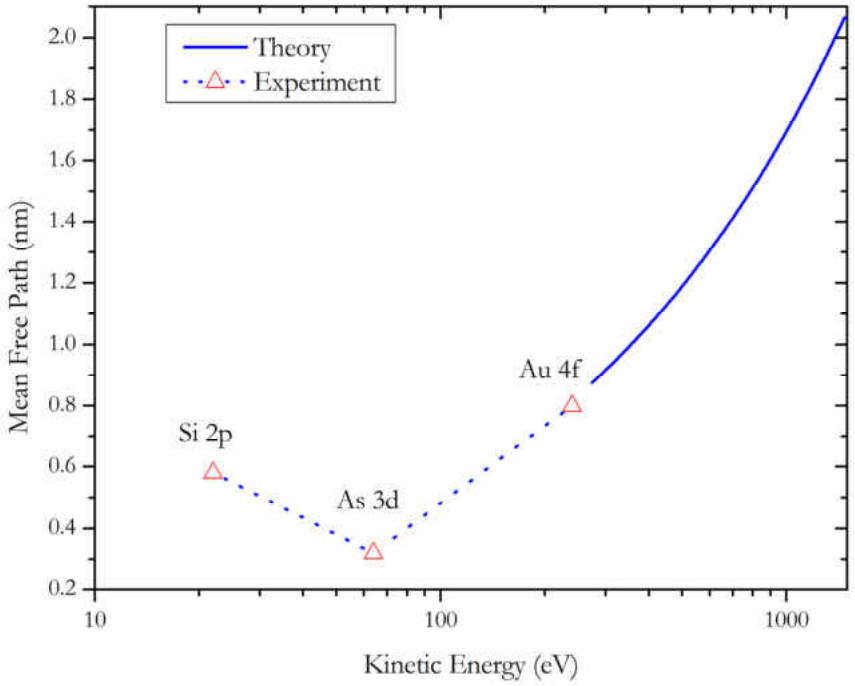

(A)

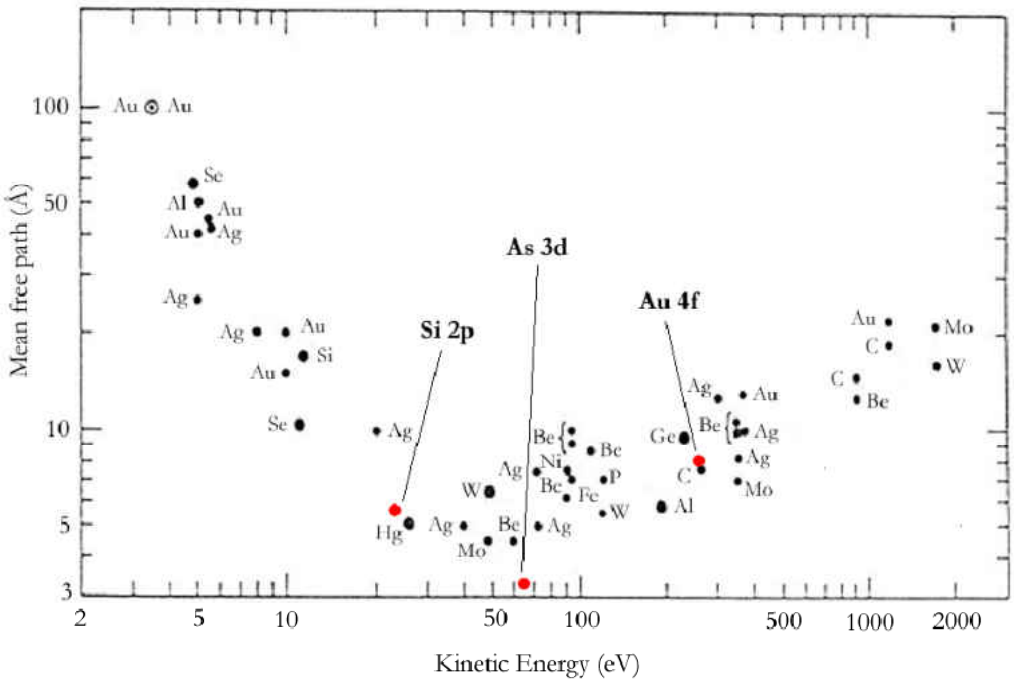

(B)

Figure 6.7 – *Mean free path of electrons plotted against kinetic energy: Panel (A) - as determined from real-time growth data for the three substrate core levels: Si 2p, As 3d and Au 4f (red triangles). The fitted empirical curve determined by Evans et al [30] for CuPc on InSb is also plotted (solid blue line). Panel (B) – the same data points plotted on the universal mean free path curve taken from [48].*

6.3.1.2 Multisnap Capability of the Array Detector

The improvement in electron detection afforded by the Aberystwyth array detector allows real-time spectra of multiple regions in the photoelectron spectrum to be measured during an experiment. The growth of SnPc on GaAs demonstrates this capability well and is presented in figure 6.8 where the attenuation of two substrate core levels (Ga 3d and As 3d), the evolution of the valence band as well as the emergence of the overlayer Sn 4d peak are all monitored during one growth experiment. This capability has great potential for determination of the evolution of interface energetics during formation of the layer. However, for the purposes of this study it is the attenuation of the core level peaks which are evaluated to determine the dynamic changes in film morphology during growth.

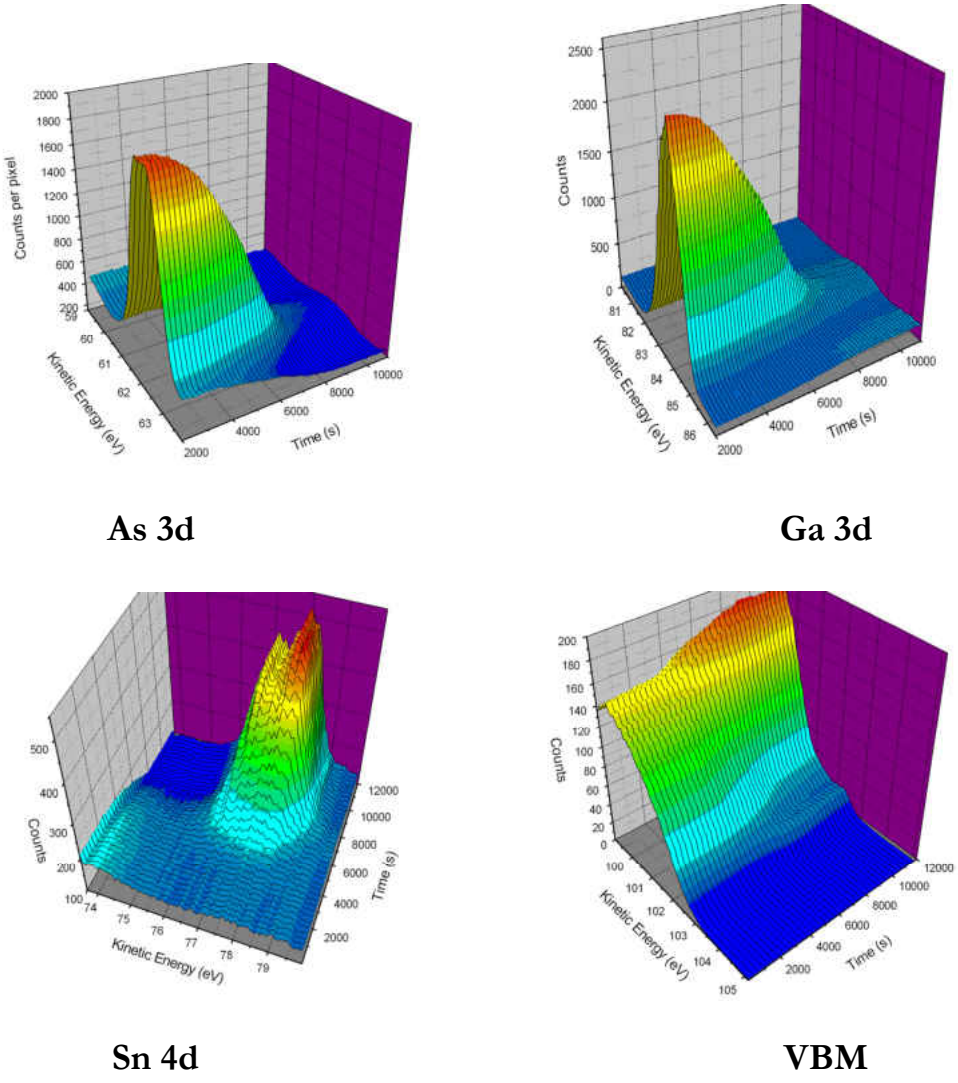

Figure 6.8 – *Real-time SXPS data for OMBD growth of SnPc on GaAs (001):S. Fast snapshots spectra were taken sequentially at four kinetic energies with an acquisition time of 1 s for the As 3d, Ga 3d and Sn 4d core levels and 10 s for the valence band maximum for each measurement cycle.*

6.3.1.3 Comparison with Conventional Spectroscopy

Other workers have monitored SnPc growth using conventional PES [49, 50]. However, these experiments take much longer to conduct since growth has to proceed in incremental steps so that measurements can be performed at a number of different coverages providing much less detailed information. Figure 6.9 (main panel) presents intensity data obtained using both conventional (large filled circles) and real-time (small filled circles) SXPS measurements. The core level intensity is stable before growth commences (labelled – 'Cell on') and then attenuates quickly until the transition point is reached giving a subsequent reduced attenuation rate until termination of growth at 4 nm (labelled – 'Cell off'). Below the transition point there is agreement between the conventional and real-time data, but then the data diverges beyond the point at which molecular clustering begins. Post-growth the real-time data shows a gradual exponential increase in the peak intensity which reaches saturation at a point which corresponds with the data obtained by conventional spectroscopy. This post-growth intensity change is attributed to post-growth clustering or re-organisation of the SnPc layer. This phenomenon proceeds over a period of around 20 - 30 minutes immediately following the termination of growth and was not detected by conventional photoelectron spectroscopy due to the delay between growth and measurement. There is evidence from the conventional data that further clustering occurs *ex situ* since an even higher intensity is measured for the As 3d peak (right hand panel) following exposure to atmosphere. This clustering is confirmed by *ex situ* AFM data (main panel – inset) which clearly shows SnPc clusters of around 20 nm in diameter are dispersed across the surface after exposure to atmosphere.

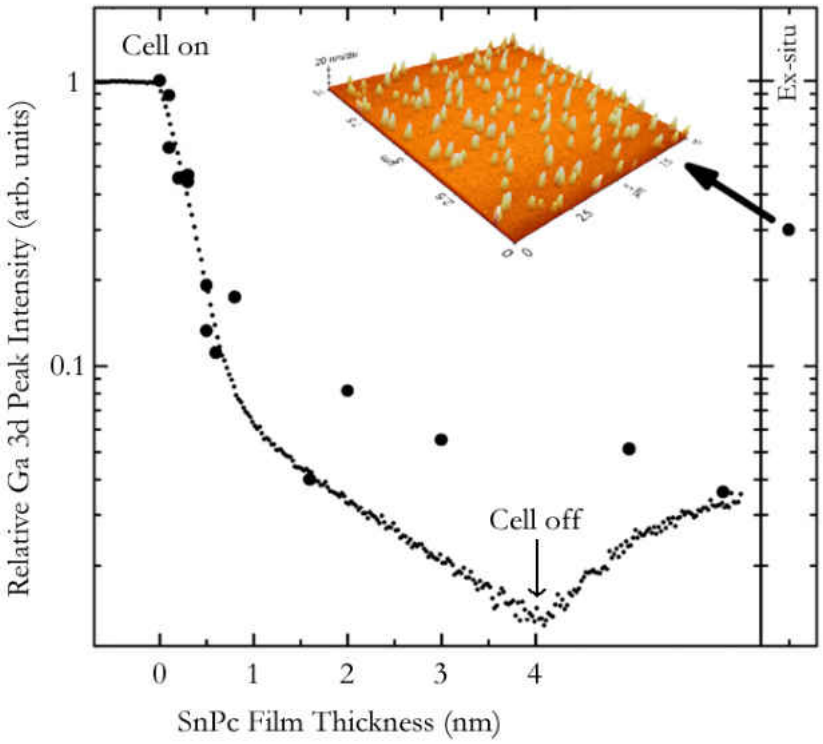

Figure 6.9 – *A plot of relative As 3d peak intensity against SnPc film thickness. Large black filled circles denote results obtained by Vearey-Roberts [32] using conventional photoelectron spectroscopy while the small black filled circles show data obtained using real-time electron spectroscopy in snapshot mode. Growth commences at 0 nm and terminates at 4 nm. Intensity measured by conventional photoelectron spectroscopy following exposure to atmosphere (right hand panel) and ex situ AFM measurement is also presented (inset).*

6.3.1.4 The Transition Point

The values for the X_c (transition point) were evaluated for Si, GaAs and Au and found to be 0.45, 0.9 and 1.3 nm respectively. These values were obtained using data from the attenuation curves presented in figure 6.10. Previous NEXAFS measurements of SnPc on passivated GaAs suggests that the molecules have a preferred orientation on the substrate [50] lying at ~ 30° with respect to the substrate plane [32]. Similar measurements on Si (111) conducted by Brieva produced a value of 24° [46]. The surface proved too rough for a corresponding value to be obtained for polycrystalline Au. In light of this, there is evidence that the transition point gives an indirect

measurement of the angle with respect to the substrate. For example, a substrate for which the relative angle with the substrate plane is high (where the molecule stands up on the surface) yields a higher value for the transition point.

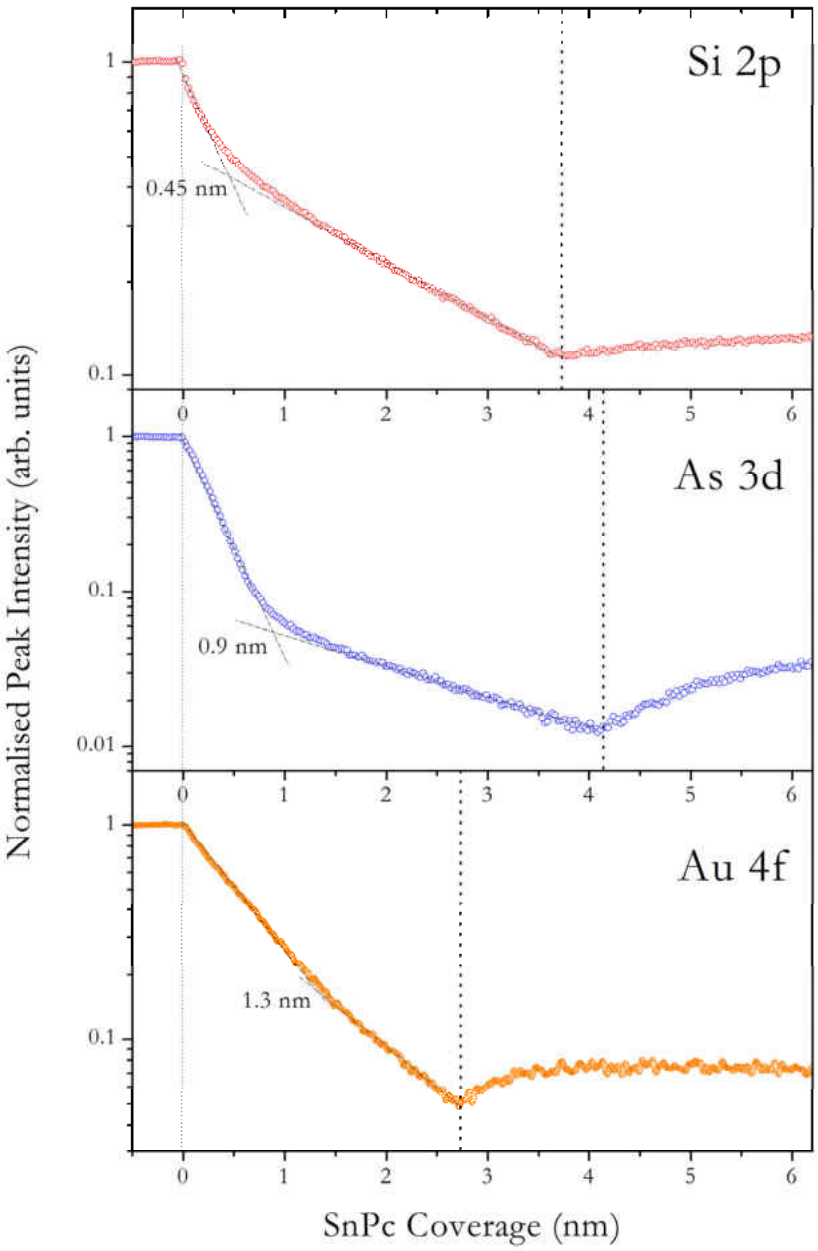

Figure 6.10 – *Plot of Log of the normalised core level intensity against the SnPc film thickness in nm for Si(111):H (top), GaAs(001):S (middle) and polycrystalline Au (bottom) substrates. The left hand dotted line at 0 nm denotes the start of deposition while the second dashed line in each panel denotes termination of deposition. The transition point (X_c) for each substrate is determined by the intercept of the two straight lines extrapolated from the two linear regions present during SnPc growth.*

The mean surface roughness was also determined for the Si, GaAs and Au substrate from AFM measurements and evaluated to be 0.2, 1 and 30 nm respectively. These values were related to X_c. A plot of X_c against mean surface roughness is presented in figure 6.11. It was found that there is a correlation between these two parameters, with the rougher surfaces related to higher values obtained for the transition points. Since it is suggested that X_c represents the transition from single layer growth to multi layer growth this finding suggests that the surface roughness has an effect in determining the nature of the first layer. An increase in X_c suggests that the first layer becomes progressively thicker due to the fact that an increase in the angle of the molecules in respect to the substrate plane allows more molecules to form part of the first layer causing a greater attenuation of the core level intensity. This is consistent with the orientation effects reported by Peisert *et al* for CuPc [36]. A schematic of this concept is presented alongside the data in figure 6.11.

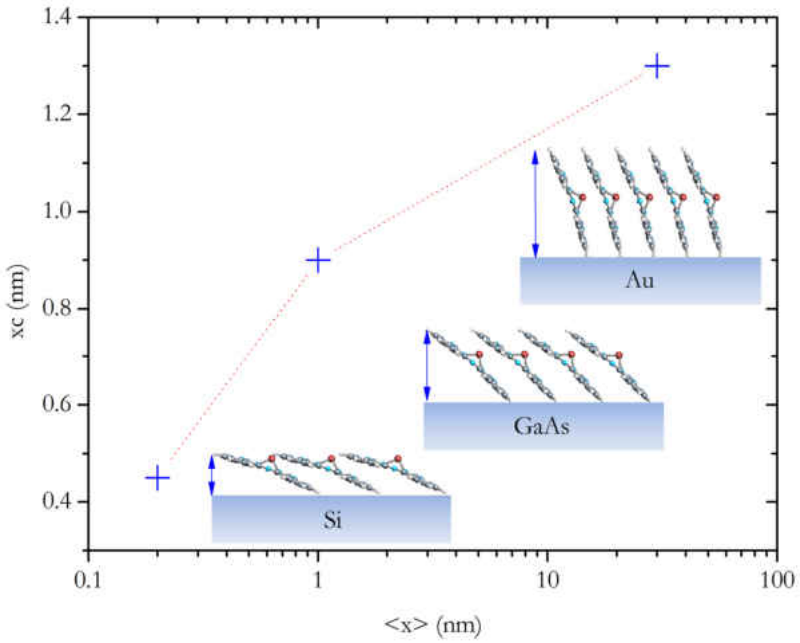

Figure 6.11 – *A plot of the transition point (X_c) against mean surface roughness for the three substrates at room temperature.*

6.3.1.5 Post-growth Clustering

The increase in intensity post-growth (region C in figure 6.6) is interpreted as a reduction in effective substrate surface coverage resulting from molecular clustering. Evidence of such a change in morphology has been reported by Krause *et al* for PTCDA where "a morphology change from a smooth or facetted film to islands" is detected on Au (111) [51, 52]. This process has been modelled using a simple exponential function to represent a time-dependent decrease in electron absorbing material (figure 6.10) and is expressed as:

$$\mathrm{I} = I_0 \left(1 - e^{-\frac{t}{\tau}} \right) \qquad (Equation\ 6.2)$$

Where: I_0 represents the intensity at infinite thickness, t time and τ is the associated time constant. The time constant, τ was found to vary for each substrate and evaluated to be 1342 ± 716 s (22 min), 1131 ± 166 s (19 min) and 366 ± 60 s (6 min) for the Si, GaAs and Au respectively as presented in figure 6.12. The error in the value for Si is particularly large due to the slower rate and due to the fact that post-deposition monitoring time was not extended to take account of this. A lower value for τ corresponds to faster clustering of the layer which suggests that the rapid clustering is much more pronounced for the Au compared to the GaAs and Si.

A qualitative correlation was found to exist between the mean substrate surface roughness and the post clustering time constant, τ (as shown in figure 6.13) suggesting that the angle of the first layer may affect the mobility of the molecules post-growth re-organisation. Alas, no quantitative conclusions can be drawn for this relationship since more experimental data is required.

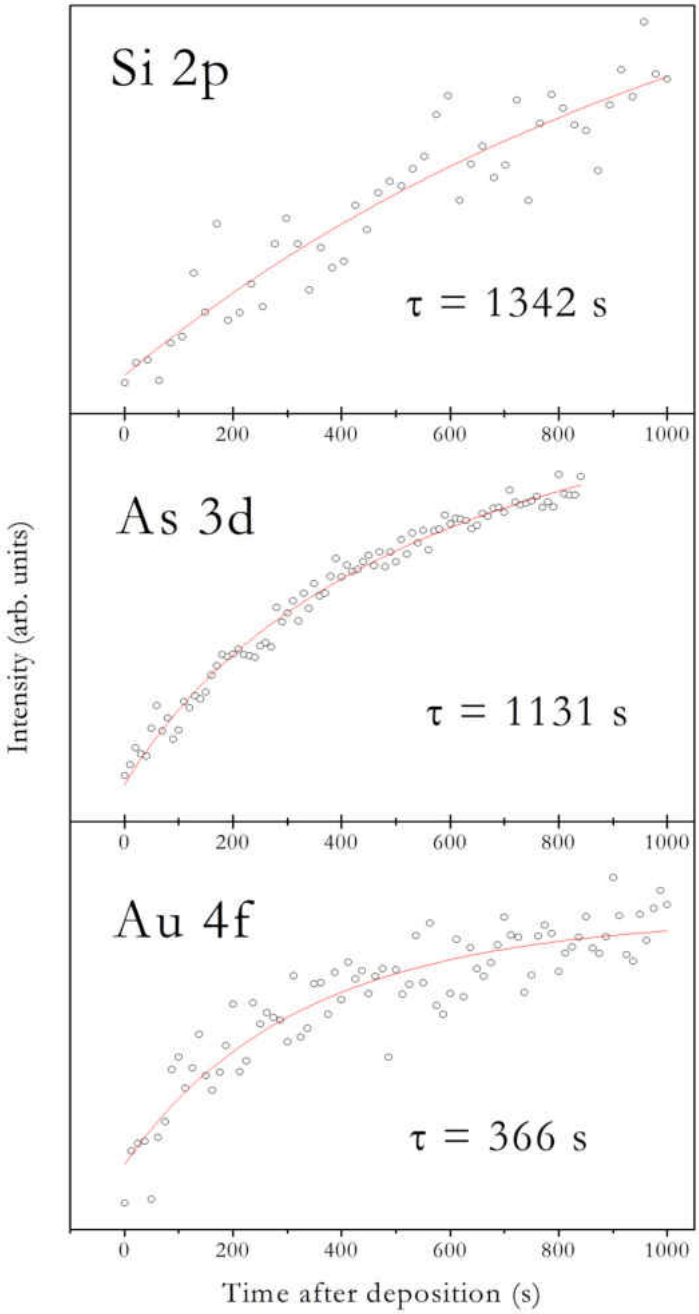

Figure 6.12 – *Fitted relative substrate core level intensities for Si, GaAs and Au core levels after termination of SnPc deposition.*

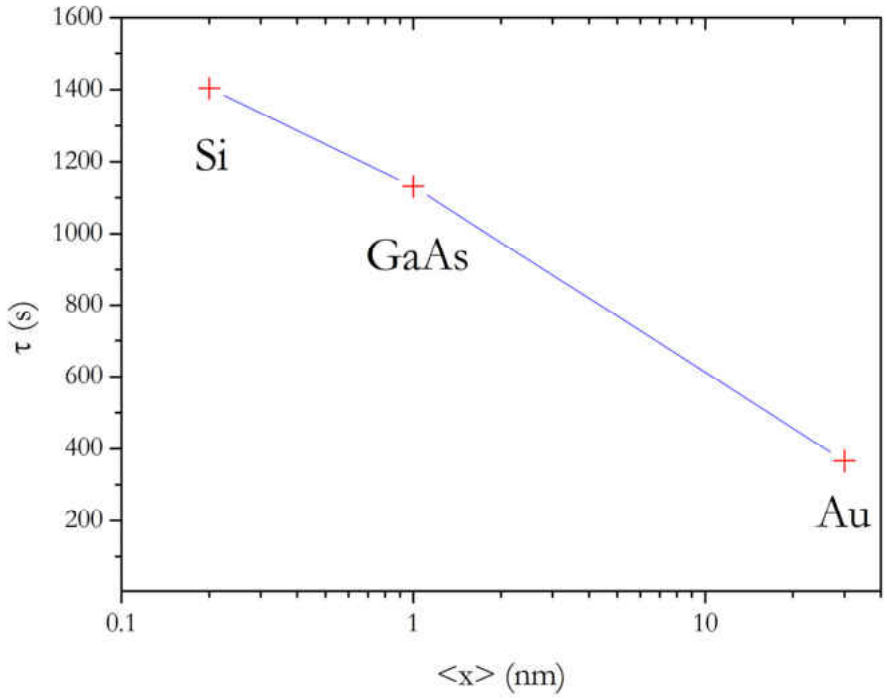

Figure 6.13 – *A plot of the post-growth clustering time constant τ against mean substrate surface roughness <x> obtained by AFM measurements.*

6.3.1.6 Low SnPc Coverages

Figure 6.14 presents data of a growth experiment where deposition is terminated before the transition point is reached. Deposition on to the polycrystalline Au substrate was only sustained for a period of 100 s giving a total coverage of ~ 0.8 nm. Following termination of growth, no post growth increase in intensity was observed suggesting that no post growth re-organisation of the molecules occurs at lower coverages. At these coverages there is significant molecule-molecule interaction and the data suggests that clustering initiates above the first monolayer. It is conceivable that growth above the first monolayer (and subsequent clustering) occurs in one part of the sample while the first monolayer is yet to be completed on another part.

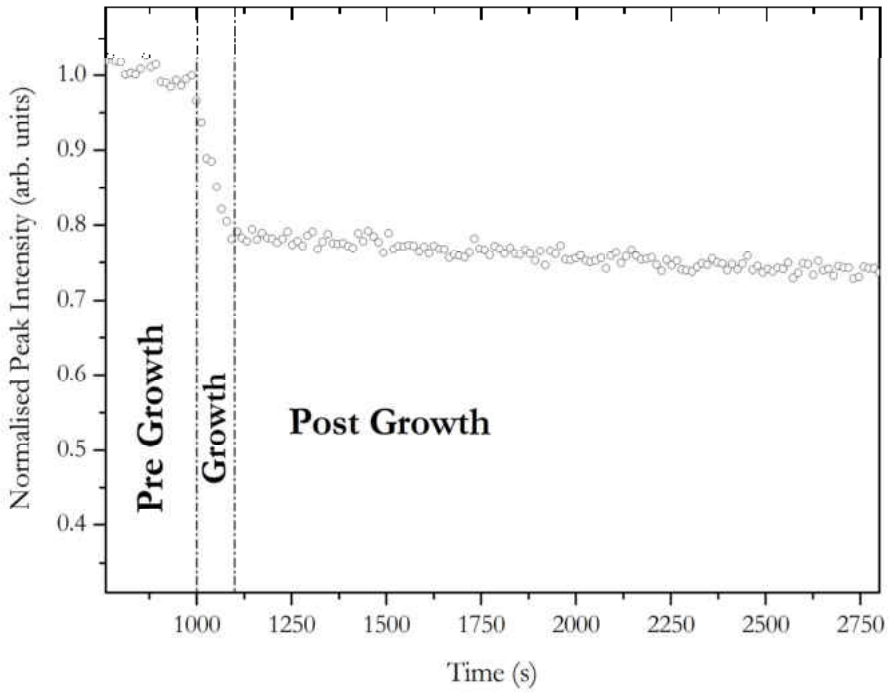

Figure 6.14 – *The Au 4f 7/2 substrate peak intensity of polycrystalline Au during deposition of SnPc with growth proceeding between 1000 - 1100 s.*

6.3.1.7 Clustering Model

A simple model for clustering was developed to explore the experimental observations and was programmed using LabVIEW by David Langstaff. The model treated the individual molecules as flat individual semi-transparent "tiles" which occupied squares on a grid when deposited on the surface. This surface was assumed to be continuous with the grid squares at the edges deemed to be next to those on the opposite edge of the square grid. A function for the attenuation in the photoemission signal (or simulated absorption) due to these semi-transparent "tiles" (which represent the molecules) was used to determine the attenuation curve which is affected by the configuration of the molecules on the surface. The assumptions made in this model will now be described.

Deposition of the molecules was simulated by placing N molecules per time step (N determined by rate parameter) into random positions in a grid of a pre-determined size (40 x 40). If no molecules are present in the adjacent grid squares the molecule retains its position in the grid even if other molecules exist "underneath" due to previous deposition into that grid square. This assumption represents the nature of the first monolayer. If the molecule is deposited into an environment where there are numerous molecules both underneath and adjacent, a post-adsorption diffusion stage determines that the molecule moves into the lowest existing adjacent grid square.

Once the molecule has been deposited and any post-adsorption diffusion movement completed the clustering component of the model analyses the environment for each molecule sequentially in the grid and determines their amount of coupling. A high number of neighbour molecules represents a high level coupling giving a lower probability for movement whereas a low number of neighbour molecules will result in low coupling and a higher probability of movement. This is determined numerically by assigning a probability of movement by the number of neighbour molecules at each quadrant (i.e. above, below and along each edge of the square "tile"). Therefore if a molecule has a total number of 8 neighbours the probability will be zero while if there are no nearest neighbours it will be one. The strength of the coupling could be tuned since two input parameters allowed the molecule to molecule interaction and the substrate to molecule interaction to be varied in strength. The total coupling factor calculated for each molecule was then subtracted from a random number taken from an exponential Boltzmann distribution curve to simulate thermal energy. If the resulting value was greater than 1 the molecule moves one grid square in a random direction. The model assumes that clustering of the "tiles" occurs throughout the deposition

period and consequently best simulates the experimental data obtained after the transition point, X_c and does not predict the existence of the transition point.

Data produced using this model is presented in figure 6.15. Molecule deposition initiates at timestep, t = 0 and continues until t = 2000. The attenuation curve presented broadly represents the attenuation observed in the real data. Since the model assumes the molecules to be flat square tiles it does not allow any variation in the angle of the molecules relative to the substrate and also assumes that clustering occurs throughout. Once deposition is terminated post-growth attenuation very closely simulates the real data obtained. Graphical representations of the configuration of the molecules at timestep 2000 and 5000 are displayed as insets in figure 6.15. These images clearly show that the model predicts a clustering behaviour which results in the formation of islands. Immediately after the end of deposition (t = 2000) the surface already shows some signs of clustering behaviour, but after 2000 timesteps the islands become much more pronounced and the change in intensity of the core level intensity closely resembles that observed in the experimental data.

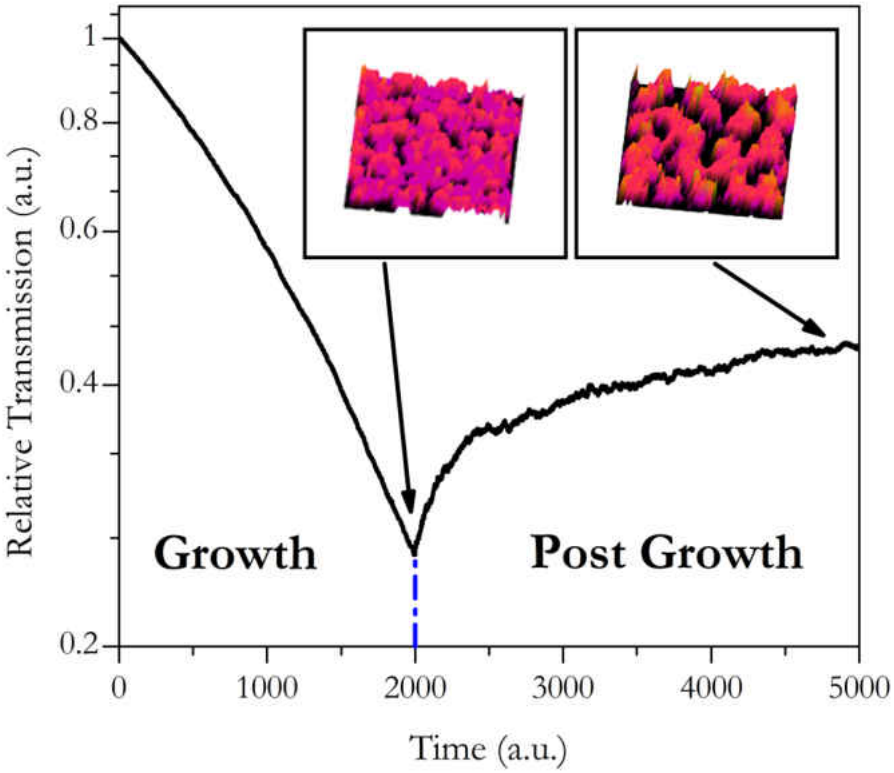

Figure 6.15 – *A simulated attenuation curve produced by the molecular model.*

6.3.2 Growth of SnPc at Elevated Temperatures

Due to the ease with which polycrystalline Au could be cleaned *in vacuo* by annealing it was considered a suitable substrate for further systematic study on the effect of substrate temperature on the growth phenomena reported on SnPc at room temperature. It has been suggested by Pfuetzner *et al* that deposition of a C_{60}/ZnPc layer on a heated substrate results in improvement in solar cell performance [53] due to the resulting change in morphology. A series of experiments performed with increasing substrate temperatures up to 430 °C are presented in figure 6.16. Polished polycrystalline Au was loaded into the UHV system and cleaned by annealing before growth. The SnPc was desorbed between each run by annealing to 1000 °C and conventional SXPS was then used to confirm the desorption. To eliminate any possible degradation effects on the surface during the course of the experiments the experimental sequence was not performed in the order of increasing or decreasing temperature e.g. 30 °C was followed by 400 °C etc. A stable substrate temperature was established by applying a constant power to the graphite/BN boroelectric heater mounted on the stage and before opening the shutter a stable growth rate of 0.5 nm min^{-1} was established using a quartz crystal microbalance while the clean substrate peak was monitored for 1000 s. Growth of the SnPc layer proceeded for another 1000 s followed by another 1000 s of post deposition monitoring.

The pre-growth signal remains stable until the shutter is opened. The initial attenuation rate is found to be constant at all substrate temperatures as expected since it is dependent only on the mean free path of the electrons during formation of the first layer. However, as was the case for the room temperature measurements a well defined

transition point (X_c) is observed where growth proceeds beyond the first layer and clustering is initiated.

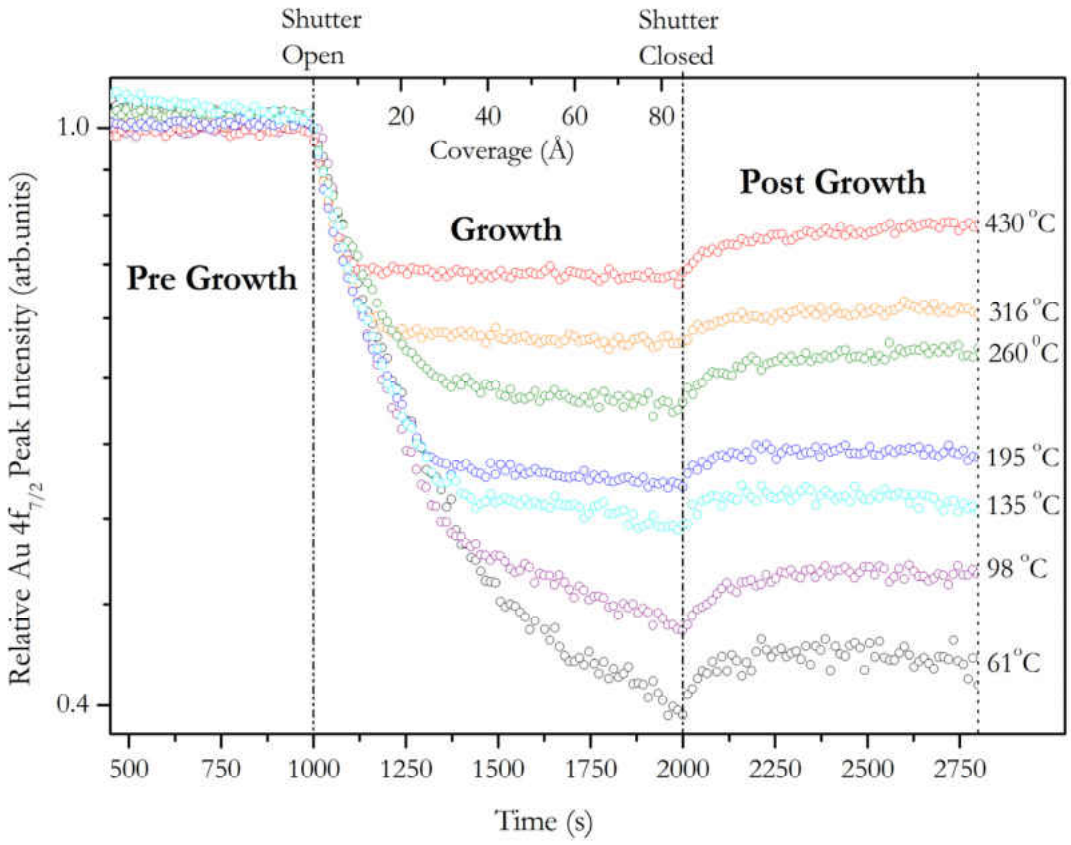

Figure 6.16 – *Relative peak intensity of the Au 4f 7/2 substrate peak of polycrystalline Au plotted against time for substrate temperatures between 30 and 430 ˚C.*

6.3.2.1 Temperature Dependent Transition Point

Analysis of the data reveals that the transition point position is temperature dependent and there is evidence that temperature has a similar effect on the critical thickness to that of surface roughness. This critical thickness decreases as the temperature of the substrate increases. One possibility is that the substrate temperature also affects the angle of the molecular plane relative to the substrates. At higher temperatures the molecules would lie flatter on the substrate causing the transition point to occur at a much lower coverage since critical thickness is achieved with fewer molecules. The

nature of this initial layer will be governed by the fine balance between molecule-molecule and molecule-substrate interaction. However, it is also conceivable that at higher temperatures the first monolayer is never completed. In this case, re-organisation would initiate earlier in the growth stage because the molecules are less tightly bound to the substrate allowing re-organisation to proceed at an increased rate (figure 6.17). Desorption from the surface is also an important consideration at high temperatures such as those encountered in this experimental run but since the rate of desorption cannot be accurately estimated it is impossible to distinguish between the two cases outlined above.

After the transition point a reduced rate of core level attenuation is observed which also depends on substrate temperature. Desorption would also account for the very low rate of attenuation observed after the transition point (which is close to zero above 200 °C). It could also be attributed to rapid molecular re-organisation. An Arrhenius plot based on the change in the attenuation rate after the transition as a function of time (figure 6.18) yields a straight line and an activation energy of 264 ± 14 kJ mol^{-1}, but due to the unknown effects of desorption this result is not conclusive.

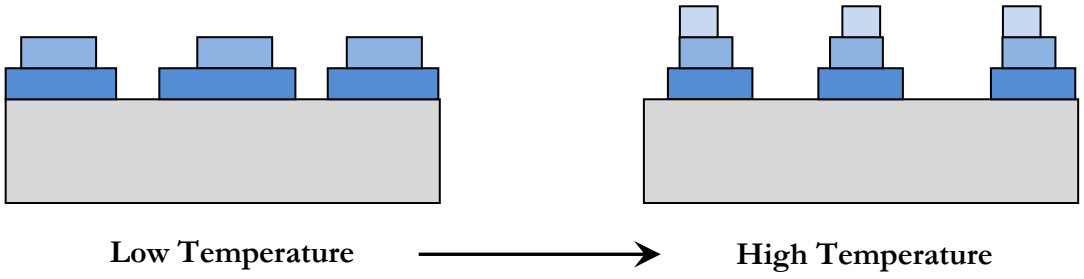

Figure 6.17 – *Schematic diagram of the proposed change in molecular organisation with substrate temperature during growth of SnPc.*

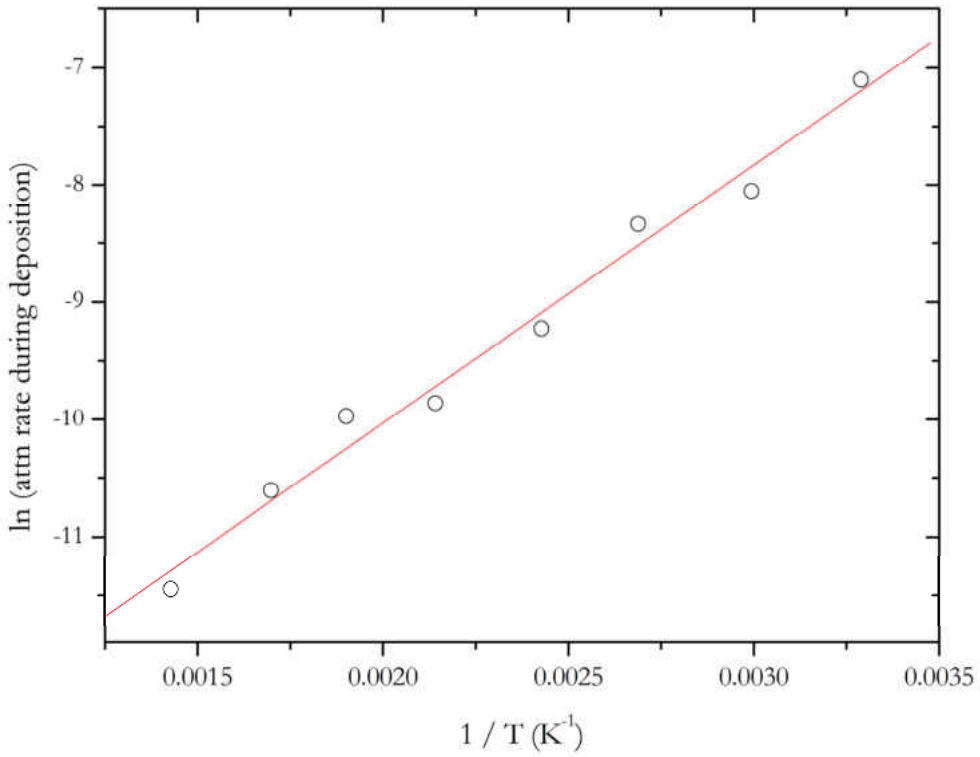

Figure 6.18 – *Arrhenius plot of the attenuation rate of the Au 4f core level following the transition point X_c until the termination of SnPc growth.*

6.3.2.2 Post-growth Clustering at Elevated Temperatures

At 2000 s the deposition of the SnPc terminates and a subsequent increase in core level intensity is observed which has already been attributed to post-growth clustering of the overlayer. However, the rate of clustering for this re-organisation process does not appear to be temperature dependent although a strong dependence is detected during growth. The intensity curves were fitted with the same exponential function as for the room temperature data (section 6.2.2.5) and the values obtained for the time constant parameter are presented in figure 6.19. This data suggests that temperature does not affect the rate of clustering after growth although there is a clear temperature dependence during growth. This inconsistency could be explained by the fact that a temperature dependency exists (with increasing clustering rates at higher temperature)

but that this trend is obscured due to the fact that high temperature clusters are closer to their most favourable configuration since clustering has been occurring for longer (since the transition point) by the end of deposition. Consequently the expected change in time constant is not observed since at the end of the growth phase all instances are in different configurations, with the higher temperature sample closer to a re-organisational energy minimum (i.e. the clustering rate also decreases as the system reaches closer to its most energetically favourable configuration). The combined effect of this is that the temperature-dependent nature of the molecular re-organisation is not observed in the core level intensities but further investigations would be required to prove this hypothesis.

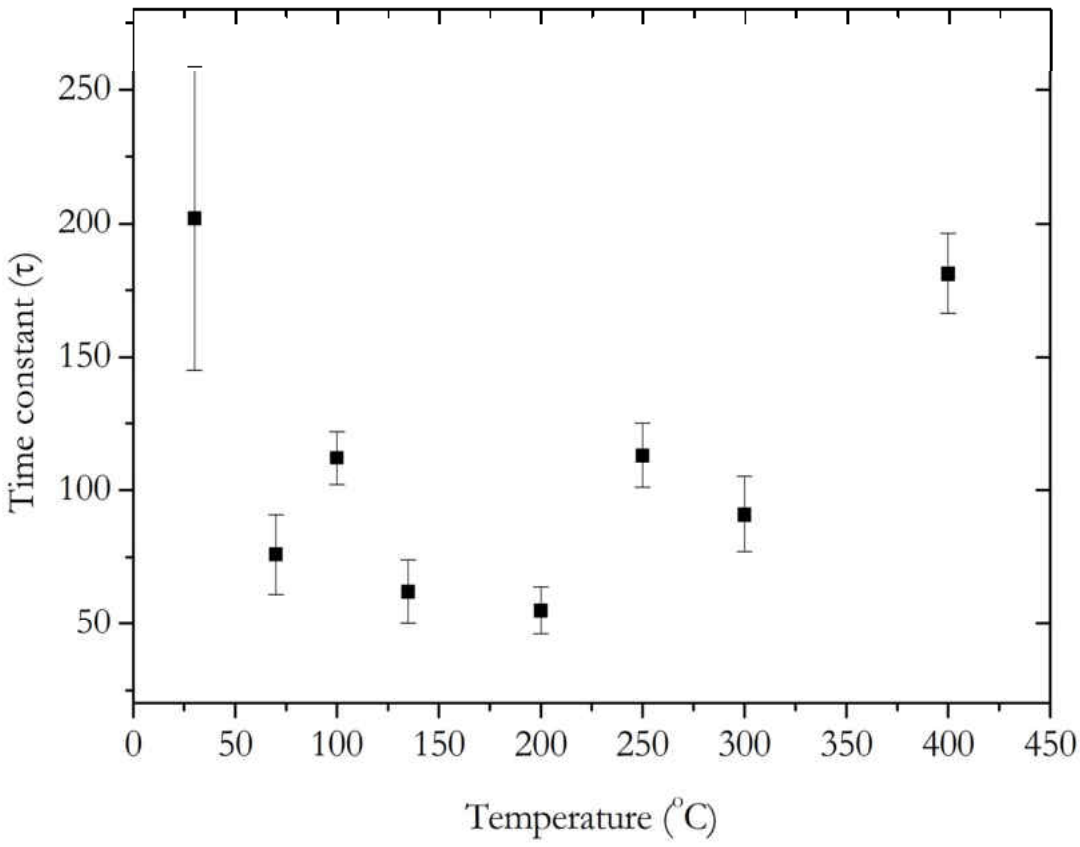

Figure 6.19 – *Post-growth clustering time constant against substrate temperature.*

6.4 Chapter Summary

The growth of SnPc on different substrates has been monitored using real-time SXPS and SnPc has been shown to undergo only weak interactions with the three substrates (Si(111):H, GaAs(001):S and polycrystalline Au) since no significant changes were observed in the core level lineshapes during growth. It has also been demonstrated that the Aberystwyth array detector has the ability to monitor multiple core levels regions (Ga 3d, As 3d, VBM and Sn 4d for GaAs) at sub-second time resolution during a single experiment while maintaining sufficient energy resolution.

The dynamic morphology of the SnPc growth on the three substrates was determined by analysis of the substrate core level intensities obtained using fitting of sequential snapshots. Reliable attenuation data was obtained for the three substrates using the Si 2p (for Si), As 3d (for GaAs) and Au 4f (for Au) core levels. The attenuation curves showed two well defined stages of growth followed by post-growth re-organisation of the SnPc overlayer into clusters, as confirmed by AFM measurements. Initially rapid attenuation of the core levels is observed. This attenuation rate was used to determine the mean free path for the electrons in the overlayer for all three substrates which corresponded with existing published data. This data was shown to agree with data obtained using conventional PES and provided extra information regarding the post-growth behaviour of thermally deposited SnPc molecules.

The onset of a well-defined transition point (referred to as X_c) was detected during growth. This point is proposed to be the transition from layer-by-layer to clustered growth and has a value that is substrate dependent. This value was suggested to be related to the arrangement of individual molecules within the first monolayer. These

molecules are deemed to stack at ever increasing angles with respect to the substrate plane for Si, GaAs and Au. This trend correlates well with the mean surface roughness of the substrates (measured using AFM). It is therefore suggested that an increased mean surface roughness results in an increased stacking angle relative to the substrate (a "standing up" configuration). Hence, more molecules are needed to achieve growth beyond the first layer causing the transition point to occur at a higher coverage.

The increase in substrate core level intensities after growth on all substrates is interpreted as post-growth molecular re-organisation on the SnPc overlayer. The rate of re-organisation was evaluated by fitting the intensity increase curves with an exponential function which gave a time constant (τ) that was dependent on the substrate and again correlated well with surface roughness. The time constant was evaluated to be 1342 ± 716 s (22 min), 1131 ± 166 s (19 min) and 366 ± 60 s (6 min) for the Si, GaAs and Au respectively. However, post-growth clustering was not observed in all cases. A short deposition of 100 s which gave a coverage of around 0.8 nm displayed only a single stage of growth (no transition point was observed) and no post-growth clustering. This suggests that it is a re-organisation phenomenon initiated only after a critical thickness is achieved.

Further studies were conducted on the effect of substrate temperature on the growth of SnPc on polycrystalline Au. The transition point X_c was found to be temperature dependent suggesting that both surface roughness and temperature has an effect on the molecular stacking within the first monolayer. There are two possible explainations for this. First, it is possible that at higher temperatures the molecules "lie flat" (or flatter) on the surface resulting in completion of the first monolayer at lower coverages. The

second explaination is that at higher temperatures clustering initiates earlier before a full monolayer is completed. The unknown effect of desorption also limits the ability to draw firm conclusions from this temperature-dependent data. The rate of post-growth clustering was further evaluated by fitting of the intensity increases occurring post-growth. Fitting of these intensities revealed that there was no obvious correlation between the rate and temperature since all time constant values obtained were between 50 and 200 s with no obvious correlation. This unexpected result may be explained by the fact that rate of clustering also depends on the time since the start of clustering, occuring sooner at higher temperatures. However, further work would be required to prove this conclusively.

References

1. Hung, L.S. and C.H. Chen, *Recent progress of molecular organic electroluminescent materials and devices.* Materials Science & Engineering R-Reports, 2002. **39**(5-6): p. 143-222.
2. Spanggaard, H. and F.C. Krebs, *A brief history of the development of organic and polymeric photovoltaics.* Solar Energy Materials and Solar Cells, 2004. **83**(2-3): p. 125-146.
3. Chua, L.L., et al., *General observation of n-type field-effect behaviour in organic semiconductors.* Nature, 2005. **434**(7030): p. 194-199.
4. Pope, M., H.P. Kallmann, and P. Magnante, *Electroluminescence in Organic Crystals.* The Journal of Chemical Physics, 1963. **38**(8): p. 2042-2043.
5. Tang, C.W., *2-Layer Organic Photovoltaic Cell.* Applied Physics Letters, 1986. **48**(2): p. 183-185.
6. Tang, C.W. and S.A. Vanslyke, *Organic Electroluminescent Diodes.* Applied Physics Letters, 1987. **51**(12): p. 913-915.
7. Burroughes, J.H., et al., *Light-emitting-diodes based on conjugated polymers.* Nature, 1990. **347**(6293): p. 539-541.
8. Mitschke, U. and P. Bauerle, *The electroluminescence of organic materials.* Journal of Materials Chemistry, 2000. **10**(7): p. 1471-1507.
9. Muccini, M., *A bright future for organic field-effect transistors.* Nature Materials, 2006. **5**(8): p. 605-613.
10. Brutting, W., *Device physics of organic light-emitting diodes based on molecular materials.* Organic Electronics, 2001. **2**: p. 1.
11. McKeown, N.B., *Phthalocyanine Materials.* Chemistry of Solid State Materials, ed. N.B. McKeown. 1998: Cambridge University Press.
12. Linstead, R.P., *Phthalocyanines. Part I. A New Type of Synthetic Colouring Matters.* Journal of the Chemical Society, 1934: p. 1016-1017.
13. Ao, R., L. Kummerl, and D. Haarer, *Present limits of data-storage using dye molecules in solid matrices.* Advanced Materials, 1995. **7**(5): p. 495.
14. Wohrle, D. and D. Meissner, *Organic Solar-Cells.* Advanced Materials, 1991. **3**(3): p. 129-138.

15. Lever, A.B.P., et al., *Recent studies in phthalocyanine chemistry.* Pure and Applied Chemistry, 1986. **58**(11): p. 1467-1476.
16. Bonnett, R., *Photosensitizers of the porphyrin and phthalocyanine series for photodynamic therapy.* Chemical Society Reviews, 1995. **24**(1): p. 19-33.
17. Robertson, J.M., *An X-Ray Study of the Structure of the Phthalocyanines. Part I. The Metal-free, Nickel, Copper, and Platinum Compounds.* Journal of the Chemical Society 1935: p. 615-621.
18. Usov, N.N. and Bendersk.Va, *Photoeffect in metal-free phthalocyanine crystals.* Physica Status Solidi, 1970. **37**(2): p. 535.
19. Day, P.N., Z. Wang, and R. Pachter, *Calculation of the structure and absorption spectra of phthalocyanines in the gas-phase and in solution.* Journal of Molecular Structure: THEOCHEM, 1998. **455**(1): p. 33-50.
20. Pan, Y.L., Chen, L.B., Wang, Y., Zhao, Y.Y., Li, F.M., Zhou, H.W., Wagiki, A., Yamashita, M., Tako, T., *Transient photocurrent and charge-transfer excitation bands in a tin-phthalocyanine (SnPc) polycrystalline film.* Applied Physics A-Materials Science & Processing, 1997. **65**: p. 425.
21. Forrest, S.R., *Ultrathin organic films grown by organic molecular beam deposition and related techniques.* Chemical Reviews, 1997. **97**(6): p. 1793-1896.
22. Schreiber, F., *Organic molecular beam deposition: Growth studies beyond the first monolayer.* Physica Status Solidi A-Applied Research, 2004. **201**(6): p. 1037-1054.
23. Kubiak, R. and J. Janczak, *X-ray analysis of phthalocyanines formed in the reaction of Au-Cu and Au-Sn alloys with 1,2-dicyanobenzene* Journal of Alloys and Compounds, 1992. **189**(1): p. 107-111.
24. Collins, R.A., A. Krier, and A.K. Abass, *Optical-properties of lead phthalocyanine (PbPc) thin-films.* Thin Solid Films, 1993. **229**(1): p. 113-118.
25. Friedel, M.K., et al., *A new metal(II) phthalocyanine structure - x-ray and mossbauer studies of triclinic tin(II) phthalocyanine.* Journal of The Chemical Society D-Chemical Communications, 1970(7): p. 400-&.
26. Ueno, N. and S. Kera, *Electron spectroscopy of functional organic thin films: Deep insights into valence electronic structure in relation to charge transport property.* Progress in Surface Science, 2008. **83**(10-12): p. 490-557.

27. Knupfer, M. and H. Peisert, *Electronic properties of interfaces between model organic semiconductors and metals.* Physica Status Solidi A-Applied Research, 2004. **201**(6): p. 1055-1074.
28. Gorgoi, M. and D.R.T. Zahn, *"Band bending" in copper phthalocyanine on hydrogen-passivated Si(111).* Organic Electronics, 2005. **6**(4): p. 168-174.
29. Steiner, H.J., *In-situ Monitoring of Copper Phthalocyanine on III-V Semiconductor Surfaces*. 2003, PhD Thesis, University of Wales, Aberystwyth.
30. Evans, D.A., et al., *Copper phthalocyanine on InSb(111)A - interface bonding, growth mode and energy band alignment.* Journal of Physics-Condensed Matter, 2003. **15**(38): p. S2729-S2740.
31. Cabailh, G., et al., *Soft X-ray photoelectron spectroscopy of metal-phthalocyanines on the (001) surface of GaAs and Ge.* J. Phys. IV, 2006. **132**: p. 11-15.
32. Vearey-Roberts, A.R., *Organic Semiconductor Interlayers and their Role in GaAs Diode Modification*. 2004, PhD Thesis, University of Wales, Aberystwyth.
33. Vearey-Roberts, A.R. and D.A. Evans, *Modification of GaAs Schottky diodes by thin organic interlayers.* Applied Physics Letters, 2005. **86**(7): p. 072105.
34. Wells, J.W., et al., *An XPS study of the interaction between tin(II) phthalocyanine and polycrystalline iron.* Journal of Electron Spectroscopy and Related Phenomena, 2004. **141**(1): p. 67-72.
35. Peltekis, N., et al., *The local electronic structure of tin phthalocyanine studied by resonant soft X-ray emission spectroscopies.* Applied Surface Science, 2007. **255**(3): p. 764-766.
36. Peisert, H., et al., *Orientation and electronic properties of phthalocyanines on polycrystalline substrates.* Physica Status Solidi B - Basic Solid State Physics, 2009. **246**(7): p. 1529-1545.
37. Kera, S., et al., *Growth mode and molecular orientation of phthalocyanine molecules on metal single crystal substrates: A NEXAFS and XPS study.* Surface Science, 2006. **600**(5): p. 1077-1084.
38. Evans, D.A., et al. *Synchrotron radiation studies of inorganic-organic semiconductor interfaces.* in *3rd International Conference on Synchrotron Radiation in Materials Science.* 2002. Singapore, Singapore: Elsevier Science Bv.
39. Zahn, D.R.T., G.N. Gavrila, and G. Salvan, *Electronic and vibrational spectroscopies applied to organic/inorganic interfaces.* Chemical Reviews, 2007. **107**(4): p. 1161-1232.

40. Peisert, H., et al., *Highly ordered phthalocyanine thin films on a technically relevant polymer substrate.* Journal of Applied Physics, 2004. **96**(7): p. 4009-4011.
41. Oehzelt, M., et al., *Crystallographic and morphological characterization of thin pentacene films on polycrystalline copper surfaces.* Journal of Chemical Physics, 2006. **124**(5): p. 6.
42. Peisert, H., et al., *Order on disorder: Copper phthalocyanine thin films on technical substrates.* Journal of Applied Physics, 2001. **90**(1): p. 466-469.
43. Karan, S. and B. Mallik, *Power spectral density analysis and photoconducting behavior in copper(II) phthalocyanine nanostructured thin films.* Physical Chemistry Chemical Physics, 2008. **10**(45): p. 6751-6761.
44. Papageorgiou, N., et al., *Physics of ultra-thin phthalocyanine films on semiconductors.* Progress in Surface Science, 2004. **77**(5-8): p. 139.
45. Gnoth, D.N., et al., *A comparison of S-passivation of III-V (001) surfaces using $(NH_4)_{2Sx}$ and S_2Cl_2.* Applied Surface Science, 1998. **123-124**: p. 120-125.
46. Brieva, A., *Structure and Morphology of Phthalocyanine Thin Films on Silicon-Based Substrates.* 2005, PhD Thesis, University of Wales, Aberystwyth.
47. Powell, C.J., *Energy and material dependence of the inelastic mean free-path of low-energy electrons in solids.* Journal of Vacuum Science & Technology A - Vacuum Surfaces and Films, 1985. **3**(3): p. 1338-1342.
48. Zangwill, A., *Physics at Surfaces.* 1988: Cambridge University Press.
49. Woolley, R.A.J., et al., *Adsorbed molecular shuttlecocks: An NIXSW study of Sn phthalocyanine on Ag(111) using Auger electron detection.* Surface Science, 2007. **601**(5): p. 1231-1238.
50. Vearey-Roberts, A.R., et al., *Growth and morphology of SnPc films on the S-GaAs(0 0 1) surface: a combined XPS, AFM and NEXAFS study.* Applied Surface Science, 2004. **234**(1-4): p. 131-137.
51. Marchetto, H., et al., *Influence of substrate morphology on organic layer growth: PTCDA on Ag(111).* Chemical Physics, 2006. **325**(1): p. 178-184.
52. Krause, B., et al., *Late growth stages and post-growth diffusion in organic epitaxy: PTCDA on Ag(111).* Surface Science, 2004. **572**(2-3): p. 385-395.
53. Pfuetzner, S., et al., *Thick C-60:ZnPc bulk heterojunction solar cells with improved performance by film deposition on heated substrates.* Applied Physics Letters, 2009. **94**(25): p. 3.

Chapter 7
Conclusions and Further Work

The primary aim of this work was to demonstrate the technique of real-time photoelectron spectroscopy and its ability to provide a greater understanding of surface processes and thin film growth in the field of carbon-based semiconductors. Real-time photoelectron spectroscopy was made possible due to a new array detector developed at Aberystwyth. This improvement in electron detection allows fast snapshot spectra to be taken during growth and annealing experiments allowing the evolution of spectral features to be monitored in real-time with sub-second time resolution.

The Aberystwyth Real-time Electron Spectroscopy (REES) system was adapted in order to allow several experimental parameters to be measured during an experiment. Parameters such as pressure, substrate temperature and evaporation source temperature were all recorded with the snapshot spectra giving a complete picture of the whole experiment and allowing an overview of the experimental system to be obtained at any given time in the experiment. This experimental configuration was deployed at

Aberystwyth for use with a laboratory Mg Kα source (Chapters 4 and 5) as well as on beamline end station chambers at the Synchrotron Radiation Source (SRS), Daresbury, UK (Chapters 5 and 6). This enabled the first reported real-time photoelectron spectroscopy experiments performed using a laboratory source. A diamond C 1s core level snapshot spectrum was also obtained in 25 ms using a synchrotron source. Progress has been made in the development of a next generation 1536 pixel detector which has a length in the dispersive direction which is twice that of the 768 pixel detector as well as an increased collection length in the non-dispersive direction. Future possible developments for this work includes the deployment of this technology in 2D allowing fast snapshot measurements to obtain angular resolution in addition to energy resolution at every time interval.

Two categories of carbon-based semiconductors were investigated during the course of these studies using this novel technique. The first category was synthetic single crystal diamond surfaces. In Chapter 4 a clean surface was obtained for a moderately doped p-type (001) synthetic single crystal diamond CVD by means of a chemical acid etch. This surface was characterised using XPS, LEED and AFM and found to be clean with sub-monolayer residual oxygen after annealing to a 1000 °C. This surface retained a 1 x 1 configuration and had a surface roughness (measured *ex situ* by AFM) of < 0.2 nm. This surface was annealed up to a maximum temperature of 1000 °C and the position of the C 1s core level peak was found to shift with temperature. This shift with temperature was found to be reversible up to ~ 800 °C with a maximum shift of ~ 1 eV to a lower kinetic energy. Beyond 800 °C the peak shift starts to decrease with increasing temperature. Then during cooling, a temperature independent region is observed until a temperature dependent path is regained at temperatures below 400 °C.

The position of this temperature independent path then set the maximum reversible peak shift attained for subsequent annealing cycles below that maximum temperature. This maximum peak shift was correlated to the amount of oxygen present on the diamond surface. A maximum shift of 1 eV was again attained following another acid etch. This effect was attributed to the creation of intermediate/temporary surface states in the band gap.

Further work required includes repeat measurements following reconstruction of the (001) surface to a 2 x 1 configuration as well as further investigations into temperature-dependent Fermi level shifts on other crystallographic planes. For example, some preliminary results for temperature dependent measurements on the (111) surface have been carried out using the 768 channel detector. *In situ* plasma for oxygen and hydrogen is currently being developed that will enable *in situ* cycling between oxygen, hydrogen and carbon terminated surfaces. Another parameter which needs to be considered is the doping concentration, therefore a systematic study of diamonds with varying levels of doping would be appropriate. Preliminary results indicate that reversible behaviour is also observed on highly boron doped single crystals. A repeat of these experiments with an n-type diamond sample would also be of great interest.

The growth of aluminium contacts *in vacuo* on the (001) diamond as well as subsequent high temperature annealing of the contact were investigated using real-time XPS. Real-time XPS provided complementary information to conventional spectroscopy by revealing the details of contact formation and contact performance at high temperature. Conventional spectroscopy revealed the formation of a Schottky barrier with the C 1s core level shifting to a lower kinetic energy. The aluminium layer was found to form a

rectifying Schottky contact with a barrier height (measured by current-voltage measurements) of 1.05 V and an ideality factor of 1.4. Annealing of the contact up to a temperature of 860 °C was found to result in the formation of a carbide species which causes loss of rectification and transition from a Schottky to an Ohmic contact. Real-time XPS of the annealing process up to 860 °C revealed that the transition is more complex than previously thought. After initial clustering of the aluminium layer at 410 °C, two distinct stages were identified at 480 °C and 770 °C which correspond to surface and sub-surface initiation of the reaction. Further work could include the study of aluminium contacts on single crystals which have different terminations such as hydrogen and reconstructed crystal surfaces as well as other metals on this surface. The formation of metal contacts on new n-type material would also be a priority due to current developments in this field.

The catalytic effect of iron in the graphitisation of diamond at high temperatures was investigated. Iron is known to substantially reduce the graphitisation temperature for diamond, and real-time SXPS gave an insight into the dynamics of this process. Conventional SXPS revealed the presence of a previously unreported carbide species on the diamond surface following deposition of a thin iron layer. Following deposition of a thicker iron layer the Fe-diamond interface was heated to a temperature of 850 °C during which real-time SXPS monitored the changes in the C 1s core level as it appeared from underneath the Fe layer during annealing. At 350 °C a carbide species was detected and increased in intensity up to a temperature of 750 °C. A second component identified as a graphitic C 1s core level was detected at 650 °C initially displaying a gradual increase in intensity followed by a rapid increase above 750 °C. This information was used to propose a mechanism for the graphitisation process

where the carbon atoms at the surface of the diamond diffuse into the iron layer resulting in the creation of carbide species within the iron layer. An increase in temperature increases the rate of graphitisation since the carbide becomes unstable resulting in the carbon atoms forming a graphite layer upon reaching the surface. Above 750 °C the increasing thickness of the graphite layers causes the iron layer to descend to a depth greater than the sampling depth for SXPS resulting in a spectrum dominated by a graphitic C 1s core level. NEXAFS and AFM measurements provided evidence that the resulting graphite layer was ordered, but further work is needed to understand this process properly. Etching of the graphite layer following graphitisation would allow measurements of the buried iron layer. This additional information could aid the understanding of the mechanism. Since the iron 'burrows' into the diamond this work could form the basis for an etching or nano patterning application for diamond. The work performed in this thesis forms the basis of a new project aimed at understanding and manipulating the nanostructures produced by Fe (as well as Co and Ni) metallic films on the diamond surface by real-time PES and PEEM. Etching of channels in diamond is currently of great interest due to the advent of diamond electronic devices. Further study of the resulting graphite layer could also determine if there is any graphene present or whether there is the possibility of manipulating this process to produce graphene.

The second category of carbon-based semiconductors investigated was thin organic films. Tin (II) phthalocyanine small molecules were deposited by organic molecular beam deposition (OMBD) using a Knudsen cell. Real-time SXPS was used to monitor the substrate core levels of Si (111), GaAs (001) and polycrystalline Au during growth with fitting of the substrate peaks providing attenuation curves for growth on the three

substrates. Analysis of the attenuation curves indicated the presence of two distinct growth stages, the first being an uniform layer-by-layer growth mode followed by a second clustered island growth mode initiating at a specific transition point which was determined with a higher accuracy than possible with conventional measurements and was found to be substrate dependent. A model has been proposed correlating the molecular orientation within the first monolayer with the measured thickness for the first layer of each substrate. After deposition was terminated an increase in the substrate peak intensity was measured and interpreted as post-growth re-organisation of the organic layer into an increasingly clustered configuration. The data suggested that the speed of this re-organisation was also substrate dependent. A theoretical molecular model for this re-organisation that qualitatively accounted for the observed PES data for clustered growth above the critical thickness was successfully developed.

Further temperature dependent growth studies were performed using a polycrystalline Au substrate held at temperatures ranging from 60 – 400 °C. This data showed evidence that the re-organisation of the SnPc molecules into clusters is initiated at a temperature-dependent transition point. The effect of desorption at elevated temperatures could not be quantified and therefore limited the ability to determine the precise nature of this temperature dependence. No clear temperature dependence was observed for the post-growth clustering phase. Further measurements where the growth is terminated at the transition point would be required to prove this conclusively. Measurements at temperatures below room temperature using a cryogenic sample cooling system would also provide important additional information. A systematic study of varying growth rates and coverage would also allow better understanding of this system. It is known that the barrier height for metal-inorganic

diodes can be modified using phthalocyanine interlayers therefore further work to determine if a similar modification behaviour occurs for metal-diamond diodes would also be of great interest. This real-time PES approach would also enable studies of other organic-diamond interfaces and would provide new opportunities to take advantage of the bio-compatibility of diamond and its potential for applications in biology and medicine.

To conclude, real-time photoelectron spectroscopy has been successfully applied to carbon-based semiconductors using new detector technology developed at Aberystwyth. The 768 array detector which forms the basis for the real-time electron spectroscopy (REES) system built at Aberystwyth produced the first real-time PES growth experiment using a laboratory X-ray source. A fast 25 ms snapshot spectrum was also obtained using a synchrotron radiation source. The technique was applied to two categories of carbon-based semiconductors, namely synthetic single crystal diamond and organic thin films. This has facilitated a deeper understanding of dynamic processes at the interfaces of these advanced materials, which is an important contribution if they are to underpin future technological advances.